

Copyright  
by  
Junting Huang  
2015

The Dissertation Committee for Junting Huang  
certifies that this is the approved version of the following dissertation:

**Sterile Neutrino Searches in MINOS and MINOS+  
Experiments**

Committee:

---

Karol Lang, Supervisor

---

Jack Ritchie

---

Roy Schwitters

---

Duane Dicus

---

Karl Gebhardt

**Sterile Neutrino Searches in MINOS and MINOS+  
Experiments**

by

**Junting Huang, B.S., M.S.**

**DISSERTATION**

Presented to the Faculty of the Graduate School of  
The University of Texas at Austin  
in Partial Fulfillment  
of the Requirements  
for the Degree of

**DOCTOR OF PHILOSOPHY**

THE UNIVERSITY OF TEXAS AT AUSTIN

May 2015

Dedicated to my family.

# Acknowledgments

The completion of this dissertation is the result of the effort of many people.

First of all I would like to thank my advisor Karol Lang who guided me through the years in graduate school with his enthusiasm on experimental particle physics. His encouragement and open-mindedness has benefited me greatly.

In the Texas group, I had many inspiring discussions with Federico Nova. His genuine interest in physics and patience for my questions boosted my interest in research. My understanding of the MINOS experiment is due to the help I received from Son Cao and Rashid Mehdiyev. Having Son as a teammate also made the work and life at Fermilab easier and more enjoyable. Marek Proga provided tremendous support on the hardware work, making many tasks possible. Simon De Rijck, Federico Nova, Paul Sail, and Thomas Carroll gave a careful reading of this dissertation and provided a lot of important feedback. Many thanks also go to Zachary Liptak, John Cesar, Adam Schreckenberger, and Will Flanagan for their fruitful support.

In the MINOS collaboration, Robert Plunkett showed me great hospitality when I moved to Fermilab. In addition, the patience of Robert Hatcher and Art Kreymer have significantly improved my skills and increased my inter-

est in computing. Discussions with Andy Blake and Joao Coelho shed much light upon the analyses of this dissertation. Alex Sousa provided much support through my work in both MINOS and NO $\nu$ A. The preceding work of Alena Gavrilenko, Joe O'Connor, Ashley Timmons, Adam Aurisano, and many others has laid a solid foundation for this dissertation. Furthermore, I would like to thank Justin Evans, Mike Kordosky, Donna Naples, Greg Pawloski, Tricia Vahle, Benton Pahlka, Ryan Nichol, and Jenny Thomas for their irreplaceable contributions to this dissertation.

Finally, I would like to thank my family for their patience and constant support for my career.

# Sterile Neutrino Searches in MINOS and MINOS+ Experiments

Publication No. \_\_\_\_\_

Junting Huang, Ph.D.

The University of Texas at Austin, 2015

Supervisor: Karol Lang

This dissertation presents the searches on sterile neutrinos using the data collected in MINOS+ Experiment from September 2013 to September 2014, and the full data set of MINOS Experiment collected from 2005 to 2012. Anomalies in short baseline experiments, such as LSND and MiniBooNE, showed hints of sterile neutrinos, a type of neutrino that does not interact with the Standard Model particles. In this work, two models are considered: 3+1 and large extra dimension (LED). In the 3+1 model, one sterile neutrino state is added into the standard oscillation scheme consisting of three known active neutrino states  $\nu_e$ ,  $\nu_\mu$  and  $\nu_\tau$ . In the LED model, sterile neutrinos arise as Kaluza-Klein (KK) states due to assumed large extra dimensions. Mixing between sterile and active neutrino states may modify the oscillation patterns observed in the MINOS detectors. Both searches yield null results. For 3+1, a combined fit of MINOS and MINOS+ data gives a stronger limit on  $\theta_{24}$  in the range of  $10^{-2} \text{ eV}^2 < \Delta m_{43}^2 < 1 \text{ eV}^2$  than previous experiments. For LED,

with the complete MINOS data set, the size of extra dimensions is constrained to be smaller than  $\sim 0.35 \mu\text{m}$  at 90% C.L. in the limit of a vanishing lightest neutrino mass.



# Table of Contents

<b>Acknowledgments</b>	<b>v</b>
<b>Abstract</b>	<b>vii</b>
<b>List of Tables</b>	<b>xiii</b>
<b>List of Figures</b>	<b>xiv</b>
<b>Chapter 1. Neutrino Physics</b>	<b>1</b>
1.1 Discovery of Neutrinos . . . . .	1
1.2 Neutrino Oscillations . . . . .	5
1.2.1 Solar Neutrinos . . . . .	5
1.2.2 Atmospheric Neutrinos . . . . .	7
1.2.3 Reactor Neutrinos . . . . .	8
1.2.4 Beam Neutrinos . . . . .	9
1.3 Oscillations Formalism . . . . .	10
1.3.1 Generic Formula . . . . .	10
1.3.2 Standard Three Flavor Oscillation Model . . . . .	13
<b>Chapter 2. Sterile Neutrinos</b>	<b>17</b>
2.1 Experimental Anomalies . . . . .	17
2.1.1 LSND . . . . .	18
2.1.2 MiniBooNE . . . . .	20
2.1.3 Reactor Anomaly . . . . .	20
2.1.4 Gallium Anomaly . . . . .	22
2.2 3+1 Model . . . . .	23
2.3 Large Extra Dimension Model . . . . .	26

<b>Chapter 3. MINOS and MINOS+ Experiments</b>	<b>46</b>
3.1 MINOS . . . . .	46
3.2 MINOS+ . . . . .	48
3.3 NuMI Beam . . . . .	51
3.4 Detectors . . . . .	54
3.4.1 Near Detector . . . . .	57
3.4.2 Far Detector . . . . .	61
3.5 Neutrino Interactions in the Detectors . . . . .	62
<b>Chapter 4. Shower Energy Reconstruction</b>	<b>66</b>
4.1 $k$ NN Shower Energy . . . . .	67
4.2 Resolution Improvement . . . . .	73
4.3 Considerations on Improving $k$ NN Shower Energy . . . . .	75
4.4 Systematic Error . . . . .	76
4.4.1 Absolute Energy Scale . . . . .	77
4.4.2 Intranuclear Rescattering with INTRANUKE . . . . .	78
4.4.3 Special MC Samples . . . . .	81
4.4.4 Combined Errors . . . . .	84
<b>Chapter 5. NC Event Selection</b>	<b>85</b>
5.1 Acceptance . . . . .	85
5.2 NC Cleaning at ND . . . . .	90
5.3 Separation of NC Events from CC Events . . . . .	92
5.4 Systematic Errors . . . . .	93
5.4.1 Acceptance . . . . .	93
5.4.2 NC Cleaning . . . . .	99
<b>Chapter 6. CC Event Selection</b>	<b>108</b>
6.1 Acceptance . . . . .	109
6.2 Separation of CC Events from NC Events . . . . .	109
6.3 Systematic Error . . . . .	120
6.3.1 Acceptance . . . . .	120
6.3.2 NC Background . . . . .	121

<b>Chapter 7. Systematic Error Bands and Covariance Matrices</b>	<b>124</b>
7.1 Overview . . . . .	125
7.1.1 Fractional Error . . . . .	125
7.1.2 Covariance Matrix . . . . .	127
7.1.3 Cross Sections . . . . .	128
7.2 Systematics for CC Sample . . . . .	128
7.3 Systematics for NC Sample . . . . .	152
7.4 Combined Systematic Errors . . . . .	173
<b>Chapter 8. The 3+1 Sterile Neutrino Analysis</b>	<b>177</b>
8.1 Strategy . . . . .	177
8.1.1 Far-over-near Ratio . . . . .	178
8.1.2 Expression of $\chi^2$ . . . . .	178
8.1.3 Binning Scheme . . . . .	181
8.2 Performing the Fit . . . . .	181
8.2.1 $\chi^2$ Surface . . . . .	183
8.2.2 Effect of the Systematics . . . . .	186
8.3 Feldman-Cousins Correction . . . . .	186
8.4 Combining with Bugey . . . . .	189
8.5 Discussions . . . . .	194
<b>Chapter 9. Large Extra Dimension Analysis</b>	<b>200</b>
9.1 Strategy . . . . .	200
9.1.1 Far-over-near Ratio . . . . .	201
9.1.2 Expression of $\chi^2$ . . . . .	204
9.2 Performing the Fit . . . . .	205
9.2.1 Ghost Fitter . . . . .	206
9.2.2 $\chi^2$ Surface . . . . .	210
9.2.3 Effect of Systematics . . . . .	210
9.3 Feldman-Cousins Correction . . . . .	210
9.4 Limits from Other Experiments . . . . .	218
<b>Chapter 10. Summary and outlook</b>	<b>220</b>

<b>Appendices</b>	<b>222</b>
<b>Appendix A. Strip-to-strip Calibration</b>	<b>223</b>
A.1 Calibration Chain . . . . .	223
A.2 Results of Strip-to-strip Calibration . . . . .	227
<b>Appendix B. Formulas of 3+1 Model</b>	<b>231</b>
B.1 Generic Formulas . . . . .	231
B.2 $\nu_\mu \rightarrow \nu_e$ Channel . . . . .	234
B.3 $\nu_\mu \rightarrow \nu_\mu$ Channel . . . . .	236
B.4 $\nu_\mu \rightarrow \nu_s$ Channel . . . . .	237
<b>Appendix C. Formulas of Large Extra Dimension Model</b>	<b>240</b>
C.1 From Action to Lagrangian . . . . .	240
C.2 From Lagrangian to Oscillation Probabilities . . . . .	244
<b>Appendix D. Neutrino Production</b>	<b>259</b>
D.1 Decays of $\pi^\pm$ and $K^\pm$ . . . . .	259
D.2 Decays of $\mu^\pm$ . . . . .	263
<b>Appendix E. Fitting with Correlated Systematics</b>	<b>274</b>
E.1 Two Methods . . . . .	274
E.2 Equivalence . . . . .	275
<b>Bibliography</b>	<b>278</b>
<b>Vita</b>	<b>295</b>

# List of Tables

1.1	Global fit result of the standard three flavor oscillation model from Reference [47]. Note that $\delta m^2 \equiv \Delta m_{21}^2$ and $\Delta m^2 \equiv m_3^2 - (m_1^2 - m_2^2)/2$ , with $+\Delta m^2$ for NH and $-\Delta m^2$ for IH. . . . .	16
2.1	Default 3+1 model parameters used in Figures 2.4 to 2.9. . . .	27
3.1	Summary of the data collected in MINOS in terms of the POT exposure. The majority of the data comes from a low energy beam (LE) with an energy peak around 3 GeV. A small fraction of the data comes from a pseudo high energy beam (pHE) with an energy peak around 7 GeV. . . . .	49
7.1	List of systematics by categories. . . . .	126
7.2	Details of the cross section systematics. The content is taken from [109]. . . . .	129
7.3	CC systematics list. . . . .	131
7.4	NC systematics list. . . . .	154
8.1	Fixed parameters used in the 3+1 model fit. . . . .	183
8.2	Best fit values by fitting to MINOS only, MINOS+ only and the combined fit. . . . .	196
8.3	Best fit values by fitting to CC only, NC only, and CC+NC. Note that $\theta_{34}$ should not affect CC so the best fit value is close to its initial value 0. . . . .	197
9.1	Fixed oscillation parameters used in the fit. . . . .	206
9.2	Discrete grid points used in the Ghost Fitter. . . . .	207
D.1	Correspondence between the general notations for leptons used in Equation D.18 and the notations of a special case used in Equation D.19. . . . .	263

## List of Figures

1.1	Measurements of the hadron production cross-section around the Z resonance. The data consist of 17 million Z decays accumulated by the ALEPH, DELPHI, L3 and OPAL experiments at LEP, and 600 thousand Z decays by the SLD experiment using a polarized beam at SLC. The curves represent the predicted cross-section for two, three and four neutrino species with Standard Model (SM) couplings and negligible mass. The plot is taken from Reference [8]. . . . .	4
1.2	The solar neutrino spectrum predicted by the BS05(OP) standard solar model [17]. The plot is taken from Reference [18]. .	6
1.3	Oscillation probabilities as a function of $L/E$ in MINOS at the near and far detectors (ND and FD). The simulated energy spectra are shown as the gray bands. . . . .	15
1.4	Schematic of the two neutrino mass hierarchies. The color coding indicates the fraction $ U_{\alpha i} ^2$ of each flavor $\nu_\alpha$ ( $\alpha = e, \mu, \tau$ ) contained in each mass eigenstate. The plot is taken from Reference [46]. . . . .	15
2.1	A $\sin^2 2\theta - \Delta m^2$ oscillation parameter fit for the entire data sample, $20 < E_e < 200$ MeV. The fit includes primary $\bar{\nu}_\mu \rightarrow \bar{\nu}_e$ oscillations and secondary $\nu_\mu \rightarrow \nu_e$ oscillations, as well as all known neutrino backgrounds. The allowed region is shown in blue (90% C.L.) and yellow (99% C.L.). Other curves are 90% CL limits from the Bugey reactor experiment [57], the CCFR experiment at Fermilab [58], the NOMAD experiment at CERN [59], and the KARMEN experiment at ISIS [60]. The plot is taken from Reference [49]. . . . .	19
2.2	MiniBooNE allowed regions in combined neutrino and antineutrino mode for events with $200 < E_\nu^{QE} < 3000$ MeV within a two-neutrino $\nu_\mu \rightarrow \nu_e$ and $\bar{\nu}_\mu \rightarrow \bar{\nu}_e$ oscillation model. Also shown is the $\bar{\nu}_\mu \rightarrow \bar{\nu}_e$ limit from the KARMEN experiment [65]. The shaded areas show the 90% and 99% C.L. LSND $\bar{\nu}_\mu \rightarrow \bar{\nu}_e$ allowed regions. The black star shows the best fit point. The plot is taken from Reference [51]. . . . .	21

2.3	Illustration of the short baseline reactor antineutrino anomaly. The red line shows a possible three active neutrino mixing solution, with $\sin^2(2\theta_{13}) = 0.06$ . The blue line displays a possible solution including a new neutrino mass state, with $ \Delta m^2  \gg 1 \text{ eV}^2$ and $\sin^2(2\theta) = 0.12$ . The plot is taken from Reference [52]. . .	22
2.4	Effect of $\Delta m_{32}^2$ on $P(\nu_\mu \rightarrow \nu_\mu)$ (top) and $1 - P(\nu_\mu \rightarrow \nu_s)$ (bottom). Other parameters are set to the values listed in Table 2.1. The simulated energy spectra for the near and far detectors (ND and FD) are shown as the gray bands. . . . .	28
2.5	Effect of $\Delta m_{41}^2$ on $P(\nu_\mu \rightarrow \nu_\mu)$ (top) and $1 - P(\nu_\mu \rightarrow \nu_s)$ (bottom). Other parameters are set to the values listed in Table 2.1. The simulated energy spectra for the near and far detectors (ND and FD) are shown as the gray bands. . . . .	29
2.6	Effect of $\theta_{23}$ on $P(\nu_\mu \rightarrow \nu_\mu)$ (top) and $1 - P(\nu_\mu \rightarrow \nu_s)$ (bottom). Other parameters are set to the values listed in Table 2.1. The simulated energy spectra for the near and far detectors (ND and FD) are shown as the gray bands. . . . .	30
2.7	Effect of $\theta_{24}$ on $P(\nu_\mu \rightarrow \nu_\mu)$ (top) and $1 - P(\nu_\mu \rightarrow \nu_s)$ (bottom). Other parameters are set to the values listed in Table 2.1. The simulated energy spectra for the near and far detectors (ND and FD) are shown as the gray bands. . . . .	31
2.8	Effect of $\theta_{34}$ on $P(\nu_\mu \rightarrow \nu_\mu)$ (top) and $1 - P(\nu_\mu \rightarrow \nu_s)$ (bottom). Other parameters are set to the values listed in Table 2.1. The simulated energy spectra for the near and far detectors (ND and FD) are shown as the gray bands. . . . .	32
2.9	Effect of $\delta_{24}$ on $P(\nu_\mu \rightarrow \nu_\mu)$ (top) and $1 - P(\nu_\mu \rightarrow \nu_s)$ (bottom). Other parameters are set to the values listed in Table 2.1. The simulated energy spectra for the near and far detectors (ND and FD) are shown as the gray bands. . . . .	33
2.10	Excluded regions in $a - m_0$ plane based on the simulated charge current sample of $7.24 \times 10^{20}$ POT $\nu_\mu$ running in MINOS by Reference [71]. $m_0$ is the lightest neutrino mass and $a$ is the extra dimension size. . . . .	38
2.11	$P(\nu_\mu \rightarrow \nu_\mu)$ at MINOS far detector. . . . .	40
2.12	LED oscillation probabilities as a function of $L/E$ for $a = 0.5 \mu\text{m}$ and $m_0 = 0 \text{ eV}$ . The simulated energy spectra for the near detector (ND) and far detector (FD) are represented by the gray bands. The darker bands contain 68% of the data and the lighter bands contain 90% of the data. . . . .	41

2.13	LED oscillation probabilities as a function of $L/E$ for $a = 1 \mu\text{m}$ and $m_0 = 0 \text{ eV}$ . . . . .	42
2.14	LED oscillation probabilities as a function of $L/E$ for $a = 0.5 \mu\text{m}$ and $m_0 = 0.1 \text{ eV}$ . . . . .	43
2.15	LED oscillation probabilities as a function of $L/E$ for different values of $\delta_{CP}$ . Curves of different $\delta_{CP}$ have different line styles. The blue curves are for $P(\nu_\mu \rightarrow \nu_\mu)$ with the solid on the top. The red curves are for $1 - P(\nu_\mu \rightarrow \nu_s)$ also with the solid on the top. . . . .	44
2.16	LED oscillation probabilities as a function of $L/E$ for normal hierarchy (NH, solid lines) and inverted hierarchy (IH, dashed lines), with $a = 0.5 \mu\text{m}$ and $m_0 = 0 \text{ eV}$ . For the inverted hierarchy, the sign of $\Delta m_{32}^2 \equiv m_3^2 - m_2^2$ is set to negative. . . .	45
3.1	The MINOS neutrino beamline. The $\nu_\mu/\bar{\nu}_\mu$ beam is produced in the NuMI facility at Fermilab. It passes through the ND at Fermilab and the FD in the Soudan mine in northern Minnesota. The baseline is 735 km. The figure is taken from Reference [73].	47
3.2	MINOS accumulated an exposure of $15.6 \times 10^{20}$ protons-on-target between 2005 and 2012. Most of the data is taken in the low energy $\nu_\mu$ -beam mode (in green) and in the $\bar{\nu}_\mu$ -beam mode (in orange). The special runs with the higher energy mode or the magnetic horn turned off are shown in red. The plot is taken from Reference [74]. . . . .	48
3.3	Results of a combined analysis of $\nu_\mu$ disappearance and $\nu_e$ appearance using its complete set of accelerator and atmospheric neutrino data. The plots are taken from Reference [39]. . . . .	50
3.4	Difference between the low energy $\nu_\mu$ beam used in MINOS (top) and the medium energy $\nu_\mu$ beam used in MINOS+ (bottom). The plots are taken from Reference [77]. . . . .	52
3.5	MINOS+ accumulated an exposure of $2.99 \times 10^{20}$ protons-on-target between September 2013 and September 2014. The plot is taken from Reference [78]. . . . .	53
3.6	A schematic of the NuMI beam. The key elements are shown, including the target, the horns, the decay pipe, the hadron absorber, and the muon shield which consists of the dolomite rock preceding the MINOS near detector. The figure is taken from Reference [79]. . . . .	55



3.7	Focusing of pions and kaons using two magnetic horns. Horn 1 and 2 are separated by a distance of 10 m. A collimating baffle upstream of the target protects the horns from direct exposure to misdirected proton beam pulses. The target and baffle system can be moved further upstream of the horns to produce higher energy neutrino beams. The vertical scale is 4 times that of the horizontal (beam axis) scale. The figure is taken from Reference [80]. . . . .	56
3.8	Structure of a single scintillator strip. Light produced by an ionizing particle is reflected multiple times inside the strip by the 0.25 mm-thick outer reflective coating. Scintillation light absorbed by the WLS fiber is re-emitted isotropically, and the wavelength-shifted photons whose directions fall within the total internal reflection cones are transported along the fiber to the edges of the strip. The figure is taken from Reference [81].	57
3.9	Illustration of the readout for a scintillator plane. The light produced in a strip (see Figure 3.8) is guided out of the module by a WLS fiber, and routed through a clear optical fiber to a pixel of the PMT. The figure is taken from Reference [81]. . .	58
3.10	End view of the near detector looking along the direction of the beam. The drawing (left) identifies detector elements shown in the photograph (right): “A” is the furthest upstream steel plane, “B” is the magnet coil, and “C” is an electronics rack on the elevated walkway. The NuMI beam intersects the near detector near the “A” label. The figure is taken from Reference [81]. . . . .	59
3.11	The four different configurations of planes used in the near detector, showing the different layouts of the scintillator modules. The upper two figures show partially instrumented planes (calorimeter region) while the lower two figures show the fully instrumented ones (tracking region). Strips oriented in the U direction are on the left, and V, on the right. These orientations alternate in the detector to provide stereo readout. The G-N notations denote the different shapes of the scintillator modules. The U and V planes require slight variations on each shape, leading to a total of 16 module types. The beam is centered midway between the coil hole and the left side of the plane, so that the scintillators only need to cover that area in the target region. The figure is taken from Reference [81]. . . . .	60

3.12	End views of the second far detector supermodule, looking toward Fermilab. The drawing (left) identifies detector elements shown in the photograph (right): “A” is the furthest downstream steel plane, “B” is the cosmic ray veto shield, “C” is the end of the magnet coil and “D” is an electronics rack on one of the elevated walkways alongside the detector. The horizontal structure above the detector is the overhead crane bridge. The figure is taken from Reference [81]. . . . .	61
3.13	Layout of U (left) and V (right) modules in far detector planes. U- and V-type planes are interleaved. A and B module types have 28 scintillator strips and the other types have 20 strips. The first (upstream) scintillator plane of each supermodule is of the V-type. The figure is taken from Reference [81]. . . . .	62
3.14	Top: Feynman diagram of a CC interaction between a $\nu_\mu$ and iron. Bottom: simulated CC event display. The colored dots represents signals of different strength in the scintillator strips. The outgoing muon forms a long track used to identify the CC interactions. The curvature of the track is caused by the magnetic field in the detector, and is used to determine the charge sign. The figures are taken from [82]. . . . .	63
3.15	$\nu_\mu$ and $\bar{\nu}_\mu$ CC interaction cross sections in the MINOS detectors.	65
3.16	Top: Feynman diagram of a NC interaction between a neutrino and iron. Bottom: simulated NC event display. The figures are taken from Reference [82]. . . . .	65
4.1	Distributions of $k$ NN shower variables in MINOS and MINOS+. The three variables used for the $k$ NN shower energy are the number of planes in a shower, energy of the first two showers, and dewighted shower energy near the track vertex. True shower energy distributions are also shown. . . . .	69
4.2	Scanning the number of neighbors $k$ . Y-axis is the $\chi^2$ at point $\Delta m^2 = 2.88 \times 10^{-3} \text{ eV}^2$ and $\sin^2 2\theta = 0.72$ . The highest point is at $k = 440$ . . . . .	71
4.3	The profile of $E_{kNN}/E_{true}$ as a function of $E_{true}$ , shown as the red histogram in the top plot, is fitted with a 14 <sup>th</sup> order logarithmic polynomial function as shown in the bottom plot. . . . .	72
4.4	The ratio of $k$ NN shower energy $E_{kNN}$ to true shower energy $E_{true}$ as a function of true shower energy $E_{true}$ before and after the three iterations of energy corrections using 14 <sup>th</sup> order polynomial functions. . . . .	73

4.5	Energy resolution improvement of $k$ NN shower energy over calorimetric shower energy as a function of true shower energy. Y-axis is the mean deviation improvement as a fraction of true shower energy. . . . .	74
4.6	MINOS+ sensitivities to the standard oscillation model with statistical error only assuming $18 \times 10^{20}$ POT worth of data. Contours of 90% C.L. for using the calorimetric shower energy, $k$ NN shower energy, and true shower energy are shown. For comparisons, the contours of pulling the calorimetric energy toward the true shower energy by 10% and 20% event by event are also plotted. . . . .	75
4.7	Systematic error of $k$ NN shower energy based on the absolute energy scale uncertainty. The result is calculated from applying $\pm 5.7\%$ shift to the calorimetric input variables. . . . .	78
4.8	Systematic shifts calculated from the INTRANUKE reweighting.	80
4.9	Systematic shifts calculated from the special MC samples. . .	83
4.10	Combined $k$ NN shower energy systematics. The red curve is the parameterization of the calorimetric shower energy systematics used in MINOS [99]. . . . .	84
5.1	XY-view of the NC event vertices at ND. The solid black shape represents the accepted region, whose boundary is 0.5 m away from edges of the partial U or V planes. . . . .	86
5.2	XY-view of the NC event vertices at FD. . . . .	87
5.3	Distribution of event vertex X position at ND. . . . .	87
5.4	Distribution of event vertex Y position at ND. . . . .	88
5.5	Distribution of event vertex Z position at ND. . . . .	88
5.6	Distribution of event vertex X position at FD. . . . .	89
5.7	Distribution of event vertex Y position at FD. . . . .	89
5.8	Distribution of event vertex Z position at FD. . . . .	90
5.9	Slice pulse height fraction variable in the ND, as used in the cleaning, for Run 11. The black points are the data, the red lines are the total MC and the hatched histograms are the poorly reconstructed events that are to be removed by the cleaning. The arrows are oriented to indicate which regions of the plots are accepted by the cuts. . . . .	91

5.10	Maximum consecutive planes variable in the ND, as used in the cleaning, for Run 11. The black points are the data, the red lines are the total MC and the hatched histograms are the poorly reconstructed events that are to be removed by the cleaning. The arrows are oriented to indicate which regions of the plots are accepted by the cuts. . . . .	92
5.11	Track extension cut at ND. The selected events are to the left of the blue line. . . . .	94
5.12	Event length cut at ND. The selected events are to the left of the blue line. . . . .	94
5.13	Track extension cut at FD. The selected events are to the left of the blue line. . . . .	95
5.14	Event length cut at FD. The selected events are to the left of the blue line. . . . .	95
5.15	Efficiency and purity for the NC selections at ND. . . . .	96
5.16	Efficiency and purity for the NC selections at FD. . . . .	96
5.17	Simulated NC event energy spectrum at ND combining both MINOS and MINOS+ samples. The main backgrounds are CC events, along with a small amount of beam $\nu_e$ . . . . .	97
5.18	Simulated NC event energy spectrum at FD combining both MINOS and MINOS+ samples. In addition to the CC events, there are also backgrounds from the $\nu_e$ and $\nu_\tau$ appearance. . . . .	98
5.19	Top: Effect of $\theta_{34}$ on $\nu_\mu \rightarrow \nu_s$ oscillation at ND. Bottom: Effect of $\Delta m_{43}^2$ and $\theta_{24}$ on the oscillation probability at ND with $\theta_{34} = 0$ . Z-axis (color) is equal to $1 - P(\nu_\mu \rightarrow \nu_s)$ . The blue region is where large ND oscillations happen. . . . .	101
5.20	Pulse height fraction distribution for energy bin $0.5 \text{ GeV} < E_{reco} < 1 \text{ GeV}$ . . . . .	102
5.21	Maximum consecutive planes distribution for energy bin $0.5 \text{ GeV} < E_{reco} < 1 \text{ GeV}$ . . . . .	102
5.22	$\chi^2$ of data-MC difference from re-scaling the poorly reconstructed components in the three energy bins. X-axis is the scaling factor reduced by 1. . . . .	103
5.23	NC event energy spectra without the preselection cuts. . . . .	104
5.24	NC event energy spectra with all cuts applied. . . . .	104
5.25	NC cleaning systematics error bands for $\theta_{34} = 0$ and each plot corresponds to a point in Fig. 5.19 for different values of $\theta_{24}$ and $\Delta m_{43}^2$ . . . . .	106

5.26	Top: NC cleaning systematics error bands by taking the largest error resulted from 120 sets of oscillation parameters for each energy bin. Bottom: A parameterization to be used in the fast generation of the shifted MC. . . . .	107
6.1	XY-view of the CC event vertices at ND (black disk). . . . .	110
6.2	Fiducial volume for CC events at ND. . . . .	110
6.3	XY-view of the CC event vertices at FD (black dot). . . . .	111
6.4	PID variables. . . . .	113
6.5	Top: PID distributions of true CC events (signal) and true NC events (background) at ND. Bottom: comparison between data and MC in the PID distribution for all events. . . . .	115
6.6	$\chi^2$ of the test point as the function of PID cut. The test point is located at $\Delta m^2 = 2.88 \times 10^{-3}$ and $\sin^2 2\theta = 0.72$ in the $\Delta m^2 - \sin^2 2\theta$ plane. The optimal value which corresponds to the largest $\chi^2$ is around 0.3. . . . .	116
6.7	MINOS+ sensitivities to the standard oscillation model with statistics only assuming $18 \times 10^{20}$ POT worth of data. Contours of 90% C.L. before and after the retraining are shown. The black contour was made with true PID representing the ideal case. . . . .	117
6.8	Efficiency and purity for the ND CC events. . . . .	118
6.9	Efficiency and purity for the FD CC events. . . . .	118
6.10	Simulated CC event spectrum at ND. . . . .	119
6.11	Simulated CC event spectrum at FD. . . . .	119
6.12	Distribution of the best fit points for 120 oscillation parameters. The largest absolute value on the NC scaling factor (Y-axis) is 0.756, and is used for calculating the NC background systematics. . . . .	122
6.13	Free scaling CC (X-axis) and NC components (Y-axis) to best match MC with data. Each plot corresponds to a different point in Figure 5.19 for different values of $\theta_{34}$ and $\Delta m_{43}^2$ . $\theta_{34}$ is set to $\pi/4$ . . . . .	123
7.1	An examination of the mis-modeling across the CC fiducial volume. The plus and minus shifts correspond to the CC events originating on the left and right half of the fiducial volume. The top four plots are the error bands for the CC sample. The bottom plot is the corresponding covariance matrix. . . . .	132

7.2	An examination of the mis-modeling of the CC fiducial volume. The shifted distribution is constructed by tightening the fiducial radius from 80 cm to 60 cm. The top four plots are the error bands for the CC sample. The bottom plot is the corresponding covariance matrix. . . . .	133
7.3	An examination of the mis-modeling of the CC fiducial volume. The shifted distribution is constructed by tightening the fiducial Z cut from 4.07710 m to 2.5 m. The top four plots are the error bands for the CC sample. The bottom plot is the corresponding covariance matrix. . . . .	134
7.4	An examination of the mis-modeling of the coil hole. The shifted distribution is constructed by turning off the coil hole cut. The top four plots are the error bands for the CC sample. The bottom plot is the corresponding covariance matrix. . . . .	135
7.5	An examination of the mis-modeling of the spectrometer join region. The shifted distribution is constructed by remove all events with a track ending within 10 planes of the start of the spectrometer. The top four plots are the error bands for the CC sample. The bottom plot is the corresponding covariance matrix.	136
7.6	An examination of the mis-modeling of side exiting tracks. The shifted distribution is constructed by turning off the containment cut. The top four plots are the error bands for the CC sample. The bottom plot is the corresponding covariance matrix.	137
7.7	An examination of the mis-modeling of back exiting tracks. The shifted distribution is constructed by removing all events with a track ending within 10 planes of the end of the near detector. The top four plots are the error bands for the CC sample. The bottom plot is the corresponding covariance matrix. . . . .	138
7.8	CC shower energy scale systematic error. The shower energy is scaled 5 – 10% depending on the energy. The top four plots are the error bands for the CC sample. The bottom plot is the corresponding covariance matrix. . . . .	139
7.9	CC track energy scale systematic error. The track energy is scaled by 2 or 3% depending on whether the range or the curvature is used [106]. The top four plots are the error bands for the CC sample. The bottom plot is the corresponding covariance matrix. . . . .	140
7.10	NC background systematic error. The NC background is scaled by $\pm 20\%$ for MINOS and $\pm 30\%$ for MINOS+. The top four plots are the error bands for the CC sample. The bottom plot is the corresponding covariance matrix. . . . .	141

7.11	Normalization systematic error. The FD normalization is varied by $\pm 1.54\%$ [111]. The top four plots are the error bands for the CC sample. The bottom plot is the corresponding covariance matrix. . . . .	142
7.12	$\nu_\mu$ KNO multiplicity systematic error. $r_{ij2}$ NEUGEN parameters are shifted by $\pm 0.1$ . The top four plots are the error bands for the CC sample. The bottom plot is the corresponding covariance matrix. . . . .	143
7.13	$\nu_\mu$ KNO multiplicity systematic error. $r_{ij3}$ NEUGEN parameters are shifted by $\pm 0.2$ . The top four plots are the error bands for the CC sample. The bottom plot is the corresponding covariance matrix. . . . .	144
7.14	$\nu_\mu$ quasi-elastic cross section systematic error. $M_A^{QE}$ is scaled by $\pm 15\%$ . The top four plots are the error bands for the CC sample. The bottom plot is the corresponding covariance matrix. . . . .	145
7.15	$\nu_\mu$ resonance cross section systematic error. $M_A^{Res}$ is scaled by $\pm 15\%$ . The top four plots are the error bands for the CC sample. The bottom plot is the corresponding covariance matrix. . . . .	146
7.16	Total $\nu_\mu$ CC cross section systematic error. The total $\nu_\mu$ CC cross section is scaled by $\pm 3.5\%$ . The top four plots are the error bands for the CC sample. The bottom plot is the corresponding covariance matrix. . . . .	147
7.17	$\bar{\nu}_\mu$ KNO multiplicity systematic error. $r_{i(3,4)2}$ NEUGEN parameters is shifted by $\pm 0.2$ . The top four plots are the error bands for the CC sample. The bottom plot is the corresponding covariance matrix. . . . .	148
7.18	Total $\bar{\nu}_\mu$ CC cross section systematic error. The total $\bar{\nu}_\mu$ CC cross section is scaled by $\pm 4\%$ . The top four plots are the error bands for the CC sample. The bottom plot is the corresponding covariance matrix. . . . .	149
7.19	$\bar{\nu}_\mu$ quasi-elastic cross section systematic error. $\bar{\nu}_\mu$ quasi-elastic cross section is scaled by $\pm 8\%$ . The top four plots are the error bands for the CC sample. The bottom plot is the corresponding covariance matrix. . . . .	150
7.20	$\bar{\nu}_\mu$ resonance cross section systematic error. $\bar{\nu}_\mu$ resonance cross section is scaled by $\pm 8\%$ . The top four plots are the error bands for the CC sample. The bottom plot is the corresponding covariance matrix. . . . .	151

7.21	An examination of the mis-modeling of the NC fiducial volume. The shifted distribution is constructed by tightening the fiducial Z cut from 4.7368 m to 2.5 m. The top four plots are the error bands for the NC sample. The bottom plot is the corresponding covariance matrix. . . . .	155
7.22	An examination of the mis-modeling the across the NC fiducial volume. The plus and minus shifts correspond to the events originating on the left and right half of the fiducial volume. The top four plots are the error bands for the NC sample. The bottom plot is the corresponding covariance matrix. . . . .	156
7.23	Absolute hadronic calibration scale systematic error. The event energy is scaled by $\pm 6.6 - 10\%$ depending on the energy [100]. The top four plots are the error bands for the NC sample. The bottom plot is the corresponding covariance matrix. . . . .	157
7.24	CC background systematic error. CC background is scaled by $\pm 15\%$ The top four plots are the error bands for the NC sample. The bottom plot is the corresponding covariance matrix.	158
7.25	FD cleaning systematic error. The event energy is scaled by upto $\pm 4.9\%$ at low energies [108]. The top four plots are the error bands for the NC sample. The bottom plot is the corresponding covariance matrix. . . . .	159
7.26	FD cosmic removal systematic error. The event energy is scaled by $\pm 0 - 2.7\%$ depending on the energy [108]. The top four plots are the error bands for the NC sample. The bottom plot is the corresponding covariance matrix. . . . .	160
7.27	ND cleaning systematic error. The event energy is scaled by upto $\pm 8.2\%$ for MINOS [114] and upto $\pm 50\%$ for MINOS+ at low energies. The top four plots are the error bands for the NC sample. The bottom plot is the corresponding covariance matrix.	161
7.28	Normalization systematic error. The FD energy spectrum is scaled by $\pm 2.2\%$ . The top four plots are the error bands for the NC sample. The bottom plot is the corresponding covariance matrix. . . . .	162
7.29	Relative hadronic calibration scale systematic error. The FD NC event energy is scaled by $\pm 2.1\%$ . The top four plots are the error bands for the NC sample. The bottom plot is the corresponding covariance matrix. . . . .	163
7.30	$\nu_\mu$ KNO multiplicity systematic error. $r_{ij2}$ NEUGEN parameters is shifted by $\pm 0.1$ . The top four plots are the error bands for the NC sample. The bottom plot is the corresponding covariance matrix. . . . .	164



7.31	$\nu_\mu$ KNO multiplicity systematic error. $r_{ij3}$ NEUGEN parameters is shifted by $\pm 0.2$ . The top four plots are the error bands for the NC sample. The bottom plot is the corresponding covariance matrix. . . . .	165
7.32	$\nu_\mu$ quasi-elastic cross section systematic error. $M_A^{QE}$ is scaled by $\pm 15\%$ . The top four plots are the error bands for the NC sample. The bottom plot is the corresponding covariance matrix.	166
7.33	$\nu_\mu$ resonance cross section systematic error. $M_A^{Res}$ is scaled by $\pm 15\%$ . The top four plots are the error bands for the NC sample. The bottom plot is the corresponding covariance matrix. .	167
7.34	Total $\nu_\mu$ CC cross section systematic error. The total $\nu_\mu$ CC cross section is scaled by $\pm 3.5\%$ . The top four plots are the error bands for the NC sample. The bottom plot is the corresponding covariance matrix. . . . .	168
7.35	$\bar{\nu}_\mu$ KNO multiplicity systematic error. $r_{i(3,4)2}$ NEUGEN parameters is shifted by $\pm 0.2$ . The top four plots are the error bands for the NC sample. The bottom plot is the corresponding covariance matrix. . . . .	169
7.36	Total $\bar{\nu}_\mu$ CC cross section systematic error. The total $\bar{\nu}_\mu$ CC cross section is scaled by $\pm 4\%$ . The top four plots are the error bands for the NC sample. The bottom plot is the corresponding covariance matrix. . . . .	170
7.37	$\bar{\nu}_\mu$ quasi-elastic cross section systematic error. $\bar{\nu}_\mu$ quasi-elastic cross section is scaled by $\pm 8\%$ . The top four plots are the error bands for the NC sample. The bottom plot is the corresponding covariance matrix. . . . .	171
7.38	$\bar{\nu}_\mu$ resonance cross section systematic error. $\bar{\nu}_\mu$ resonance cross section is scaled by $\pm 8\%$ . The top four plots are the error bands for the NC sample. The bottom plot is the corresponding covariance matrix. . . . .	172
7.39	Covariance matrix from hadron production uncertainty for the CC sample (top) and the NC sample (bottom). This is calculated by the authors of [115]. . . . .	174
7.40	Covariance matrix from beam optics uncertainty for the CC sample (top) and NC sample (bottom). . . . .	175
7.41	Total fractional errors on the far-over-near ratio for the CC (top) and the NC (bottom) samples. . . . .	176

8.1	Far-over-near ratios for the CC sample (top) and the NC sample (bottom) using the combined data of MINOS and MINOS+. The error bars represent the statistical uncertainty. The standard oscillation predictions are shown as the red histograms along with the systematic uncertainty. . . . .	179
8.2	Simulated FD spectra with the binning scheme defined for the fitting. There are 74 bins for the CC sample (top), and 38 bins for the NC sample (bottom). . . . .	182
8.3	$\chi^2$ surface based on data. . . . .	184
8.4	$\chi^2$ surface based on the fake data assuming three-flavor oscillations. . . . .	184
8.5	A comparison between the data contour and the sensitivity contour. . . . .	185
8.6	Top: 90% C.L. sensitivity contours with and without systematics included. Bottom: Cumulative effect of the systematics on the 90% C.L. sensitivity contour. The systematics covariance matrices are added individually for each contour. . . . .	187
8.7	Individual effect of systematics on the 90% C.L. sensitivity contour. The bottom plot is a scaled version of the top plot. . . .	188
8.8	$\Delta\chi^2$ distribution for 1000 fake experiments at point ( $\theta_{24} = 0.2, \Delta m_{41}^2 = 20 \text{ eV}^2$ ) which is represented by a solid green triangle in Figure 8.10. The dashed line is drawn at $\Delta\chi^2 = 5.78$ such that 90% of the fake experiments give a smaller $\Delta\chi^2$ . This indicates a deviation from 4.61 for 90% C.L., which is based on an assumption of Gaussian probability density function. A small fraction of the fake experiments has $\Delta\chi^2 < 0$ due to fitting failure, but they do not affect the result much. . . . .	190
8.9	Fluctuated fake data, shown as the red, for the CC sample (top) and the NC sample (bottom). They correspond to the grid point represented by the green triangle in the top plot of Figure 8.10. The predictions without fluctuations are shown as black. . . .	191
8.10	90% C.L. $\Delta\chi^2$ surface. The 90% C.L. contour before and after the correction are shown as the cyan and the blue, respectively. . . .	192
8.11	90% C.L. Feldman-Cousins corrected contour. The excluded region is to the right. The limit from MINOS data is shown as the blue curve. The results from other $\nu_\mu$ disappearance experiments, CDHS [124], CCFR [125], and MiniBooNE/SciBooNE [126] are shown as the shaded region. . . . .	193

8.12	Combined limit of MINOS and MINOS+ with Bugey. The excluded region is on the right of the red curve. Results from $\nu_e/\bar{\nu}_e$ appearance experiments, including LSND [49], MiniBooNE [50, 51], ICARUS [127], and OPERA [128], are also shown. . . . .	194
8.13	Far-over-near double ratio for MINOS only. The CC sample is shown on the left and the NC sample is shown on the right. . . . .	196
8.14	Far-over-near double ratio for MINOS+ only. The CC sample is shown on the left and the NC sample is shown on the right. . . . .	196
8.15	Far-over-near double ratio for the combined fit of MINOS and MINOS+. The CC sample is shown on the left and the NC sample is shown on the right. . . . .	197
8.16	$\chi^2$ surface by fitting to the CC sample only (top) and the NC sample only (bottom). . . . .	198
9.1	Far-over-near ratio of the MINOS CC (top) and NC (bottom) data. The standard oscillation prediction is shown as the red. The LED model prediction with $a = 1 \mu\text{m}$ and $m_0 = 0 \text{ eV}$ , as an example, is shown as the blue. . . . .	202
9.2	Sensitivities for using the beam matrix method and the far-over-near fit method. Only the CC sample is used. The beam matrix method does not apply for $m_0 > 30 \text{ meV}$ (shaded region) due to ND oscillations. . . . .	203
9.3	Sensitivity for NC sample only, CC sample only, and the combined CC and NC sample. . . . .	204
9.4	Sensitivity for different flux uncertainties. $50\%N_{MC}$ is used in the current analysis, where $N_{MC}$ is the number of MC events. . . . .	205
9.5	An illustration of 2D linear interpolation. The value at point $E$ is weighted average of the values at the neighboring four points $A, B, C,$ and $D$ . The weight for each point is equal to the area of the sub-rectangle on the opposite end. For example the weight for point $A$ is $S_D/(S_A + S_B + S_C + S_D)$ as in Equation 9.3. . . . .	208
9.6	An example of a template used in the Ghost Fitter. It consists of the far-over-near ratio for the CC sample (top) and the NC sample (bottom). The two histograms are computed based on the parameters of a grid point in the four dimensional space spanned by $m_0, a, \theta_{23},$ and $\Delta m_{32}^2$ . . . . .	209
9.7	Top: $\chi^2$ surface based on MINOS data. $m_0$ is the smallest neutrino mass and $a$ is the large extra dimension size. $Z$ -axis is the $\chi^2$ value. Bottom: The same as the top plot but with a linear scale for the $Z$ -axis. . . . .	211

9.8	$\chi^2$ surface of the sensitivity. The fake data is made with the standard oscillation assumption. . . . .	212
9.9	A comparison of the 90 C.L. contours between data and sensitivity.	212
9.10	Individual effect of the systematics on the 90% C.L. sensitivity contour. The statistics only contour is on the very left, buried under the contour for the beam optics. . . . .	213
9.11	Cumulative effect of the systematics on the 90% C.L. sensitivity contour. The systematics covariance matrices are added one by one for each contour. . . . .	214
9.12	Fluctuated far-over-near ratio for the CC sample (top) and the NC sample (bottom). . . . .	215
9.13	Top: 90% C.L. Feldman-Cousins corrected contour. The $Z$ -axis represents the computed Feldman-Cousins values. The corrected contour is drawn where the $\chi^2$ is larger than the corresponding Feldman-Cousins value. Bottom: $\Delta\chi^2$ distribution for the point represented by the solid yellow triangle in the $m_0 - a$ plane. . . . .	216
9.14	90% C.L. Feldman-Cousins corrected contour for the LED model based on $10.56 \times 10^{20}$ POT $\nu_\mu$ running MINOS data. $m_0$ is the smallest neutrino mass and $a$ is the large extra dimension size. The shaded area means that the excluded region is to the right of the plot. . . . .	217
9.15	World's search for extra dimensions. The plot is provided by Machado, Nunokawa and Zukanovich Funchal. $M_D$ , $R$ and $\delta$ have the same definitions as those of $m_D$ , $a$ and $n$ in Equation 2.9, representing the fundamental scale, extra dimension size and number of extra dimensions respectively. The left green dashed line ( $M_D > 1700$ TeV for $\delta = 2$ ) is the limit from requiring that neutron stars are not excessively heated by KK graviton decays into photons [129]. The right green dashed line ( $M_D > 100$ TeV for $\delta = 2$ ) is the cosmological constraint based on the restriction on the amount of relic gravitons in the universe [130]. The solid blue line ( $M_D > 27$ TeV for $\delta = 2$ ) is the limit from supernova SN1987A requiring that the graviton luminosity agrees with certain stellar models [131]. It is also the limit of MINOS based on the simulations done by the authors of this plot. The purple dashed line ( $a < 37 \mu m$ at 95% CL for $n = 2$ ) is the limit from torsion balance experiments [132]. The right-most red circle ( $M_D > 1.60$ TeV for $\delta = 2$ ) is the limit from a combination of the LEP results on graviton emission [133, 134]. . . . .	219

10.1	Sensitivity of $10 \times 10^{20}$ POT MINOS+ to the 3+1 model. . . .	221
A.1	Calibration chain of the MINOS detectors. The plot is taken from Reference [95]. . . . .	224
A.2	Response of Near Detector as a function of detector position for U planes using MINOS+ cosmic data. Pre-Calibration plot shows raw ADC distribution. Mid-Calibration plot shows the effect of linearity, drift and strip-to-strip calibrations ( <b>sigCor</b> ). Post-Calibration plot shows the effect of fiber attenuation ( <b>sigMap</b> ) calibration. . . . .	225
A.3	Response of Near Detector as a function of detector position for V planes using MINOS+ cosmic data. Pre-Calibration plot shows raw ADC distribution. Mid-Calibration plot shows the effect of linearity, drift and strip-to-strip calibrations ( <b>sigCor</b> ). Post-Calibration plot shows the effect of fiber attenuation ( <b>sigMap</b> ) calibration. . . . .	225
A.4	Response of Far Detector as a function of detector position for U planes using MINOS+ cosmic data. Pre-Calibration plot shows raw ADC distribution. Mid-Calibration plot shows the effect of linearity, drift and strip-to-strip calibrations ( <b>sigCor</b> ). Post-Calibration plot shows the effect of fiber attenuation ( <b>sigMap</b> ) calibration. . . . .	226
A.5	Response of Far Detector as a function of detector position for V planes using MINOS+ cosmic data. Pre-Calibration plot shows raw ADC distribution. Mid-Calibration plot shows the effect of linearity, drift and strip-to-strip calibrations ( <b>sigCor</b> ). Post-Calibration plot shows the effect of fiber attenuation ( <b>sigMap</b> ) calibration. . . . .	226
A.6	Mean (top) and median (bottom) of the strip-to-strip calibration constant distribution at ND as a function of time. . . . .	227
A.7	Systematics of the strip-to-strip calibration at ND. Top: Ratio of the mean and the median (as shown in Figure A.6). Bottom: Ratio of the median for the full detector (nominal) to the median for the fiducial volume. . . . .	228
A.8	Mean (top) and median (bottom) of the strip-to-strip calibration constant distribution at FD as a function of time. . . . .	229
A.9	Systematics of the strip-to-strip calibration at FD. Top: Ratio of the mean and the median (as shown in Figure A.8). Bottom: Ratio of the median for the full detector (nominal) to the median for the fiducial volume. . . . .	230
D.1	Schematic of pion/kaon decay in the lab frame. . . . .	261

D.2	Feynman diagram of a lepton decaying into another lepton plus two neutrinos. . . . .	264
D.3	Sketch of $d^2\omega/dxd\cos\theta$ as a function of $\cos\theta$ for a 50 GeV $\mu^-$ and $x = 0.5$ . $\theta$ is the angle between the momentum of $\nu_\mu$ and that of $\mu^-$ in the lab frame. . . . .	273

# Chapter 1

## Neutrino Physics

Since its proposal in 1930, a large amount of knowledge has been accumulated about neutrinos. They are the most abundant fundamental constituents of the Universe. They are neutral, weakly interacting, and spin 1/2 particles created with three definite flavors: electron, muon and tau. Their small yet non-vanishing mass allows the phenomenon of neutrino oscillations. This chapter lays the background and theoretical foundation of this dissertation. Firstly, a brief history on the discovery of the neutrinos is given, followed by an introduction of a series of experiments leading to the establishment of the neutrino oscillation theory. The formalism of neutrino mixing is outlined in the last section of this chapter.

### 1.1 Discovery of Neutrinos

In 1914, James Chadwick measured a continuous energy spectrum of electrons from beta decay using a magnetic spectrometer [1]. To explain this, in 1930, Wolfgang Pauli proposed the emission of a neutrino [2] in beta decay

$$n \rightarrow p + e^{-} + \nu, \tag{1.1}$$

where the neutrino shares part of the decay energy resulting in a continuous electron energy spectrum. In 1956, Frederick Reines and Clyde Cowan reported the discovery of the electron antineutrino  $\bar{\nu}_e$  at Savannah River Plant, using the inverse beta decay

$$\bar{\nu}_e + p \rightarrow n + e^+. \quad (1.2)$$

The events were selected based on the coincidence of the signals from neutron capture on cadmium and positron annihilation [3].

In 1959, the muon neutrino  $\nu_\mu$  was predicted by Bruno Pontecorvo [4] and was discovered by Leon Lederman, Melvin Schwartz and Jack Steinberger in 1962 at Brookhaven National Laboratory [5] using the first-ever neutrino beam. In their experiment, a 15 GeV proton beam striking a beryllium target was used to create pions, which subsequently decayed into muon neutrinos. Muons from muon neutrinos interacting with matter were then observed in a spark chamber.

The tau neutrino  $\nu_\tau$  was postulated after the discovery of the tau lepton in 1975 [6]. It was discovered in 2000 by the DONUT experiment at Fermilab where four tau neutrino events with an estimated background of 0.34 events were observed in the nuclear emulsion detectors [7].

The number of light neutrino species is determined to be  $2.9840 \pm 0.0082$  by the measurements performed at the SLAC Linear Collider and the Large Electron-Positron collider at CERN, in agreement with the three observed generations of fundamental fermions [8]. Comparing the total width of the



Z boson resonance to the width from its decays to visible particles yields the width for its decay to neutrinos. Assuming equal coupling strengths of the Z to all neutrino types, the fit to the number of light neutrino species is shown in Figure 1.1.

On the other hand, combining Planck observations on the cosmic microwave background radiation with other astrophysical data gives  $N_{eff} = 3.15 \pm 0.23$  for the effective number of relativistic degrees of freedom, consistent with the value from the Z boson decay, and the sum of neutrino masses is constrained to  $m_\nu < 0.23$  eV [9]. Additionally, in Reference [10], combining WMAP (Wilkinson Microwave Anisotropy Probe) with other data yields  $N_{eff} = 3.55^{+0.49}_{-0.48}$ , which is consistent with the Planck result, and  $m_\nu < 0.44$  eV.

All neutrinos are left-handed and all antineutrinos are right-handed assuming they are Dirac particles like all other fermions. Chirality (left-handed or right-handed) of a particle is a Lorentz invariant property related to helicity. The latter is defined as

$$\frac{\mathbf{s} \cdot \mathbf{p}}{|\mathbf{s}| |\mathbf{p}|}, \quad (1.3)$$

where  $\mathbf{s}$  and  $\mathbf{p}$  are the particle's spin and momentum, respectively. In the limit of small mass, such as that of neutrinos, chirality is equal to helicity, i.e., right-handedness corresponds to positive helicity, and vice versa. The first hint of neutrino helicity came from Chien-Shiung Wu's experiment in 1956 [11]. The result of observing  $\beta$  decay of polarized  $^{60}\text{Co}$  suggested a preference of the antineutrinos to take positive helicity ( $\mathbf{s} \cdot \mathbf{p} > 0$ , right-handed). This

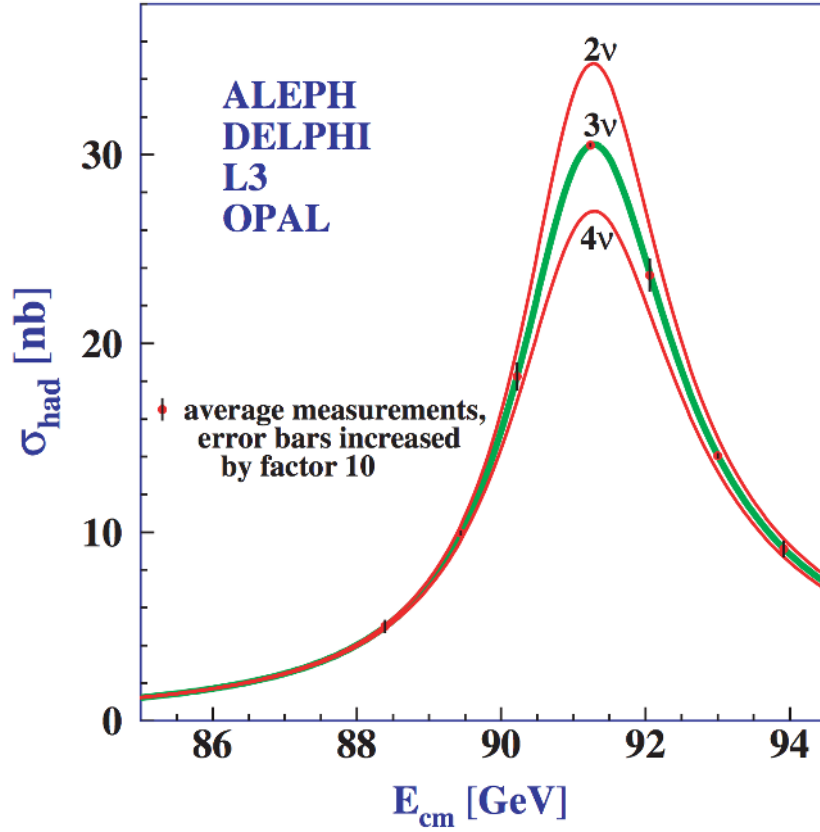


Figure 1.1: Measurements of the hadron production cross-section around the Z resonance. The data consist of 17 million Z decays accumulated by the ALEPH, DELPHI, L3 and OPAL experiments at LEP, and 600 thousand Z decays by the SLD experiment using a polarized beam at SLC. The curves represent the predicted cross-section for two, three and four neutrino species with Standard Model (SM) couplings and negligible mass. The plot is taken from Reference [8].

proved parity violation in weak interactions since  $\mathbf{s} \cdot \mathbf{p}$  changes sign under parity transformation. In 1958, Maurice Goldhaber, Lee Grodzins and Andrew Sunyar measured the polarization of the neutrino in the electron capture  $e^- + {}^{152}\text{Sm} \rightarrow {}^{152}\text{Sm}^* + \nu_e$ , with the subsequent decay  ${}^{152}\text{Sm}^* \rightarrow {}^{152}\text{Sm} + \gamma$ . They found that the measured polarization of the photon implies that the electron neutrino takes negative helicity ( $\mathbf{s} \cdot \mathbf{p} < 0$ , left-handed) [12].

## 1.2 Neutrino Oscillations

Neutrino oscillation was first proposed by Bruno Pontecorvo in 1957 [13, 14], and he pursued this work over many years. Independently, in 1962, Ziro Maki, Masami Nakagawa and Shoichi Sakata also arrived at the idea of neutrino masses and mixing [15]. In the past few decades, the oscillation theory has been established through various experiments that measure solar, atmospheric, reactor and beam neutrinos.

### 1.2.1 Solar Neutrinos

Solar neutrinos are produced by some of the fusion reactions in the pp chain or CNO cycle occurring in the Sun. The combined effect of these reactions is written as



The average energy carried away by neutrinos is  $\sim 0.6\text{MeV}$  [16]. The most elaborate standard solar model (SSM) calculations have been developed by

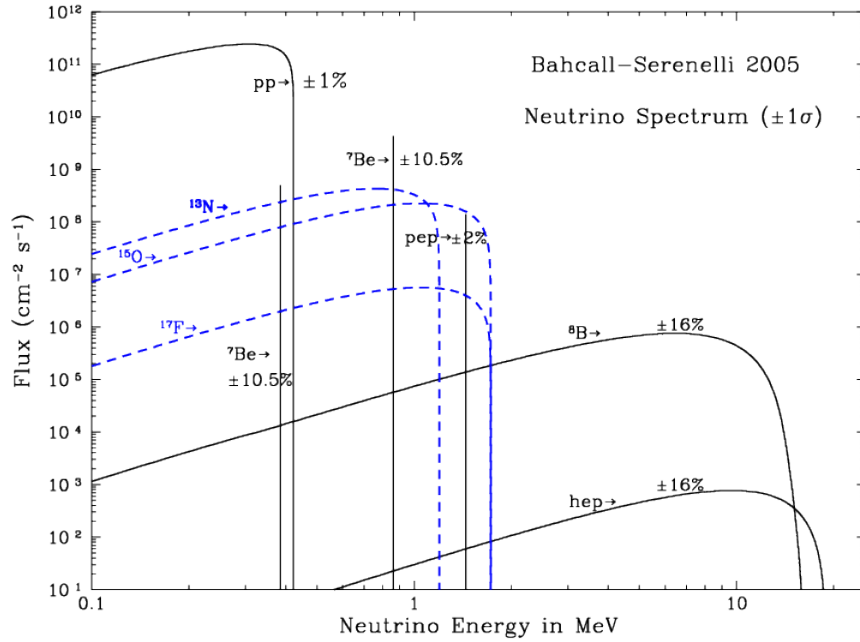


Figure 1.2: The solar neutrino spectrum predicted by the BS05(OP) standard solar model [17]. The plot is taken from Reference [18].

John Bahcall and his collaborators. The solar-neutrino spectra calculated with the BS05(OP) model by Bahcall is shown in Fig. 1.2.

A pioneering solar neutrino experiment was performed by Ray Davis and his collaborators at Homestake Mine in late 1960's. The first result was published in 1968, and it showed that the detected flux of solar neutrinos was about 2-3 times smaller than the flux predicted by the standard solar model [19]. This effect was called “the solar neutrino problem”. In 1989, the Kamiokande experiment made the first directional counting observation of solar neutrinos and confirmed the deficit [20]. SAGE [21] and GALLEX

[22] confirmed the solar neutrino deficit in radiochemical experiments in 1991 and 1992, respectively. In 2001 and 2002, SNO announced the observation of neutral currents from solar neutrinos, along with charged currents and elastic scatters, providing convincing evidence that neutrino oscillations are the cause of the solar neutrino problem [23, 24]. In 2008, with a detection threshold as low as 250 keV, the flux of monochromatic 0.862 MeV  ${}^7\text{Be}$  solar neutrinos was observed by the Borexino experiment using a liquid scintillation detector [25]. Then in 2014, the Super-Kamiokande experiment reported a  $2.7\sigma$  indication of non-zero day-night asymmetry of  ${}^8\text{B}$  solar neutrinos, which implies the Earth matter effects on flavor oscillations of solar neutrinos [26].

### 1.2.2 Atmospheric Neutrinos

Atmospheric neutrinos are produced as decay products in hadronic showers resulting from collisions of cosmic rays with nuclei in the upper atmosphere. Production of electron and muon neutrinos is dominated by the processes

$$\pi^\pm \rightarrow \mu^\pm + \nu_\mu/\bar{\nu}_\mu, \quad (1.5)$$

$$\mu^\pm \rightarrow e^\pm + \nu_e/\bar{\nu}_e + \bar{\nu}_\mu/\nu_\mu. \quad (1.6)$$

The expected ratio of the  $(\nu_\mu + \bar{\nu}_\mu)$  flux to the  $(\nu_e + \bar{\nu}_e)$  flux at low energies (1 GeV) is approximately

$$\phi(\nu_\mu + \bar{\nu}_\mu) : \phi(\nu_e + \bar{\nu}_e) \approx 2 : 1. \quad (1.7)$$

More detailed flux calculations for a broader energy range can be found in Reference [27–30].

The first compelling evidence for atmospheric neutrino oscillation was presented by the Super-Kamiokande Collaboration in 1998 [31] from the observation of atmospheric neutrinos. The zenith-angle distributions of the  $\mu$ -like events which are mostly muon neutrino and muon antineutrino initiated charged-current interactions, showed a clear deficit compared to the no-oscillation expectation.

### 1.2.3 Reactor Neutrinos

Nuclear power plants are the most intense man-controlled sources of neutrinos. With an average energy of about 200 MeV released per fission and 6 neutrinos produced along the  $\beta$ -decay chain of the fission products, one expects some  $2 \times 10^{20} \nu/s$  to be emitted in a  $4\pi$  solid angle from a 1 GW reactor. Since unstable fission products are neutron-rich nuclei all  $\beta$ -decays are of  $\beta^-$  type and the neutrino flux consists purely of electron antineutrinos ( $\bar{\nu}_e$ ) [32].

KamLAND was a long-baseline (flux-weighted average distance  $L \sim 180$  km) neutrino oscillation experiment that measures  $\bar{\nu}_e$  emitted from nuclear power reactors. In 2002, KamLAND began operations in January and announced in November the detection of a deficit of  $\bar{\nu}_e$  from reactors [33]. With a much shorter baseline ( $L \sim 1$  km), the three reactor neutrino experiments Double Chooz [34], Daya Bay [35], and RENO [36] reported their first results

on reactor  $\bar{\nu}_e$  disappearance in 2012.

#### 1.2.4 Beam Neutrinos

Neutrino beams generated at accelerator facilities provide another source to study neutrino oscillations. The technique is to collide a high-energy proton beam with a nuclear target to derive a beam of pion and kaon secondaries, whose decays in turn yield a neutrino beam. The precise selection and manipulation of the pion/kaon beam control the energy spectrum and type of the neutrino beam [37].

K2K (KEK-to-Kamioka) is the first accelerator-based experiment with a neutrino path length extending hundreds of kilometers. Data taken in K2K between 1999 and 2004 confirmed neutrino oscillation through  $\nu_\mu$  disappearance [38]. MINOS is the second long-baseline neutrino oscillation experiment which ran from 2005 to 2012. The combined analysis of  $\nu_\mu$  disappearance and  $\nu_e$  appearance using beam and atmospheric data is reported in Reference [39]. Additionally, MINOS observed muon antineutrino disappearance with the NuMI beam line optimized for  $\bar{\nu}_\mu$  production [40, 41]. The T2K experiment is the first off-axis long-baseline neutrino oscillation experiment. A narrow-band  $\nu_\mu$  beam with a peak energy of 0.6 GeV, produced by 30 GeV protons from the J-PARC Main Ring, is directed  $2.5^\circ$  off-axis to Super-Kamiokande [42]. The only experiment to identify  $\nu_\tau$  appearance event by event is OPERA, with a target mass of 1290 tons, a neutrino source at CERN and a detector at Gran Sasso with a baseline distance of 730 km. As of July 2013, OPERA

found three  $\nu_\tau$  candidate in the  $\tau \rightarrow \mu$  channel [43].

### 1.3 Oscillations Formalism

This section gives a brief introduction on the formalism of the neutrino oscillations. Following a general form of the oscillation formula, the three flavor mixing case, also referred to as the standard oscillation model, is applied to the case of  $\nu_\mu$  disappearance as measured by MINOS.

#### 1.3.1 Generic Formula

One can define a unitary matrix  $U$  as

$$|\nu_i\rangle = \sum_{\alpha} U_{i\alpha} |\nu_{\alpha}\rangle \text{ or } |\nu_{\alpha}\rangle = \sum_i U_{\alpha i}^* |\nu_i\rangle, \quad (1.8)$$

where  $|\nu_{\alpha}\rangle$  and  $|\nu_i\rangle$  are the flavor and mass eigen states, respectively. Given the time evolution of a flavor state

$$|\nu_{\alpha}(t)\rangle = \sum_i U_{\alpha i}^* e^{-i(E_i t - p_i L)} |\nu_i\rangle, \quad (1.9)$$

where  $t$  and  $L$  are the time and distance for which the neutrino travels, and  $E$  is the neutrino energy, the oscillation probability between two flavors,  $\alpha$  and



$\beta$ , can be written as

$$\begin{aligned}
P(\nu_\alpha \rightarrow \nu_\beta) &= |\langle \nu_\alpha | \nu_\beta(t) \rangle|^2 \\
&= \left| \left( \sum_i U_{\alpha i} \langle \nu_i | \right) \left( \sum_j U_{\beta j}^* e^{-i(E_j t - p_j L)} | \nu_j \rangle \right) \right|^2 \\
&= \delta_{\alpha\beta} - 4 \sum_{i>j} \Re [U_{\alpha i} U_{\alpha j}^* U_{\beta i}^* U_{\beta j}] \sin^2(\Delta_{ij}/2) \\
&\quad + 2 \sum_{i>j} \Im [U_{\alpha i} U_{\alpha j}^* U_{\beta i}^* U_{\beta j}] \sin \Delta_{ij}. \tag{1.10}
\end{aligned}$$

where

$$\Delta_{ij} \equiv (E_i - E_j)t - (p_i - p_j)L. \tag{1.11}$$

The average neutrino speed  $v$  can be approximated as  $(p_i + p_j)/(E_i + E_j)$  using  $v = p/E$  where the natural unit is applied. Inserting the time of flight  $t = L/v \approx L(E_i + E_j)/(p_i + p_j)$  in Equation 1.12, one has

$$\begin{aligned}
\Delta_{ij} &= (E_i - E_j)t - (p_i - p_j)L \\
&\approx \frac{E_i^2 - E_j^2}{p_i + p_j} L - \frac{p_i^2 - p_j^2}{p_i + p_j} L \\
&\approx \frac{m_i^2 - m_j^2}{2} \left( \frac{L}{E} \right) \\
&= \frac{\Delta m_{ij}^2}{2} \left( \frac{L}{E} \right), \tag{1.12}
\end{aligned}$$

where  $p_i \approx p_j \approx E$  is applied, and  $\Delta m_{ij}^2 \equiv m_i^2 - m_j^2$ . The factor of 2 in the denominator is treated more rigorously in Reference [44] using wave packets rather than plane waves. A more detailed derivation of the formalism can be found in Appendix B.1.

Assuming there are  $N$  flavor and mass eigenstates, the unitary matrix  $U$  has dimension  $N$ . Following Reference [45], a  $N \times N$  unitary matrix can be parameterized as a matrix product

$$\begin{aligned}
U &= (\Omega_{N-1,N} \Omega_{N-2,N} \Omega_{N-3,N} \cdots \Omega_{1,N}) \\
&\times (\Omega_{N-2,N-1} \Omega_{N-3,N-1} \Omega_{N-4,N-1} \cdots \Omega_{1,N-1}) \\
&\times \cdots \times \Omega_{1,2}
\end{aligned} \tag{1.13}$$

where

$$\Omega_{ij} = \begin{pmatrix} 1 & & & & & & & \\ & \ddots & & & & & & \\ & & 1 & & & & & \\ & & & \cos(\theta_{ij}) & \sin(\theta_{ij}) & & & \\ & & & -\sin(\theta_{ij}) & \cos(\theta_{ij}) & & & \\ & & & & & 1 & & \\ & & & & & & \ddots & \\ & & & & & & & 1 \end{pmatrix} \tag{1.14}$$

for  $j - i = 1$ , and

$$\Omega_{ij} = \begin{pmatrix} 1 & & & & & & & & & & \\ & \ddots & & & & & & & & & \\ & & 1 & & & & & & & & \\ & & & \cos(\theta_{ij}) & 0 & \dots & 0 & \sin(\theta_{ij})e^{-i\delta_{ij}} & & & \\ & & & 0 & 1 & & & 0 & & & \\ & & & \vdots & & \ddots & & \vdots & & & \\ & & & 0 & & & 1 & 0 & & & \\ & & & -\sin(\theta_{ij})e^{i\delta_{ij}} & 0 & \dots & 0 & \cos(\theta_{ij}) & & & \\ & & & & & & & & 1 & & \\ & & & & & & & & & \ddots & \\ & & & & & & & & & & 1 \end{pmatrix} \tag{1.15}$$

for  $j - i \geq 2$ . Note that the order of the factors in Equation 1.13 is critical. The  $N = 3$  case will be given in the next section.

### 1.3.2 Standard Three Flavor Oscillation Model

It is known that the standard three flavor model works well describing most of the experimental data to date. In this case, in Equation 1.8,  $\alpha$  represents  $e$ ,  $\mu$  or  $\tau$ ,  $i$  runs from 1 to 3, and  $U$  is a  $3 \times 3$  matrix. Using Equation 1.14 and 1.15, we have

$$\begin{aligned}\Omega_{1,2} &= \begin{pmatrix} \cos(\theta_{12}) & \sin(\theta_{12}) & 0 \\ -\sin(\theta_{12}) & \cos(\theta_{12}) & 0 \\ 0 & 0 & 1 \end{pmatrix}, \\ \Omega_{1,3} &= \begin{pmatrix} \cos(\theta_{13}) & 0 & e^{-i\delta_{13}} \sin(\theta_{13}) \\ 0 & 1 & 0 \\ -e^{i\delta_{13}} \sin(\theta_{13}) & 0 & \cos(\theta_{13}) \end{pmatrix}, \\ \Omega_{2,3} &= \begin{pmatrix} 1 & 0 & 0 \\ 0 & \cos(\theta_{23}) & \sin(\theta_{23}) \\ 0 & -\sin(\theta_{23}) & \cos(\theta_{23}) \end{pmatrix}.\end{aligned}\tag{1.16}$$

$\delta_{13}$  is also written as  $\delta_{CP}$  representing the CP violating phase. Using Equation 1.13, the matrix  $U$  can be written as

$$\begin{aligned}U &= \Omega_{1,2}\Omega_{1,3}\Omega_{2,3} \\ &= \begin{pmatrix} c_{12}c_{13} & c_{13}s_{12} & e^{-i\delta_{CP}}s_{13} \\ -c_{23}s_{12} - e^{i\delta_{CP}}c_{12}s_{13}s_{23} & c_{12}c_{23} - e^{i\delta_{CP}}s_{12}s_{13}s_{23} & c_{13}s_{23} \\ s_{12}s_{23} - e^{i\delta_{CP}}c_{12}c_{23}s_{13} & -e^{i\delta_{CP}}c_{23}s_{12}s_{13} - c_{12}s_{23} & c_{13}c_{23} \end{pmatrix},\end{aligned}\tag{1.17}$$

where  $s_{ij} \equiv \sin(\theta_{ij})$  and  $c_{ij} \equiv \cos(\theta_{ij})$ . This matrix is called the PMNS matrix to acknowledge the pioneering ideas of Pontecorvo and Maki and Nakagawa and Sakata. For example, the MINOS experiment is designed to measure

$\nu_\mu \rightarrow \nu_\mu$ , and according to Equation 1.10, we have

$$\begin{aligned}
P(\nu_\mu \rightarrow \nu_\mu) &= 1 - 4 \sum_{i>j} \Re [U_{\mu i} U_{\mu j}^* U_{\mu i}^* U_{\mu j}] \sin^2 (\Delta_{ij}/2) \\
&\quad + 2 \sum_{i>j} \Im [U_{\mu i} U_{\mu j}^* U_{\mu i}^* U_{\mu j}] \sin \Delta_{ij} \\
&= 1 - 4 |U_{\mu 3}|^2 (|U_{\mu 2}|^2 + |U_{\mu 1}|^2) \sin^2 (\Delta_{32}/2), \tag{1.18}
\end{aligned}$$

where the approximations of  $\Delta_{31} \approx \Delta_{32}$  and  $\sin^2 (\Delta_{21}/2) \sim 0$  are used due to  $\Delta_{21} \ll \Delta_{31}$ , and

$$\begin{aligned}
|U_{\mu 1}|^2 &= \cos^2 (\theta_{23}) \sin^2 (\theta_{12}) \\
&\quad + \cos^2 (\theta_{12}) \sin^2 (\theta_{13}) \sin^2 (\theta_{23}) \\
&\quad + \frac{1}{2} \cos (\delta_{CP}) \sin (2\theta_{12}) \sin (\theta_{13}) \sin (2\theta_{23}), \\
|U_{\mu 2}|^2 &= \cos^2 (\theta_{12}) \cos^2 (\theta_{23}) \\
&\quad + \sin^2 (\theta_{12}) \sin^2 (\theta_{13}) \sin^2 (\theta_{23}) \\
&\quad - \frac{1}{2} \cos (\delta_{CP}) \sin (2\theta_{12}) \sin (\theta_{13}) \sin (2\theta_{23}), \\
|U_{\mu 3}|^2 &= \cos^2 (\theta_{13}) \sin^2 (\theta_{23}). \tag{1.19}
\end{aligned}$$

Equation 1.18, along with the oscillation probabilities of  $\nu_\mu \rightarrow \nu_e$  and  $\nu_\mu \rightarrow \nu_\tau$ , are plotted as a function of  $L/E$  (a factor of  $\Delta_{ij}$  as shown in Equation 1.12) in Figure 1.3 using the baselines and the neutrino energy range of MINOS.

So far most of the oscillation parameters have been precisely measured using neutrinos from solar, atmospheric, accelerator and reactor sources. The global fit result from Reference [47] is shown in Table 1.1. Three pieces of information remain unknown:

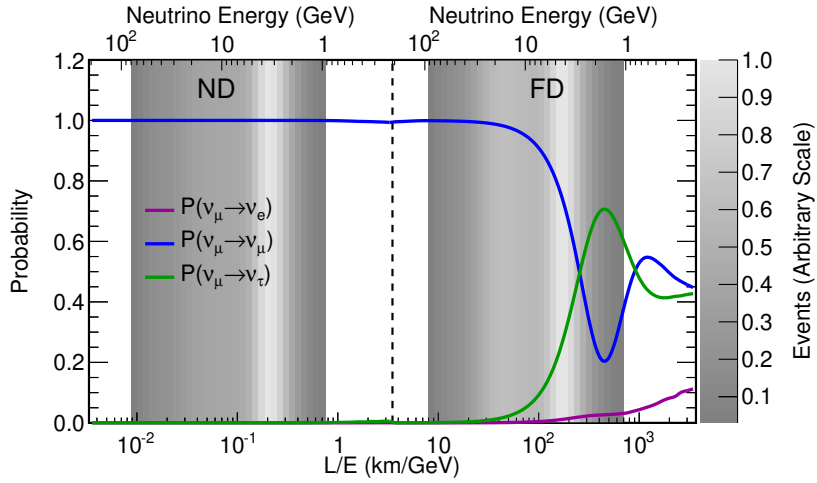


Figure 1.3: Oscillation probabilities as a function of  $L/E$  in MINOS at the near and far detectors (ND and FD). The simulated energy spectra are shown as the gray bands.

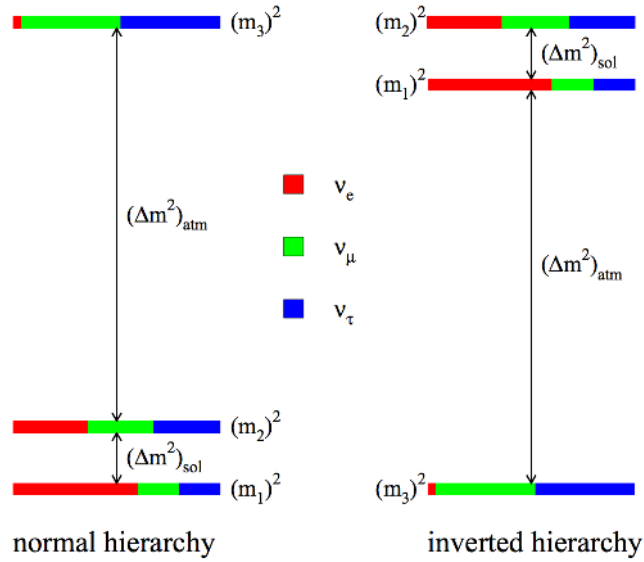


Figure 1.4: Schematic of the two neutrino mass hierarchies. The color coding indicates the fraction  $|U_{\alpha i}|^2$  of each flavor  $\nu_\alpha$  ( $\alpha = e, \mu, \tau$ ) contained in each mass eigenstate. The plot is taken from Reference [46].

1. The value of the CP violating phase  $\delta_{CP}$ .
2. The sign of  $\Delta m_{31}^2$ . This is known as the mass hierarchy problem. The case of normal hierarchy (NH,  $\Delta m_{31}^2 > 0$ ) and inverted hierarchy (IH,  $\Delta m_{31}^2 < 0$ ) are demonstrated in Figure 1.4.
3. Octant of  $\theta_{23}$ . It is not clear whether  $\theta_{23}$  is smaller or larger than  $\pi/4$ .

Parameter	Hierarchy	Best fit	$1\sigma$ range
$\delta m^2/10^{-5}$ eV <sup>2</sup>	NH or IH	7.54	7.32 – 7.80
$\sin^2 \theta_{12}/10^{-1}$	NH or IH	3.08	2.91 – 3.25
$\Delta m^2/10^{-3}$ eV <sup>2</sup>	NH	2.43	2.37 – 2.49
$\Delta m^2/10^{-3}$ eV <sup>2</sup>	IH	2.38	2.32 – 2.44
$\sin^2 \theta_{13}/10^{-3}$	NH	2.34	2.15 – 2.54
$\sin^2 \theta_{13}/10^{-3}$	IH	2.40	2.18 – 2.59
$\sin^2 \theta_{23}/10^{-3}$	NH	4.37	4.14 – 4.70
$\sin^2 \theta_{23}/10^{-3}$	IH	4.55	4.24 – 5.94
$\delta_{CP}/\pi$	NH	1.39	1.12 – 1.77
$\delta_{CP}/\pi$	IH	1.31	0.98 – 1.60

Table 1.1: Global fit result of the standard three flavor oscillation model from Reference [47]. Note that  $\delta m^2 \equiv \Delta m_{21}^2$  and  $\Delta m^2 \equiv m_3^2 - (m_1^2 - m_2^2)/2$ , with  $+\Delta m^2$  for NH and  $-\Delta m^2$  for IH.

# Chapter 2

## Sterile Neutrinos

Although the mixing of the three flavor neutrino states has been experimentally well established, there have been hints of the presence of additional neutrino states with masses at the eV scale. Since the number of active neutrino states is constrained to be three as discussed in Chapter 1, these additional neutrinos are not allowed to interact with Standard Model particles. They are called *sterile neutrinos*, terminology introduced by Pontecorvo in 1969 [48].

The motivations to search for sterile neutrinos are outlined in the first section, followed by the introduction of two sterile neutrino models: 3+1 and large extra dimension (LED). These models will be tested by the powerful and unique data collected in MINOS/MINOS+ in this dissertation.

### 2.1 Experimental Anomalies

There is growing evidence for short-baseline neutrino anomalies occurring at an  $L/E \sim 1$  m/MeV, where  $E$  is the neutrino energy and  $L$  is the distance that the neutrino traveled before detection. Such evidence has come from the LSND (Liquid Scintillator Neutrino Detector)  $\bar{\nu}_\mu \rightarrow \bar{\nu}_e$  appearance

experiment at the Los Alamos Neutron Science Center [49], MiniBooNE (Mini Booster Neutrino Experiment) at Fermilab [50, 51], the reactor anomaly [52], and radioactive source calibrations of the GALLEX (Gallium Experiment) [53, 54] and SAGE (Russian-American Gallium Experiment) [55, 56] solar neutrino experiments.

### 2.1.1 LSND

The primary search in LSND is for  $\bar{\nu}_\mu \rightarrow \bar{\nu}_e$  oscillations.  $\bar{\nu}_\mu$  arise from the decay at rest of  $\mu^+$ , which are produced by directing a 798 MeV proton beam on a target. The  $\bar{\nu}_e$  are identified through the reaction  $\bar{\nu}_e p \rightarrow e^+ n$  in a tank of liquid scintillator surrounded by 1220 8-inch Hamamatsu photomultiplier tubes (PMTs). This reaction allows a coincidence of signals from positron annihilation and a correlated 2.2 MeV  $\gamma$  from neutron capture on a free proton. The center of the detector is located 30 m from the neutrino source.

A total excess of  $87.9 \pm 22.4 \pm 6.0$   $\bar{\nu}_e p \rightarrow e^+ n$  events with  $e^+$  energy between 20 and 60 MeV is observed above the expected neutrino-induced backgrounds. A fit to all of the LSND neutrino processes, including the  $\nu_\mu \rightarrow \nu_e$  oscillation where  $\nu_\mu$  comes from  $\pi^+$  decay-in-flight, determines the allowed oscillation parameters in a two-flavor model. The result is shown in Figure 2.1. Together with other available neutrino oscillation limits, the LSND data suggest that neutrino flavor oscillations occur with a  $\Delta m^2$  in the range 0.2–10 eV<sup>2</sup>. This is much higher than the results obtained from the atmospheric and beam



neutrino experiments (see Table 1.1), and is therefore called an anomaly.

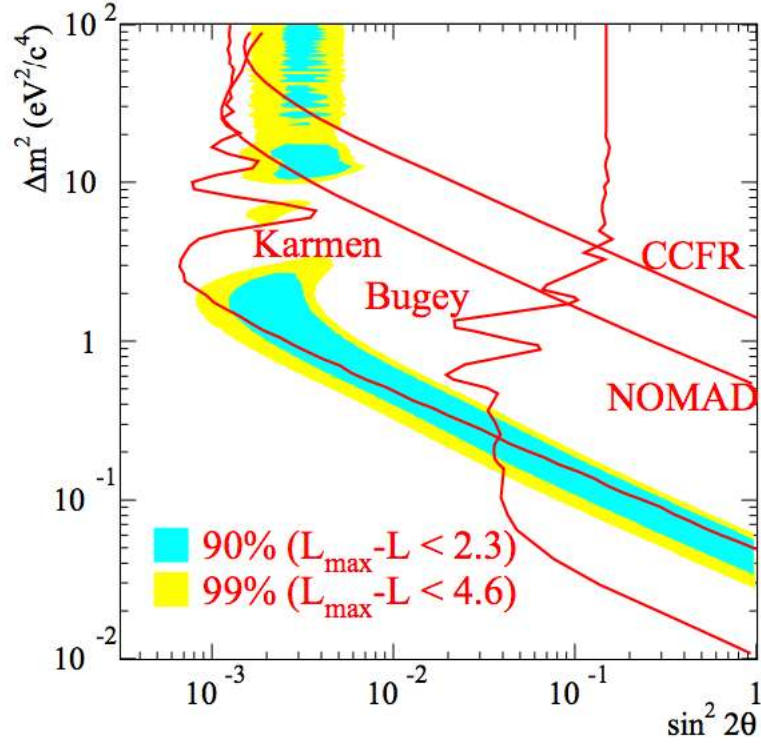


Figure 2.1: A  $\sin^2 2\theta - \Delta m^2$  oscillation parameter fit for the entire data sample,  $20 < E_e < 200$  MeV. The fit includes primary  $\bar{\nu}_\mu \rightarrow \bar{\nu}_e$  oscillations and secondary  $\nu_\mu \rightarrow \nu_e$  oscillations, as well as all known neutrino backgrounds. The allowed region is shown in blue (90% C.L.) and yellow (99% C.L.). Other curves are 90% CL limits from the Bugey reactor experiment [57], the CCFR experiment at Fermilab [58], the NOMAD experiment at CERN [59], and the KARMEN experiment at ISIS [60]. The plot is taken from Reference [49].

### 2.1.2 MiniBooNE

MiniBooNE was designed to search for  $\nu_\mu \rightarrow \nu_e$  and  $\bar{\nu}_\mu \rightarrow \bar{\nu}_e$  oscillations by detecting  $\nu_e$  and  $\bar{\nu}_e$  charged-current quasi-elastic (CCQE) events in a 40-foot diameter sphere filled with 806 tons of pure mineral oil. Neutrino interactions in the detector produce charged particles (electrons, muons, protons, pions, and kaons) which in turn produce scintillation and Cherenkov light. This light is detected by the 1520 8-inch PMTs that line the interior of the detector and an optically isolated outer veto region.

The  $\nu_\mu$  ( $\bar{\nu}_\mu$ ) flux is produced by colliding 8 GeV protons from the Fermilab Booster with a beryllium target placed inside a magnetic focusing horn set at positive (negative) polarity. The target is located 541 m from the detector.

The MiniBooNE experiment observed a total excess of  $240.3 \pm 62.9$   $\nu_e$  and  $\bar{\nu}_e$  events ( $3.8\sigma$ ) in the neutrino oscillation energy range  $200 < E_\nu^{QE} < 1250$  MeV. The allowed regions from a two-flavor fit to the data, shown in Figure 2.2, are consistent with the allowed region reported by the LSND experiment [49, 61–64] and the limits from the KARMEN experiment [65].

### 2.1.3 Reactor Anomaly

The reactor neutrino anomaly [52] results from a re-analysis of the short baseline (SBL) reactor neutrino oscillation data using the results of a new and very detailed calculation of the reactor  $\bar{\nu}_e$  fluxes [32]. The new fluxes are found to be larger than the fluxes widely used in the past by approximately

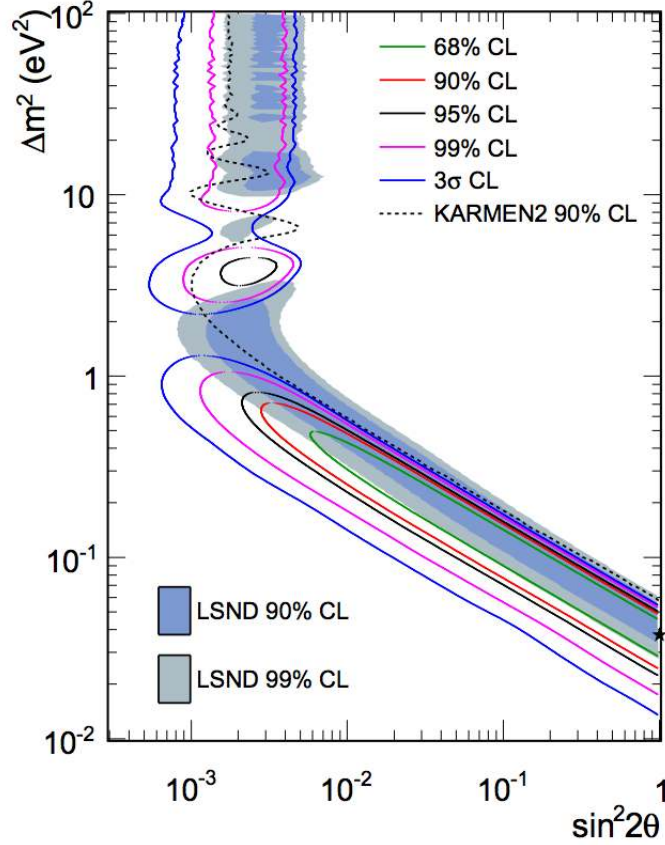


Figure 2.2: MiniBooNE allowed regions in combined neutrino and antineutrino mode for events with  $200 < E_{\nu}^{QE} < 3000$  MeV within a two-neutrino  $\nu_{\mu} \rightarrow \nu_e$  and  $\bar{\nu}_{\mu} \rightarrow \bar{\nu}_e$  oscillation model. Also shown is the  $\bar{\nu}_{\mu} \rightarrow \bar{\nu}_e$  limit from the KARMEN experiment [65]. The shaded areas show the 90% and 99% C.L. LSND  $\bar{\nu}_{\mu} \rightarrow \bar{\nu}_e$  allowed regions. The black star shows the best fit point. The plot is taken from Reference [51].

3.5%. With the old flux, the synthesis of published experiments at reactor-detector distances smaller than 100 m led to a ratio of observed event rate to predicted rate of  $0.976 \pm 0.024$ . With the new flux evaluation, this ratio shifts to  $0.943 \pm 0.023$ , leading to a deviation from unity at 98.6% C.L. This shows

a possible disappearance of the reactor  $\bar{\nu}_e$ , as illustrated in Figure 2.3.

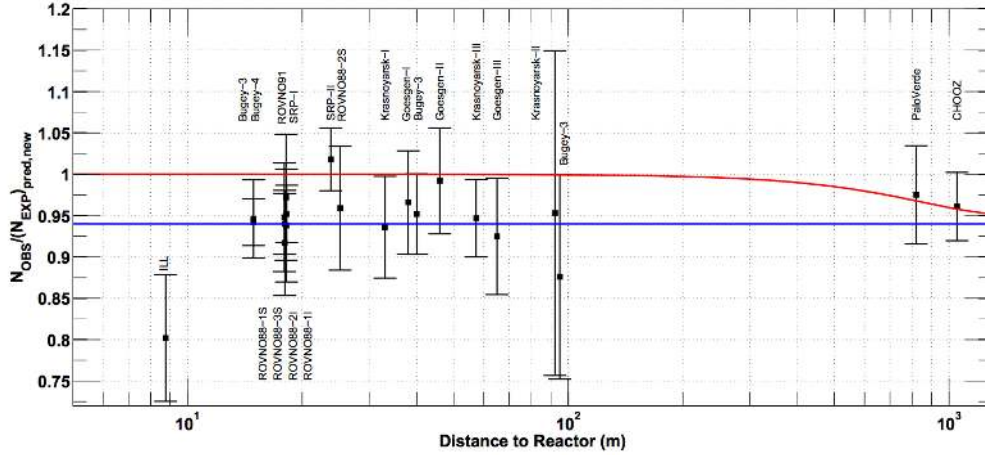


Figure 2.3: Illustration of the short baseline reactor antineutrino anomaly. The red line shows a possible three active neutrino mixing solution, with  $\sin^2(2\theta_{13}) = 0.06$ . The blue line displays a possible solution including a new neutrino mass state, with  $|\Delta m^2| \gg 1 \text{ eV}^2$  and  $\sin^2(2\theta) = 0.12$ . The plot is taken from Reference [52].

### 2.1.4 Gallium Anomaly

Radioactive source calibrations of the GALLEX [53, 54] and SAGE [55, 56] solar neutrino experiments also showed a deficit in the measured fluxes compared to the expected fluxes. This is called the Gallium Anomaly, as both experiments use gallium as the medium for neutrino detection. The results may be interpreted as hints for  $\nu_e$  disappearance at short distances which is not predicted by the standard three flavor oscillation model.

The neutrino capture rate measured by SAGE is well below that predicted by solar models. To guarantee the reliability of the experimental tech-

niques and test the neutrino oscillation hypothesis, the response of the experiment to low-energy neutrinos was calibrated by a 517 kCi (19.1 PBq) source of  $^{51}\text{Cr}$  which mainly emits monoenergetic 747 keV neutrinos. The source was placed at the center of a 13.1 ton target of liquid gallium and the cross section for the production of  $^{71}\text{Ge}$  by the inverse beta decay reaction  $^{71}\text{Ga}(\nu_e, e^-)^{71}\text{Ge}$  was measured to be  $[5.55 \pm 0.60 \text{ (stat)} \pm 0.32 \text{ (syst)}] \times 10^{-45} \text{ cm}^2$ . This is a few percent smaller than the model predictions. The ratio of this cross section to the theoretical cross section of Bahcall for this reaction is  $0.95 \pm 0.12 \text{ (expt)} \begin{smallmatrix} +0.035 \\ -0.027 \end{smallmatrix} \text{ (theor)}$  and to the cross section of Haxton is  $0.87 \pm 0.11 \text{ (expt)} \pm 0.09 \text{ (theor)}$ .

For the same reason, GALLEX performed an investigation with two intense  $^{51}\text{Cr}$  neutrino sources ( $> 60 \text{ PBq}$ ) that were produced in the Siloé nuclear reactor and used at the Gran Sasso National Laboratory. The ratio,  $R$ , of the the neutrino source strength derived from the measured rate of  $^{71}\text{Ge}$  production, divided by the directly determined source strength is  $R = 1.01^{+0.12}_{-0.11}$  for the first source and  $R = 0.84^{+0.12}_{-0.11}$  for the second one. The combined value of  $R$  for the two source experiments is  $R = 0.93 \pm 0.08$ .

## 2.2 3+1 Model

Among various models of sterile neutrinos, 3+1 is the simplest, with one sterile neutrino state  $\nu_s$  added to the standard three flavor oscillation picture. In this model,  $U$  in Equation 1.8 is a  $4 \times 4$  unitary matrix accounting for four neutrino flavor states:  $\nu_e$ ,  $\nu_\mu$ ,  $\nu_\tau$ , and  $\nu_s$ . Detailed calculations on

the oscillation probabilities can be found in Appendix B. Two channels are relevant to this dissertation,  $P(\nu_\mu \rightarrow \nu_\mu)$  and  $P(\nu_\mu \rightarrow \nu_s)$ . In the MINOS detectors, the former, also referred to as the  $\nu_\mu$  disappearance probability, is measured from the charged current events. The latter, on the other hand, is measured from the neutral current events.

For the  $\nu_\mu$  disappearance, Equation 1.10 takes the form

$$\begin{aligned}
P(\nu_\mu \rightarrow \nu_\mu) &= \delta_{\mu\mu} - 4 \sum_{i>j} \Re(U_{\mu i} U_{\mu j}^* U_{\mu i}^* U_{\mu j}) \sin^2(\Delta_{ij}/2) \\
&\quad + 2 \sum_{i>j} \Im(U_{\mu i} U_{\mu j}^* U_{\mu i}^* U_{\mu j}) \sin \Delta_{ij} \\
&= 1 - A_{31} \sin^2(\Delta_{31}/2) \\
&\quad - A_{41} \sin^2(\Delta_{41}/2) \\
&\quad - A_{43} \sin^2(\Delta_{43}/2), \tag{2.1}
\end{aligned}$$

where

$$\begin{aligned}
A_{31} &= 4 |U_{\mu 3}|^2 (1 - |U_{\mu 3}|^2 + |U_{\mu 4}|^2), \\
A_{41} &= -4 |U_{\mu 4}|^2 (1 - |U_{\mu 3}|^2 + |U_{\mu 4}|^2), \\
A_{43} &= -4 |U_{\mu 4}|^2 |U_{\mu 3}|^2. \tag{2.2}
\end{aligned}$$

In deriving Equation 2.1 and 2.2, the unitary condition  $|U_{\mu 1}|^2 + |U_{\mu 2}|^2 + |U_{\mu 3}|^2 + |U_{\mu 4}|^2 = 1$  is used, as well as the approximation of  $m_1 \approx m_2$  which leads to  $\Delta_{21} = 0$ ,  $\Delta_{41} = \Delta_{42}$ , and  $\Delta_{32} = \Delta_{31}$ . Note that by definition,  $\Delta_{41} = \Delta_{43} + \Delta_{31}$ . The matrix  $U$  can be parameterized according to Equation 1.13. In the analysis of this dissertation,  $\theta_{14}$  is set to 0 due to the strong constraints from reactor

experiments. For example, Reference [66] gives  $\sin^2 \theta_{14} < 0.04$  at 90% C.L.

Relevant terms in Equation 2.2 are

$$\begin{aligned} |U_{\mu 3}|^2 &= \cos^2(\theta_{13}) \cos^2(\theta_{24}) \sin^2(\theta_{23}), \\ |U_{\mu 4}|^2 &= \sin^2(\theta_{24}). \end{aligned} \quad (2.3)$$

In the case of  $\nu_\mu \rightarrow \nu_s$ , Equation 1.10 gives

$$\begin{aligned} P(\nu_\mu \rightarrow \nu_s) &= -4 \sum_{i>j} \Re(U_{\mu i} U_{\mu j}^* U_{s i}^* U_{s j}) \sin^2(\Delta_{ij}/2) \\ &\quad + 2 \sum_{i>j} \Im(U_{\mu i} U_{\mu j}^* U_{s i}^* U_{s j}) \sin \Delta_{ij} \\ &= 1 - B_{31} \sin^2(\Delta_{31}/2) \\ &\quad - B_{41} \sin^2(\Delta_{41}/2) \\ &\quad - B_{43} \sin^2(\Delta_{43}/2), \end{aligned} \quad (2.4)$$

where

$$\begin{aligned} B_{31} &= 4 |U_{\mu 3}|^2 |U_{s 3}|^2 + 4 \Re(U_{\mu 4} U_{\mu 3}^* U_{s 4}^* U_{s 3}) + 2 \Im(U_{\mu 4} U_{\mu 3}^* U_{s 4}^* U_{s 3}) \\ B_{41} &= 4 |U_{\mu 4}|^2 |U_{s 4}|^2 + 4 \Re(U_{\mu 4} U_{\mu 3}^* U_{s 4}^* U_{s 3}) - 2 \Im(U_{\mu 4} U_{\mu 3}^* U_{s 4}^* U_{s 3}) \\ B_{43} &= -4 \Re(U_{\mu 4} U_{\mu 3}^* U_{s 4}^* U_{s 3}) + 2 \Im(U_{\mu 4} U_{\mu 3}^* U_{s 4}^* U_{s 3}) \end{aligned} \quad (2.5)$$

In addition to Equation 2.3, relevant terms in Equation 2.5 are

$$\begin{aligned}
\Im(U_{\mu 4} U_{\mu 3}^* U_{s 4}^* U_{s 3}) &= \frac{1}{4} \cos^2(\theta_{13}) \cos^2(\theta_{24}) \sin(\delta_{24}) \sin(2\theta_{23}) \sin(\theta_{24}) \sin(2\theta_{34}) \\
\Re(U_{\mu 4} U_{\mu 3}^* U_{s 4}^* U_{s 3}) &= -\cos^2(\theta_{13}) \cos^2(\theta_{24}) \cos(\theta_{34}) \sin(\theta_{23}) \sin(\theta_{24}) \\
&\quad \times [\cos(\theta_{34}) \sin(\theta_{23}) \sin(\theta_{24}) + \cos(\delta_{24}) \cos(\theta_{23}) \sin(\theta_{34})] \\
|U_{s 4}|^2 &= \cos^2(\theta_{24}) \cos^2(\theta_{34}), \\
|U_{s 3}|^2 &= \frac{1}{2} \cos(\delta_{24}) \sin(2\theta_{23}) \sin(\theta_{24}) \sin(2\theta_{34}) \cos^2(\theta_{13}) \\
&\quad + \cos^2(\theta_{34}) \sin^2(\theta_{23}) \sin^2(\theta_{24}) \cos^2(\theta_{13}) \\
&\quad + \cos^2(\theta_{23}) \sin^2(\theta_{34}) \cos^2(\theta_{13}). \tag{2.6}
\end{aligned}$$

The individual effect of the parameters ( $\Delta m_{32}^2$ ,  $\Delta m_{41}^2$ ,  $\theta_{23}$ ,  $\theta_{24}$ ,  $\theta_{34}$ , and  $\delta_{24}$ ) appearing in the oscillation probabilities, Equation 2.1 and Equation 2.4, is demonstrated in Figures 2.4 to 2.9 with default values listed in Table 2.1. For example, in Figure 2.5, each curve corresponds to a value of  $\Delta m_{41}^2$  while the rest of the parameters are set to the values in Table 2.1. Each plot in the figure is divided by a dashed line, with the near detector baseline 1.04 km for the left part and the far detector baseline 735 km for the right part.

The model will be tested with  $10.56 \times 10^{20}$  POT  $\nu_\mu$  running data of MINOS and  $2.99 \times 10^{20}$  POT  $\nu_\mu$  running data of MINOS+ in Chapter 8.

## 2.3 Large Extra Dimension Model

There are at least two seemingly fundamental energy scales in nature, the electroweak scale  $m_{EW} \sim 10^3$  GeV, which is a typical energy of processes



Parameter	Value
$\Delta m_{21}^2$	$7.54 \times 10^{-5} \text{ eV}^2$
$\Delta m_{32}^2$	$2.37 \times 10^{-3} \text{ eV}^2$
$\Delta m_{41}^2$	0.5
$\theta_{12}$	0.554
$\theta_{13}$	0.149
$\theta_{14}$	0
$\theta_{23}$	0.695
$\theta_{24}$	0.2
$\theta_{34}$	0.5
$\delta_{13}$	0
$\delta_{14}$	0
$\delta_{24}$	0

Table 2.1: Default 3+1 model parameters used in Figures 2.4 to 2.9.

described by the electroweak theory, and the Planck scale  $m_P = G^{-1/2} \sim 10^{18}$  GeV (in natural unit), where gravity becomes as strong as the gauge interactions. The large gap between the two energy scales is referred to as the gauge hierarchy problem. The large extra dimension model was initially proposed by Nima Arkani-Hamed *et al* [67] to solve this problem. The authors suggested that  $m_{EW}$  is the only fundamental scale and the large  $m_P$  is caused by  $n$  extra compact spatial dimensions of radius  $a$ . According to Newton's law of universal gravitation, the gravitational potential between two masses  $M_1$  and  $M_2$  separated by a distance  $r$  is

$$V = G \frac{M_1 M_2}{r} = \frac{M_1 M_2}{m_P^2 r}. \quad (2.7)$$

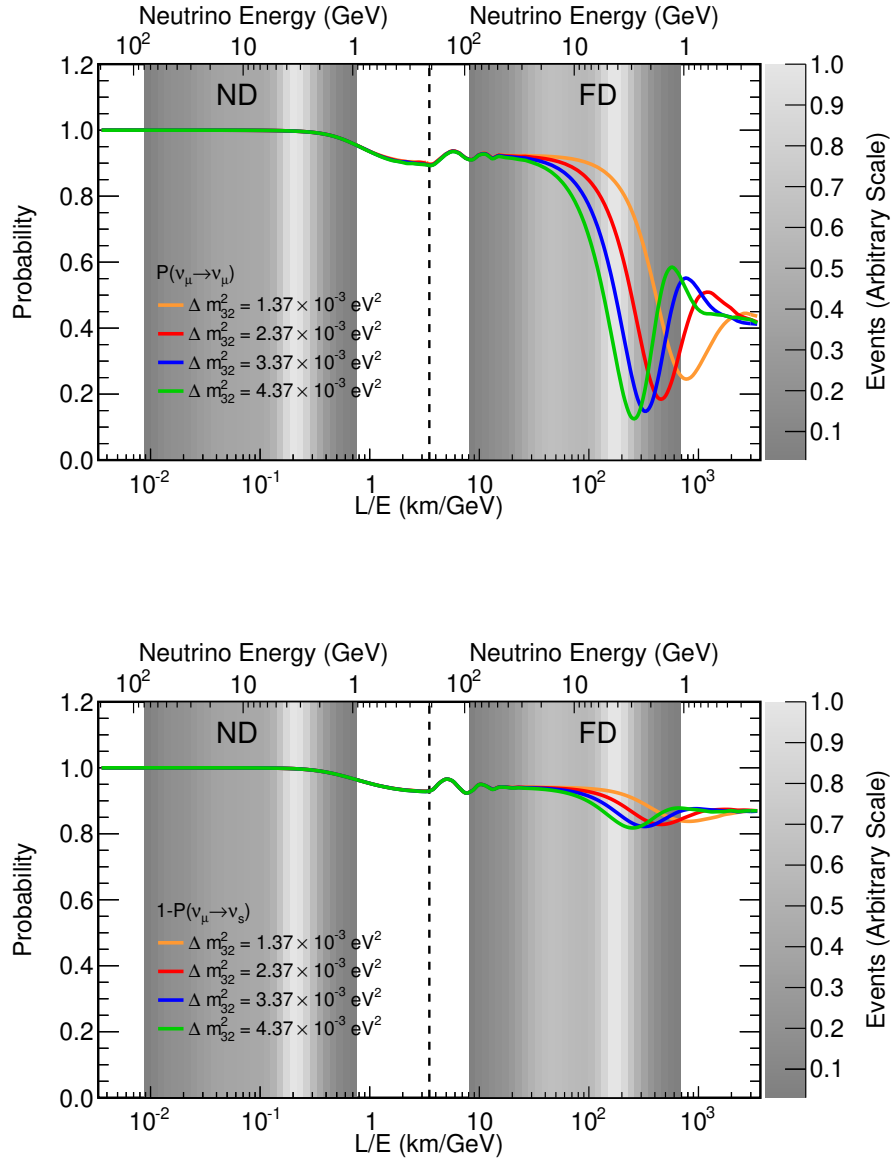


Figure 2.4: Effect of  $\Delta m_{32}^2$  on  $P(\nu_\mu \rightarrow \nu_\mu)$  (top) and  $1 - P(\nu_\mu \rightarrow \nu_s)$  (bottom). Other parameters are set to the values listed in Table 2.1. The simulated energy spectra for the near and far detectors (ND and FD) are shown as the gray bands.

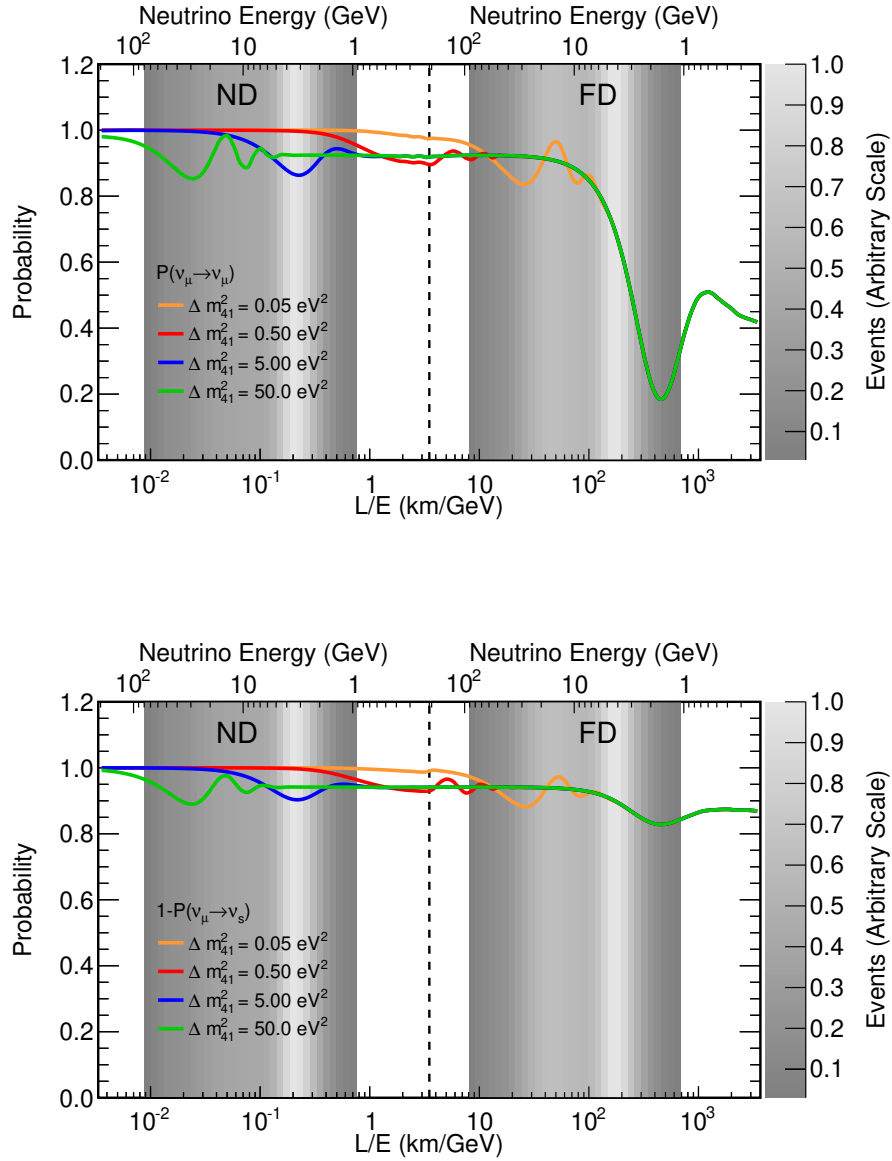


Figure 2.5: Effect of  $\Delta m_{41}^2$  on  $P(\nu_\mu \rightarrow \nu_\mu)$  (top) and  $1 - P(\nu_\mu \rightarrow \nu_s)$  (bottom). Other parameters are set to the values listed in Table 2.1. The simulated energy spectra for the near and far detectors (ND and FD) are shown as the gray bands.

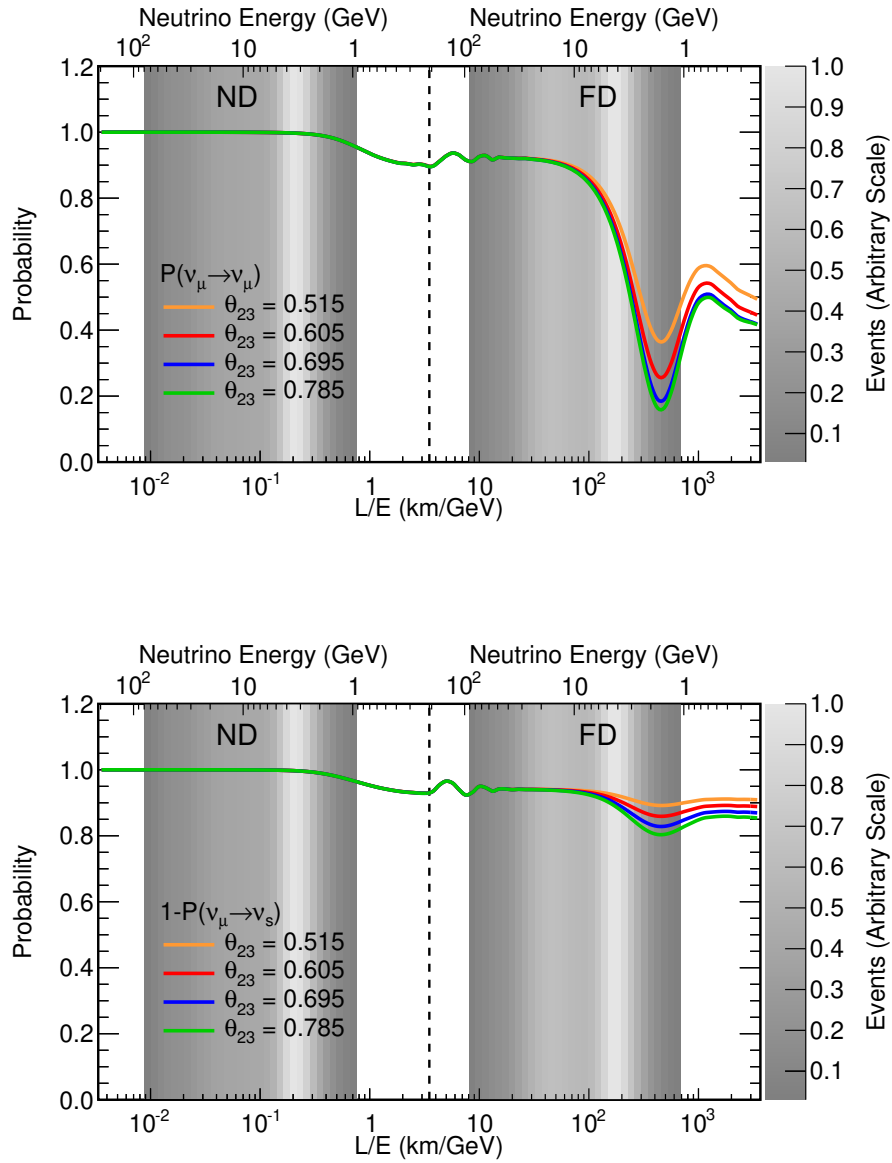


Figure 2.6: Effect of  $\theta_{23}$  on  $P(\nu_\mu \rightarrow \nu_\mu)$  (top) and  $1 - P(\nu_\mu \rightarrow \nu_s)$  (bottom). Other parameters are set to the values listed in Table 2.1. The simulated energy spectra for the near and far detectors (ND and FD) are shown as the gray bands.

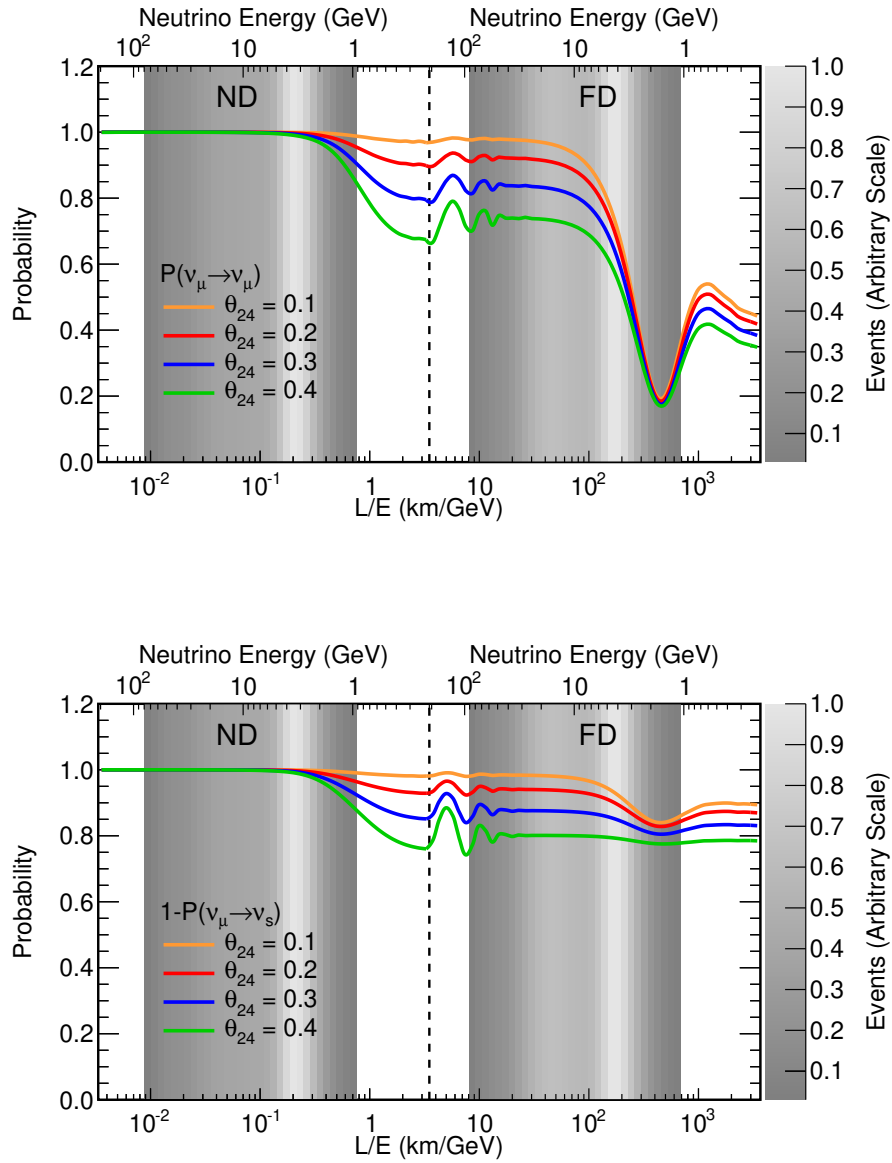


Figure 2.7: Effect of  $\theta_{24}$  on  $P(\nu_\mu \rightarrow \nu_\mu)$  (top) and  $1 - P(\nu_\mu \rightarrow \nu_s)$  (bottom). Other parameters are set to the values listed in Table 2.1. The simulated energy spectra for the near and far detectors (ND and FD) are shown as the gray bands.

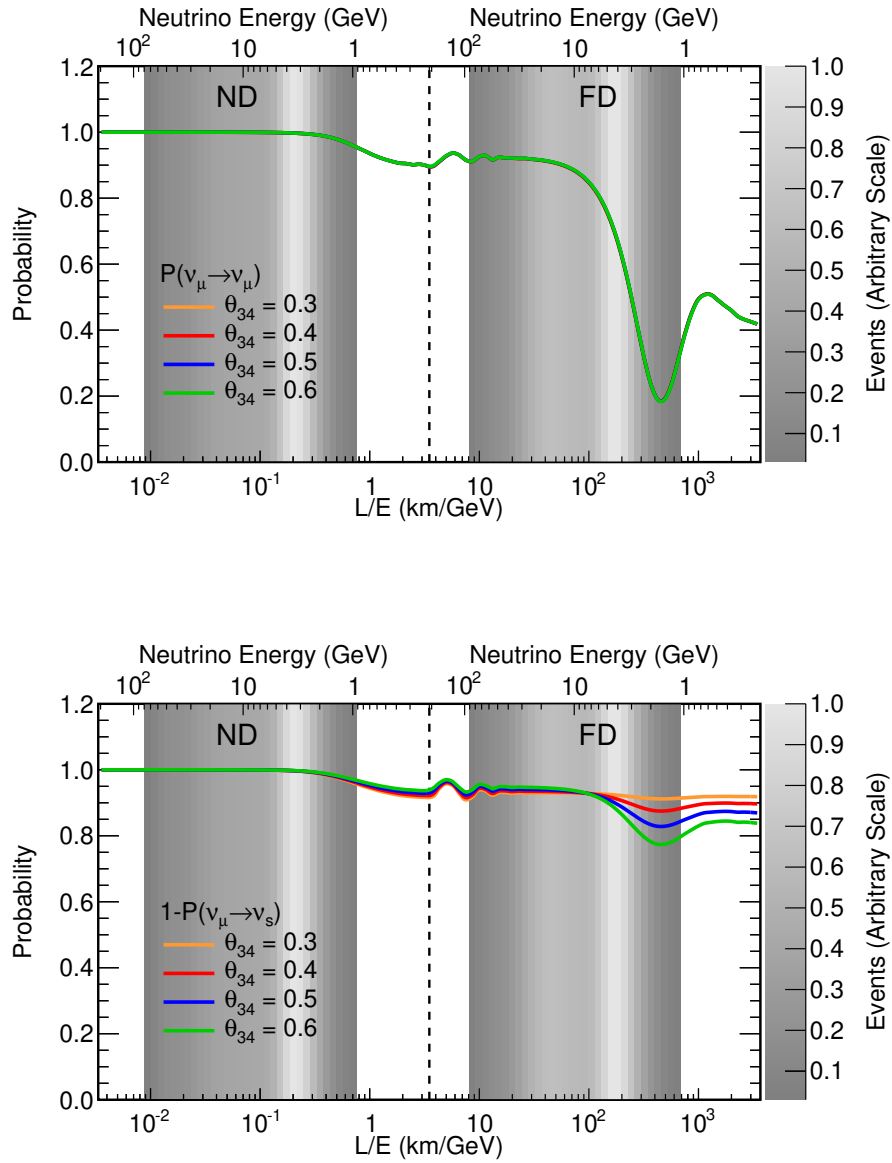


Figure 2.8: Effect of  $\theta_{34}$  on  $P(\nu_\mu \rightarrow \nu_\mu)$  (top) and  $1 - P(\nu_\mu \rightarrow \nu_s)$  (bottom). Other parameters are set to the values listed in Table 2.1. The simulated energy spectra for the near and far detectors (ND and FD) are shown as the gray bands.

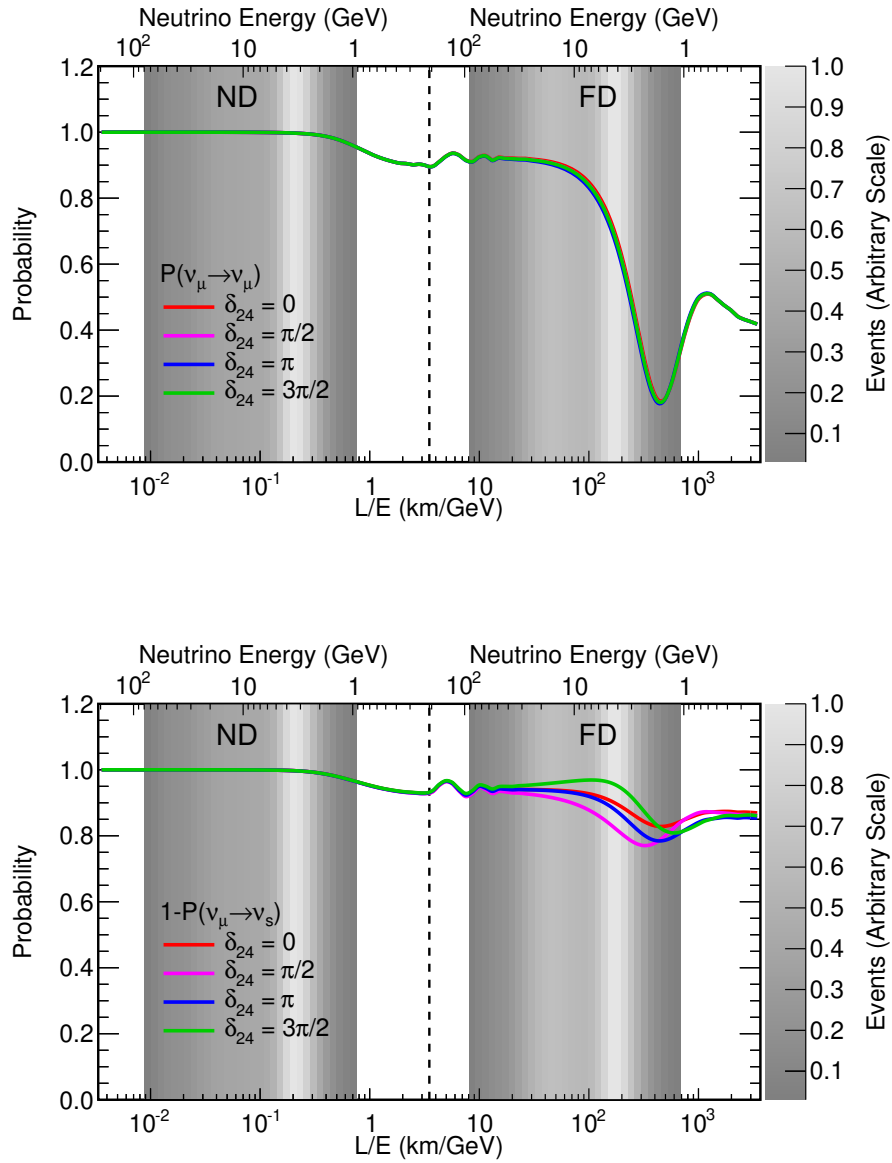


Figure 2.9: Effect of  $\delta_{24}$  on  $P(\nu_\mu \rightarrow \nu_\mu)$  (top) and  $1 - P(\nu_\mu \rightarrow \nu_s)$  (bottom). Other parameters are set to the values listed in Table 2.1. The simulated energy spectra for the near and far detectors (ND and FD) are shown as the gray bands.

On the other hand Gauss's law in  $(4+n)$  dimensions, where 4 refers to the usual 4-dimensional spacetime, requires that

$$V \sim \begin{cases} \frac{M_1 M_2}{m_{P(4+n)}^{n+2} r^{n+1}} & (r \ll a), \\ \frac{1}{m_{P(4+n)}^{n+2} a^n} \frac{M_1 M_2}{r} & (r \gg a), \end{cases} \quad (2.8)$$

where  $m_{P(4+n)}$  is the Planck scale in  $(4+n)$  dimensions. Comparing Equation 2.7 and Equation 2.8 for  $r \gg a$ , and denoting  $m_D \equiv m_{P(4+n)}$  as the fundamental scale, we have

$$m_P^2 \sim m_D^{n+2} a^n. \quad (2.9)$$

Setting  $m_D \sim m_{EW}$ , for  $n = 1$ , we have  $a \sim 10^{13}$  cm. Considering that the distance from the Earth to the Sun is  $1.5 \times 10^{13}$  cm,  $n = 1$  should cause observable deviations from Newtonian gravity, so this case is empirically excluded. For  $n \geq 2$ , the modification of gravity only becomes noticeable at distances smaller than those probed by current experiments. For example, for  $n = 2$ ,  $a \sim 200$   $\mu$ m. However, while this model has not been ruled out by any direct measurement on gravity, it creates a problem for the neutrino mass. Traditionally small neutrino masses are explained by a seesaw model assuming neutrinos are Majorana particles. In this case, the Lagrangian contains the mass term

$$(\bar{\nu}_L, N_R) \begin{pmatrix} 0 & m \\ m & M \end{pmatrix} \begin{pmatrix} \nu_L \\ N_R \end{pmatrix}, \quad (2.10)$$

where  $\nu_L$  and  $N_R$  are the left and right-handed neutrino states. The mass eigenstates are found by diagonalizing the matrix. With the eigenvalues

$$\lambda = \frac{M \pm \sqrt{M^2 + 4m^2}}{2} \approx \begin{cases} 2M \\ -m^2/M^2 \end{cases}, \quad (2.11)$$



the diagonalized matrix takes the form

$$\begin{pmatrix} -m^2/M & 0 \\ 0 & 2M \end{pmatrix}. \quad (2.12)$$

From this, it follows that a large sterile neutrino mass  $M$  gives rise to a small active neutrino mass  $m^2/M$ . In models with LEDs, the seesaw model cannot be used, since physics at energy scales well above a TeV (such as  $M$ ) is no longer part of the theory.

There is, however, an alternative mechanism as described in Reference [68], for either Dirac or Majorana neutrino masses. For Dirac masses, the basic idea is that any fermionic state that propagates in  $4 + n$  dimensions must, by definition, be a Standard Model singlet and, furthermore, that it couples to the Standard Model states which are confined to the 4-dimensional spacetime precisely as a right-handed neutrino with a naturally small coupling. The small coupling is a result of the large relative volume of the “bulk” manifold ( $4 + n$  dimensions) compared to the thin “brane” (4-dimensional spacetime) where Standard Model states propagate. The interaction probability of the Kaluza-Klein (KK) zero mode of the bulk right-handed neutrino state  $\nu_R$  with the “brane localized” Higgs and lepton doublet fields is thus small, resulting in a greatly suppressed coupling. For the Majorana case, small neutrino masses can be obtained using the generic mechanism of Reference [69] for generating small couplings by breaking symmetries on distant branes in the bulk.

This dissertation focuses on the scenario with Dirac masses. Based on

the model, Reference [68] gives the following expression for neutrino mass

$$m_\nu = \kappa \frac{v}{\sqrt{a^n m_D^n}}. \quad (2.13)$$

where  $v \sim 10^2$  GeV is the vacuum expectation value of the Higgs,  $\kappa$  is a dimensionless coefficient, and  $a^n$  is the volume spanned by  $n$  extra dimensions.

Writing  $a^n$  in terms of  $m_P$  using Equation 2.9, Equation 2.13 becomes

$$m_\nu = m_D \kappa \frac{v}{m_P} \sim 10^{-16} m_D \kappa. \quad (2.14)$$

For  $m_D \kappa \sim 1 - 100$  TeV, this prediction for the neutrino masses is roughly in the right range to explain the atmospheric and solar neutrino observations.

Constraints on this model based on the data of neutrino oscillation experiments including SNO, Super-Kamiokande, and various reactor and accelerator experiments are discussed in Reference [70]. The authors provide a bound of  $a < 0.82 \mu\text{m}$  on the largest extra dimension size assuming that the manifold on which the extra dimensions are compactified is highly asymmetric, with one dimension much larger than the rest. Note that this is different from most collider, astrophysical and cosmological bounds, which are largely independent of the compactification manifold's shape and only constrain its volume.

Given by Reference [70], the mass terms in the Lagrangian for this model take the form

$$\mathcal{L}_{mass} = m_{\alpha\beta} \left( \bar{\nu}_R^{\alpha(0)} \nu_L^{\beta(0)} + \sqrt{2} \sum_{n=1}^{\infty} \bar{\nu}_R^{\alpha(n)} \nu_L^{\beta(0)} \right) + \sum_{n=1}^{\infty} \frac{n}{a} \bar{\nu}_R^{\alpha(n)} \nu_L^{\alpha(n)} + \text{h.c.}, \quad (2.15)$$

where  $\alpha, \beta = 1, 2, 3$ .  $\nu_L^{\beta(0)}$  represents the “brane-localized” Standard Model neutrino states  $\nu_e, \nu_\mu$  or  $\nu_\tau$ .  $\nu_L^{\alpha(n)}$  and  $\nu_R^{\alpha(n)}$  are the KK states living in the “bulk”. They do not carry any Standard Model charges (singlets), and therefore are sterile.  $m_{\alpha\beta}$  is the Dirac mass matrix

$$\kappa_{\alpha\beta} m_D \frac{v}{m_P}, \quad (2.16)$$

where  $\kappa_{\alpha\beta}$  is a matrix of dimensionless coefficients. Note that Equation 2.16 is a version of Equation 2.14 with three mass eigen states. After a diagonalization procedure, the oscillation amplitude among active neutrino states can be written as

$$\mathcal{A}(\nu_\alpha \rightarrow \nu_\beta) = \sum_{i,j,k=1}^3 \sum_{n=0}^{+\infty} U_{\alpha i} U_{\beta k}^* W_{ij}^{(0n)*} W_{kj}^{(0n)} e^{i \frac{(\lambda_j^{(n)}/a)^2 L}{2E}}. \quad (2.17)$$

where  $E$  is the neutrino energy, and  $L$  is the baseline.  $\lambda_j^{(n)}$  are the eigenvalues of the Hamiltonian based on Equation 2.15.  $U$  and  $W$  are the mixing matrices for the active and KK neutrino modes, respectively. A detailed derivation of Equation 2.17 can be found in Appendix C. Squaring the amplitude gives the oscillation probability

$$P(\nu_\alpha \rightarrow \nu_\beta) = |\mathcal{A}(\nu_\alpha \rightarrow \nu_\beta)|^2. \quad (2.18)$$

In addition to the extra dimension size  $a$ , the oscillation probabilities also depend on the three active neutrino masses  $m_1, m_2$ , and  $m_3$  coming from the eigenvalues of the mass matrix  $m_{\alpha\beta}$  in Equation 2.15. They can be calculated from the lightest mass  $m_0$  and the mass splittings of active neutrinos.

Using the same approach, but by a different group, the sensitivities of CHOOZ, KamLAND, MINOS are calculated in Reference [71]. A combined limit of  $a < 1.0(0.6) \mu\text{m}$  at 99% C.L. is obtained for normal (inverted) mass hierarchy. Their result for MINOS  $7.24 \times 10^{20}$  POT  $\nu_\mu$  running is shown in Figure 2.10. The same authors also tried to explain the reactor anomaly using this model [72].

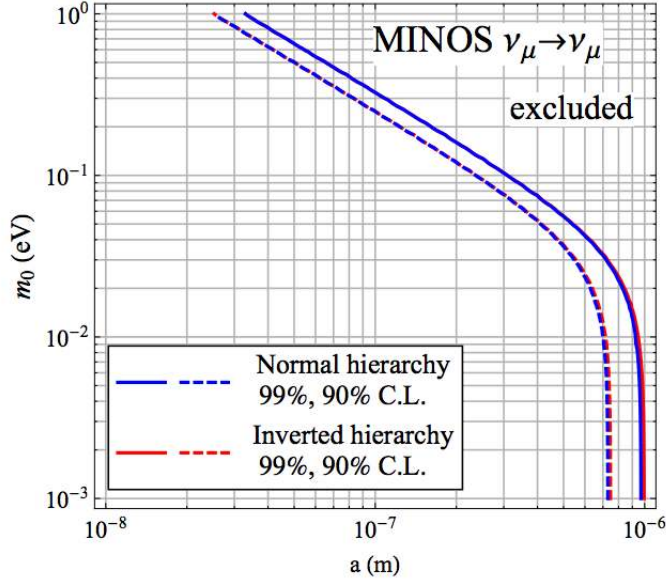


Figure 2.10: Excluded regions in  $a - m_0$  plane based on the simulated charge current sample of  $7.24 \times 10^{20}$  POT  $\nu_\mu$  running in MINOS by Reference [71].  $m_0$  is the lightest neutrino mass and  $a$  is the extra dimension size.

To calculate the oscillation probability in Equation 2.18, GNU Scientific Library is used to find eigenvalues and eigenstates of the  $N \times N$  Hamiltonian matrix shown in Appendix C. The size of the matrix  $N$  is equal to three times the number of orders of KK states for there are three neutrinos in each order.

In principle  $N \rightarrow \infty$  as there are infinite orders of KK states. However, as a good approximation, the maximum order of KK states is limited to 5 to reduce the computing time. Together with the zeroth order, we have  $N = 3 \times 6 = 18$ .

Similar to the 3+1 model, two oscillation probabilities are measured in the MINOS detectors:  $P(\nu_\mu \rightarrow \nu_\mu)$  by the charged current events, and  $P(\nu_\mu \rightarrow \nu_s)$  by the neutral current events. Note that the  $\nu_s$  represents all sterile neutrinos arising from  $KK$  states. In practice,  $P(\nu_\mu \rightarrow \nu_s)$  is calculated as

$$P(\nu_\mu \rightarrow \nu_s) = 1 - P(\nu_\mu \rightarrow \nu_e) - P(\nu_\mu \rightarrow \nu_\tau). \quad (2.19)$$

A few examples of  $P(\nu_\mu \rightarrow \nu_\mu)$  at the MINOS far detector are shown in Figure 2.11. The wiggles associated with large  $a$  are the original motivation to study this model, because in the far detector data some wiggles have also been observed and may be caused by an exotic model like LED. Oscillation probabilities as a function of  $L/E$  are useful to demonstrate the oscillations at the near detector in addition to those at the far detector. An example is shown in Figure 2.12, where the simulated energy spectra in the near and far detectors are represented by the gray bands. The darker bands contain 68% of the data and the lighter bands contain 90% of the data. For demonstration purpose, the oscillation probabilities shown in Figure 2.12 have been smeared using the charge current event energy resolution

$$P_{smeared}(E) = \int P(x) \frac{1}{\sigma\sqrt{2\pi}} e^{-\frac{(x-E)^2}{\sigma^2(x)}} dx, \quad (2.20)$$

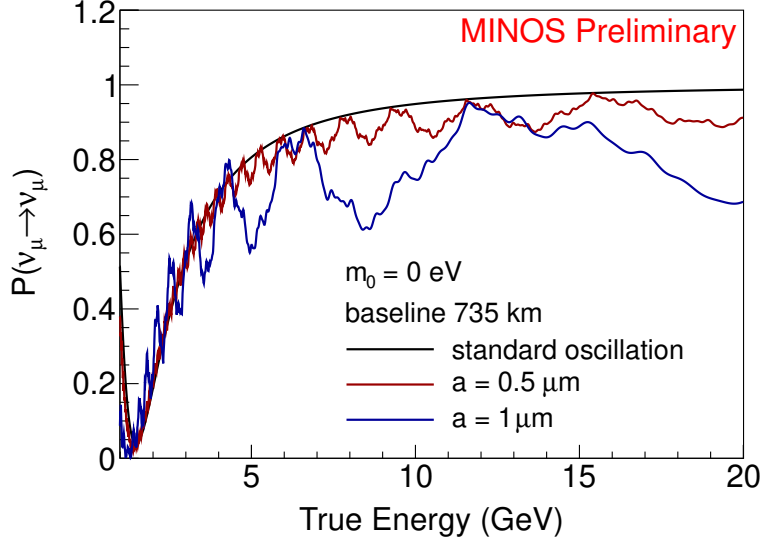


Figure 2.11:  $P(\nu_\mu \rightarrow \nu_\mu)$  at MINOS far detector.

The total energy resolution is the sum of the track energy resolution and the shower energy resolution

$$\sigma(E) = \sigma(E_{trk}) \oplus \sigma(E_{shw}), \quad (2.21)$$

where

$$\sigma(E_{shw}) = 0.257 \text{ GeV} \oplus 40.4\% \sqrt{E_{shw}} \oplus 8.6\% E_{shw}, \quad (2.22)$$

$$\sigma(E_{trk}) = 5.1\% \sqrt{E_{trk}} \oplus 6.9\% E_{trk}. \quad (2.23)$$

Equation 2.22 and 2.23 are the parameterized functions taken from [73].

As additional examples, the oscillation probabilities for a large  $a$  are shown in Figure 2.13 and those for a large  $m_0$  are shown in Figure 2.14.

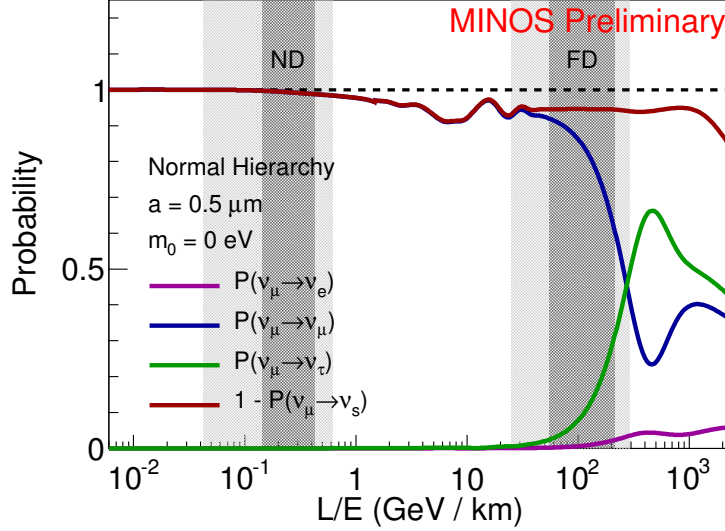


Figure 2.12: LED oscillation probabilities as a function of  $L/E$  for  $a = 0.5 \mu\text{m}$  and  $m_0 = 0 \text{ eV}$ . The simulated energy spectra for the near detector (ND) and far detector (FD) are represented by the gray bands. The darker bands contain 68% of the data and the lighter bands contain 90% of the data.

Since  $\delta_{CP}$  remains unknown, its effect has been tested and is shown in Figure 2.15, where the curves with different  $\delta_{CP}$  overlap, implying small dependence of oscillation probabilities on this parameter.

As mentioned earlier, oscillation probabilities depend on the three neutrino masses  $m_1$ ,  $m_2$  and  $m_3$ . For this reason, the effect of neutrino mass hierarchy should also be considered, and this is shown in Figure 2.16. However, the MINOS sensitivities in Reference [71] show little dependence on the choice of mass hierarchy (see Figure 2.10), unlike the results for other experiments in the paper. To reduce the computing time, only normal hierarchy is considered in this dissertation.

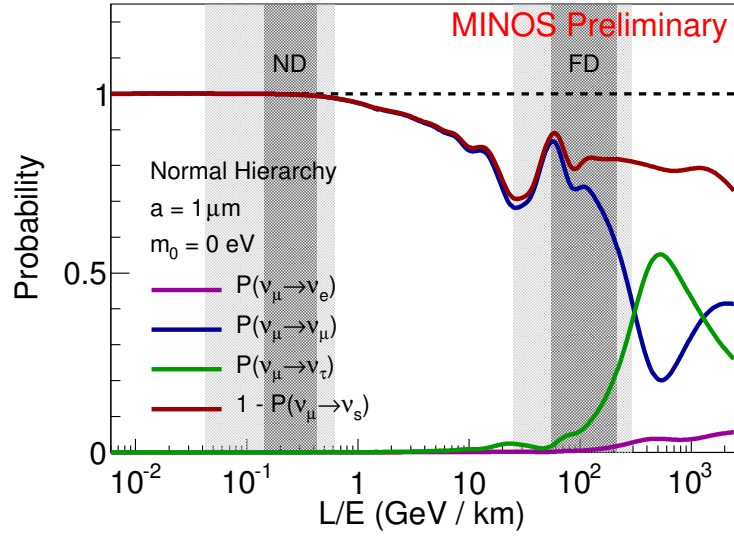


Figure 2.13: LED oscillation probabilities as a function of  $L/E$  for  $a = 1 \mu\text{m}$  and  $m_0 = 0 \text{ eV}$ .

The model will be tested with  $10.56 \times 10^{20}$  POT  $\nu_\mu$  running data of MINOS in Chapter 9.



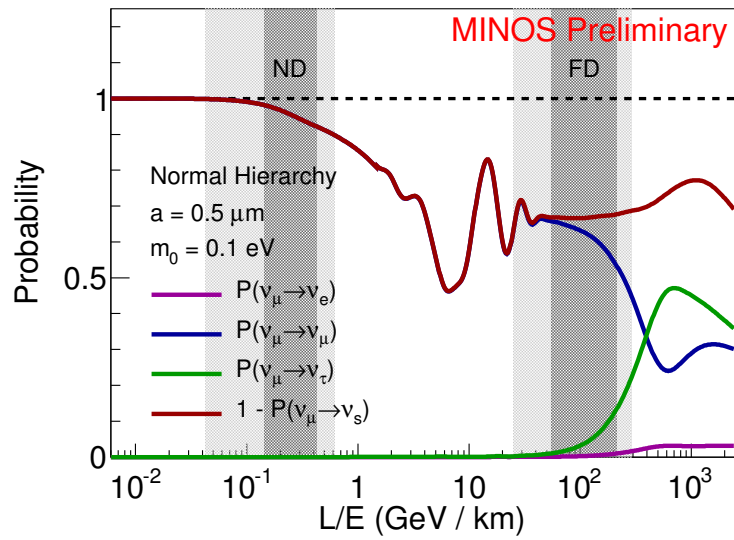


Figure 2.14: LED oscillation probabilities as a function of  $L/E$  for  $a = 0.5 \mu\text{m}$  and  $m_0 = 0.1 \text{ eV}$ .

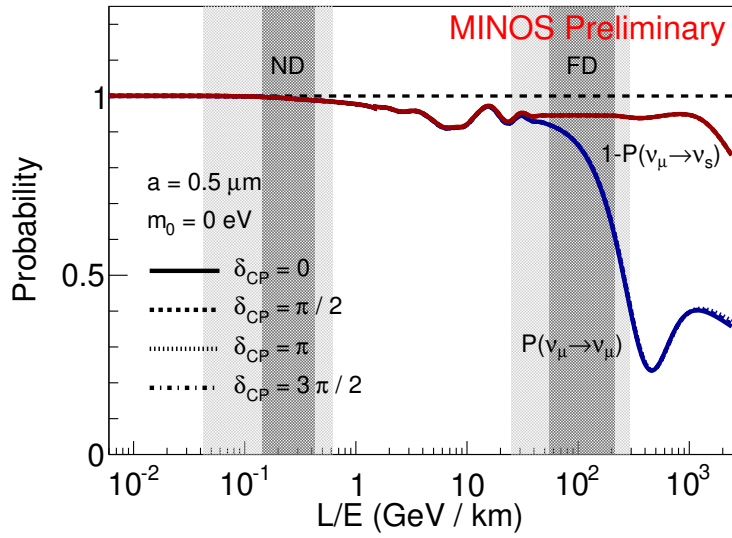


Figure 2.15: LED oscillation probabilities as a function of  $L/E$  for different values of  $\delta_{CP}$ . Curves of different  $\delta_{CP}$  have different line styles. The blue curves are for  $P(\nu_\mu \rightarrow \nu_\mu)$  with the solid on the top. The red curves are for  $1 - P(\nu_\mu \rightarrow \nu_s)$  also with the solid on the top.

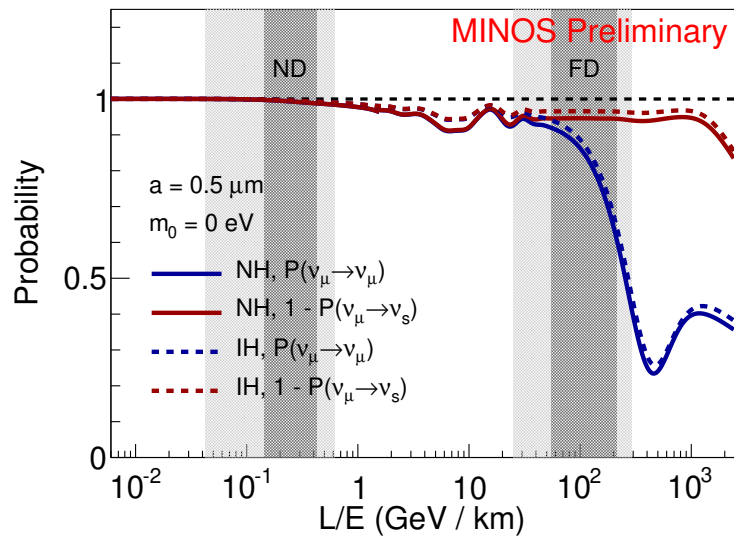


Figure 2.16: LED oscillation probabilities as a function of  $L/E$  for normal hierarchy (NH, solid lines) and inverted hierarchy (IH, dashed lines), with  $a = 0.5 \mu\text{m}$  and  $m_0 = 0 \text{ eV}$ . For the inverted hierarchy, the sign of  $\Delta m_{32}^2 \equiv m_3^2 - m_2^2$  is set to negative.

## Chapter 3

### MINOS and MINOS+ Experiments

This chapter gives a brief review of the MINOS and MINOS+ experiments. Following a general introduction on the experiments, descriptions about the neutrino beam and the detectors are provided. Neutrino interactions in the detectors are discussed in the last section.

#### 3.1 MINOS

MINOS (Main Injector Neutrino Oscillation Search) is a long baseline neutrino oscillation experiment, designed to measure  $\nu_\mu/\bar{\nu}_\mu$  disappearance from the  $\nu_\mu/\bar{\nu}_\mu$  beam produced by the NuMI (Neutrinos at the Main Injector) facility at Fermilab. MINOS uses two detectors, the near detector (ND) and the far detector (FD). The ND is located 1.04 km from the beam source at Fermilab to characterize the beam. The FD is located 735 km away in the Soudan mine in northern Minnesota to measure the disappearance of  $\nu_\mu/\bar{\nu}_\mu$ . The beamline is illustrated in Figure 3.1.

The experiment ran from March 2005 to April 2012, collecting both  $\nu_\mu$  and  $\bar{\nu}_\mu$  beam data. The beam exposure is shown in Figure 3.2. Most of the data was gathered in the low energy beam mode, with an energy peak around



Figure 3.1: The MINOS neutrino beamline. The  $\nu_\mu/\bar{\nu}_\mu$  beam is produced in the NuMI facility at Fermilab. It passes through the ND at Fermilab and the FD in the Soudan mine in northern Minnesota. The baseline is 735 km. The figure is taken from Reference [73].

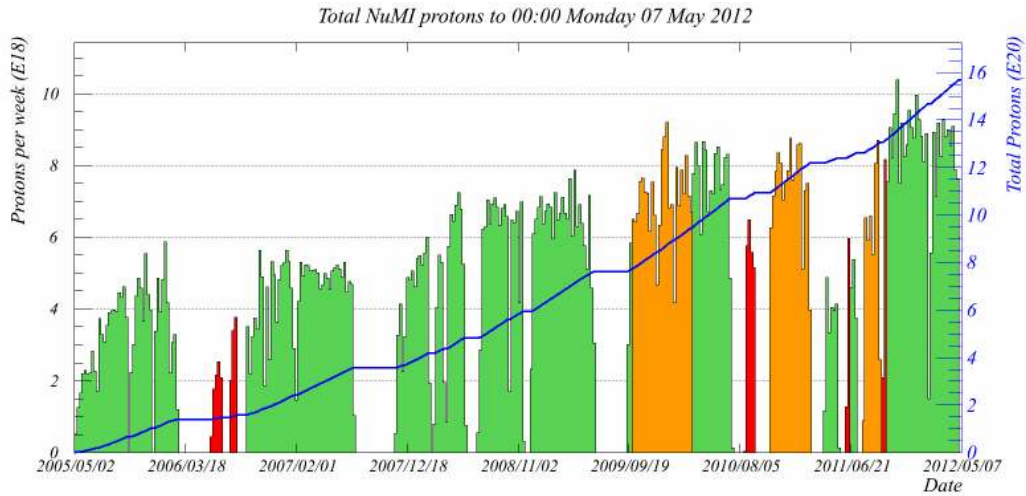


Figure 3.2: MINOS accumulated an exposure of  $15.6 \times 10^{20}$  protons-on-target between 2005 and 2012. Most of the data is taken in the low energy  $\nu_\mu$ -beam mode (in green) and in the  $\bar{\nu}_\mu$ -beam mode (in orange). The special runs with the higher energy mode or the magnetic horn turned off are shown in red. The plot is taken from Reference [74].

3 GeV. A summary of all runs taken since 2005 is shown in Table 3.1.

MINOS has provided the best measurement to date of  $\Delta m_{32}^2$  and a competitive measurement on  $\theta_{23}$ . Combining the analysis from  $\nu_e$  appearance,  $\nu_\mu$  disappearance and atmospheric neutrinos, the final result on  $\Delta m^2$  and  $\theta_{23}$  is shown in Figure 3.3.

### 3.2 MINOS+

MINOS+ is an experiment that uses the same two MINOS detectors and a medium energy beam designed for NO $\nu$ A, a long baseline experiment designed to measure  $\nu_e/\bar{\nu}_e$  appearance. While for NO $\nu$ A the beam energy

Run	Configuration	Horn polarity	Good data POT( $\times 10^{18}$ )
1	LE	Forward	126.93
1	pHE	Forward	15.31
2	LE	Forward	194.27
3	LE	Forward	388.71
4	LE	Forward	8.84
4	LE	Reverse	170.85
5	LE	Forward	45.89
6	LE	Forward	61.62
7	LE	Reverse	124.08
8	LE	Forward	12.58
9	LE	Reverse	40.80
10	LE	Forward	238.31
Total good physics data			1428.19
$\nu_\mu$ beam run periods (1, 2, 3, 5, 6, 10)			1071.04
$\nu_\mu$ LE beam run periods (1, 2, 3, 5, 6, 10)			1055.73
$\bar{\nu}_\mu$ beam run periods (4, 7, 9)			335.73

Table 3.1: Summary of the data collected in MINOS in terms of the POT exposure. The majority of the data comes from a low energy beam (LE) with an energy peak around 3 GeV. A small fraction of the data comes from a pseudo high energy beam (pHE) with an energy peak around 7 GeV.

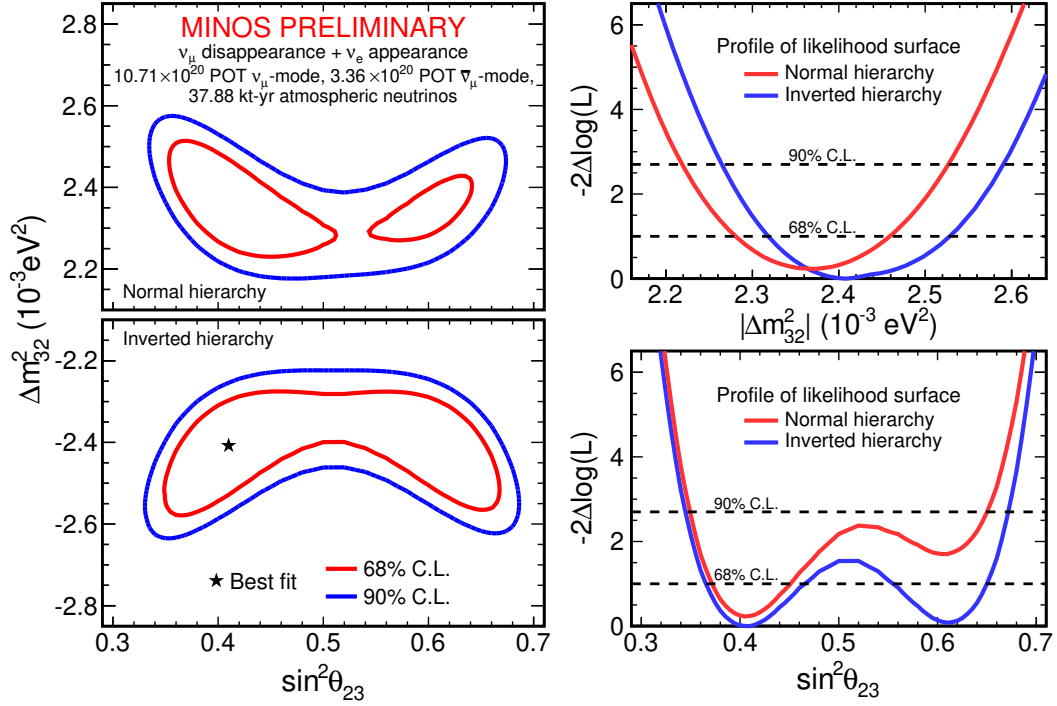


Figure 3.3: Results of a combined analysis of  $\nu_\mu$  disappearance and  $\nu_e$  appearance using its complete set of accelerator and atmospheric neutrino data. The plots are taken from Reference [39].



centers around 2 GeV, the energy peak in MINOS+ is at about 6 GeV. This is because MINOS detectors measure neutrinos at the beam center while NO $\nu$ A detectors are 14.6 milliradians off the beam axis. A comparison between the low energy beam used in MINOS and the medium energy beam used in MINOS+ is shown in Figure 3.4.

MINOS+ further exploits the potential of the NuMI beam. In addition to improving the accuracy on the standard parameters, it offers unique opportunities to explore physics beyond the three-neutrino mixing model. High statistics neutrino data can be collected in the FD to test the existence of non-standard neutrino interactions, sterile neutrinos, and extra dimensions among others [75].

The first run of MINOS+, Run 11, started in September 2013 and ended on September 5, 2014. A total of  $2.99 \times 10^{20}$  protons on target (POT) worth of data has been collected [76]. The beam exposure as a function of time is shown in Figure 3.5. MINOS+ will continue to take data at least through 2016.

### **3.3 NuMI Beam**

A schematic of the NuMI beamline is shown in Figure 3.6. 120 GeV protons from Fermilab's Main Injector are directed to a graphite target, creating pions and kaons. The neutrino beam is produced by the decay of pions,

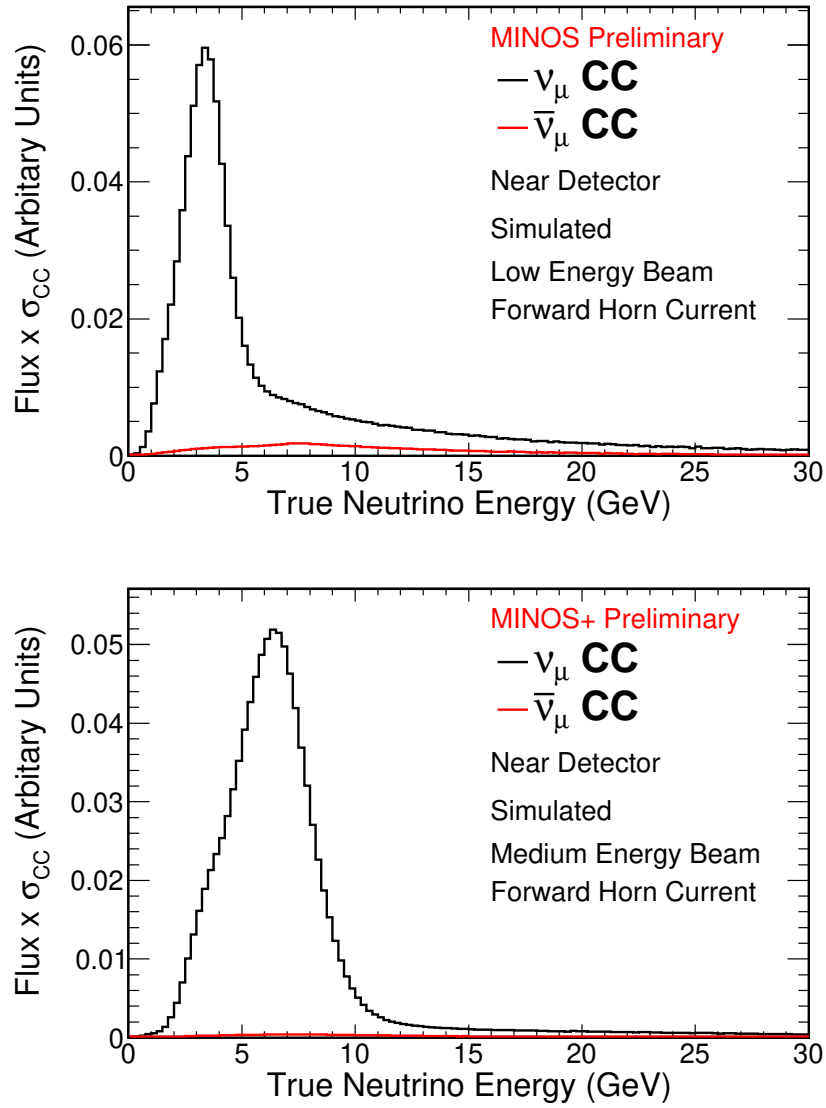


Figure 3.4: Difference between the low energy  $\nu_\mu$  beam used in MINOS (top) and the medium energy  $\nu_\mu$  beam used in MINOS+ (bottom). The plots are taken from Reference [77].

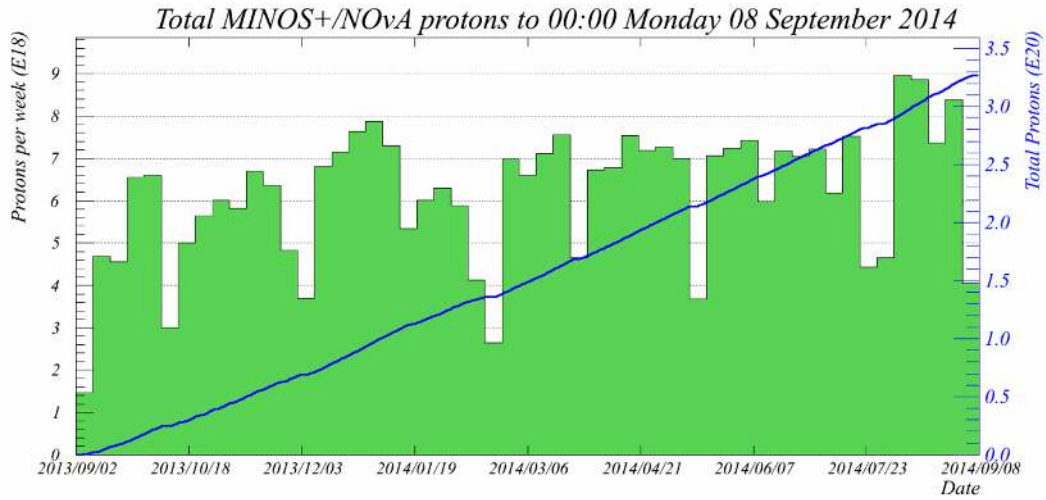


Figure 3.5: MINOS+ accumulated an exposure of  $2.99 \times 10^{20}$  protons-on-target between September 2013 and September 2014. The plot is taken from Reference [78].

kaons and muons in the decay pipe:

$$\pi^\pm \rightarrow \mu^\pm + \nu_\mu/\bar{\nu}_\mu, \quad (3.1)$$

$$K^\pm \rightarrow \mu^\pm + \nu_\mu/\bar{\nu}_\mu, \quad (3.2)$$

$$\mu^\pm \rightarrow e^\pm + \bar{\nu}_\mu/\nu_\mu + \nu_e/\bar{\nu}_e. \quad (3.3)$$

Detailed calculations of these three decay processes can be found in Appendix D. The energy spectrum and content of the neutrino beam is controlled by two magnetic horns, as illustrated in Figure 3.7. The relative distance between the target and the first horn controls the energy peak. In MINOS+, the target is placed closer to the horn than in MINOS, resulting a higher energy beam. The current direction in the horn determines the fractions of  $\bar{\nu}_\mu$  in the beam. In the forward horn current (FHC) configuration,  $\pi^+$  and  $K^+$  are focused and

$\nu_\mu$  is the dominant component in the beam as shown in Figure 3.4. This is referred to as the  $\nu_\mu$  running. Most of the data in MINOS ( $10.71 \times 10^{20}$  POT) and all the data so far in MINOS+ ( $2.99 \times 10^{20}$  POT) were taken in this mode. In the reversed horn current (RHC) configuration,  $\pi^-$  and  $K^-$  are focused to increase the  $\bar{\nu}_\mu$  fraction in the beam.

### 3.4 Detectors

The ND and FD are designed to be as similar as possible in order to reduce systematic errors. For example, in the analyses of this dissertation, the fitting is performed on the ratio of the FD spectrum over the ND spectrum. While the simulated ND and FD spectrum is subject to the systematic error of the neutrino interaction cross sections, the ratio is not.

The detectors are described in great detail in Reference [81]. Both detectors are steel-scintillator sampling calorimeters with tracking, energy and topology measurement capabilities. This is achieved by using alternate planes of polystyrene scintillator strips and 2.54 cm thick steel plates.

Steel plates serve as a neutrino interaction target. Their high density increases the probability for neutrinos to interact inside the detectors. Neighboring steel plates are 5.95 cm apart.

Each scintillator strip is extruded to be 1 cm thick and 4.1 cm wide. A double-clad wave-length-shifting (WLS) fiber with a diameter of 1.2 mm is embedded in the strip to collect the scintillation light and guide it to a

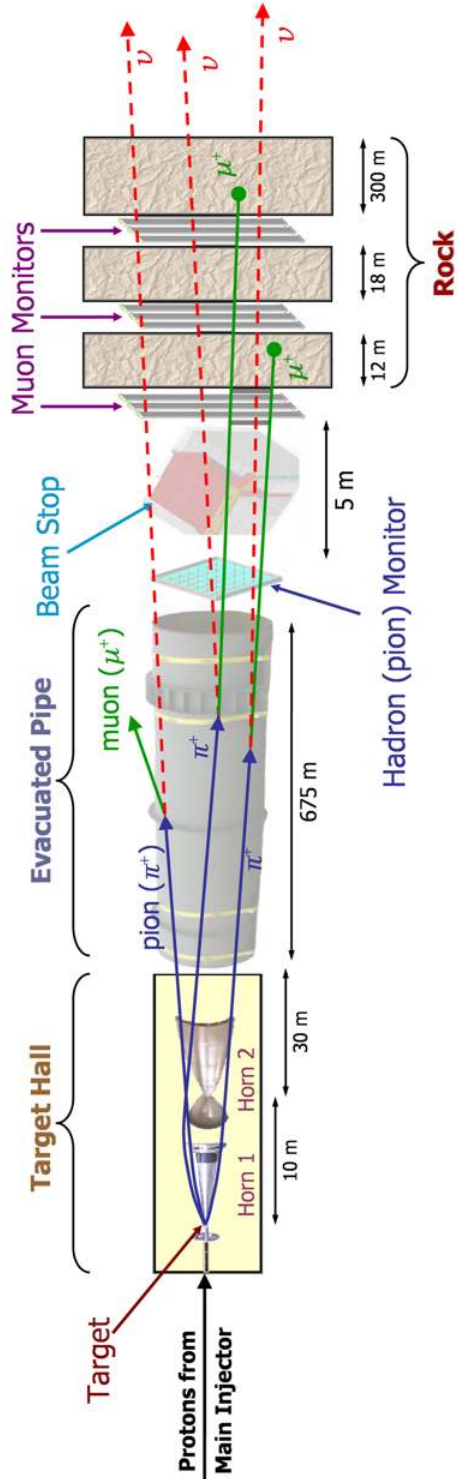


Figure 3.6: A schematic of the NuMI beam. The key elements are shown, including the target, the horns, the decay pipe, the hadron absorber, and the muon shield which consists of the dolomite rock preceding the MINOS near detector. The figure is taken from Reference [79].

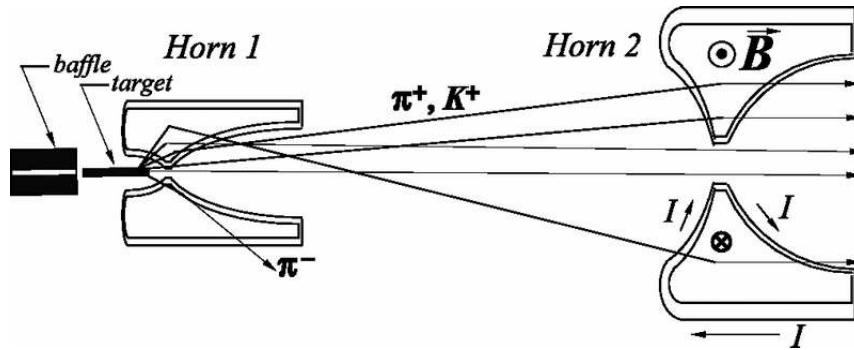


Figure 3.7: Focusing of pions and kaons using two magnetic horns. Horn 1 and 2 are separated by a distance of 10 m. A collimating baffle upstream of the target protects the horns from direct exposure to misdirected proton beam pulses. The target and baffle system can be moved further upstream of the horns to produce higher energy neutrino beams. The vertical scale is 4 times that of the horizontal (beam axis) scale. The figure is taken from Reference [80].

pixel of a multi-anode PMT tubes. The WLS fiber is essential because it has a much longer absorption length compared to that of the scintillator strip. Additionally, with 175 ppm of Y11 (K27) fluor, it shifts the wavelength of the scintillation light to a wavelength range that corresponds to a higher PMT quantum efficiency. The strip surface is covered by a thin (0.25 mm) co-extruded titanium-dioxide (TiO<sub>2</sub>)-loaded polystyrene layer that serves as a diffuse reflector to minimize light losses. The structure of the strip and the PMT readout is shown in Figure 3.8 and Figure 3.9.

Each scintillator plane is made of modules, which are groups of scintillator strips covered by flat aluminum sheets for light-tightness. The scintillator strips in each module are close-packed to minimize inactive zones between strips.

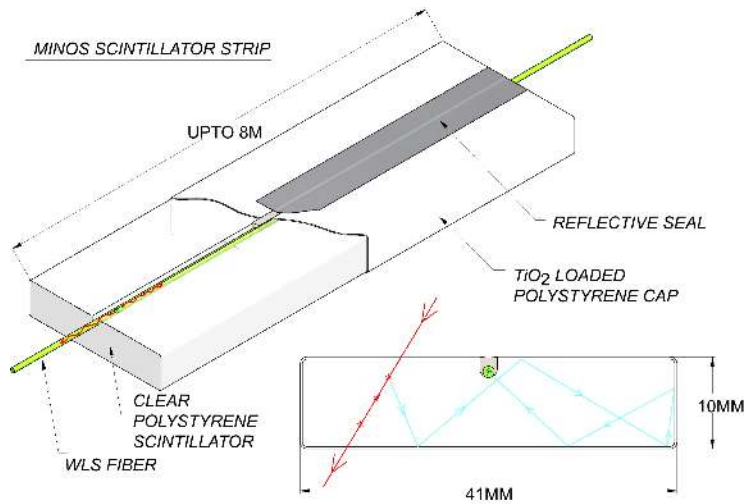


Figure 3.8: Structure of a single scintillator strip. Light produced by an ionizing particle is reflected multiple times inside the strip by the 0.25 mm-thick outer reflective coating. Scintillation light absorbed by the WLS fiber is re-emitted isotropically, and the wavelength-shifted photons whose directions fall within the total internal reflection cones are transported along the fiber to the edges of the strip. The figure is taken from Reference [81].

Both detectors are magnetized to allow charge separation, i.e. to distinguish  $\nu_\mu$  and  $\bar{\nu}_\mu$  on a event by event basis.

### 3.4.1 Near Detector

The 980 ton MINOS near detector is located at the end of the NuMI beam facility at Fermilab in a 100 m deep underground cavern. It has a cross-section of a squashed-octagon (4.8 m by 3.8 m), as shown in Figure 3.10. The ND magnetic field is generated by a current flowing through an off-center coil. The beam axis is displaced 1.48 m horizontally from the coil, to limit the number of events depositing energy in the hole.

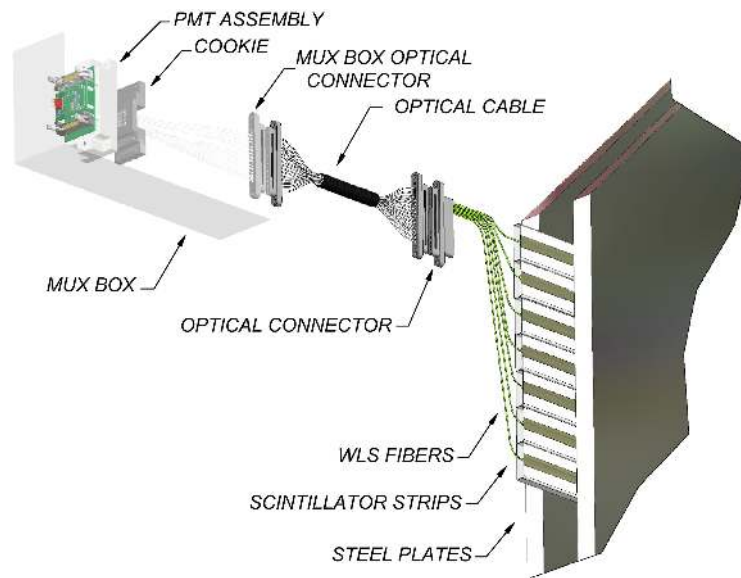


Figure 3.9: Illustration of the readout for a scintillator plane. The light produced in a strip (see Figure 3.8) is guided out of the module by a WLS fiber, and routed through a clear optical fiber to a pixel of the PMT. The figure is taken from Reference [81].



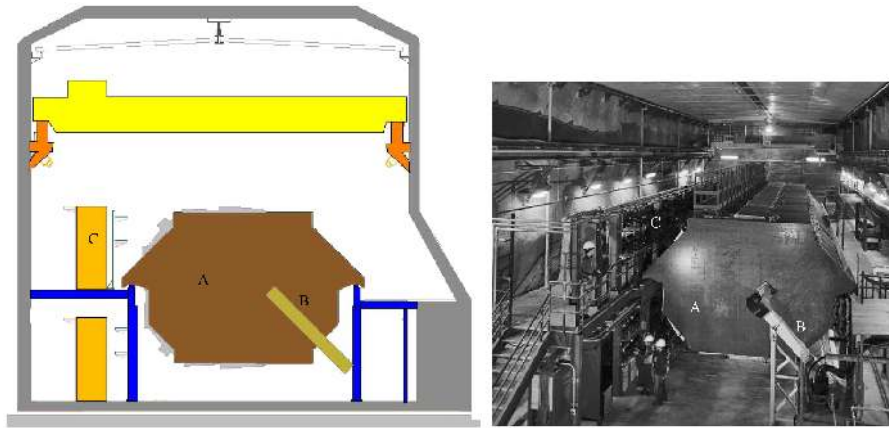


Figure 3.10: End view of the near detector looking along the direction of the beam. The drawing (left) identifies detector elements shown in the photograph (right): “A” is the furthest upstream steel plane, “B” is the magnet coil, and “C” is an electronics rack on the elevated walkway. The NuMI beam intersects the near detector near the “A” label. The figure is taken from Reference [81].

Only 153 of the 282 planes ND planes are active. They are instrumented with four distinct scintillation module patterns: full U-view (FU), full V-view (FV), partial U-view (PU), and partial V-view (PV), as shown in Figure 3.11. The U and V-view correspond to the X and Y axis rotated by  $45^\circ$ . The detector can be divided into two sections, the calorimeter and the spectrometer. The first 120 planes make up the calorimeter section and are all interleaved with planes of plastic scintillator strips in order to yield a high resolution view of the neutrino interactions. In the spectrometer section, planes 121-281, a full-view plane is included in every fifth plane only. This downstream section is used solely to track muons created in neutrino interactions.

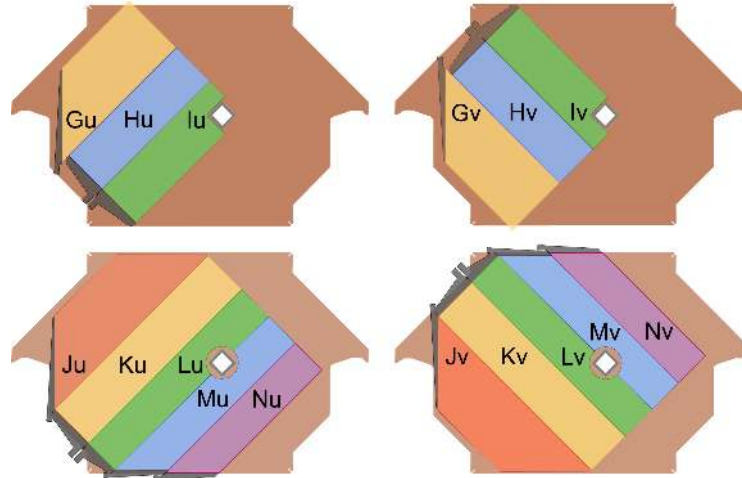


Figure 3.11: The four different configurations of planes used in the near detector, showing the different layouts of the scintillator modules. The upper two figures show partially instrumented planes (calorimeter region) while the lower two figures show the fully instrumented ones (tracking region). Strips oriented in the U direction are on the left, and V, on the right. These orientations alternate in the detector to provide stereo readout. The G-N notations denote the different shapes of the scintillator modules. The U and V planes require slight variations on each shape, leading to a total of 16 module types. The beam is centered midway between the coil hole and the left side of the plane, so that the scintillators only need to cover that area in the target region. The figure is taken from Reference [81].

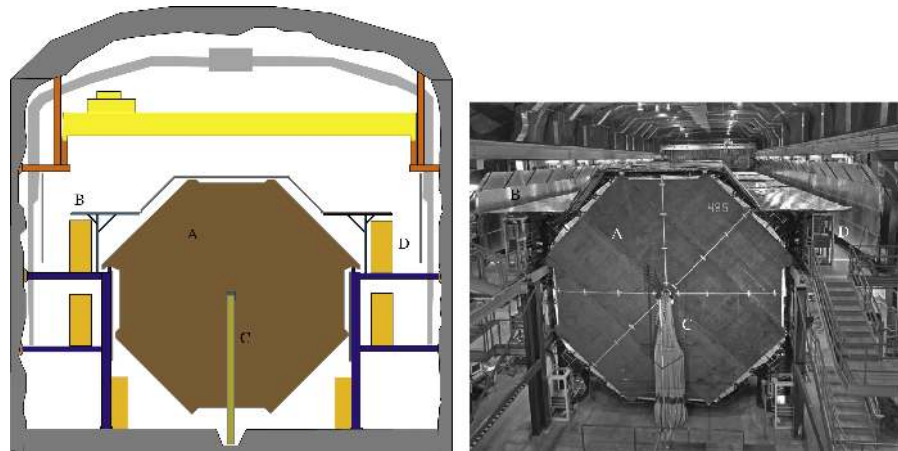


Figure 3.12: End views of the second far detector supermodule, looking toward Fermilab. The drawing (left) identifies detector elements shown in the photograph (right): “A” is the furthest downstream steel plane, “B” is the cosmic ray veto shield, “C” is the end of the magnet coil and “D” is an electronics rack on one of the elevated walkways alongside the detector. The horizontal structure above the detector is the overhead crane bridge. The figure is taken from Reference [81].

### 3.4.2 Far Detector

The MINOS far detector laboratory is located 710 m below the surface, 735 km from Fermilab, in Soudan, MN. This 5400 ton detector comprises two “supermodules” axially separated by a 1.15 m gap. The far detector consists of 486 octagonal steel planes (249 in the first supermodule and 237 in the second), with an edge to edge dimension of 8 m, interleaved with planes of plastic scintillator strips. The FD has a 1.3 T cylindrical magnetic field generated by a current flowing through a coil along the center of the detector. A FD plane consists of eight modules of different shape. The layout is illustrated in Figure 3.13.

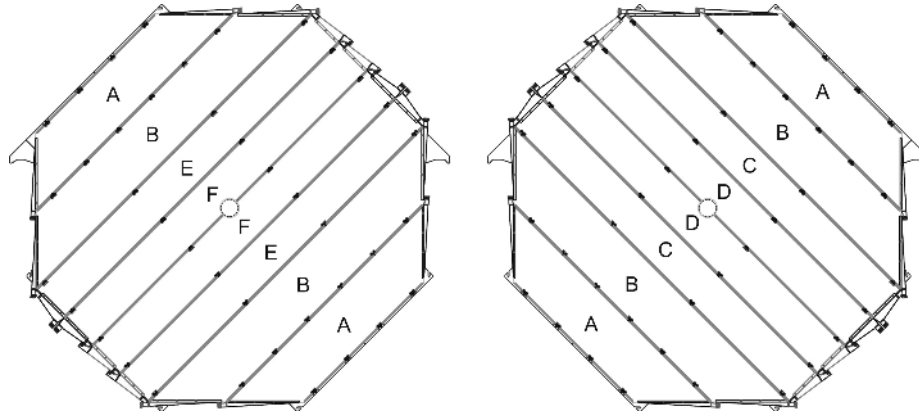


Figure 3.13: Layout of U (left) and V (right) modules in far detector planes. U- and V-type planes are interleaved. A and B module types have 28 scintillator strips and the other types have 20 strips. The first (upstream) scintillator plane of each supermodule is of the V-type. The figure is taken from Reference [81].

### 3.5 Neutrino Interactions in the Detectors

There are two types of neutrino interactions, charge current (CC) interactions which are mediated by  $W^\pm$  bosons, and neutral current (NC) interactions which are mediated by  $Z$  boson.

The final state of a CC interaction consists of a charged lepton and a hadronic shower. An example of a simulated CC event in the MINOS detector is shown in Figure 3.14. In the neutrino energy range considered in this dissertation, 0-40 GeV, CC interactions can be divided in dominant classes [82].

1. Quasi-elastic scattering dominates below 1 GeV:

$$\begin{aligned}
 \nu_\mu n &\rightarrow \mu^- p, \\
 \bar{\nu}_\mu p &\rightarrow \mu^+ n.
 \end{aligned}
 \tag{3.4}$$

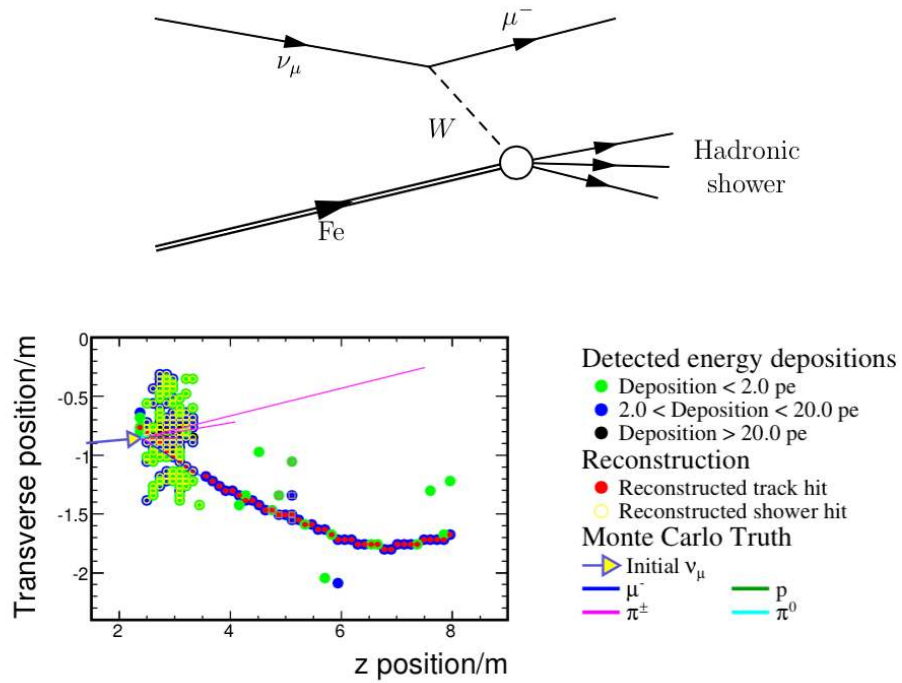


Figure 3.14: Top: Feynman diagram of a CC interaction between a  $\nu_\mu$  and iron. Bottom: simulated CC event display. The colored dots represents signals of different strength in the scintillator strips. The outgoing muon forms a long track used to identify the CC interactions. The curvature of the track is caused by the magnetic field in the detector, and is used to determine the charge sign. The figures are taken from [82].

In MINOS, quasi-elastic interactions result in little or no hadronic activity. Typically only the muon track is visible in the detector.

2. At a few GeV, resonance production becomes important. In this process, the struck nucleus (N) is excited to a baryon resonance ( $N^*$ ) which most likely decays to a nucleon-pion final state:

$$\begin{aligned}\nu_\mu N &\rightarrow \mu^- N^*, \\ N^* &\rightarrow \pi N'.\end{aligned}\tag{3.5}$$

The pion can give a shower-like topology if it undergoes hadronic interactions, or else a track-like signature in the case of the  $\pi^\pm$ .

3. Deep inelastic scattering (DIS) dominates above a few GeV. In this process, the neutrinos probe inside the nucleons and scatter off the constituent quarks. In MINOS, DIS produces events with a large hadronic shower.

The cross sections of these processes in MINOS detectors is shown in Figure 3.15.

The final state of a NC interaction consists of the scattered incoming neutrino and a hadronic shower. A simulated NC event display is shown in Figure 3.16.

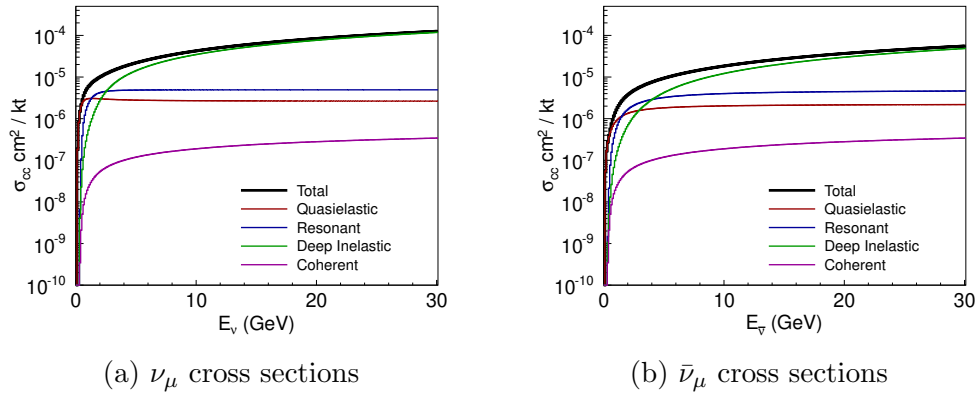


Figure 3.15:  $\nu_\mu$  and  $\bar{\nu}_\mu$  CC interaction cross sections in the MINOS detectors.

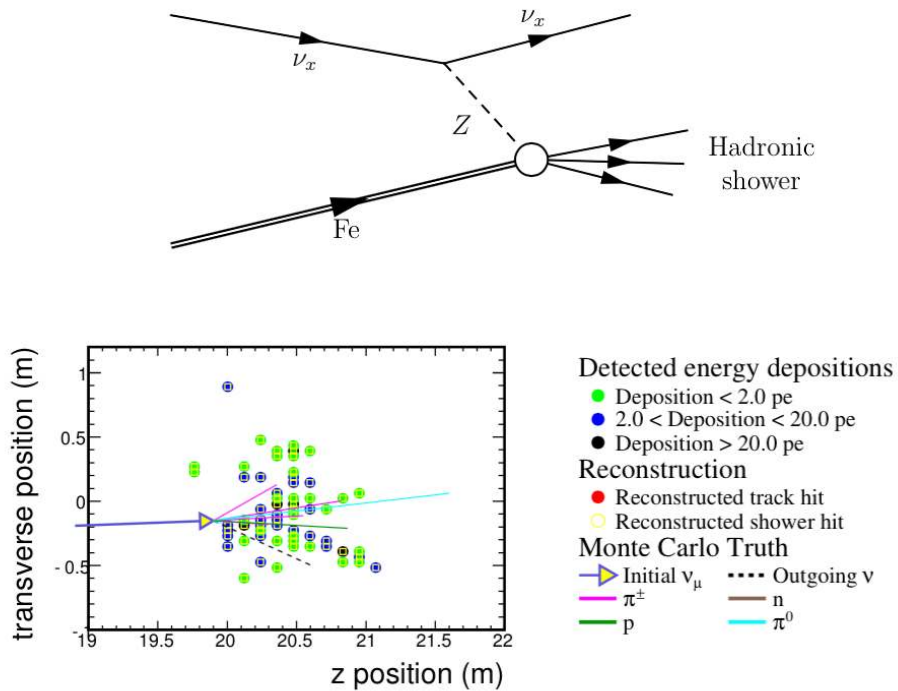


Figure 3.16: Top: Feynman diagram of a NC interaction between a neutrino and iron. Bottom: simulated NC event display. The figures are taken from Reference [82].

# Chapter 4

## Shower Energy Reconstruction

This chapter focuses on the hadronic shower energy reconstruction for CC events in MINOS+. Both CC and NC events contribute to the two analyses in this dissertation. Due to having a higher energy resolution, CC events play a dominant role in constraining model parameters, as will be shown in Chapter 8 and Chapter 9. The total energy of a CC event is the sum of the track energy and shower energy. MINOS detectors were designed to precisely measure muon tracks, and the energy is reconstructed based on the track curvature caused by the magnetic field in the detector or the track range. The energy resolution of CC events is mainly limited by the shower energy reconstruction. In the early stage of MINOS analysis, shower energy was simply the sum of the charge collected from all strips in a shower. The energy reconstructed by this approach is referred as calorimetric shower energy. A major improvement was made in 2010 analysis by utilizing additional shower features, such as the shower topology [83], which are passed to the  $k$ -Nearest-Neighbor ( $k$ NN) algorithm [84] to better estimate the energy. In MINOS+, the same procedure was followed, with the change of using MINOS+ MC samples.



## 4.1 $k$ NN Shower Energy

The basic idea of reconstructing shower energy using the  $k$ NN technique is to find a group of closest matching MC events ( $k$  nearest neighbors) for a given data event, and use the averaged true energy of these MC events as the reconstructed energy for that data event.

To decide which MC events have the greatest similarity with a given data event, it is necessary to find the shower features that are relevant to the energy. In MINOS, a number of variables were studied and the combination of the following three were considered to be the best in terms of improving the standard oscillation sensitivity [85]:

1. The number of planes in the primary shower.
2. The deweighted energy within 1m of the track vertex.
3. The calorimetric energy in the first two showers if there are more than one reconstructed shower.

The first one is related to the shower topology. The second one is a subset of the total shower energy. A deweighting procedure is performed, where a nonlinear function is applied to the calorimetric energy in order to account for the nonlinear detector response to lower energy events [86]. The third one comes from the fact that in a event, there are sometimes multiple showers as identified by clusters of hits. The primary shower is used for the calorimetric shower energy. This variable not only uses the primary shower, but also adds

the second shower. A comparison of these variables in MC for MINOS and MINOS+, along with the true shower energy is shown in Figure 4.1. For the increased number of high energy neutrinos, the mean of these distributions are shifted up in MINOS+.

Having obtained relevant shower features, the question becomes how to decide the similarity or closeness of two events quantitatively. One natural index is the Euclidean metric, which can be defined as

$$d = \sqrt{\frac{\sum_i (x_i - y_i)^2}{\sigma_i^2}}, \quad (4.1)$$

where  $i = 1, 2,$  and  $3$  for the three shower variables considered.  $1/\sigma_i^2$  is the importance weight of variable  $i$ . In this work,  $\sigma_i$  is chosen as the standard deviation of the variable  $i$  distribution such that all the variables are treated with equal importance.

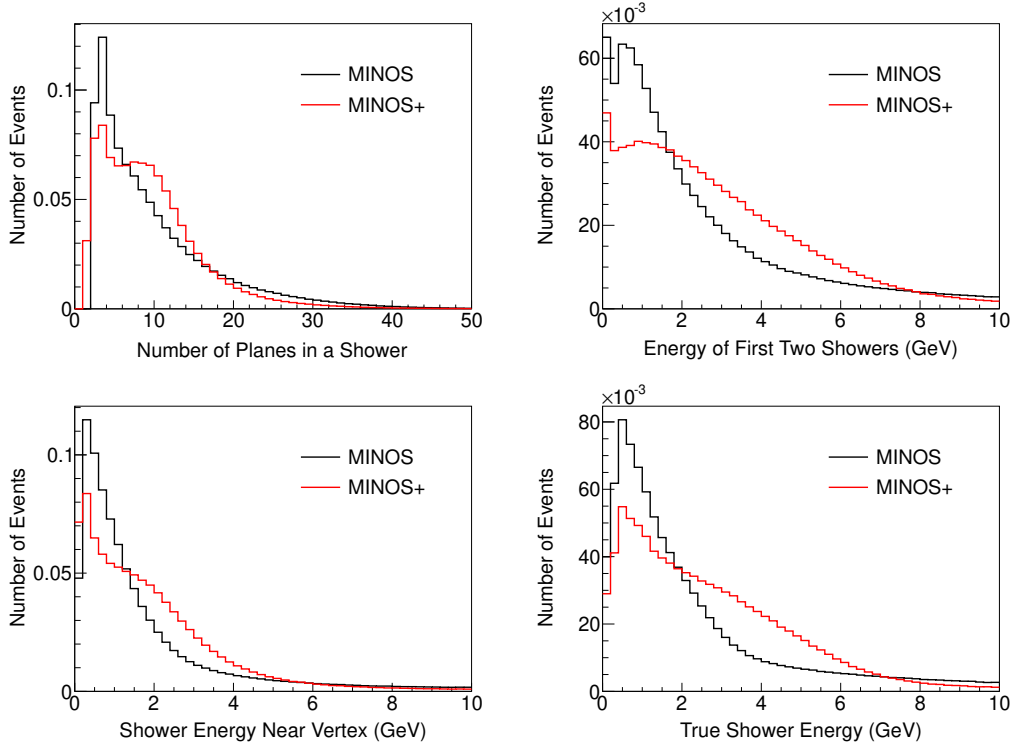


Figure 4.1: Distributions of  $k$ NN shower variables in MINOS and MINOS+. The three variables used for the  $k$ NN shower energy are the number of planes in a shower, energy of the first two showers, and dewighted shower energy near the track vertex. True shower energy distributions are also shown.

Using Equation 4.1, for each data event, one can find  $k$  nearest MC events in a very large set of MC events often referred to as the training set. In this study, after simple cuts on fiducial volume, particle ID (see Chapter 6), and charge sign ( $\mu^-$  for neutrino selection), a total of 961293 events are used in the training set of FD and 1082125 for that of ND. To find  $k$  nearest neighbors efficiently, in MINOS, the  $k$ -d tree algorithm [87] was used. In MINOS+, a similar algorithm, v-p tree [88, 89] was employed with an improved search

speed. The number of neighbors,  $k$ , cannot be too large, because events that are far away have little relevance to the target data event.  $k$  cannot be too small either, because it may result in biased results due to lack of statistics. To find the optimal  $k$ , sensitivity to the standard oscillation model was used as the criterion. This is because both sterile neutrino models considered in this dissertation, 3+1 and LED, are treated as perturbations to the standard oscillation model. A test point was chosen on the  $\Delta m^2 - \sin^2 2\theta$  plane with  $\Delta m^2 = 2.88 \times 10^{-3} \text{ eV}^2$  and  $\sin^2 2\theta = 0.72$ . It is located near the contour of 90% C.L. (see Figure 4.6).  $\chi^2$ s at this point are calculated by comparing the oscillated FD MC spectra reconstructed by different  $k$  to a simulated FD spectrum. A larger  $\chi^2$ , which indicates a smaller contour around the best fit point, corresponds to a better sensitivity. Note that in this simple approach, the position of the best fit point is fixed and given by the input, as all oscillation parameters are fixed and no systematics are included. The result of scanning  $k$  is shown in Figure 4.2 and  $k = 440$  was found to be the optimum value, in comparison to  $k = 400$  used in MINOS.

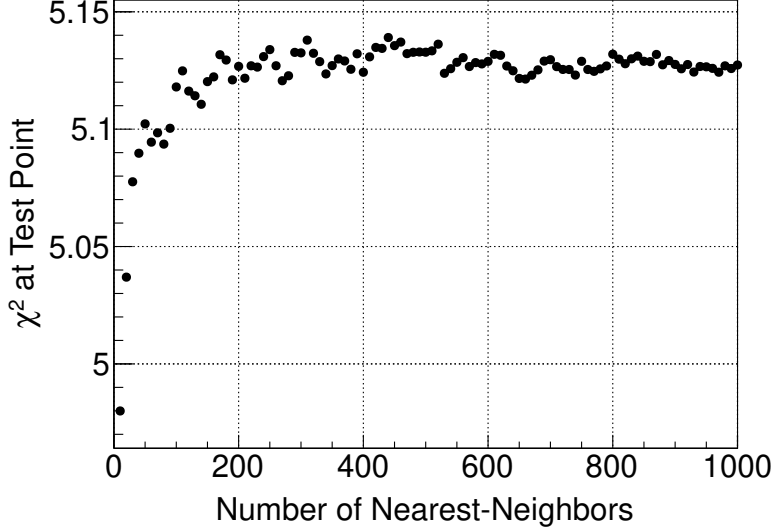


Figure 4.2: Scanning the number of neighbors  $k$ . Y-axis is the  $\chi^2$  at point  $\Delta m^2 = 2.88 \times 10^{-3} \text{ eV}^2$  and  $\sin^2 2\theta = 0.72$ . The highest point is at  $k = 440$ .

To avoid biases in neutrino energy spectrum,  $k$ NN shower energy was further corrected by a logarithmic polynomial function [85]

$$f(E) = \sum_{n=0}^N C_n \ln(E)^n. \quad (4.2)$$

The constants  $C_n$  are determined by performing a fit to the profile histogram of  $E_{kNN}/E_{true}$  as the function  $E_{true}$ , where  $E_{kNN}$  and  $E_{true}$  represent the  $k$ NN shower energy and true shower energy, respectively. In order to obtain a good fit, the polynomial order  $N$  was set to be 14. One fitting example is shown in Figure 4.3. A corrected  $k$ NN shower energy is obtained after the parameterized function  $f(E)$  is applied. Iterating this process three times gives a small enough bias as shown in Figure 4.4.

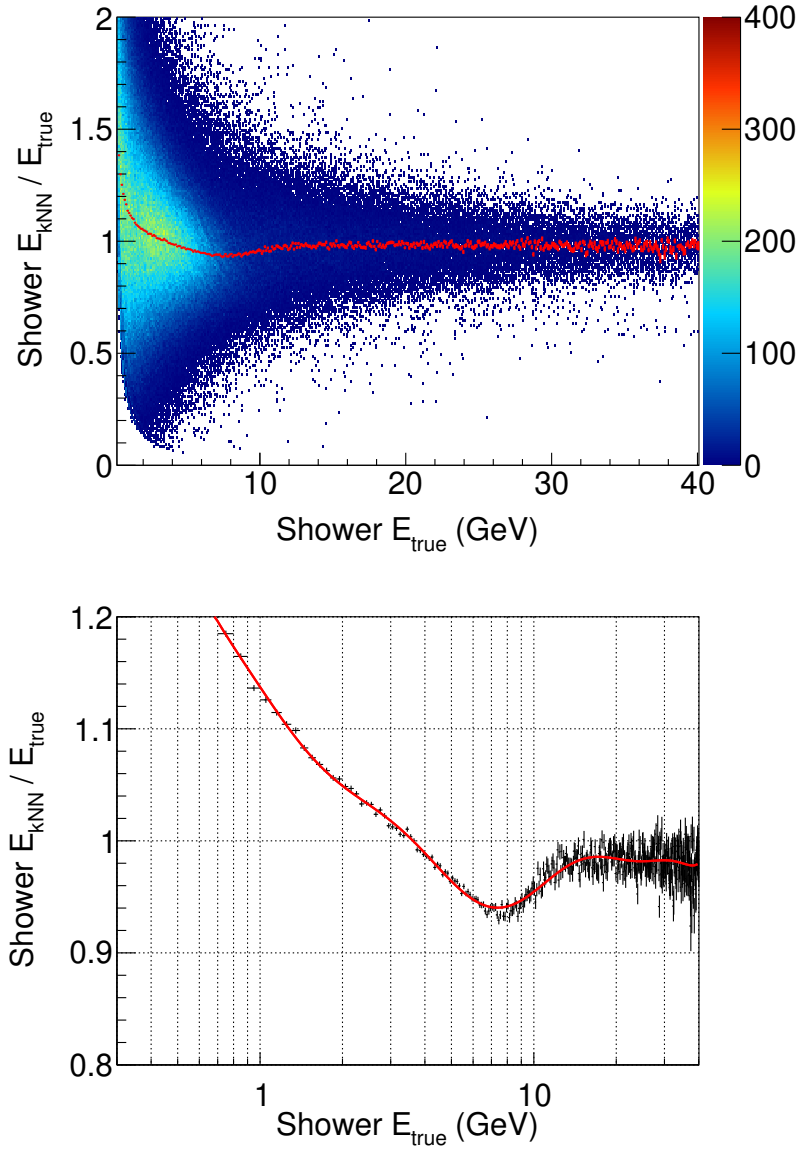


Figure 4.3: The profile of  $E_{kNN}/E_{true}$  as a function of  $E_{true}$ , shown as the red histogram in the top plot, is fitted with a 14<sup>th</sup> order logarithmic polynomial function as shown in the bottom plot.

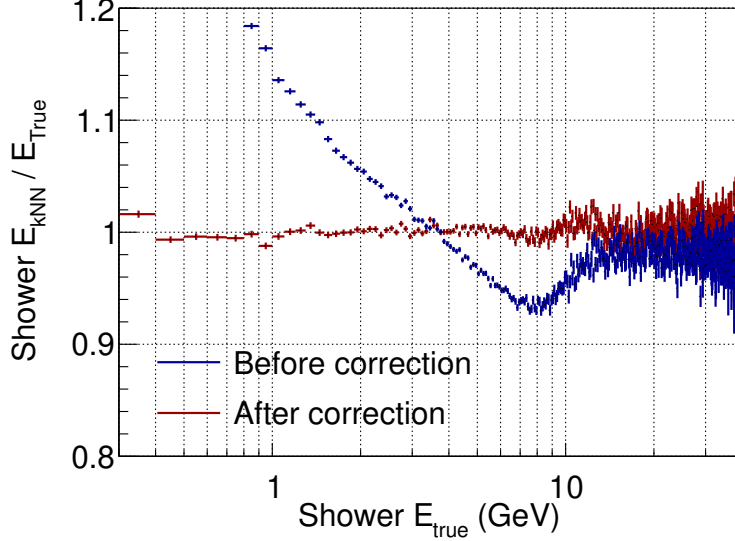


Figure 4.4: The ratio of  $k$ NN shower energy  $E_{kNN}$  to true shower energy  $E_{true}$  as a function of true shower energy  $E_{true}$  before and after the three iterations of energy corrections using  $14^{th}$  order polynomial functions.

## 4.2 Resolution Improvement

To evaluate the improvement of  $k$ NN shower energy over the calorimetric shower energy, for each event, one can define [85]

$$R = \frac{|E_{calo} - E_{true}|}{E_{true}} - \frac{|E_{kNN} - E_{true}|}{E_{true}}, \quad (4.3)$$

where  $E_{calo}$  is the calorimetric shower energy. Filling  $R$  event by event in the bins of  $E_{true}$  and normalizing each bin by the number of events, one can observe the mean deviation improvement as a function of  $E_{true}$ . This is shown in Figure 4.5.

A more direct way to look at the improvement is to check the sensi-

tivity to the standard oscillation model, for the previously mentioned reasons applying to  $k$  optimization. In Figure 4.6, the contours of 90% C.L. for using calorimetric shower energy,  $k$ NN shower energy, and true shower energy are shown. In the true energy case, the energy resolution is perfect, i.e. the deviation  $\sigma_E$  is zero. The contours of pulling calorimetric energy toward the true shower energy by 10% and 20% event by event are also shown.

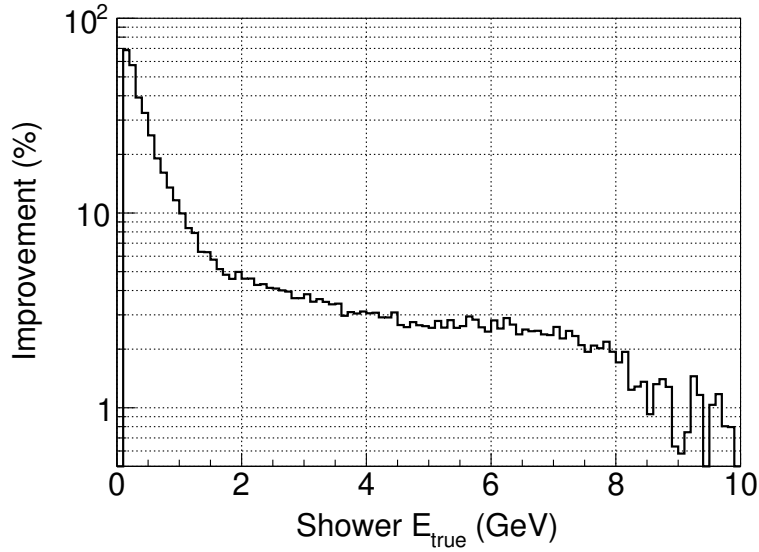


Figure 4.5: Energy resolution improvement of  $k$ NN shower energy over calorimetric shower energy as a function of true shower energy. Y-axis is the mean deviation improvement as a fraction of true shower energy.



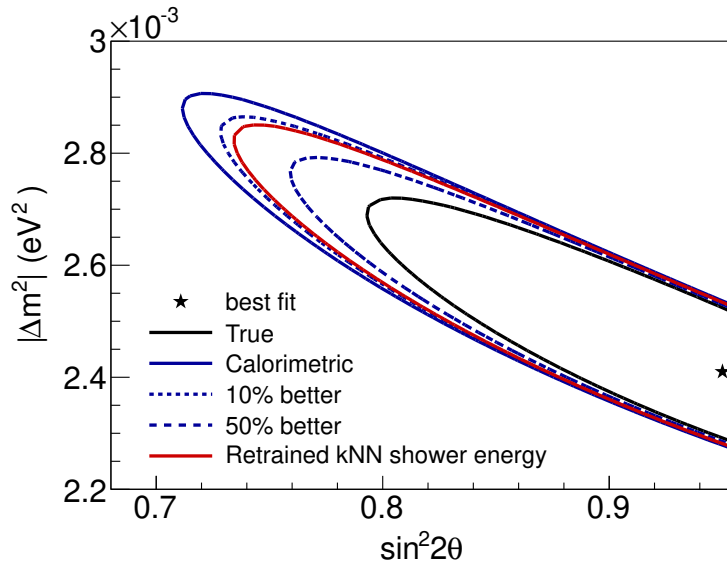


Figure 4.6: MINOS+ sensitivities to the standard oscillation model with statistical error only assuming  $18 \times 10^{20}$  POT worth of data. Contours of 90% C.L. for using the calorimetric shower energy,  $k$ NN shower energy, and true shower energy are shown. For comparisons, the contours of pulling the calorimetric energy toward the true shower energy by 10% and 20% event by event are also plotted.

### 4.3 Considerations on Improving $k$ NN Shower Energy

One challenge in using  $k$ NN is to find a good distance metric. The application of Mahalanobis metric [90] was explored in this work. As the general form of the Euclidean metric, Mahalanobis distance between two vectors  $\mathbf{x}$  and  $\mathbf{y}$  takes the form

$$d = \sqrt{(\mathbf{x} - \mathbf{y})^T M (\mathbf{x} - \mathbf{y})}, \quad (4.4)$$

where  $M$  is a symmetric positive definite matrix that can be decomposed as  $M = A^T A$ , with  $A$  being an upper triangular matrix (Cholesky decomposition, e.g., see Reference [91]). The Euclidean metric is recovered when  $M$  is equal to identity. Due to a large number of degrees of freedom (for example  $3 \times 3$  matrix  $A$  contains 6 non-zero entries) and fluctuations in MC samples, the technique of simulated annealing (e.g., see Reference [92]) was employed in optimizing  $A$ . On the other hand, the performance of  $k$ NN naturally depends on the input variables. A list of new variables was reconstructed and tested, such as the average hit MIP in a shower, angle of outgoing muon track, width of transverse hit distribution, etc. Overall, a 5% improvement in sensitivity was achieved with the modified  $k$ NN. This is on a similar level as the shower energy scale uncertainty which will be discussed in Section 4.4. As a result, the old  $k$ NN as detailed in the first section is still used in MINOS+ analysis.

In a parallel approach, the performance of the boosted decision tree was evaluated using TMVA (Toolkit for Multivariate Data Analysis) package [93]. The percentage gain is similar to that of the modified  $k$ NN described above.

## 4.4 Systematic Error

The evaluation of the systematic error on the  $k$ NN shower energy in MINOS+ follows the same procedure as described in Reference [85]. The uncertainty in the calibration of the response of the MINOS detectors to hadronic showers originating from single particles has been well determined

by test beam measurements at CalDet and by studies of cosmic ray events in the two detectors. In Section 4.4.1, this uncertainty in  $k$ NN shower energy is discussed. In Section 4.4.2 and Section 4.4.3, the mis-modeling of physical processes in MINOS detectors, such as the neutrino interactions and the scattering of hadrons, are evaluated by INTRANUKE reweighting which directly comes from the weights stored in the MC output and special MC samples where different shifts are applied in the simulation.

#### 4.4.1 Absolute Energy Scale

The response of the MINOS detectors to the passage of single particles (protons, pions and muons) was determined from the exposure of a calibration detector (CalDet) to test beams at CERN [94]. Absolute energy scale systematic errors, which represent the uncertainty in tuning the MC energy response to data, were evaluated mainly through CalDet: 2.5-5% from tuning hadron (pion) MC to data; 2% from beam energy uncertainty; 1.4% from stopping-muon calibration; 0.8% from tuning stopping-muon MC to data. Combining the difference of 1.0% between the ND response for spill and cosmic muon events, the total systematic error is about 5.7% [95]. This error propagates through two calorimetric variables used by the  $k$ NN: shower energy near the track vertex and the sum of the energy from the first two showers. The result of shifting those two variables by 5.7% is shown in Fig. 4.7.

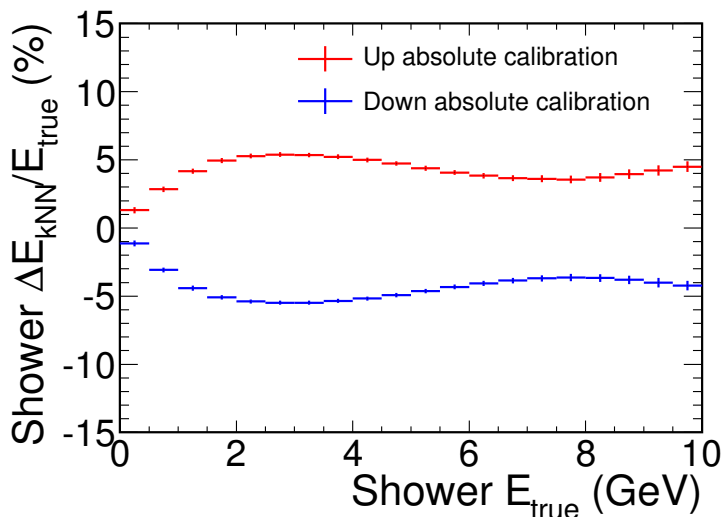


Figure 4.7: Systematic error of  $k$ NN shower energy based on the absolute energy scale uncertainty. The result is calculated from applying  $\pm 5.7\%$  shift to the calorimetric input variables.

#### 4.4.2 Intranuclear Rescattering with INTRANUKE

In most neutrino interactions in MINOS, the produced hadrons have to escape from an iron nucleus, with a significant chance of re-interaction, before they can be seen in the detector. This re-scattering process is simulated by a semi-classical intranuclear cascade model, INTRANUKE [96]. Sufficient information is contained in the MC output events to enable the effect of varying INTRANUKE parameters to be studied using a reweighting scheme [97]. Below are listed the systematic shifts evaluated through INTRANUKE reweighting:

1. Pion cross section: Pion interaction cross-section is adjusted by  $\pm 10\%$ .
2. Nucleon cross section: Total nucleon interaction cross-section is adjusted

by  $\pm 15\%$ .

3. Pion charge exchange: Branching ratio for  $\pi^- p \rightarrow \pi^0 n$  is varied by  $\pm 50\%$ .
4. Pion elastic scattering: Branching ratio for elastic scattering is varied by  $\pm 10\%$ .
5. Pion inelastic scattering: Inelastic scattering branching ratio is varied by  $\pm 40\%$ .
6. Pion secondary pion production: Fraction of pion interactions creating a second pion is scaled by  $\pm 20\%$ .
7. Nucleon secondary pion production: Fraction of nucleon interactions that create a pion is scaled by  $\pm 20\%$ .
8. Pion absorption: Pion absorption cross-section is adjusted by  $\pm 30\%$ .
9. Nucleon knockout: Nucleon absorption cross-sections are shifted by  $\pm 20\%$ .
10. Formation time: Free traveling time of newly formed hadrons through nucleus before a re-interaction happens is shifted by  $\pm 50\%$ .

The reweighting results are shown in Fig. 4.8.

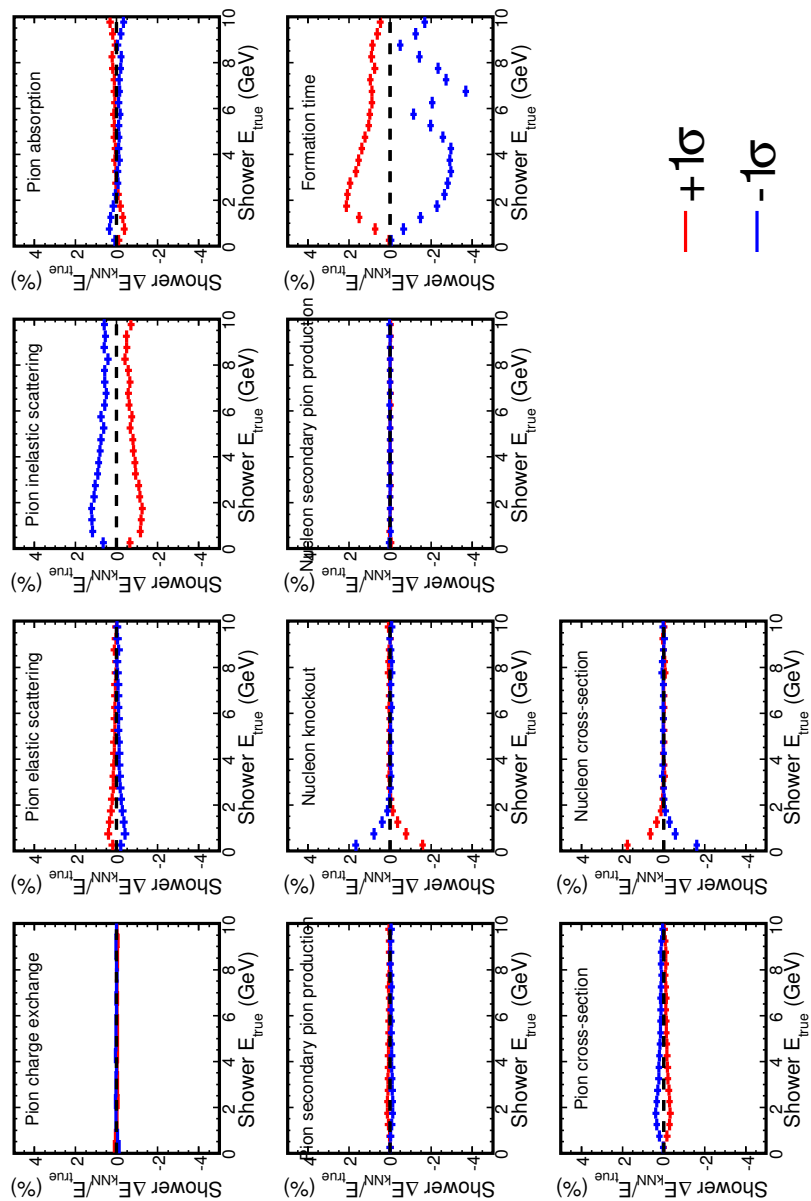


Figure 4.8: Systematic shifts calculated from the INTRANUKE reweighting.

### 4.4.3 Special MC Samples

For the systematic effects that cannot be studied through the reweighting technique, a list of special Monte Carlo samples were generated for ND using the the MINOS+ beam flux. In total, there are thirteen such samples, some representing a discrete model change, others, in pairs, reflecting  $\pm\sigma$  shifts in model input parameters. Below are listed all the systematic shifts considered:

1. Pion/nucleon absorption: Pion and nucleon absorption cross-sections are shifted by  $\pm 30\%$  and  $\pm 20\%$ . This is the same as item 1 and 2 in the INTRANUKE reweighting procedure.
2. Baryon  $x_F$  selection: The AGKY model was implemented to model the hadronization in MINOS [98]. When a neutrino strikes a constituent quark of a nucleon, the final state baryon is most likely to form from the remaining two quarks in the backwards hemisphere in the center of mass frame. This leaves the pions to be formed in the forward hemisphere and to thus have higher energies when boosting back to the lab frame. The baryon  $x_F$  distribution has been measured in bubble chamber data, confirming this effect, and the AGKY model [98] draws from this distribution. This effect is switched off in this sample.
3. Formation zone: Free traveling distance of newly formed hadrons through nucleus before a re-interaction happens is shifted by  $\pm 50\%$ . This is the same as item 10 in the INTRANUKE reweighting procedure.

4. INTRANUKE assumptions (absorption): Energy of the absorbed pion is most often distributed between 3 or 4 nucleons. The numbers are doubled in this sample.
5. INTRANUKE assumptions (de Broglie ring): The probability of low energy pion interacting with nucleus increases as its de Broglie wavelength  $\lambda = hc/p$  decreases. Empirically, this is realized by increasing the size of the nucleus. By default  $0.5\lambda$  increase is used. In this sample,  $\pm 0.6\lambda$  is used for  $\pm\sigma$  shifts.
6. Charged/neutral particle correlations: AGKY model generates correlated charged and neutral particles. This sample uses an updated model where the multiplicities are chosen independently.
7.  $\pi^0$  probability: The relative probability for AGKY to produce a  $\pi^0$  pair instead of  $\pi^+\pi$  is 0.30. It is shifted by  $\pm 30\%$  in this sample.
8. Two-body decays: In simulation, all decays to two-body hadronic final states are made isotropically in the center of mass. These samples consist of two extreme (unphysical) modifications. In one sample, the particles are produced perpendicular to the direction of momentum transfer, in the other they are produced in parallel.

The error bands evaluated by the special MC samples are shown in Fig. 4.9.



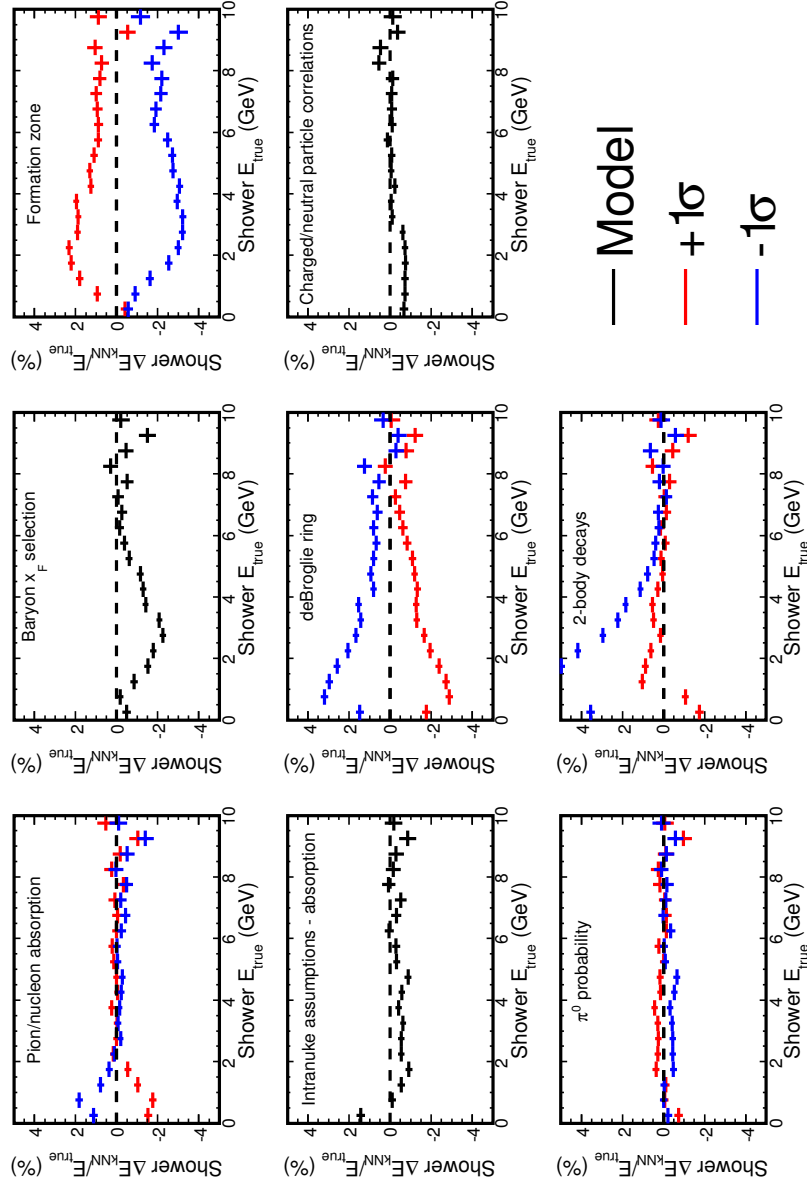


Figure 4.9: Systematic shifts calculated from the special MC samples.

#### 4.4.4 Combined Errors

To combine the systematic errors together, a quadratic sum was taken, and the result is shown in Figure 4.10. Note that since the items 1, 2, and 10 in the INTRANUKE reweighting procedure described in Section 4.4.2 are covered by the special MC samples 1 and 3 described in Section 4.4.3, they are excluded from the summation to avoid double counting. The red curve in Figure 4.10 is a parameterized function based on the calorimetric shower energy in MINOS [99]. It takes the form

$$6.6 + 3.5 \exp(-E_{true}/1.44). \quad (4.5)$$

Since it still fully covers the MINOS+ the  $k$ NN shower energy error band, it was decided to use the same function in MINOS+.

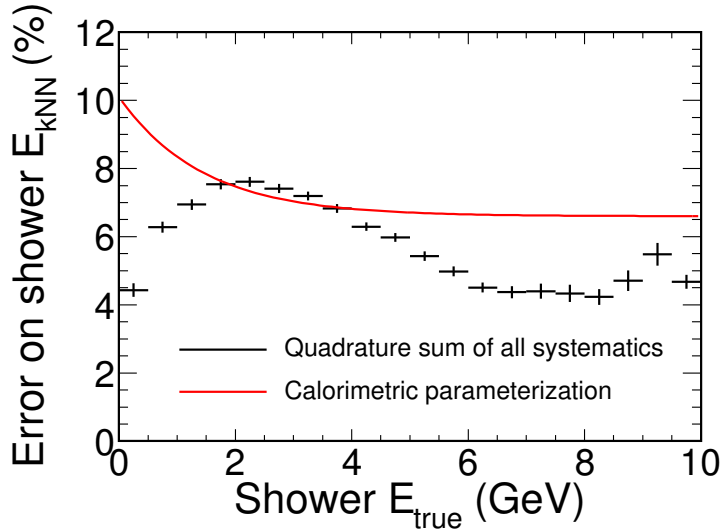


Figure 4.10: Combined  $k$ NN shower energy systematics. The red curve is the parameterization of the calorimetric shower energy systematics used in MINOS [99].

## Chapter 5

### NC Event Selection

This chapter focuses on the NC event selections in MINOS+. NC events traditionally serve as a model independent probe in searching for sterile neutrinos. The same selection rules are applied in both MINOS and MINOS+, as no significant changes in the selection variables are observed. Following the definitions on the fiducial volume, comparisons between data and MC event vertex distributions are presented. For the ND, the procedure of NC cleaning for removing poorly reconstructed events is introduced, followed by the selection cuts that separate NC events from CC events. Lastly, two systematic errors related to the event selections are discussed.

#### 5.1 Acceptance

Fiducial volumes are defined in MINOS detectors to ensure a good energy containment [100]. At ND, the XY-view of the event vertex distribution is shown in Figure 5.1. The cut is made such that the event vertices are 0.5 m away from the edges of U or V planes. Event vertex  $Z$  positions satisfy  $1.7 \text{ m} < Z < 4.7368 \text{ m}$ . Distributions of vertices X, Y and Z for data and MC are shown in Figure 5.3, Figure 5.4 and Figure 5.5, respectively.

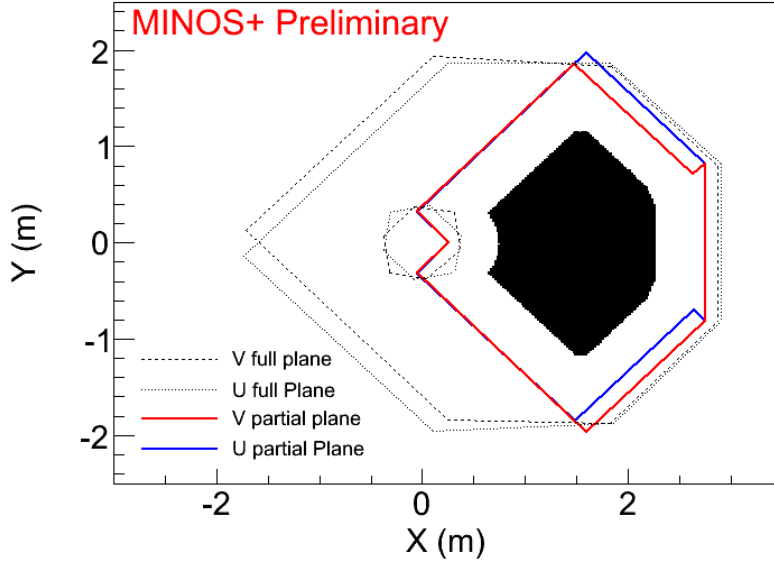


Figure 5.1: XY-view of the NC event vertices at ND. The solid black shape represents the accepted region, whose boundary is 0.5 m away from edges of the partial U or V planes.

At FD, the XY-view of the event vertex are shown in Figure 5.2, where the event vertices are kept 0.4 m away from the edges of the U or V planes, and 0.6 m from the coil hole center. Event vertex  $Z$  positions satisfy  $0.21 \text{ m} < Z < 13.72 \text{ m}$  and  $16.12 \text{ m} < Z < 28.96 \text{ m}$  for the two modules of FD. Distributions of the event vertex  $X$ ,  $Y$  and  $Z$  positions are shown in Figure 5.6, Figure 5.7 and Figure 5.8 respectively, where the standard oscillation is applied to MC.

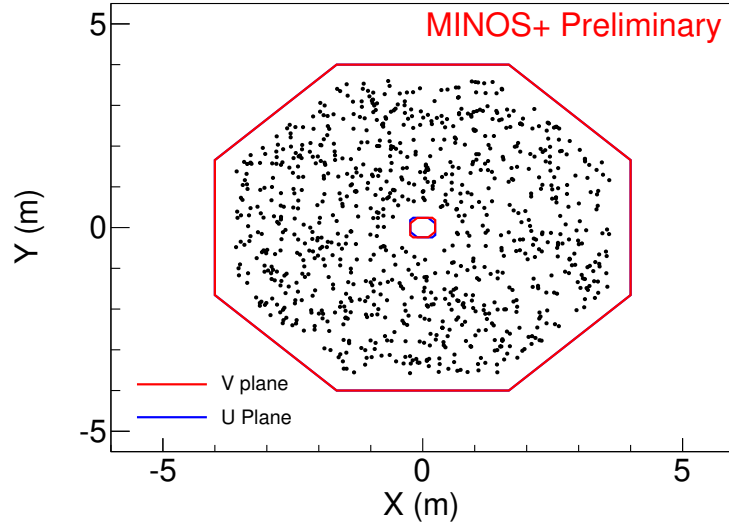


Figure 5.2: XY-view of the NC event vertices at FD.

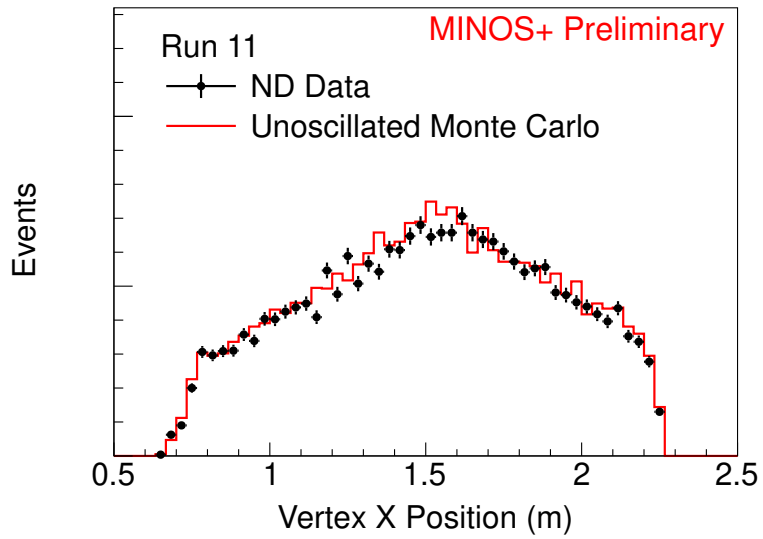


Figure 5.3: Distribution of event vertex X position at ND.

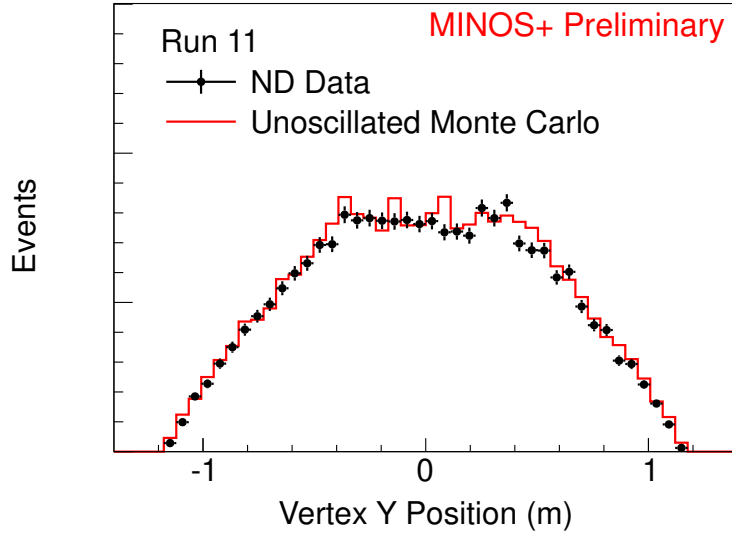


Figure 5.4: Distribution of event vertex Y position at ND.

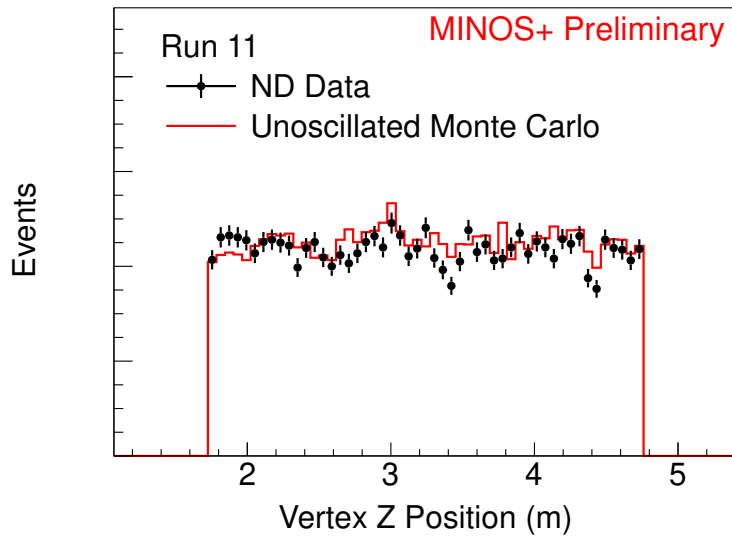


Figure 5.5: Distribution of event vertex Z position at ND.

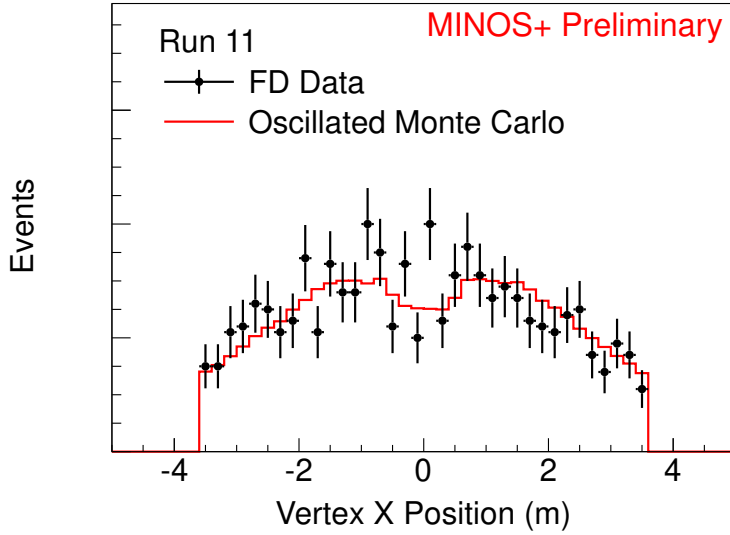


Figure 5.6: Distribution of event vertex X position at FD.

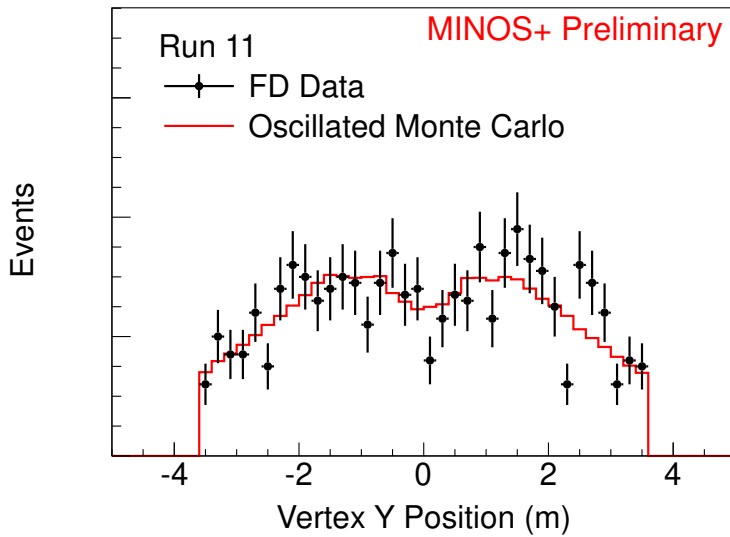


Figure 5.7: Distribution of event vertex Y position at FD.

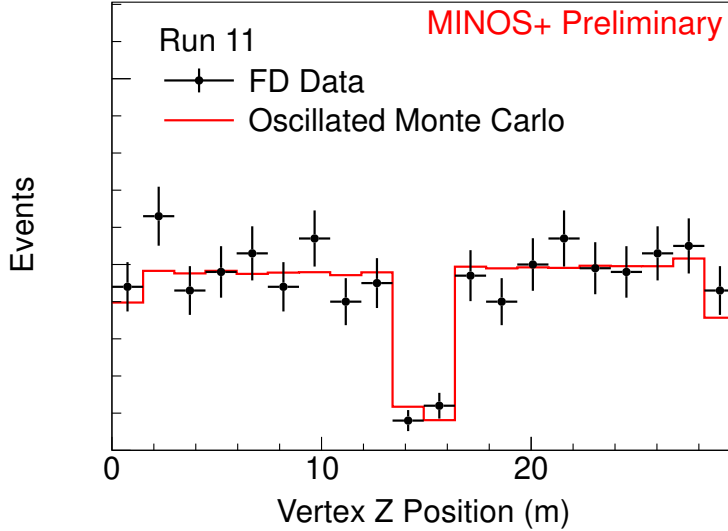


Figure 5.8: Distribution of event vertex Z position at FD.

## 5.2 NC Cleaning at ND

Low energy NC events are known to be difficult to reconstruct. This motivated two cuts at ND to remove events that are poorly reconstructed, which are defined as  $E_{reco}/E_{true} < 0.3$  where  $E_{reco}$  and  $E_{true}$  are the reconstructed and true energy.

The first cut requires the fraction of the event pulse height in a slice, later referred to as pulse height fraction, to be larger than 50%. A slice is made in the initial stage of the reconstruction to roughly group together hits that possibly belong to one event based on space and time. An event is reconstructed from these hits with the possibility that some hits are left out. Pulse height of an event is therefore a subset of that in a slice. This cut is



demonstrated in Figure 5.9.

The second cut requires the maximum number of planes consecutively hit by an event, later referred as maximum consecutive planes, to be larger or equal to 3. When a shower develops longitudinally, it deposits energy in successive planes. Poorly reconstructed events, as caused by reconstruction failures, have a small number of maximum contiguous planes as shown in Figure 5.10. The systematic errors associated with these two cleaning cuts are discussed in Section 5.4.

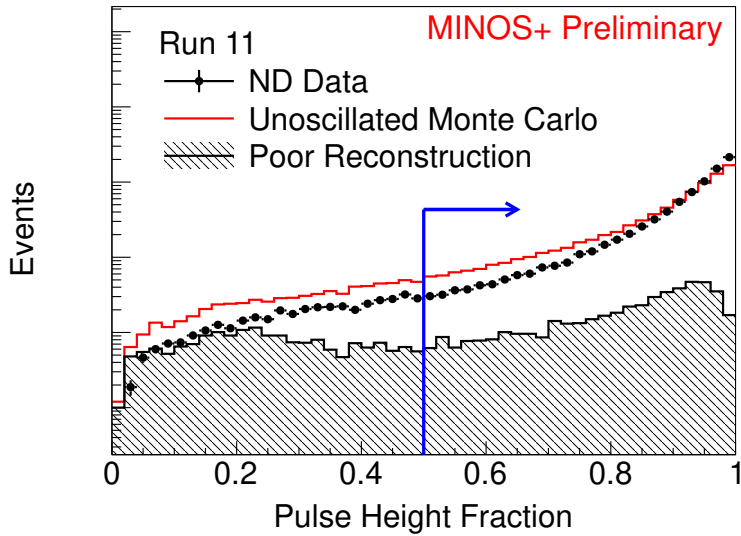


Figure 5.9: Slice pulse height fraction variable in the ND, as used in the cleaning, for Run 11. The black points are the data, the red lines are the total MC and the hatched histograms are the poorly reconstructed events that are to be removed by the cleaning. The arrows are oriented to indicate which regions of the plots are accepted by the cuts.

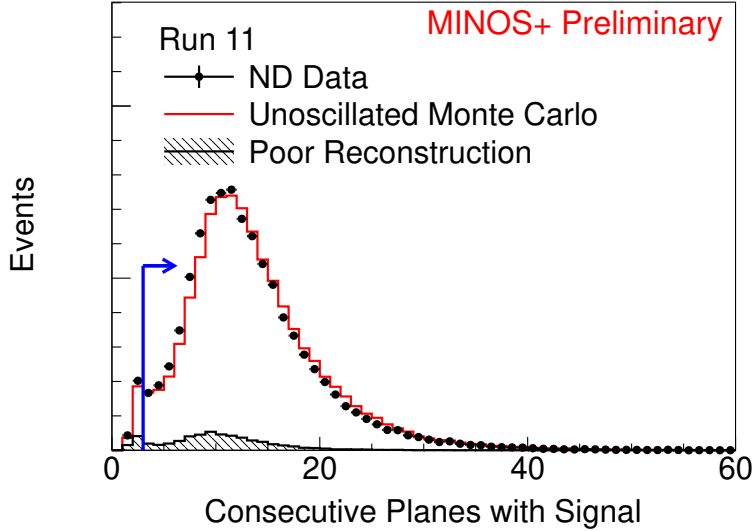


Figure 5.10: Maximum consecutive planes variable in the ND, as used in the cleaning, for Run 11. The black points are the data, the red lines are the total MC and the hatched histograms are the poorly reconstructed events that are to be removed by the cleaning. The arrows are oriented to indicate which regions of the plots are accepted by the cuts.

### 5.3 Separation of NC Events from CC Events

The cuts that separate NC events from CC events are the same for both ND and FD. First of all, the event length needs be smaller than 47 planes. This is shown in Figure 5.12 for ND and Figure 5.14 for FD. Secondly, in the case that a track is reconstructed in an event, the track length cannot be longer than the shower length by more than 5 planes. This is illustrated in Figure 5.11 for ND and Figure 5.13 for FD.

Selector performance can be evaluated through purity and efficiency.

The former is defined as

$$\frac{\text{number of selected true signal events}}{\text{total number of selected events}}, \quad (5.1)$$

and the latter is defined as

$$\frac{\text{number of selected true signal events}}{\text{total number of signal events before selection}}. \quad (5.2)$$

In this case, the denominator for the efficiency is the total number of true NC events before the two NC selection cuts (event length and track extension). The results for the NC selections are shown in Figure 5.15 for ND and Figure 5.16 for FD.

Integrating over the energy window used in the fitting in Chapter 8 and 9, the efficiency is 79.9% and the purity is 60.3% for the ND; the efficiency is 86.5% and the purity is 64.9% for the FD. The simulated NC event energy spectra combining both MINOS and MINOS+ samples are shown in Figure 5.17 and Figure 5.18 for ND and FD, respectively.

## 5.4 Systematic Errors

Two of the systematic errors related to the NC event selections, acceptance and NC cleaning, were studied for this dissertation. They correspond to the selection cuts described in Section 5.1 and Section 5.2, respectively.

### 5.4.1 Acceptance

Spatial uniformities of the event reconstructions in MINOS detectors have been studied in Reference [101], where the energy spectra of data and MC

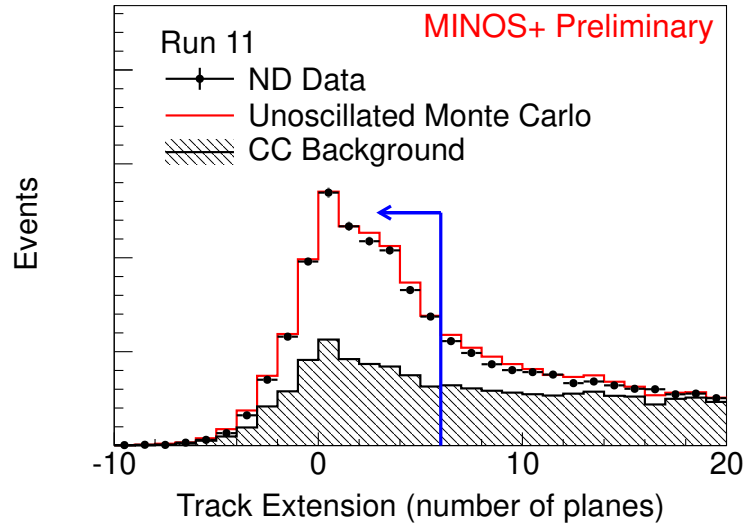


Figure 5.11: Track extension cut at ND. The selected events are to the left of the blue line.

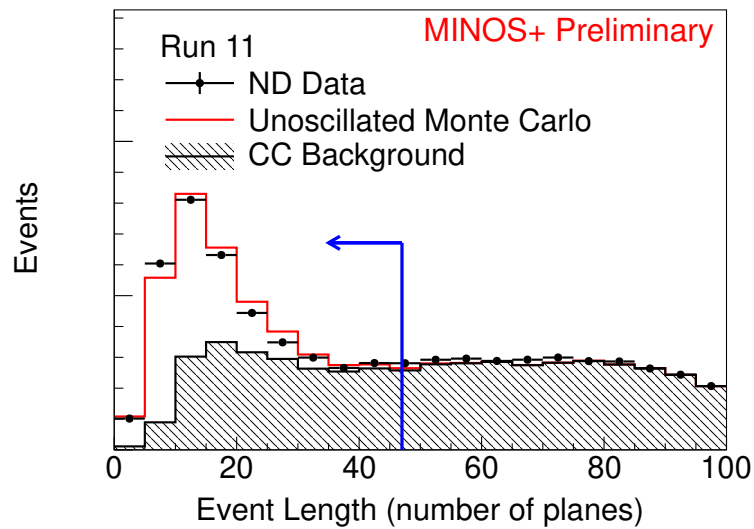


Figure 5.12: Event length cut at ND. The selected events are to the left of the blue line.

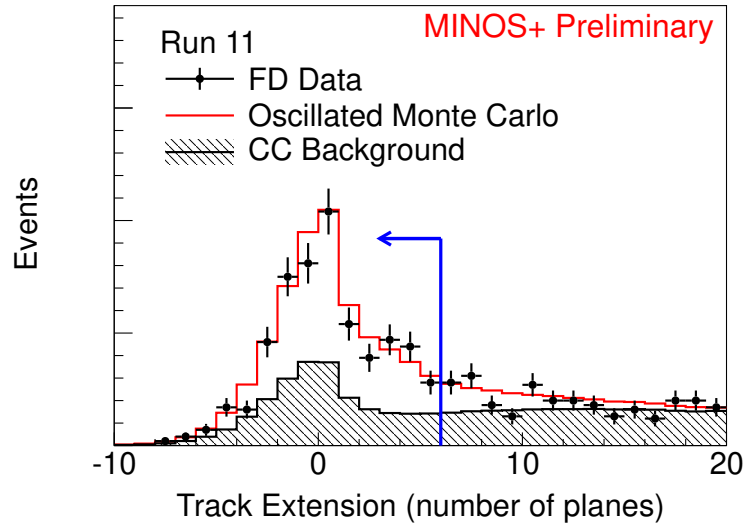


Figure 5.13: Track extension cut at FD. The selected events are to the left of the blue line.

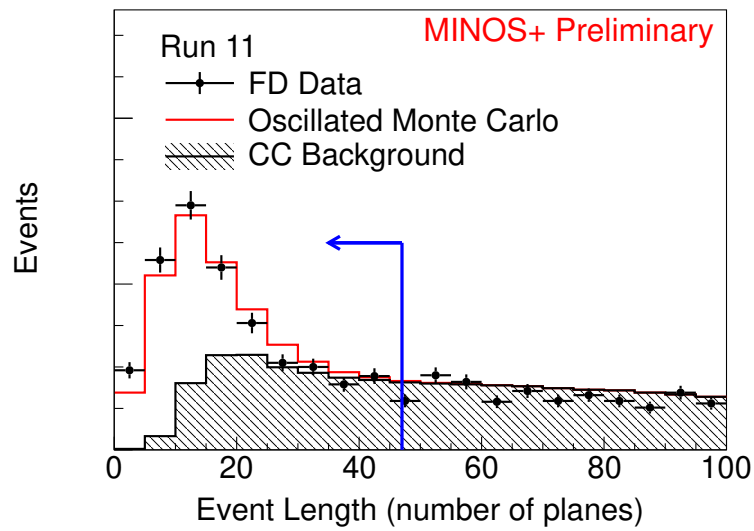


Figure 5.14: Event length cut at FD. The selected events are to the left of the blue line.

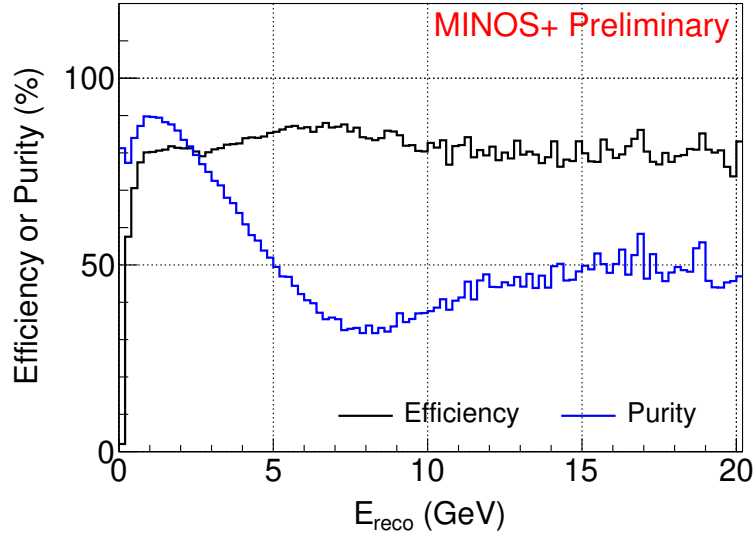


Figure 5.15: Efficiency and purity for the NC selections at ND.

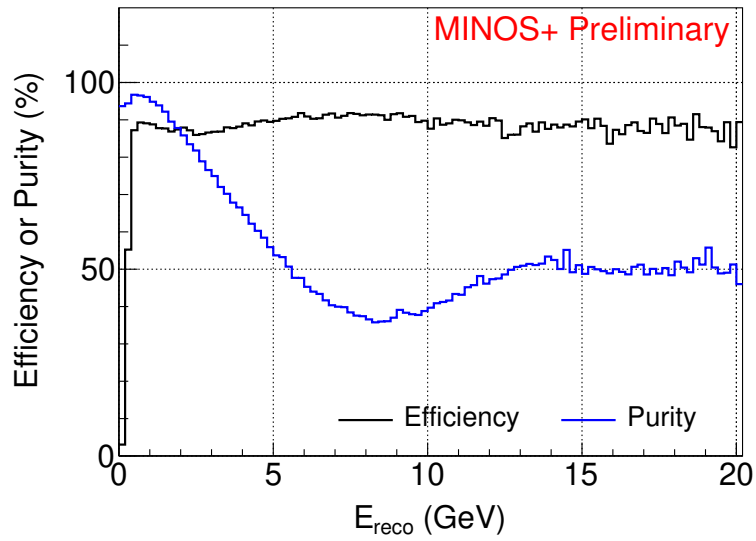


Figure 5.16: Efficiency and purity for the NC selections at FD.

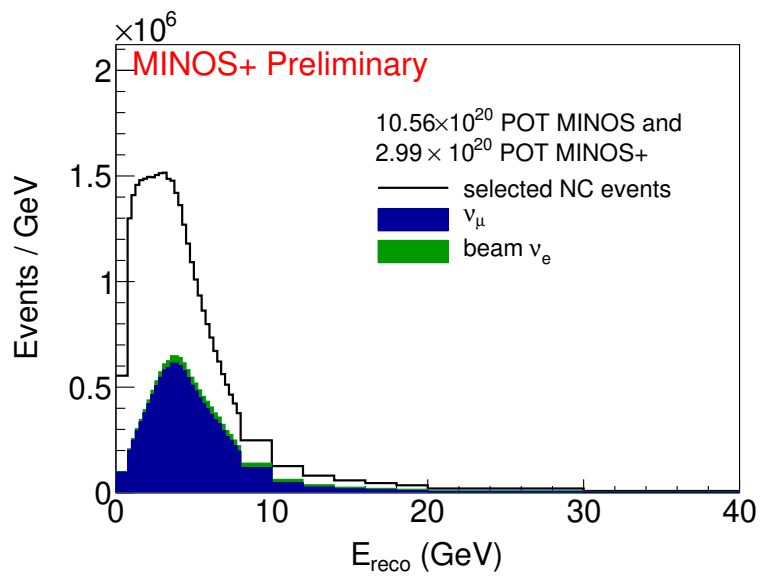


Figure 5.17: Simulated NC event energy spectrum at ND combining both MINOS and MINOS+ samples. The main backgrounds are CC events, along with a small amount of beam  $\nu_e$ .

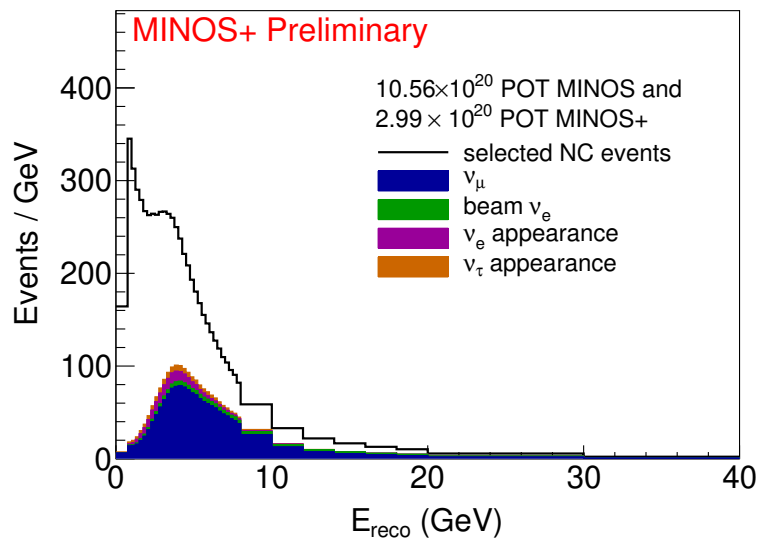


Figure 5.18: Simulated NC event energy spectrum at FD combining both MINOS and MINOS+ samples. In addition to the CC events, there are also backgrounds from the  $\nu_e$  and  $\nu_\tau$  appearance.



from different quadrants, radial annuli and  $Z$ -segments of ND are compared. A good agreement can be seen within the limit of statistical fluctuations. As small as they are, two spatial variations are taken as the systematic errors for the analyses of this dissertation:

1. The plus and minus shifts correspond to the events originating on the left and right half of the fiducial volume.
2. The shifted distribution is constructed by tightening the fiducial  $z$  cut from 4.7368 m to 2.5 m.

The fractional errors on the data-MC ratio as a function of the reconstructed energy are shown in Figure 7.21 and Figure 7.22 in Chapter 7. Overall it is less than 0.5% for both shifts.

#### 5.4.2 NC Cleaning

The basic technique of evaluating the NC cleaning systematic error is to find a pair of shifted cleaning cuts (pulse height fraction and maximum consecutive planes) so that the MC could best match with data at ND [100]. Since the reconstructed energies of the poorly reconstructed events are mostly smaller than 2 GeV, three reconstructed energy bins are considered:  $E_{reco} < 0.5$  GeV,  $0.5$  GeV  $< E_{reco} < 1$  GeV, and  $E_{reco} > 1$  GeV. The evaluation follows a two-step procedure:

1. For each energy bin, free scale the poorly reconstructed components so

that the MC best matches with data in terms of the distributions of the two cleaning variables.

2. After the scaling, a shifted cut is chosen such that it rejects the same number of events in data and MC. The fractional change in the energy spectra caused by the shifted cuts is taken as the systematic error. In other words,

$$\text{error} = \frac{\text{energy spectrum based on the shifted cut}}{\text{energy spectrum based on the nominal cut}}. \quad (5.3)$$

However, in the analysis of the 3+1 model (see Chapter 8), problems arise when the oscillations at ND are considered. More specifically, with the baseline of 1.04 km at ND, the oscillation of  $\nu_\mu \rightarrow \nu_s$  as measured by the NC events are affected by three model parameters,  $\theta_{34}$ ,  $\theta_{24}$  and  $\Delta m_{43}^2$ , as shown in Figure 5.19. For this reason, the procedure described above is no longer valid, because the results of matching the MC with data vary depending on the oscillation parameters. This is demonstrated in Figure 5.20, 5.21 where the distributions of the pulse height fraction and max consecutive planes in the energy bin of  $0.5 \text{ GeV} < E_{reco} < 1 \text{ GeV}$  are shown with and without ND oscillations. The resultant best fit scaling factors are shown in Figure 5.22. In addition, the oscillation effect on the energy spectra with and without the preselection cuts are shown in Figure 5.23 and Figure 5.24, respectively. In Figures 5.20 to 5.24, ND oscillations are applied to the right plot with  $\theta_{34} = 0$ ,  $\theta_{24} = 0.272$  and  $\Delta m_{43}^2 = 11.2 \text{ eV}^2$ . The values for  $\theta_{24}$  and  $\Delta m_{43}^2$  correspond to point 21 in Figure 5.19.

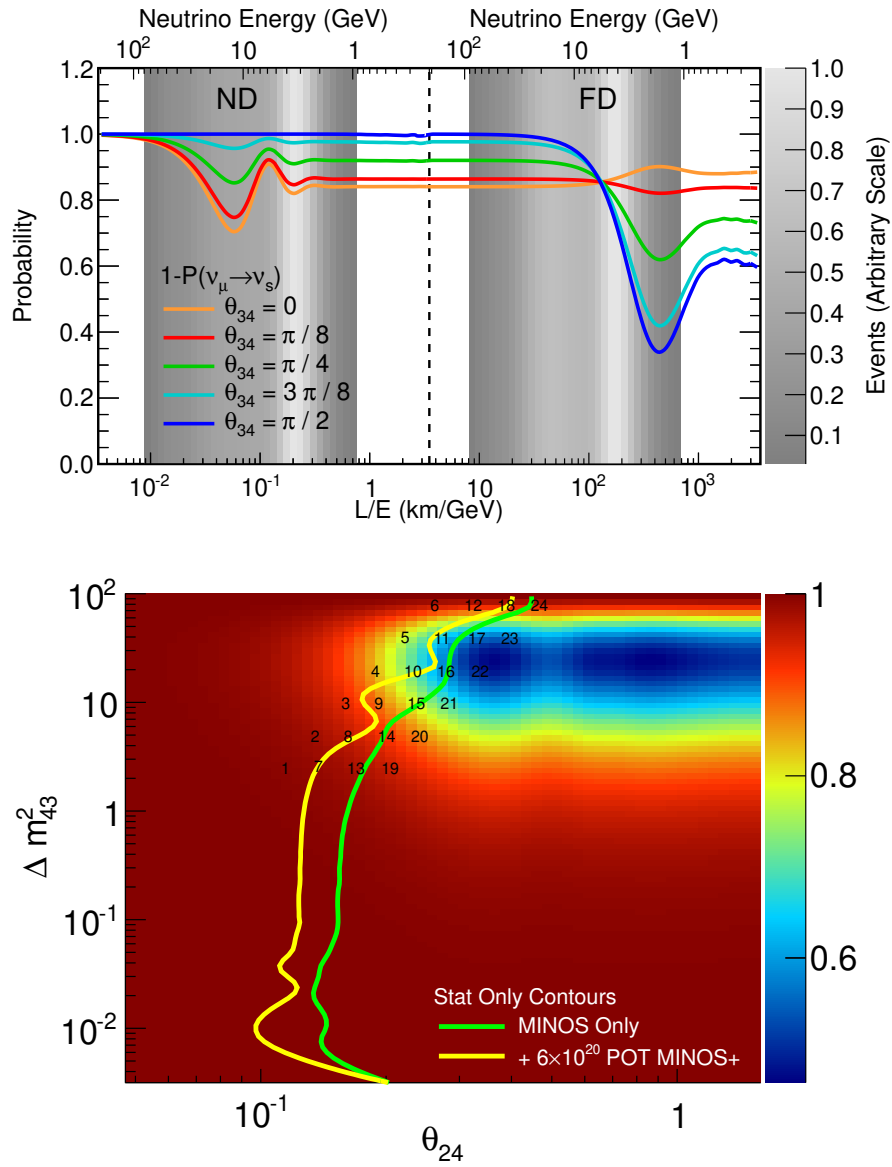


Figure 5.19: Top: Effect of  $\theta_{34}$  on  $\nu_\mu \rightarrow \nu_s$  oscillation at ND. Bottom: Effect of  $\Delta m^2_{43}$  and  $\theta_{24}$  on the oscillation probability at ND with  $\theta_{34} = 0$ . Z-axis (color) is equal to  $1 - P(\nu_\mu \rightarrow \nu_s)$ . The blue region is where large ND oscillations happen.

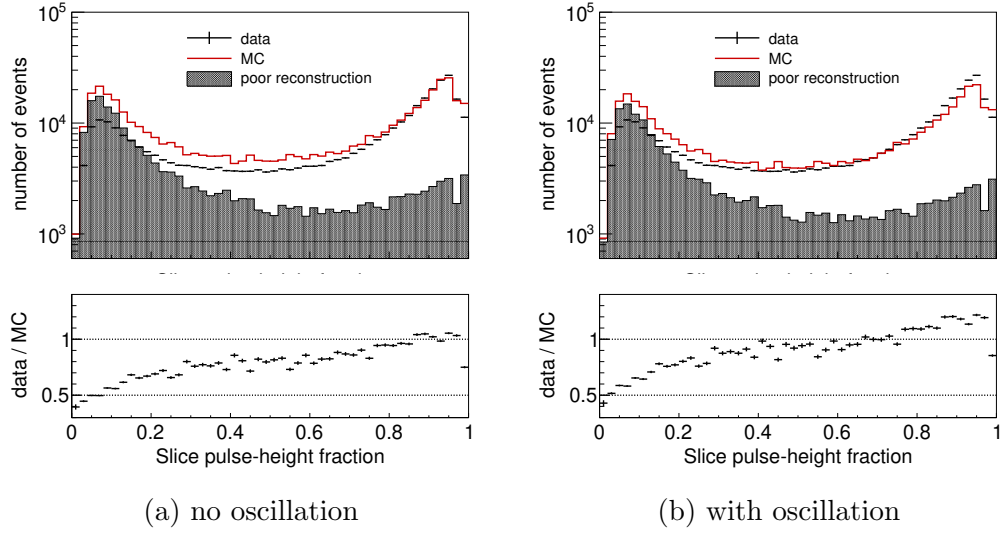


Figure 5.20: Pulse height fraction distribution for energy bin  $0.5 \text{ GeV} < E_{reco} < 1 \text{ GeV}$ .

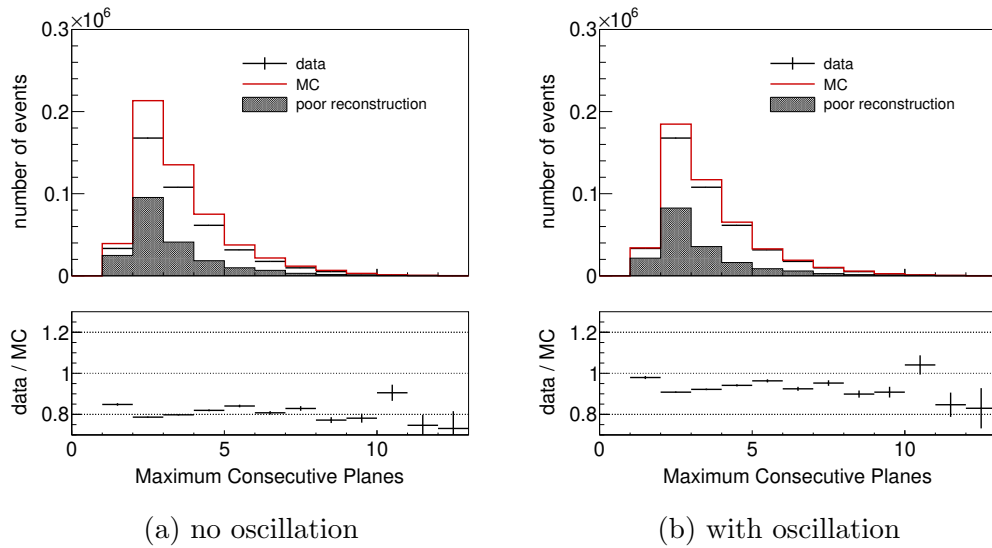


Figure 5.21: Maximum consecutive planes distribution for energy bin  $0.5 \text{ GeV} < E_{reco} < 1 \text{ GeV}$ .

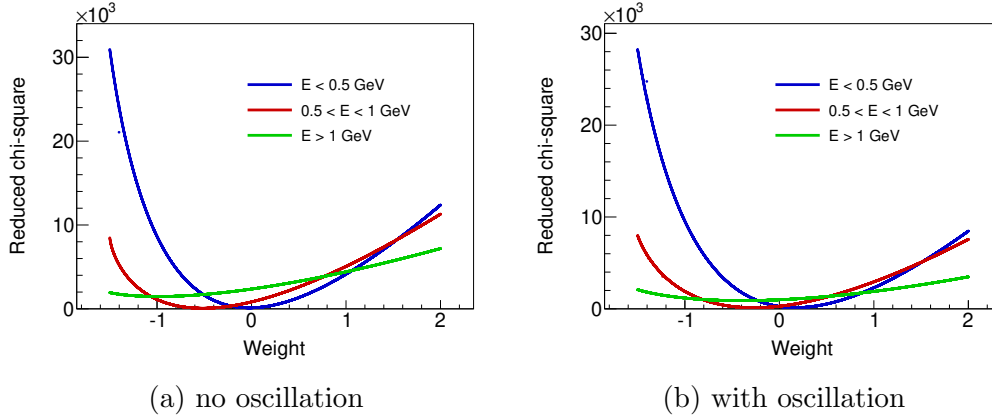


Figure 5.22:  $\chi^2$  of data-MC difference from re-scaling the poorly reconstructed components in the three energy bins. X-axis is the scaling factor reduced by 1.

There are two possible solutions for this problem. One is to completely cut off low energy NC events. This would remove all the poorly reconstructed events, and the cleaning cuts are no longer needed. However, the drawback is that good events are also removed along the way. This is not ideal because significant statistics of the NC sample lie in the low energy bins.

The other solution, which is adopted in this dissertation, is to match oscillated MC with data. Due to a large parameter space spanned by  $\theta_{34}$ ,  $\theta_{24}$  and  $\Delta m_{43}^2$ , the strategy was to try only a limited set of the oscillation parameters in the sensitive region and take the largest resultant error as a conservative measure. In practice, 120 sets of parameters, which come from 5 different values for  $\theta_{34}$  in combination with 24 different values for  $\theta_{24}$  and  $\Delta m_{43}^2$  as shown in Figure 5.19, are used to generate 120 different error bands (see Fig. 5.25 for an example). To combine these error bands into one, for

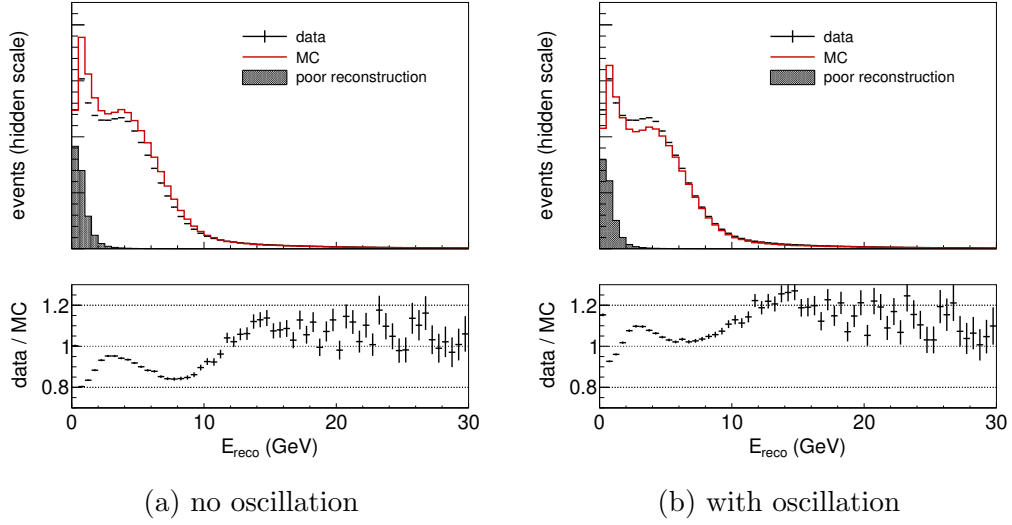


Figure 5.23: NC event energy spectra without the preselection cuts.

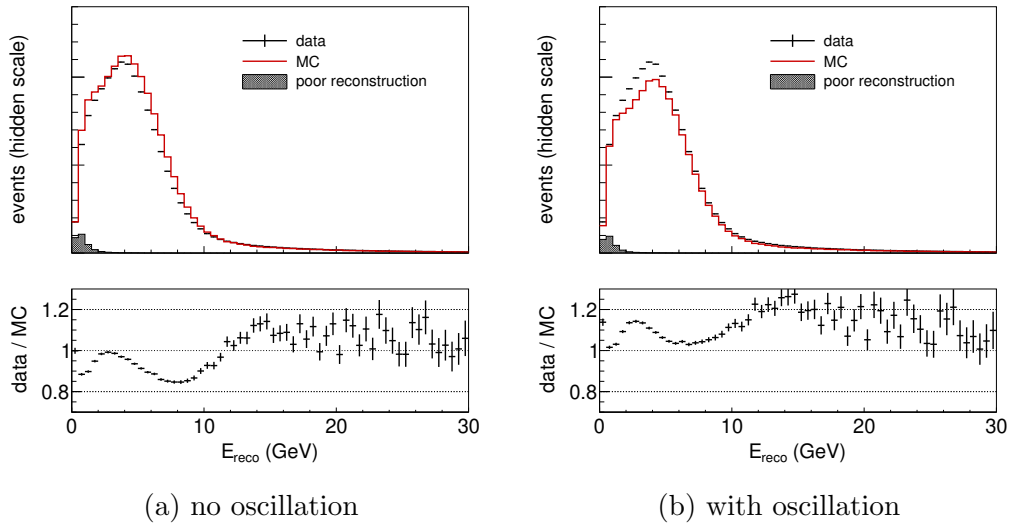


Figure 5.24: NC event energy spectra with all cuts applied.

each energy bin, the largest error is adopted, and the result is shown in Figure 5.26, where the function

$$1 + \frac{0.98}{1 + (E/0.54)^2}, \quad (5.4)$$

is used to provide a parameterization of the band for fast generation of the shifted MC sample.

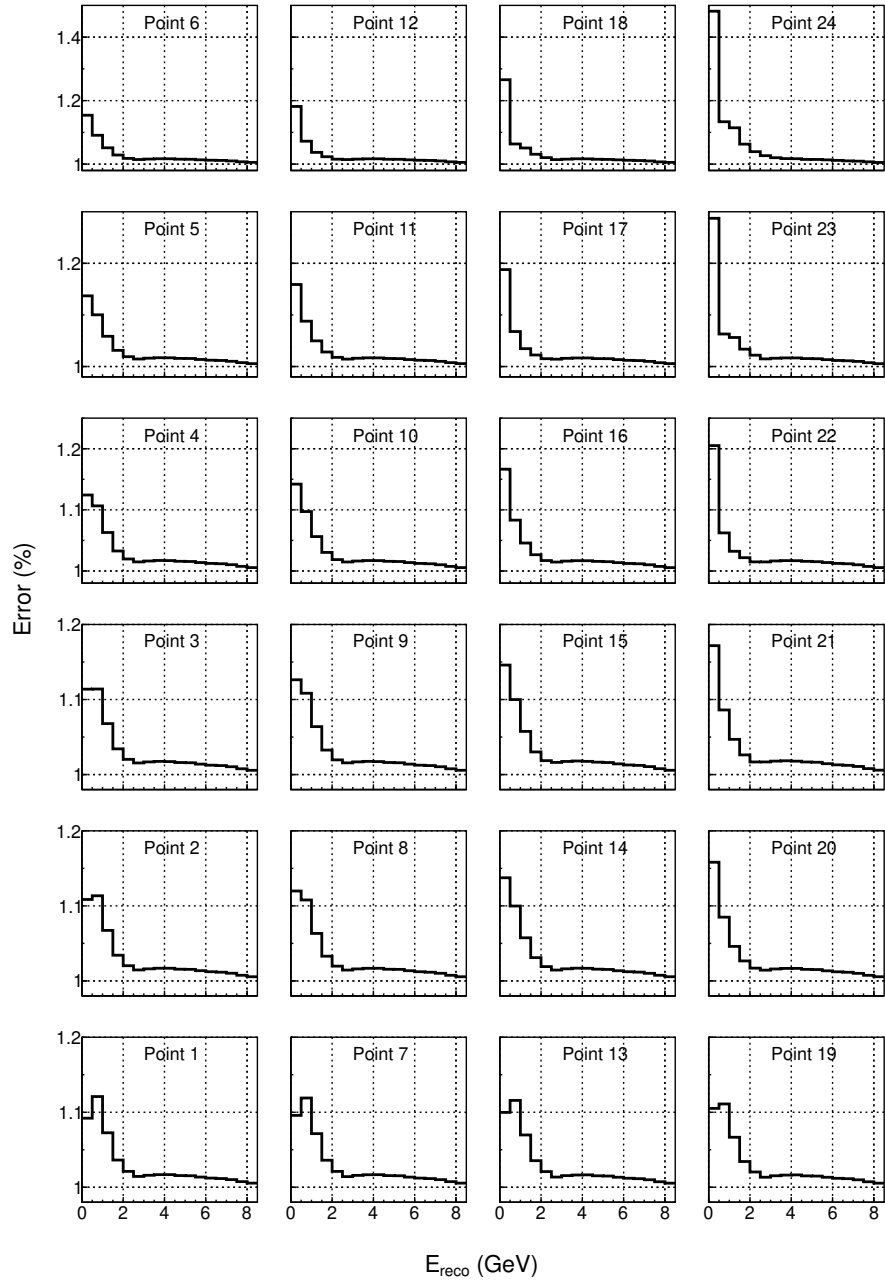


Figure 5.25: NC cleaning systematics error bands for  $\theta_{34} = 0$  and each plot corresponds to a point in Fig. 5.19 for different values of  $\theta_{24}$  and  $\Delta m_{43}^2$ .



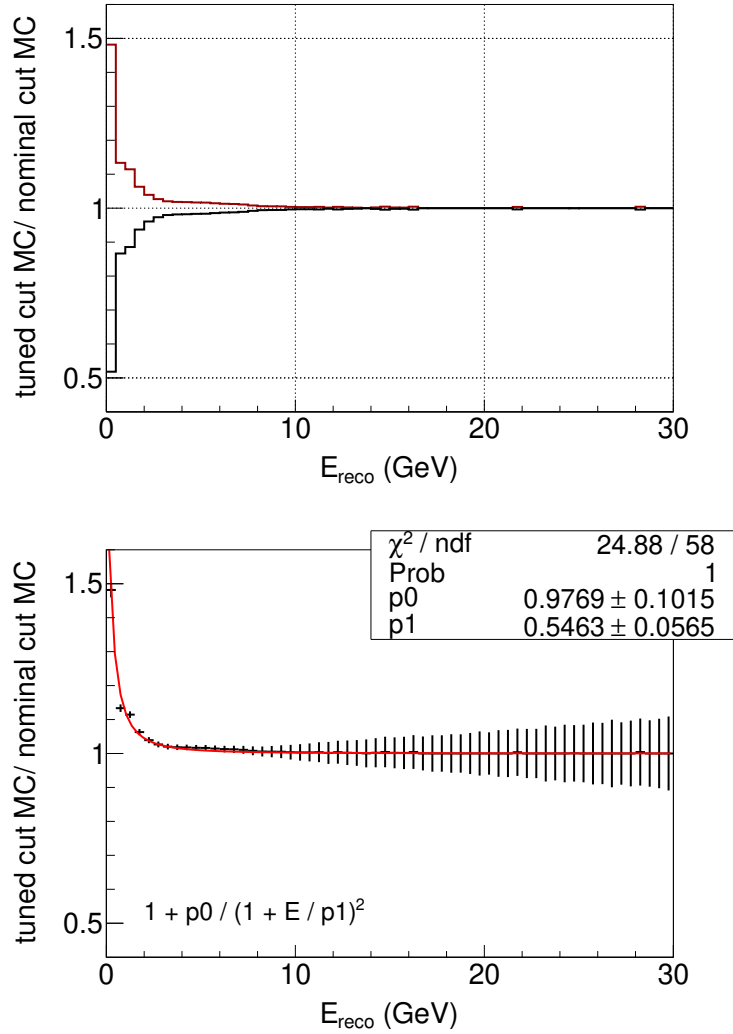


Figure 5.26: Top: NC cleaning systematics error bands by taking the largest error resulted from 120 sets of oscillation parameters for each energy bin. Bottom: A parameterization to be used in the fast generation of the shifted MC.

# Chapter 6

## CC Event Selection

This chapter focuses on the CC event selection in MINOS+. To avoid double counting, the CC sample and the NC sample are made to be exclusive. In practice, NC selections are applied first. For the events not selected by the NC selector, the CC selector picks up the CC-like events for the CC sample. Due to historical reasons, the CC and NC selectors took different approaches. The former uses a  $k$ NN-based method, with the latter employing a simple cuts-based method described in Chapter 5.

Having the same goal of selecting more CC events and less NC events, the study of the CC event selection is shared between the sterile neutrino and the standard oscillation analyses. Following a brief description of the fiducial volume cuts which are critical to ensure good energy containment, the retraining of the PID used for CC and NC event separation is discussed. The systematic errors associated with the selection cuts are presented in the last section.

## 6.1 Acceptance

At the ND, the XY-view of the event vertices is shown in Figure 6.1, where beam neutrinos are traveling along positive  $Z$  direction pointing toward the reader, and  $Z = 0$  is defined to be the front surface of the detector. The disk formed by the event vertices centers at the beam spot ( $X_0 = 1.4828$  m,  $Y_0 = 0.2384$  m) with a radius  $R = 0.8$  m. Event  $Z$  positions lie within  $0.81$  m  $< Z < 4.08$  m which gives the fiducial volume a cylinder shape as shown in Fig. 6.2.

The coil hole is not well modeled in the simulation of the ND. Events with a track ending in the calorimeter and 0.6 m from the coil hole center are not selected. This is referred to as the coil hole cut.

At the FD, the XY-view of the selected CC event vertices is shown in Figure 6.3. They are contained in a disk with  $0.5$  m  $< R < 3.74$  m, where the lower limit accounts for the coil hole cut.  $Z$ -axis is defined in the same way as that of ND, and there are two sections in this direction,  $0.49$  m  $< Z < 14.29$  m and  $16.27$  m  $< Z < 27.98$  m, accounting for the two modules of FD.

## 6.2 Separation of CC Events from NC Events

To select a CC event, the minimum requirement is that it contains at least one reconstructed track. Events that pass this criterion can be a real charged current event (signal) for which the track is formed by an outgoing muon, or it can be a neutral current event (background) for which the track is

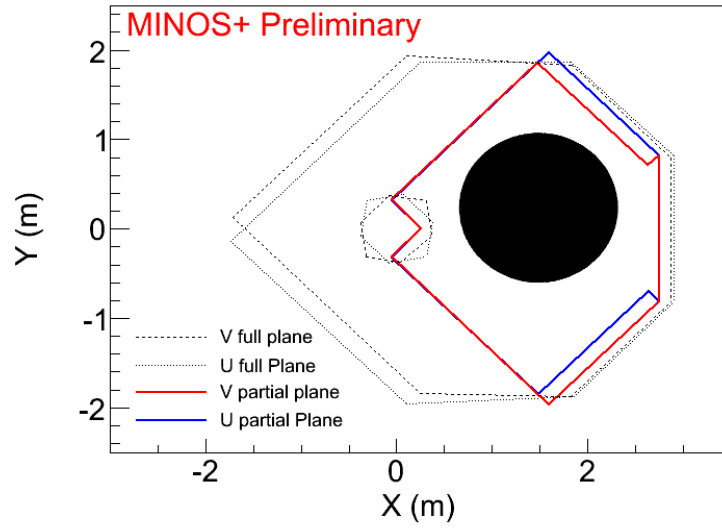


Figure 6.1: XY-view of the CC event vertices at ND (black disk).

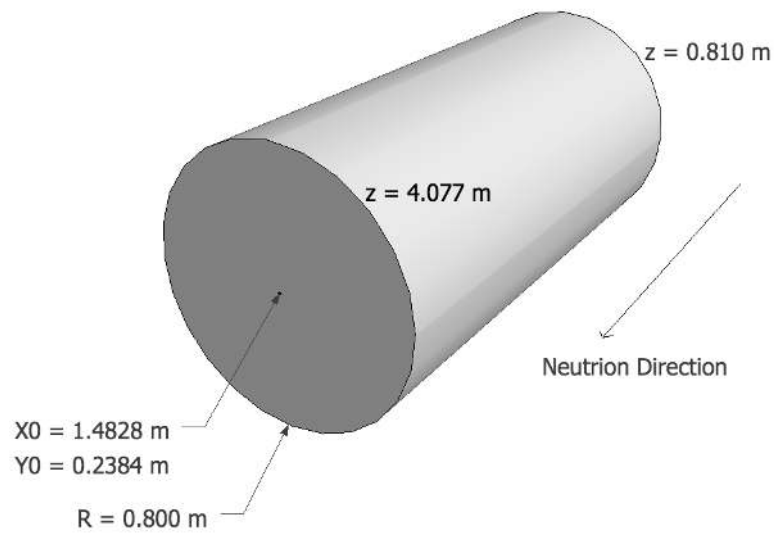


Figure 6.2: Fiducial volume for CC events at ND.

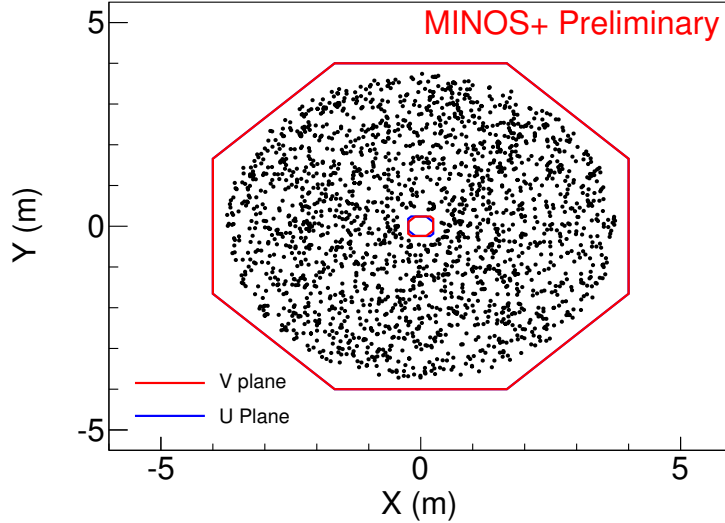


Figure 6.3: XY-view of the CC event vertices at FD (black dot).

reconstructed from the hits created by the hadronic shower. For this reason, further identification is needed. In MINOS,  $k$ NN algorithm was adopted to separate charge current events from neutral current events that contain reconstructed track(s). Two particle identification indices (PIDs) were developed based on this technique: `roID` [102] and `jmID` [103]. The latter was motivated by selecting more low energy events to improve the sensitivity to the models of neutrino decay and decoherence. The final PID cut takes an “or” of the two: (`roID` > 0.25 || `jmID` > 0.5). In MINOS+, due to very low statistics of the low energy events, `jmID` was dropped. This section focuses on retraining `roID` (referred as PID in the later text) in MINOS+, which involves applying MINOS+ MC samples in the training sets and reoptimizing the PID cut.

Similar to the  $k$ NN shower energy, the basic idea of using  $k$ NN algo-

rithm for PID is to find  $k$  closest matching MC events ( $k$  nearest neighbors) for a given data event, and take the fraction of the signal events to be the PID. Thus, the PID can be defined as

$$\frac{k_S}{k_S + k_B} = \frac{k_S}{k}. \quad (6.1)$$

where  $k_S$  and  $k_B$  are the number of signal events and the number of background events, respectively. The neighborhood is determined by the Euclidean metric defined in Equation 4.1. Four event parameters are involved [102]

1. Number of scintillator planes in a track.
2. Mean pulse height of the track hits.
3. Ratio of the mean of low pulse height hits over the mean of high pulse height hits. Low and high pulse height hits are separated by a threshold tuned in a sensitivity optimization procedure [102].
4. Ratio of the pulse height of the track hits to that of the event hits.

Distributions of the four variables using MINOS+ MC samples are shown in Figure 6.4, where the histograms are filled with equal numbers of signal and background events used in the training sets. More precisely, there are 221,778 signal or background events in the ND training set and 187,288 in the FD training set.

The computed PID distribution at ND is shown in Figure 6.5, where the number of neighbors is set to  $k = 80$ , the same with that used in MINOS.

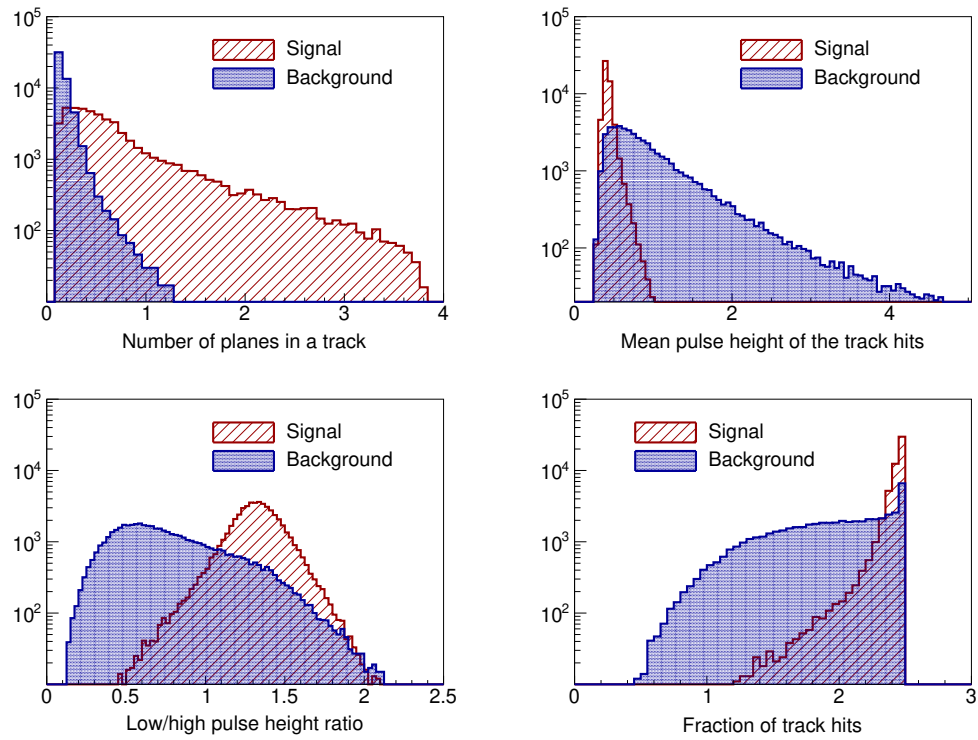


Figure 6.4: Variables used in  $k$ NN PID. Histograms are filled with an equal number of signal events and background events used for the training set.

The systematic error of the NC background in the CC sample is partially based on the difference between data and MC in the PID distribution, as shown in the bottom plot of Figure 6.5, and will be discussed in the last section of this chapter. A similar PID distribution was obtained for FD.

An optimization of the PID cut was performed based on the same criterion as that used for  $k$ NN shower energy, i.e. the sensitivity to the standard oscillation model. More specifically, a test point was chosen in the  $\Delta m^2 - \sin^2 2\theta$  plane with  $\Delta m^2 = 2.88 \times 10^{-3}$  and  $\sin^2 2\theta = 0.72$ . It is located near the contour of the 90% C.L. for MINOS+ (see Figure 6.7 for an example). For each cut between 0 and 1, a  $\chi^2$  is computed. The result of performing the scan on the cut is shown in Figure 6.6. Because a larger  $\chi^2$  corresponds to a better sensitivity,  $\text{PID} > 0.3$  is found to be optimal. The improvement brought by the retraining is shown in Figure 6.7, where the old PID uses MINOS MC samples as the training set, together with the MINOS PID cut.

The purity and the efficiency, which are respectively defined in Equation 5.1 and Equation 5.2, are shown in Figure 6.8 for the ND, and Figure 6.9 for the FD. The denominator for the efficiency in this case is the total number of true  $\nu_\mu/\bar{\nu}_\mu$  CC events that contain at least one track and originate inside the fiducial volume. Integrating over the energy window, the efficiency is 56.4% and the purity is 99.1% at ND. At FD, the efficiency is 85.1% and the purity is 99.3%. The CC event energy spectra by MC combining both MINOS and MINOS+ samples are shown in Figure 6.10 and Figure 6.11 for ND and FD, respectively.



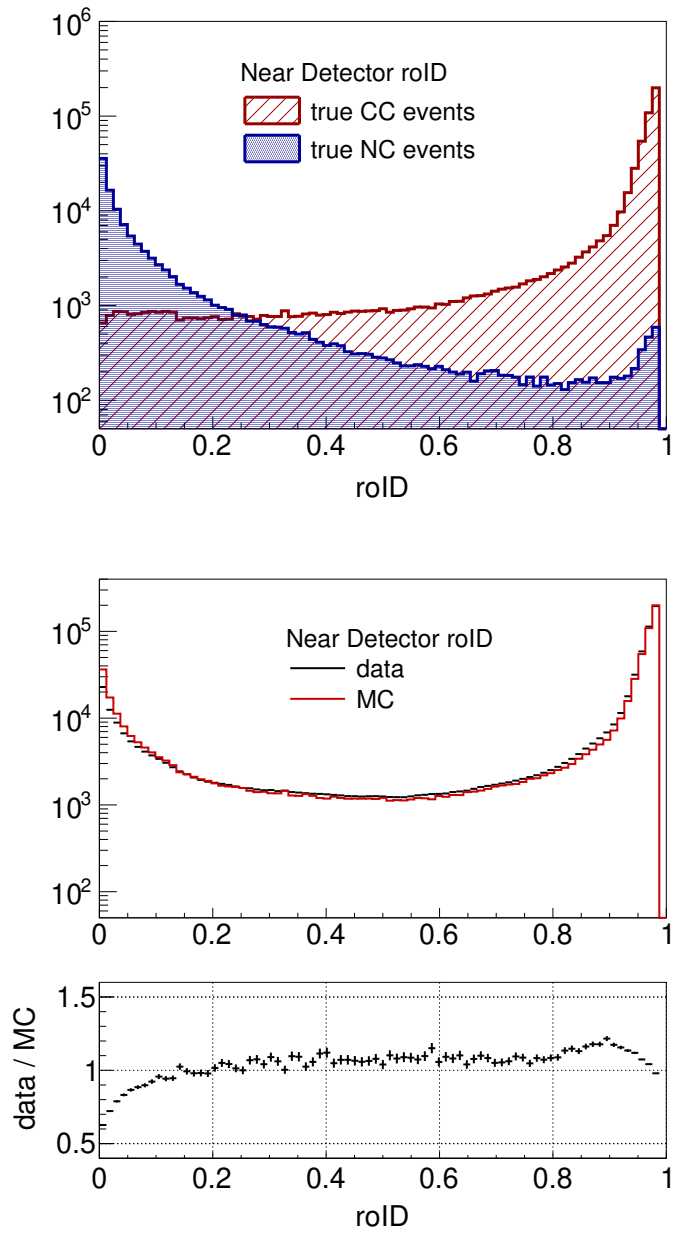


Figure 6.5: Top: PID distributions of true CC events (signal) and true NC events (background) at ND. Bottom: comparison between data and MC in the PID distribution for all events.

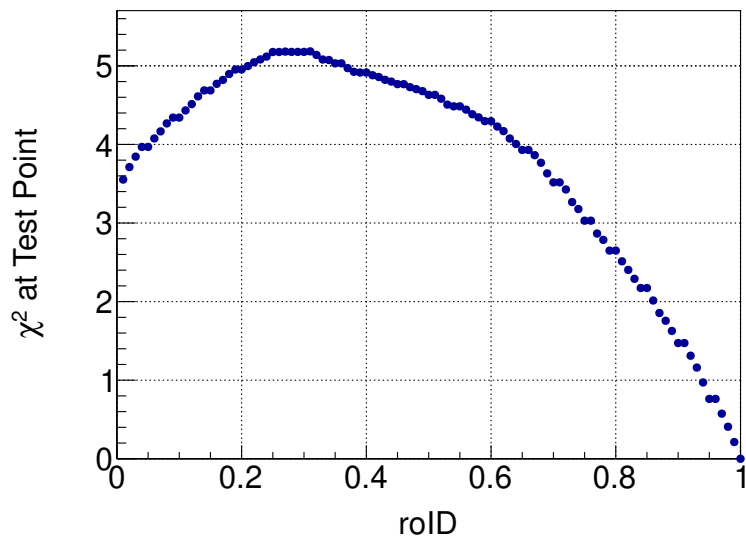


Figure 6.6:  $\chi^2$  of the test point as the function of PID cut. The test point is located at  $\Delta m^2 = 2.88 \times 10^{-3}$  and  $\sin^2 2\theta = 0.72$  in the  $\Delta m^2 - \sin^2 2\theta$  plane. The optimal value which corresponds to the largest  $\chi^2$  is around 0.3.

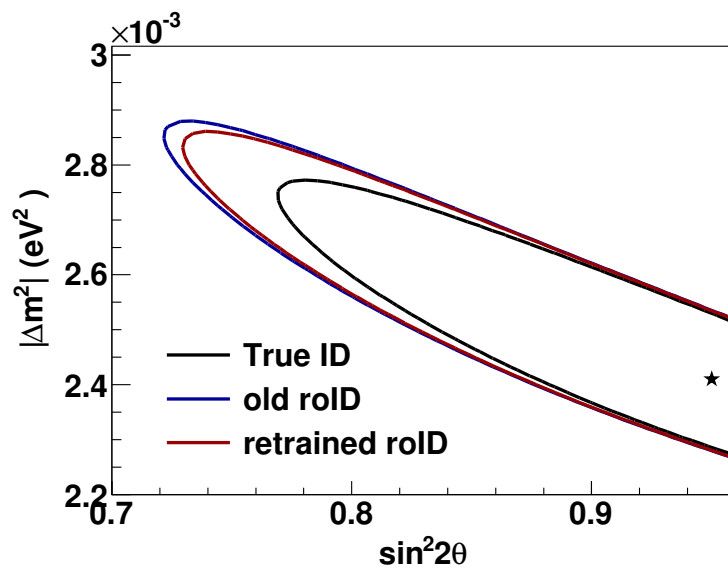


Figure 6.7: MINOS+ sensitivities to the standard oscillation model with statistics only assuming  $18 \times 10^{20}$  POT worth of data. Contours of 90% C.L. before and after the retraining are shown. The black contour was made with true PID representing the ideal case.

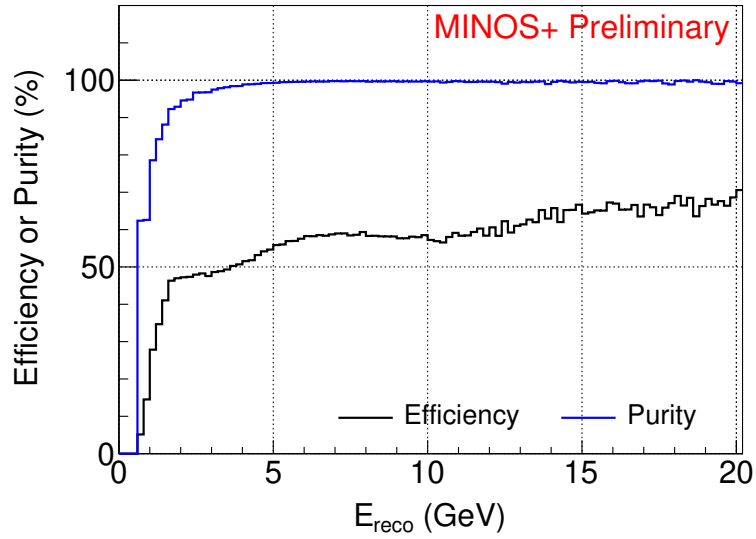


Figure 6.8: Efficiency and purity for the ND CC events.

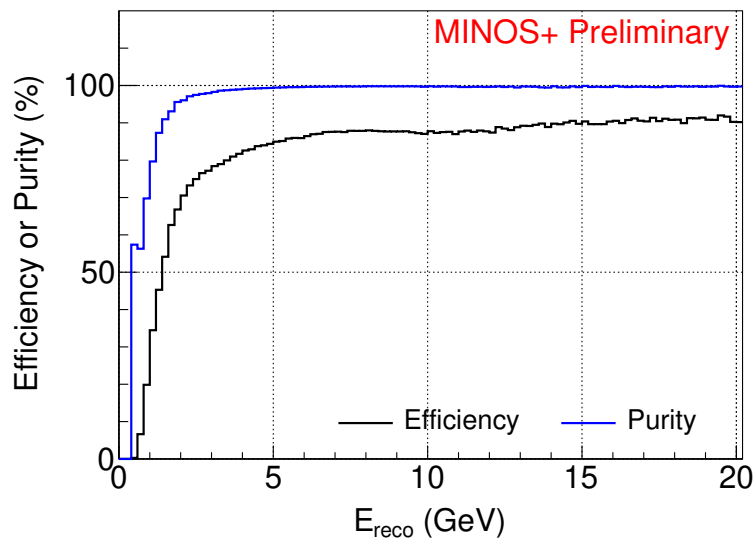


Figure 6.9: Efficiency and purity for the FD CC events.

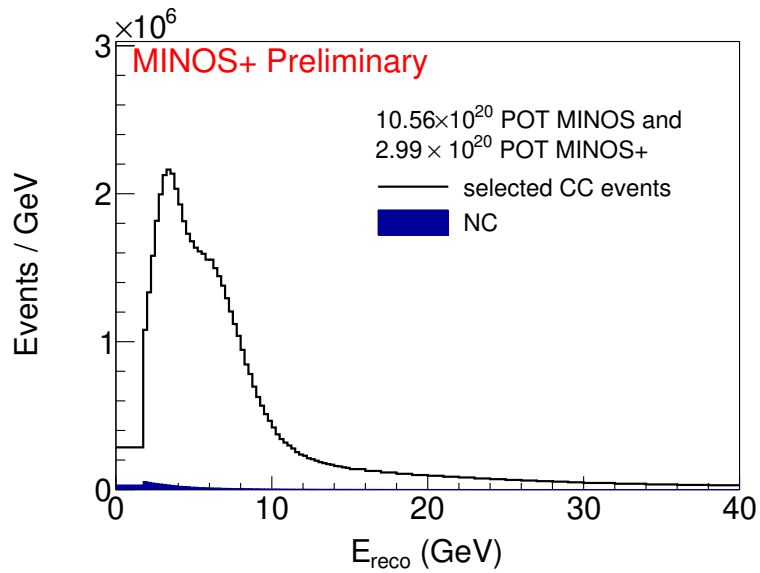


Figure 6.10: Simulated CC event spectrum at ND.

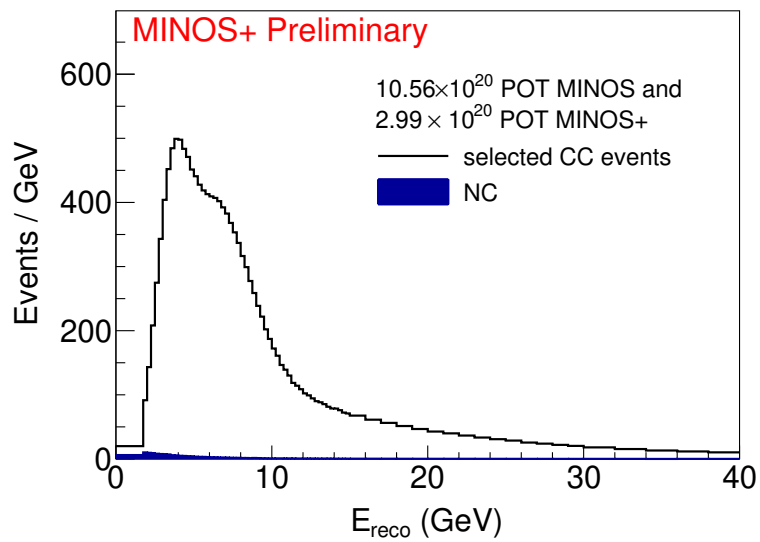


Figure 6.11: Simulated CC event spectrum at FD.

## 6.3 Systematic Error

The systematic errors due to the acceptance cuts and the CC/NC separation cuts are discussed in this section. For the acceptance systematic errors, the considerations are restricted to ND since FD has inadequate statistics.

### 6.3.1 Acceptance

Similar to the NC case discussed in Chapter 5, a list of systematic errors comes from shifting the acceptance cuts as follows:

1. Plus and minus shifts correspond to the events originating on the left and right half of the fiducial volume.
2. Shifted distribution is constructed by tightening the fiducial  $z$  cut from 4.07710 m to 2.5 m.
3. Shifted distribution is constructed by tightening the fiducial radius from 80 cm to 60 cm.
4. Shifted distribution is constructed by turning off the coil hole cut.
5. Shifted distribution is constructed by removing all events with a track ending within 10 planes of the start of the spectrometer.
6. Shifted distribution is constructed by turning off the cut on events with a track exiting the side of the calorimeter.
7. Shifted distribution is constructed by removing all events with a track ending within 10 planes of the end of ND.

The fractional errors on the data-MC ratio based on these shifts are shown in Figures 7.1 to 7.7 for the combined MINOS and MINOS+ samples.

It should be noted that the shifts in item 2-7 are one-sided and considered as the plus shifts in Figures 7.2 to 7.7. The minus shifts are taken as the mirror of the plus shifts.

### 6.3.2 NC Background

The NC background systematic error was evaluated by two independent methods for the standard oscillation analysis in MINOS [104]. In the first method, muon removed charged currents (MRCC) events from data were used to imitate the NC data events. After letting them go through the reconstruction chain, and comparing the results with that from the simulated NC events, a systematic error of 15% was identified. The second method relies on the PID distributions in data and MC (see Figure 6.5). By freely scaling the CC component and the NC component in MC to best match MC with data, a scaling factor of 11% on the NC component was obtained and used as the systematics error. Combining the results from the two methods, a total of 20% was adopted for MINOS NC background systematics.

In the sterile analysis, oscillations at the near detector may occur for large  $\Delta m_{43}^2$ . This creates a difficulty for the second method described above. For a better treatment, oscillations should be applied to MC before the comparison with data. Similar to the case of evaluating the NC cleaning systematics in Chapter 5, a total of 120 oscillation parameter sets were tested.

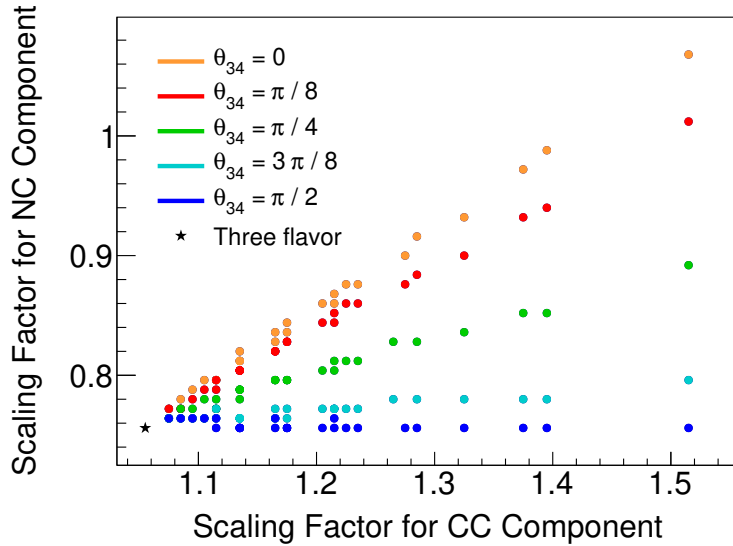


Figure 6.12: Distribution of the best fit points for 120 oscillation parameters. The largest absolute value on the NC scaling factor (Y-axis) is 0.756, and is used for calculating the NC background systematics.

Examples for  $\theta_{34} = 0$  and various values for  $\theta_{24}$  and  $\Delta m_{43}^2$  are shown in Figure 6.13, where each plot corresponds to a point in Fig. 5.19. The best fit results are summarized in Figure 6.12, together with a point from the case of no ND oscillations. The largest NC scaling factor (Y-axis) away from unity is 0.756. For a conservative estimation, this leads to a systematic error of 24.4%. Taking a quadratic sum with the 15% from the MRCC method [104], the total systematic error is set to 30% for MINOS+.



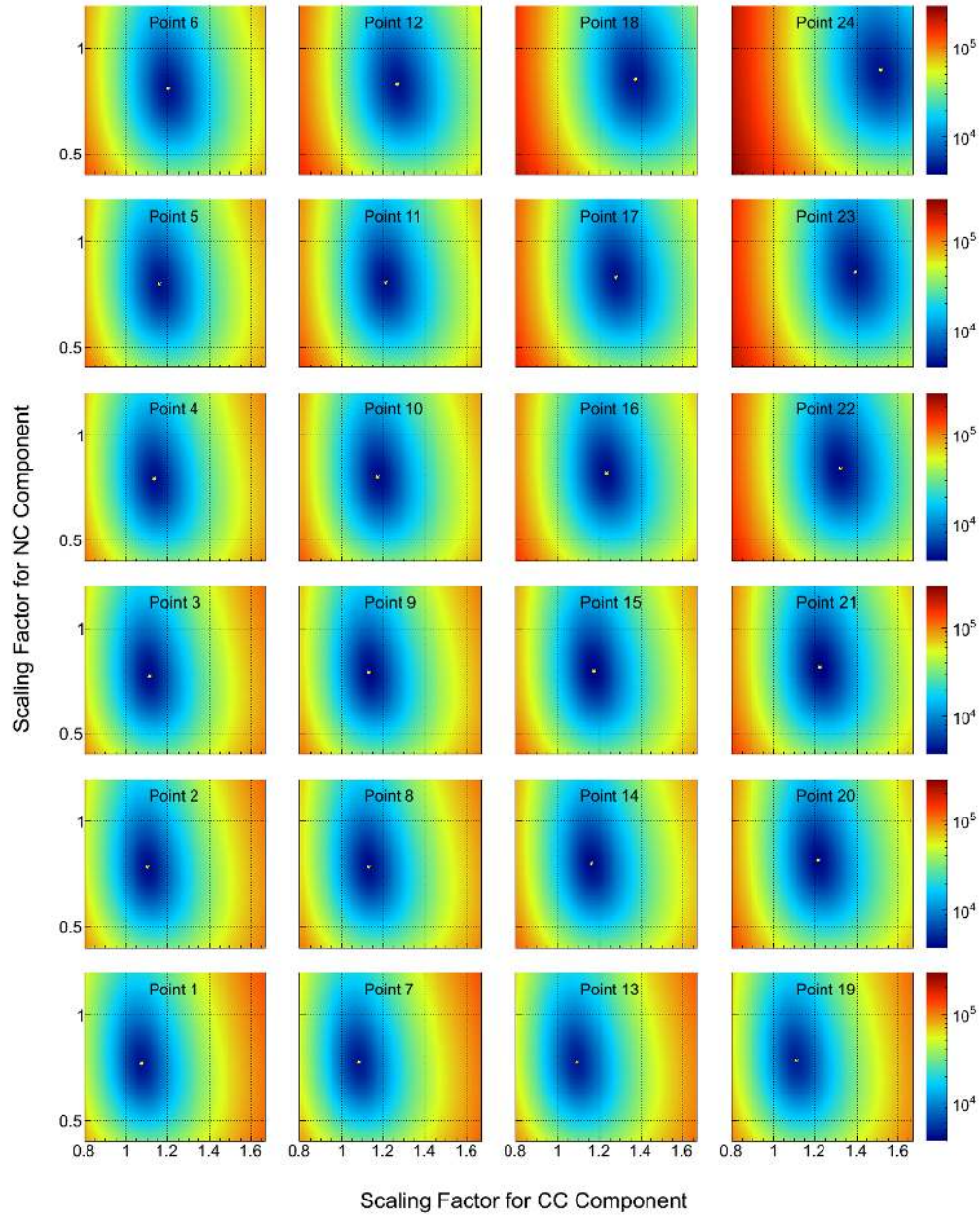


Figure 6.13: Free scaling CC (X-axis) and NC components (Y-axis) to best match MC with data. Each plot corresponds to a different point in Figure 5.19 for different values of  $\theta_{34}$  and  $\Delta m_{43}^2$ .  $\theta_{34}$  is set to  $\pi/4$ .

# Chapter 7

## Systematic Error Bands and Covariance Matrices

A blind analysis procedure was adopted for this dissertation. Before looking at the real data, we examined the effect of all possible systematic uncertainties that may impact the result, as they can well fake or bury a physics signal. This chapter gives the complete list of the systematic errors that have been considered.

The systematic error bands as a function of reconstructed energy, together with the corresponding covariance matrices, are built with the combined MINOS and MINOS+ samples. They will serve as inputs to the analysis of the 3+1 model in Chapter 8.

For the analysis of the LED model in Chapter 9, only MINOS data are used. The error bands and the covariance matrices are taken from Reference [105], where the results are calculated with the MINOS sample only. They are not very different from the ones presented in this chapter, because so far there are not as much data collected in MINOS+ as in MINOS.

## 7.1 Overview

A list of systematics for CC and NC samples (except for the beam related ones) is shown in Table 7.1 grouped by category. It follows the systematics considered in References [105] and [100]. Between MINOS and MINOS+, the systematics in the list are treated as correlated quantities, i.e a  $+1\sigma$  shift in MINOS corresponds to a  $+1\sigma$  shift in MINOS+, and vice versa. To generate error bands for the combined MINOS and MINOS+ samples,  $+1\sigma$  shifted MINOS MC energy spectra are added to the  $+\sigma$  shifted MINOS+ MC energy spectra, and the same for the  $-\sigma$  shift.

### 7.1.1 Fractional Error

As will be discussed in Chapter 8 and 9, the fit is performed on the ratio of FD energy spectra to ND energy spectra. This is referred to as the far-over-near fit. Computing the fractional error on the far-over-near ratio is needed to provide necessary inputs to the fit. The acceptance systematics, which are evaluated using ND data as discussed in Chapter 5 and 6, concern the mis-modeling of MC in terms of the event selections. Due to the possible oscillations at ND, the ratio of the shifted and nominal data-MC ratio, i.e. double ratio

$$\frac{(\text{data/MC})_{\text{shifted}}}{(\text{data/MC})_{\text{nominal}}} - 1. \quad (7.1)$$

is used as a handle on the systematics. The shifted sample is associated with a modified acceptance cut which makes it a subset or superset of the nominal

Category	Event type	Systematic error	Reference
acceptance	CC	left/right fiducial volume tightened fiducial Z tightened fiducial R cut spectrometer join region no containment cut no coil hole cut back exiting cut	Chapter 5, 6
	NC	tightened fiducial Z left/right fiducial volume	
energy scale	CC	shower energy scale	Chapter 4
		track energy scale	[106]
	NC	NC absolute hadronic calibration scale NC relative hadronic calibration scale	[100]
normalization	CC	CC normalization	[104]
	NC	NC normalization	[100]
background	CC	NC background	Chapter 6
	NC	CC background	[107]
NC cleaning	NC	ND cleaning	Chapter 5
		FD cleaning FD cosmics	[108]
cross sections	CC/NC	$\nu_\mu$ KNO multiplicity 2 $\nu_\mu$ KNO multiplicity 3 $\nu_\mu$ resonance cross section $\nu_\mu$ quasi-elastic cross section $\nu_\mu$ total CC cross section $\bar{\nu}_\mu$ KNO multiplicity 2 $\bar{\nu}_\mu$ total CC cross section $\bar{\nu}_\mu$ quasi-elastic cross section $\bar{\nu}_\mu$ resonance cross section	[109]

Table 7.1: List of systematics by categories.

sample. The errors, as will be shown in later plots, are treated as binomial. Equation 7.1 can be used as the percentage error on  $1/(\text{near detector MC})$ , and is therefore equal to the percentage error of far-over-near ratio since the far detector MC is kept unshifted.

Other systematics, which include that of the energy scale, normalization, background, NC cleaning, and cross sections are evaluated using both ND and FD MC samples:

$$\frac{(\text{far/near})_{\text{shifted}}}{(\text{far/near})_{\text{nominal}}} - 1. \quad (7.2)$$

### 7.1.2 Covariance Matrix

The fitting in Chapter 8 and 9 uses the approach of covariance matrix. The dominant term in  $\chi^2$  takes the form  $\Delta\Lambda^{-1}\Delta$ , where  $\Delta$  is a vector with each element representing a reconstructed energy bin and is evaluated as the difference between MC prediction and data.  $\Lambda$  is the covariance constructed from the fractional errors in the bins of the reconstructed energy. Before constructing a covariance matrix, a smoothing procedure is applied to remove the effect of random fluctuation in MC samples.

Based on its definition, the covariance matrix  $\Lambda$  can be calculated numerically. Let  $X$  be a vector with each element  $X_i$  equal to the error in energy bin  $i$ . The covariance matrix can be written as

$$\Lambda_{ij} = \text{cov}(X_i, X_j) = E[(X_i - \mu_i)(X_j - \mu_j)], \quad (7.3)$$

where  $E[\cdot]$  represents the operation of taking the expectation value, and  $\mu_i = E(X_i)$  is the mean of  $X_i$ . Fluctuation of  $X_i$  is correlated to that of  $X_j$ . The correlation, as well as the magnitude of the fluctuation is given by the error band.  $\Lambda_{ij}$  is evaluated as the average of  $(X_i - \mu_i)(X_j - \mu_j)$  for 1000 random  $X$ s. Each random  $X$  is obtained by scaling the error band, which is the  $\pm 1\sigma$  case of  $X$ , with a random number drawn from a Gaussian distribution with the mean of 0 and the standard deviation of 1.

### 7.1.3 Cross Sections

Systematic errors due to the uncertainties in the knowledge of the neutrino interaction cross sections are common to both CC and NC samples. Neutrino cross sections are simulated by the NEUGEN package [110]. At low energies (less than 1 GeV), quasi-elastic scattering and resonant production dominate. The KNO parameters in NEUGEN are scaling parameters that change the multiplicity distributions of the hadronization in the final state. The details are listed in Table 7.2 as given by Reference [109]. The error bands and the associated covariance matrices are shown in Figures 7.12 to 7.20 for the CC sample and Figures 7.30 to 7.38 for the NC sample.

## 7.2 Systematics for CC Sample

In addition to cross section systematics, other CC systematics are listed in Table 7.3. More specifically:

1. The acceptance systematics has been discussed in Chapter 6. The error

#	$\nu$ type	Systematics	Details
1		KNO multiplicity 2	A $\pm 0.1$ shift of the $r_{ij2}$ NEUGEN parameters.
2		KNO multiplicity 3	A $\pm 0.2$ shift of the $r_{ij3}$ NEUGEN parameters.
3	$\nu_\mu$	resonance cross section	A 15% scale on $M_A^{Res}$ .
4		quasi-elastic cross section	A 15% scale on $M_A^{QE}$ .
5		total CC cross section	A 3.5% scale on the total CC cross section.
6		KNO multiplicity 2	A $\pm 0.2$ shift of the $r_{i(3,4)2}$ NEUGEN parameters.
7		total CC cross section	A 4% scale of the total $\bar{\nu}_\mu$ CC cross section.
8	$\bar{\nu}_\mu$	quasi-elastic cross section	An 8% scale of the $\bar{\nu}_\mu$ quasi-elastic cross section.
9		resonance cross section	An 8% scale of the $\bar{\nu}_\mu$ resonance cross section.

Table 7.2: Details of the cross section systematics. The content is taken from [109].

bands and their covariance matrices are shown in Figures 7.1 to 7.7.

2. The shower energy scale systematics has been discussed in Chapter 4. The calculated error band and the covariance matrix are shown in Figure 7.8.
3. The NC background systematics has been evaluated to be 30% for MINOS+ in Chapter 6, in comparison to 20% used for MINOS [104]. The error band and the covariance matrix is shown in Figure 7.10.
4. The track energy scale systematics comes from factors common to both detectors. A 2% adjustment is made to energies measured by range, with a fully correlated 3% shift for tracks whose energies are measured from curvature. The range-based error is calculated from the combination of known uncertainties in the detector simulation and particle propagation. The curvature-based error includes an additional component from observed differences in the range and curvature measurements for individual tracks [106]. The error band and the covariance are shown in Figure 7.9.
5. The relative normalization systematics comes from the differences between ND and FD, including steel thickness, scintillator thickness, FD live time, ND fiducial volume bias, and selection bias. A 1.54% scale factor is applied to the far detector spectrum [111]. The error band is shown in Figure 7.11.



Category	#	Systematic error source	Details
acceptance	1	left/right fiducial volume	The up and down shifts correspond to the events originating on the left and right half of the fiducial volume.
	2	tightened fiducial volume	The shifted distribution is constructed by tightening the fiducial radius from 80 cm to 60 cm.
	3	tightened fiducial Z	The shifted distribution is constructed by tightening the fiducial z cut from 4.07710 m to 2.5 m.
	4	no coil hole cut	The shifted distribution is constructed by turning off the coil hole cut.
	5	cut spectrometer joint region	The shifted distribution is constructed by removing all events with a track ending within 10 planes of the start of the spectrometer.
	6	no containment cut	The shifted distribution is constructed by turning off the containment cut.
	7	back exiting cut	The shifted distribution is constructed by removing all events with a track ending within 10 planes of the end of the near detector.
others	8	shower energy scale	The shower energy is scaled by 5 – 10% depending on the energy.
	9	track energy scale	The track energy is scaled by 2 or 3% depending on whether the range or the curvature is used [106].
	10	NC background	The NC background is scaled by $\pm 20\%$ for MINOS and $\pm 30\%$ for MINOS+.
	11	normalization	The FD spectrum is scaled by $\pm 1.54\%$ [111].

Table 7.3: CC systematics list.

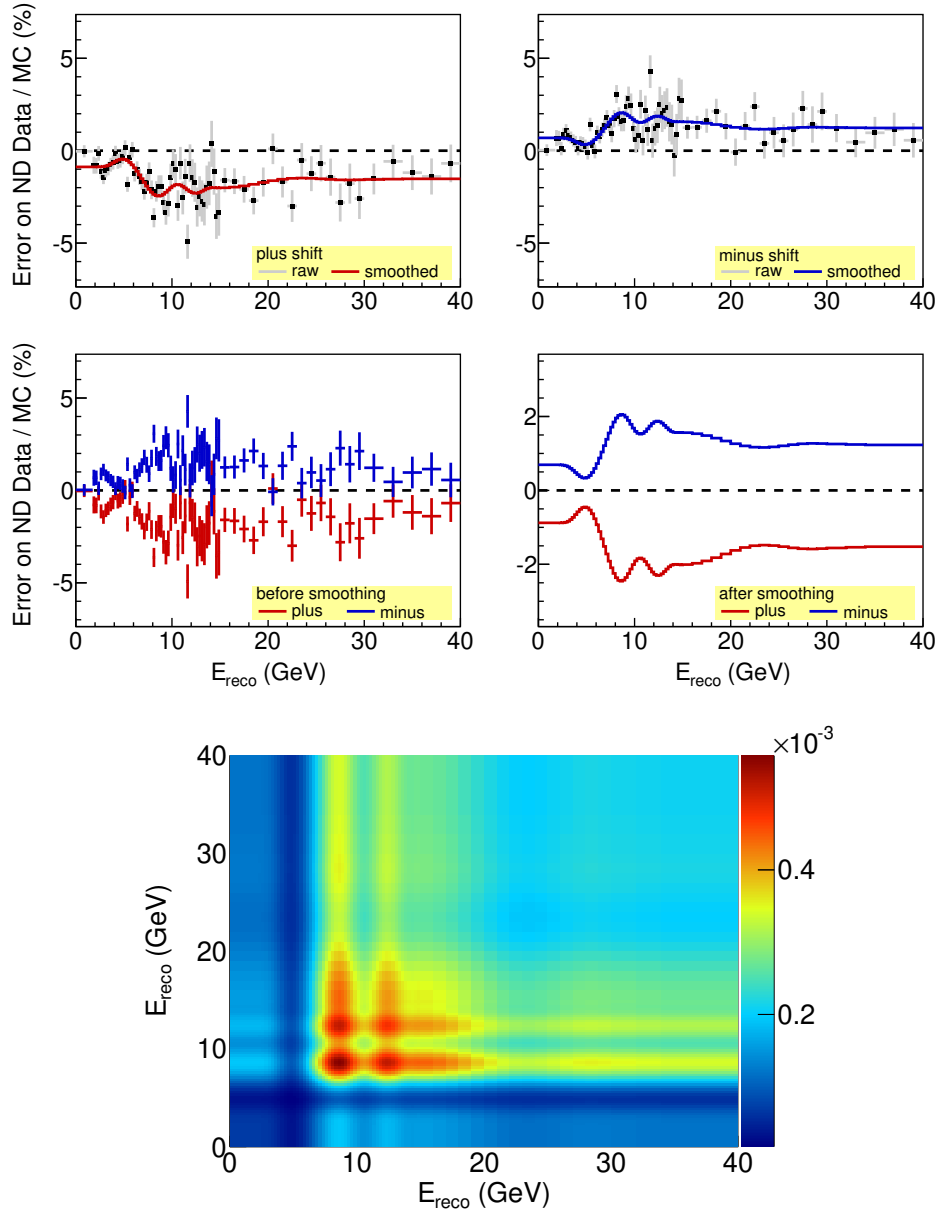


Figure 7.1: An examination of the mis-modeling across the CC fiducial volume. The plus and minus shifts correspond to the CC events originating on the left and right half of the fiducial volume. The top four plots are the error bands for the CC sample. The bottom plot is the corresponding covariance matrix.

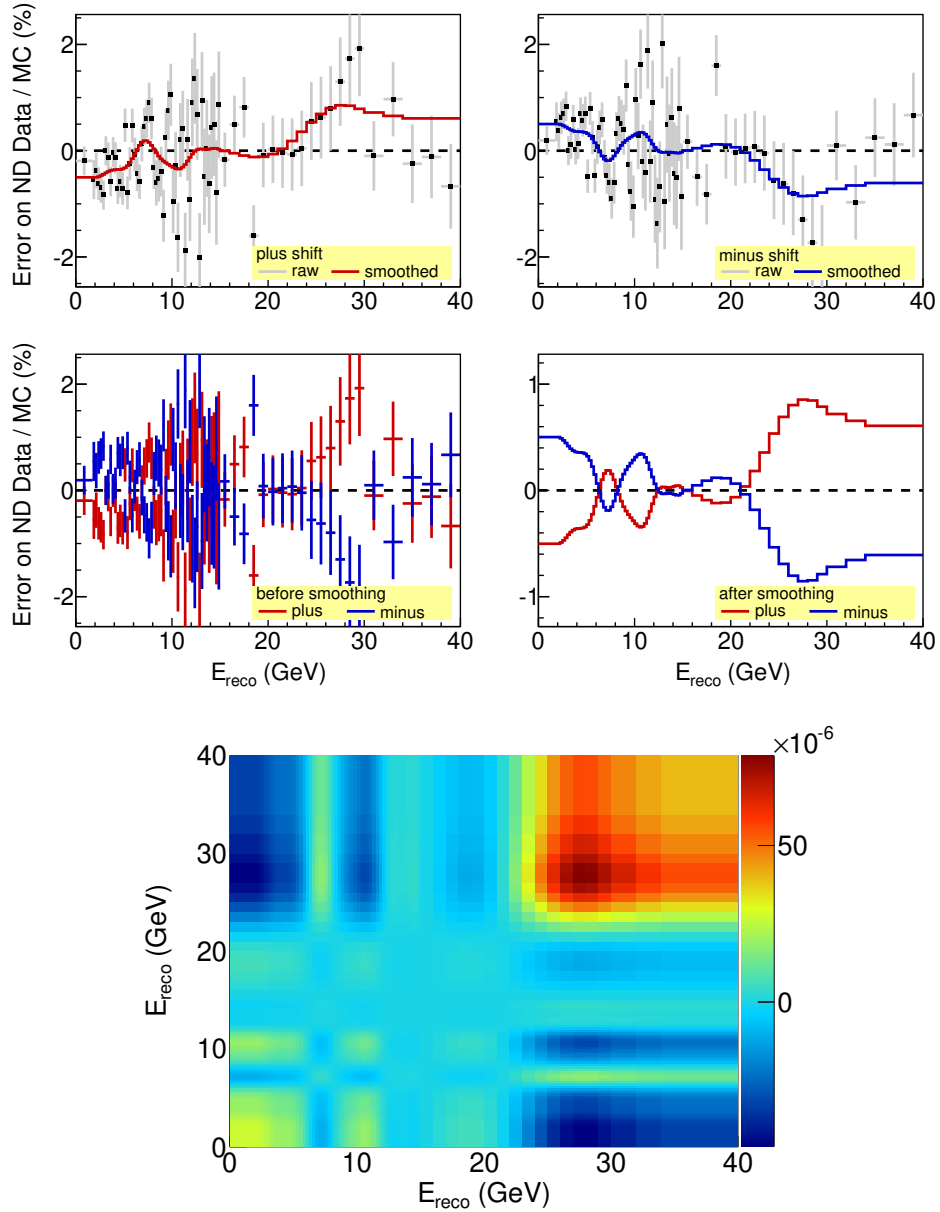


Figure 7.2: An examination of the mis-modeling of the CC fiducial volume. The shifted distribution is constructed by tightening the fiducial radius from 80 cm to 60 cm. The top four plots are the error bands for the CC sample. The bottom plot is the corresponding covariance matrix.

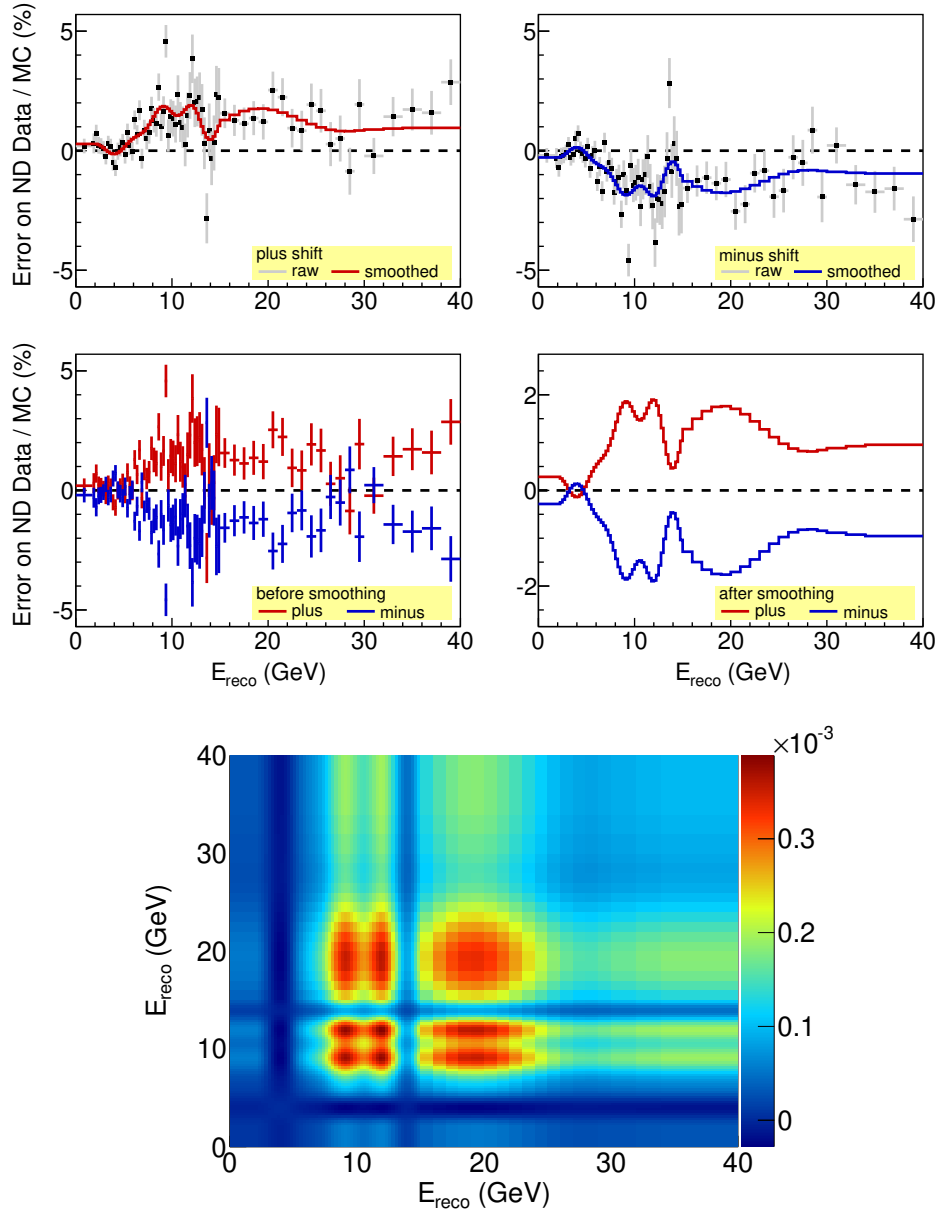


Figure 7.3: An examination of the mis-modeling of the CC fiducial volume. The shifted distribution is constructed by tightening the fiducial Z cut from 4.07710 m to 2.5 m. The top four plots are the error bands for the CC sample. The bottom plot is the corresponding covariance matrix.

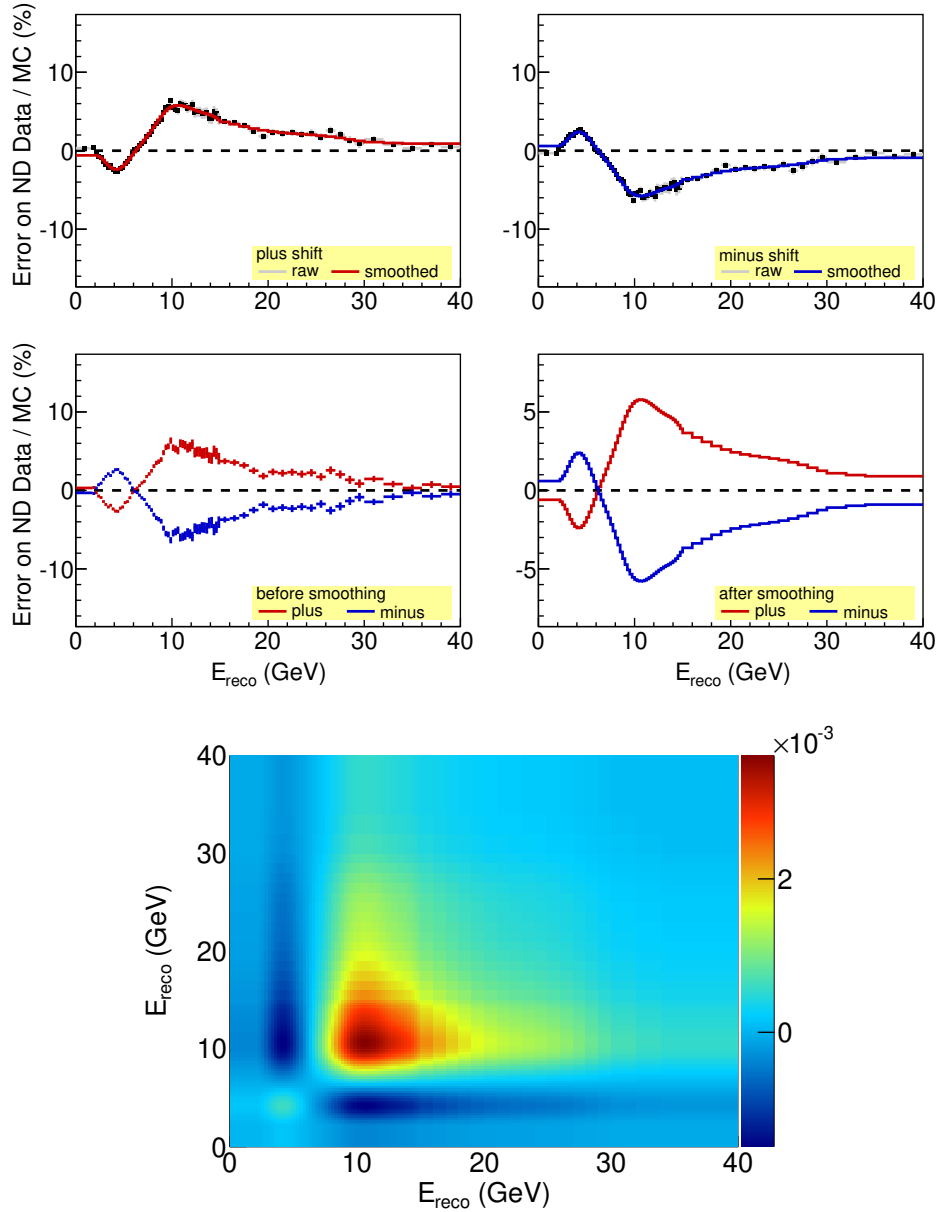


Figure 7.4: An examination of the mis-modeling of the coil hole. The shifted distribution is constructed by turning off the coil hole cut. The top four plots are the error bands for the CC sample. The bottom plot is the corresponding covariance matrix.

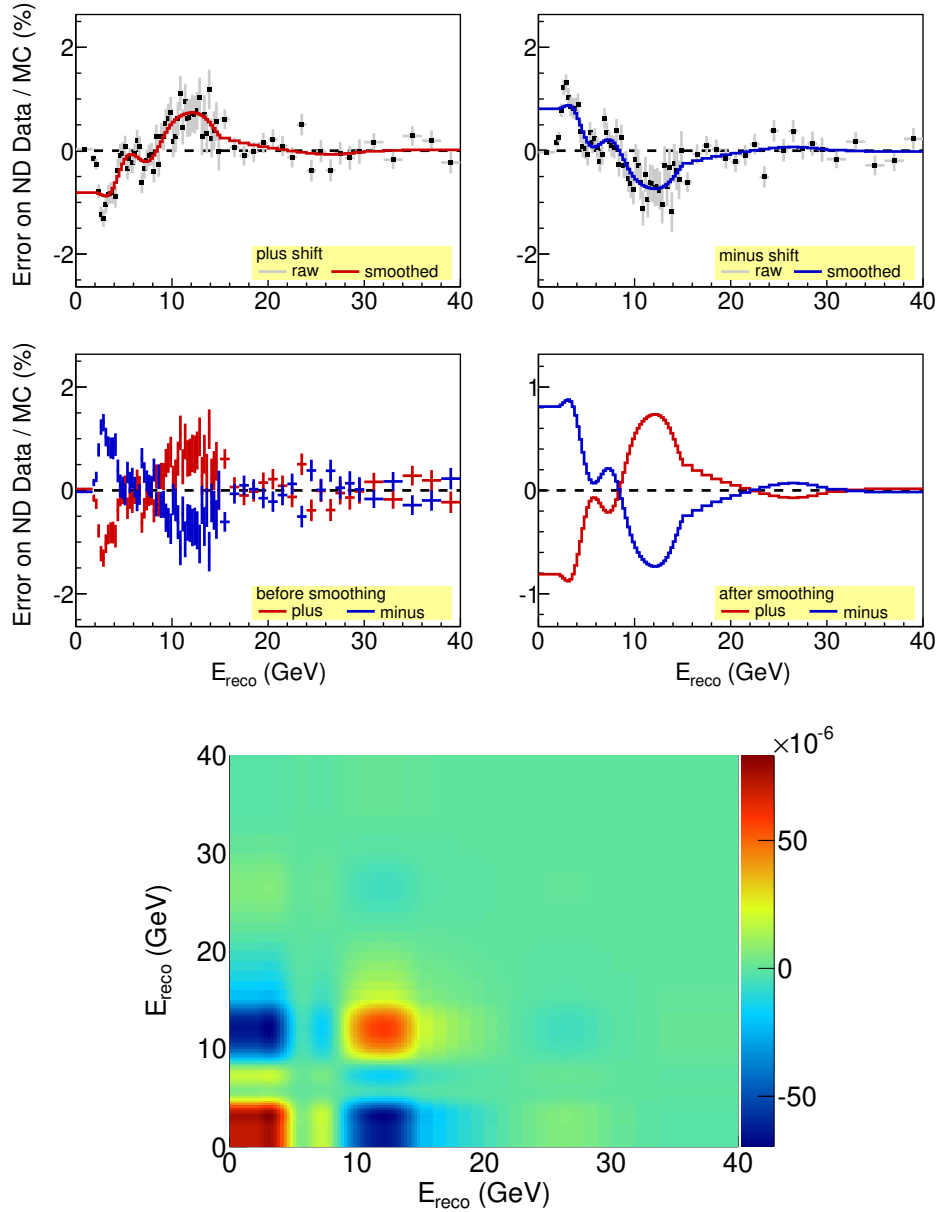


Figure 7.5: An examination of the mis-modeling of the spectrometer join region. The shifted distribution is constructed by remove all events with a track ending within 10 planes of the start of the spectrometer. The top four plots are the error bands for the CC sample. The bottom plot is the corresponding covariance matrix.

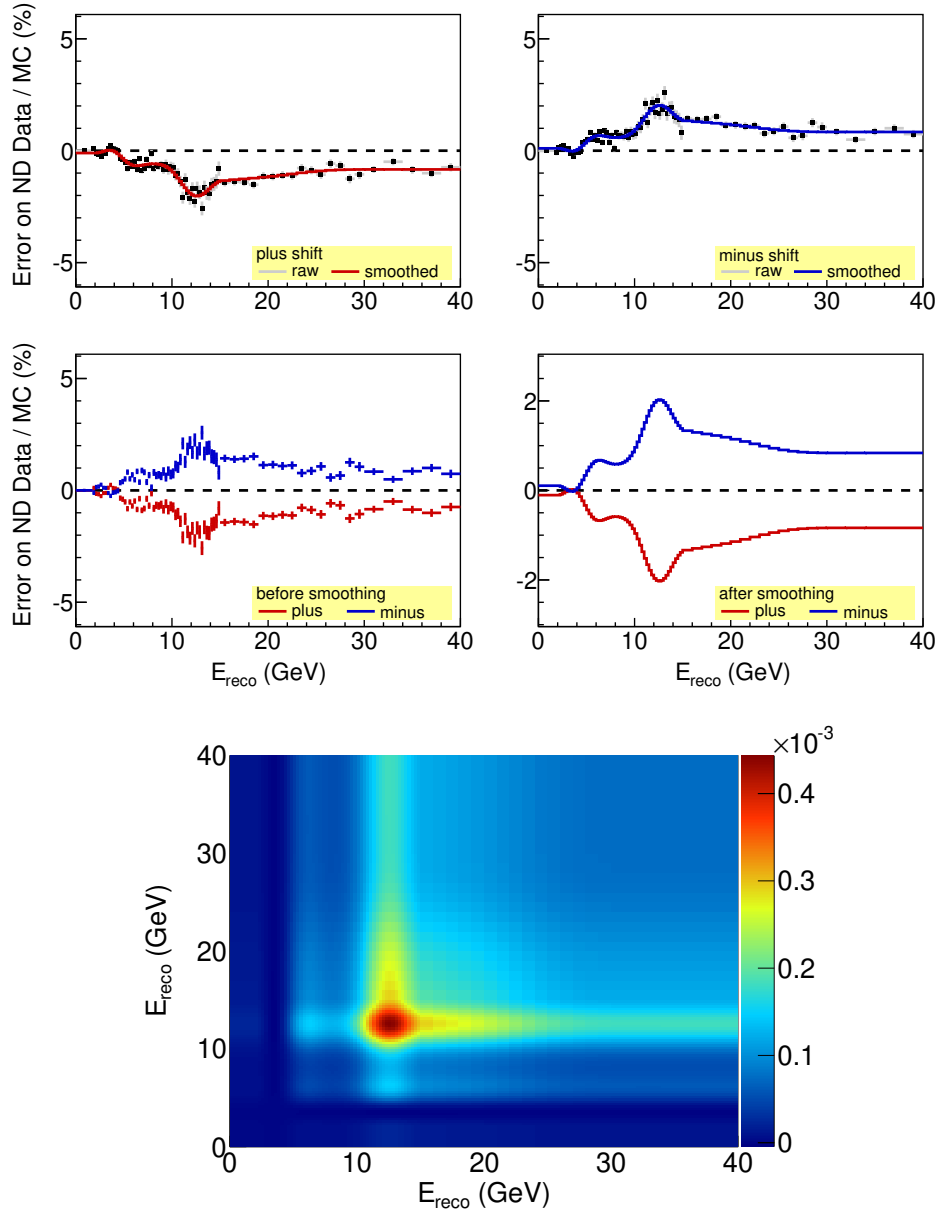


Figure 7.6: An examination of the mis-modeling of side exiting tracks. The shifted distribution is constructed by turning off the containment cut. The top four plots are the error bands for the CC sample. The bottom plot is the corresponding covariance matrix.

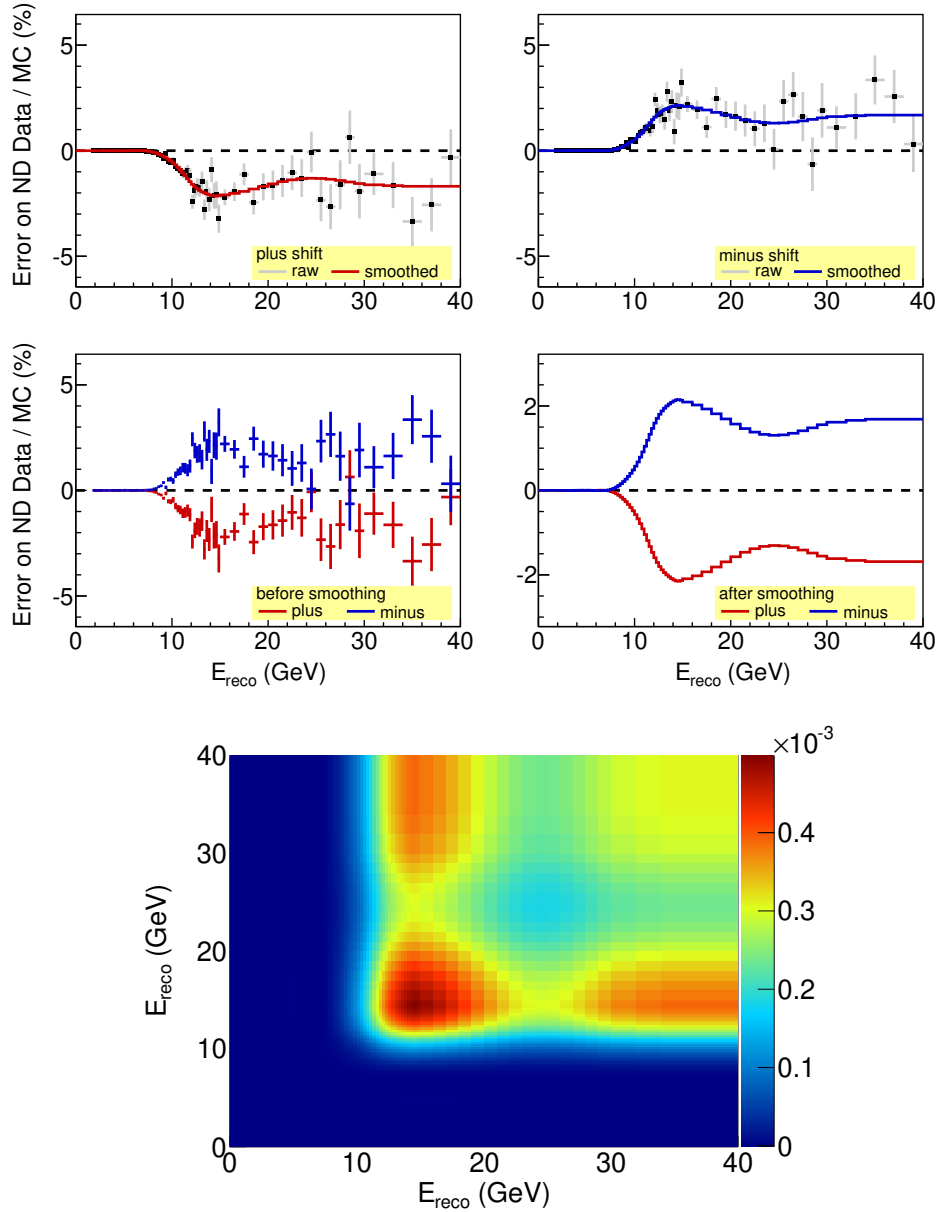


Figure 7.7: An examination of the mis-modeling of back exiting tracks. The shifted distribution is constructed by removing all events with a track ending within 10 planes of the end of the near detector. The top four plots are the error bands for the CC sample. The bottom plot is the corresponding covariance matrix.



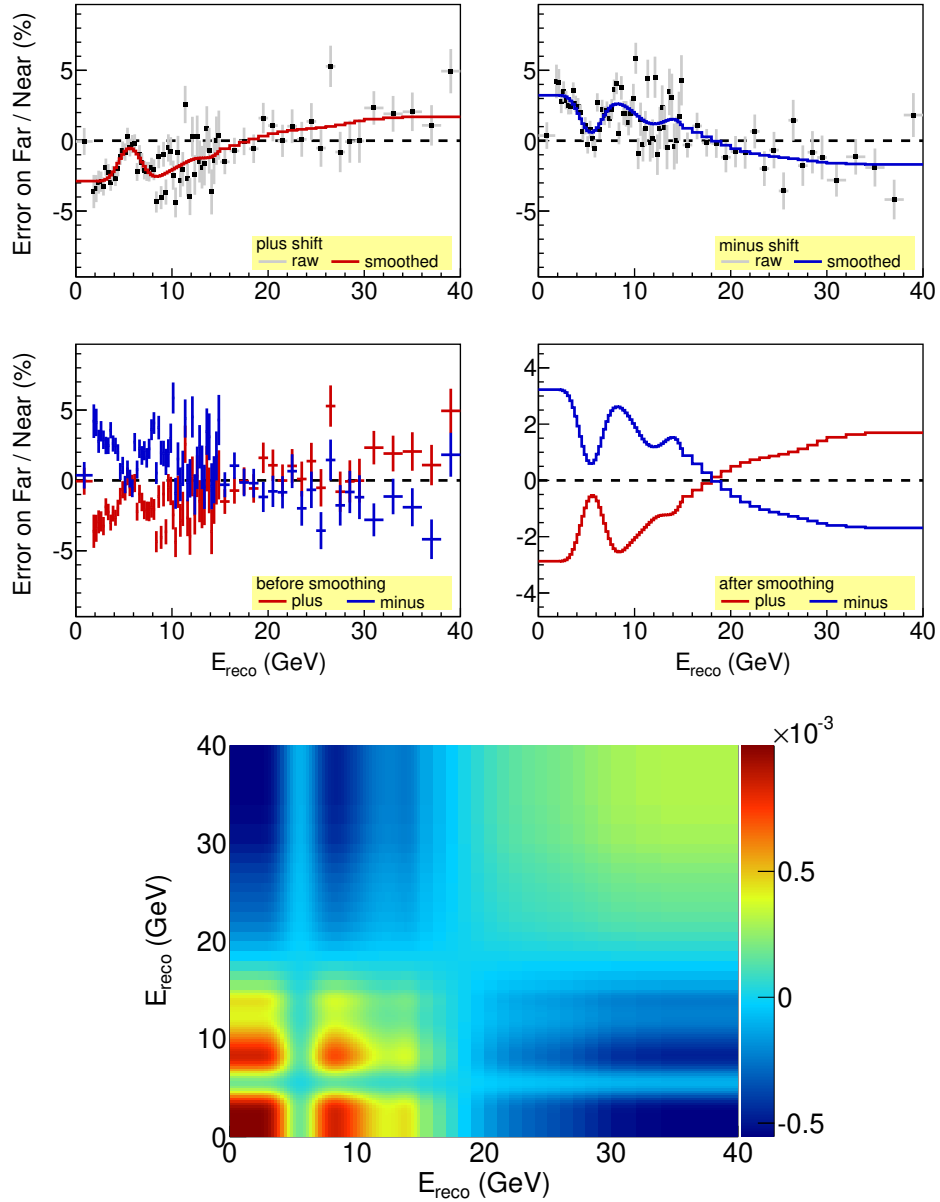


Figure 7.8: CC shower energy scale systematic error. The shower energy is scaled 5–10% depending on the energy. The top four plots are the error bands for the CC sample. The bottom plot is the corresponding covariance matrix.

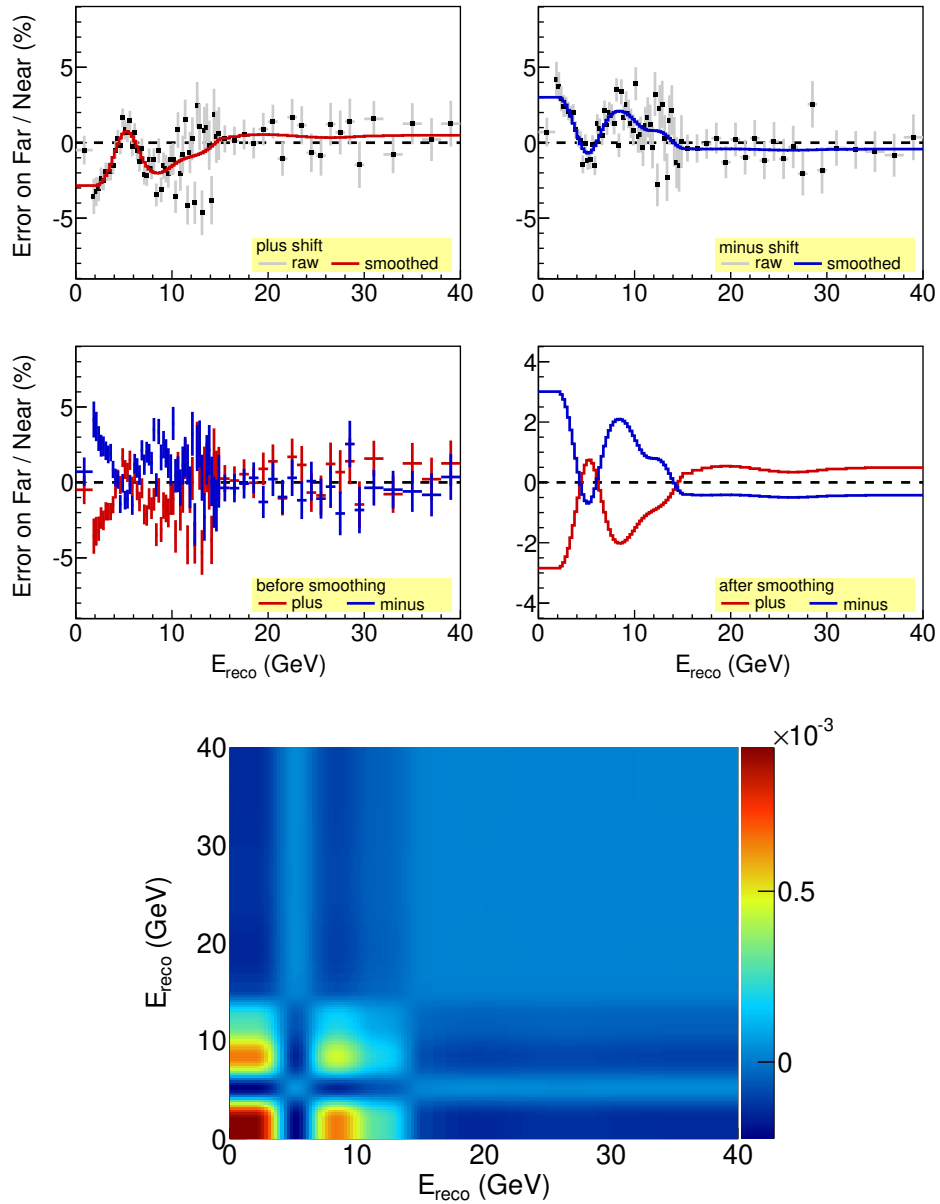


Figure 7.9: CC track energy scale systematic error. The track energy is scaled by 2 or 3% depending on whether the range or the curvature is used [106]. The top four plots are the error bands for the CC sample. The bottom plot is the corresponding covariance matrix.

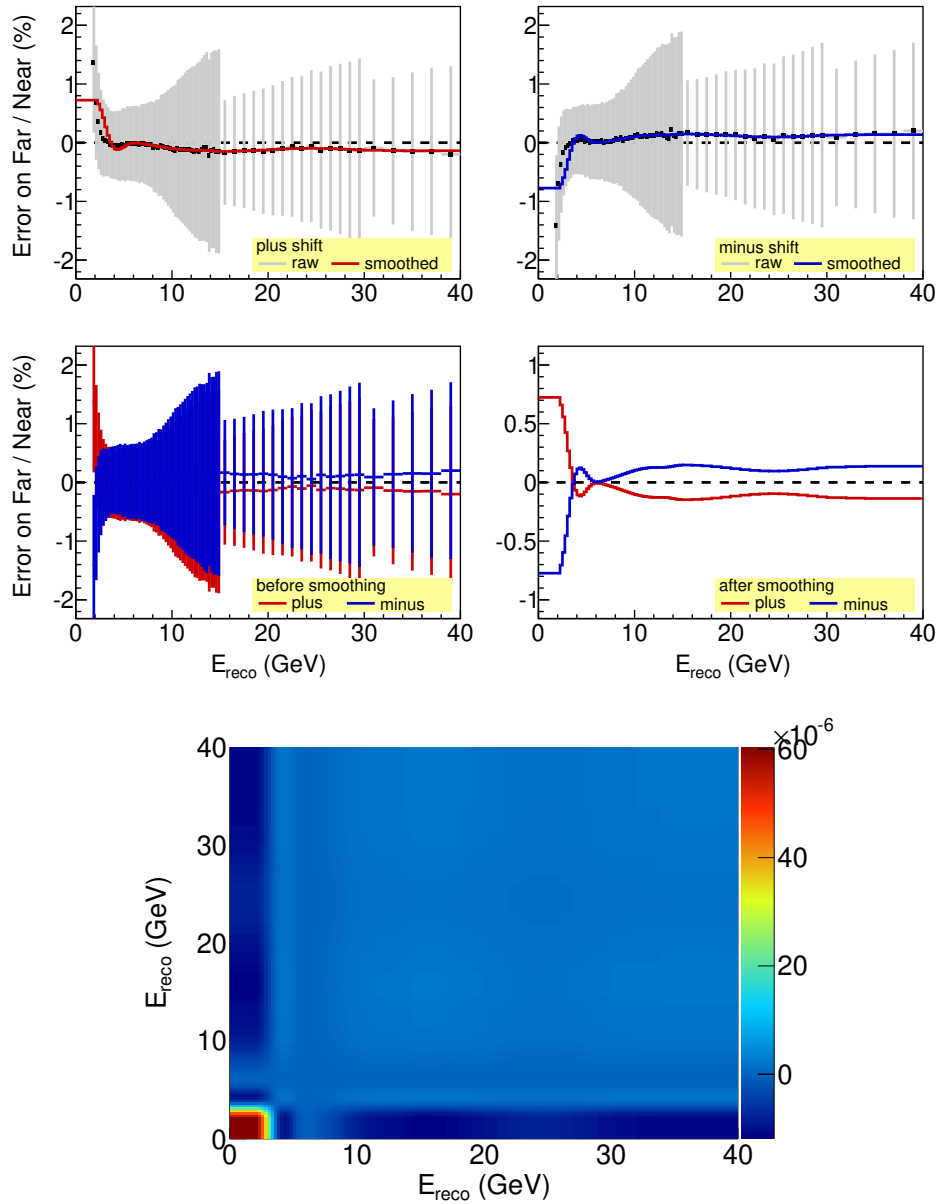


Figure 7.10: NC background systematic error. The NC background is scaled by  $\pm 20\%$  for MINOS and  $\pm 30\%$  for MINOS+. The top four plots are the error bands for the CC sample. The bottom plot is the corresponding covariance matrix.

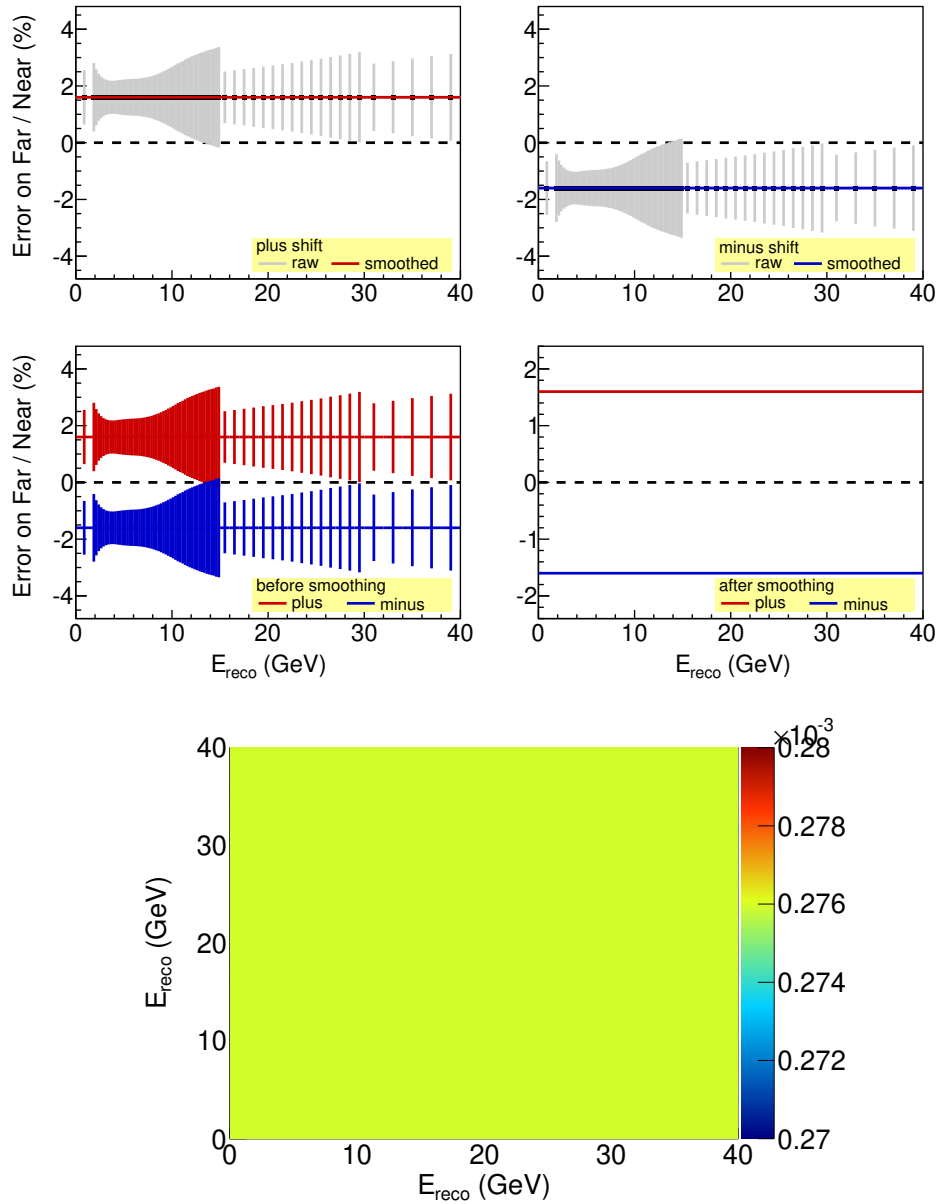


Figure 7.11: Normalization systematic error. The FD normalization is varied by  $\pm 1.54\%$  [111]. The top four plots are the error bands for the CC sample. The bottom plot is the corresponding covariance matrix.

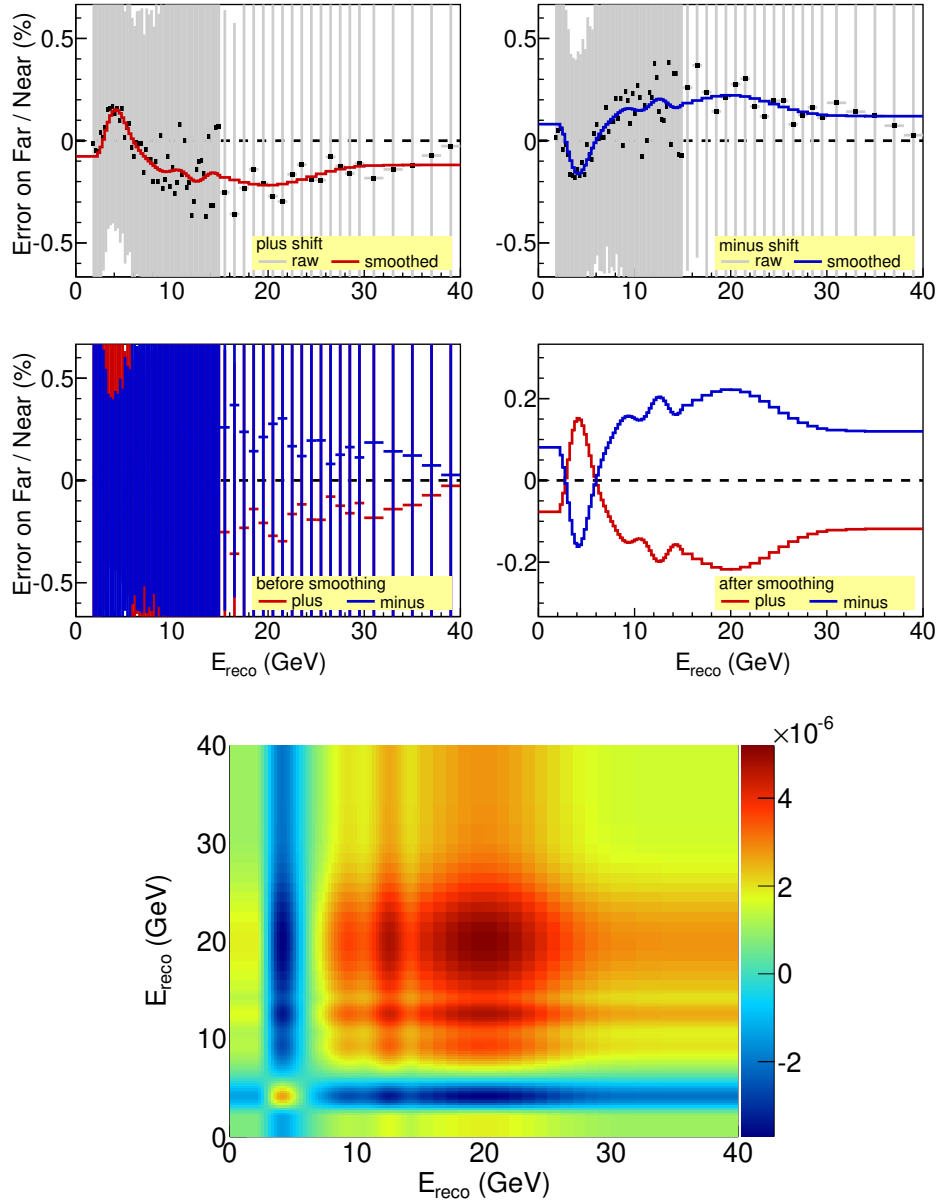


Figure 7.12:  $\nu_\mu$  KNO multiplicity systematic error.  $r_{ij2}$  NEUGEN parameters are shifted by  $\pm 0.1$ . The top four plots are the error bands for the CC sample. The bottom plot is the corresponding covariance matrix.

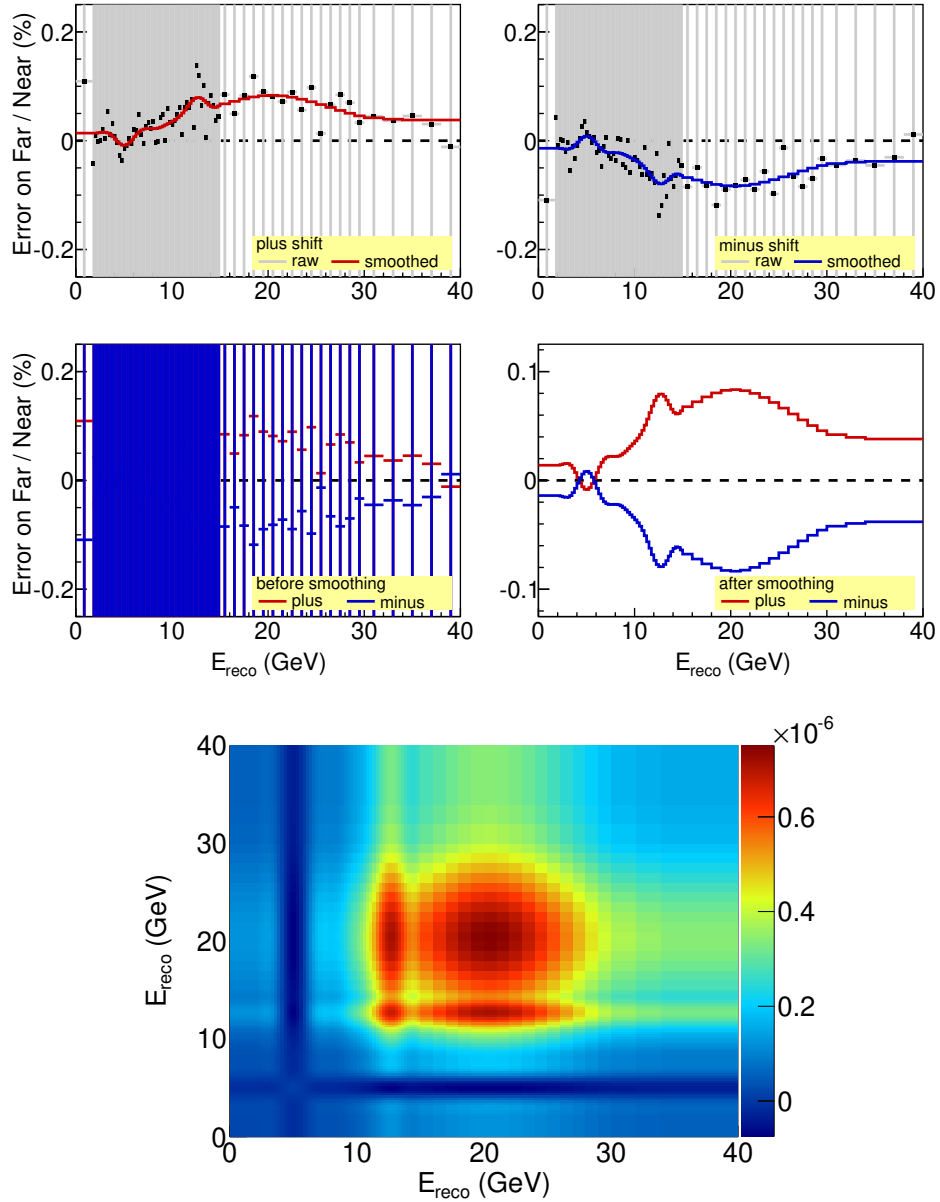


Figure 7.13:  $\nu_\mu$  KNO multiplicity systematic error.  $r_{ij3}$  NEUGEN parameters are shifted by  $\pm 0.2$ . The top four plots are the error bands for the CC sample. The bottom plot is the corresponding covariance matrix.

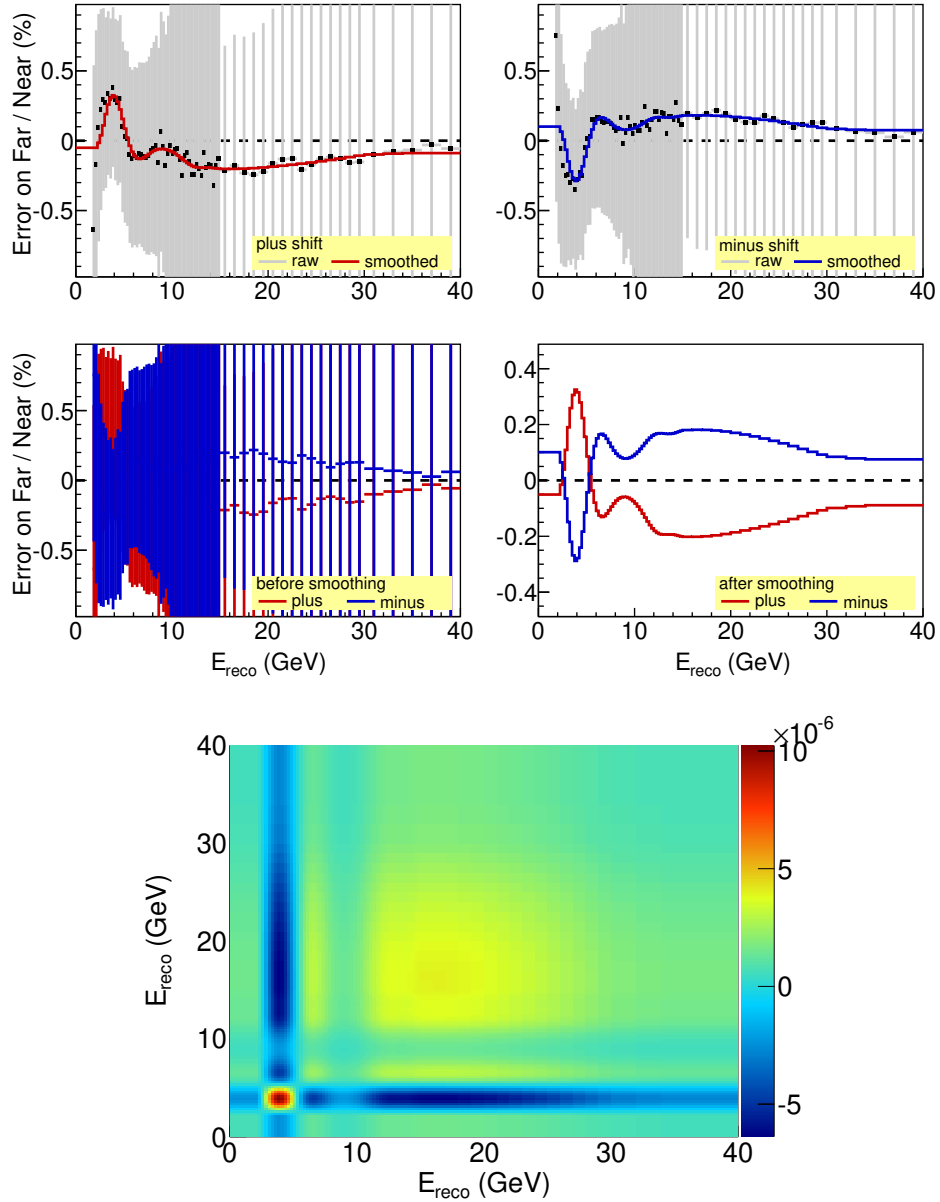


Figure 7.14:  $\nu_\mu$  quasi-elastic cross section systematic error.  $M_A^{QE}$  is scaled by  $\pm 15\%$ . The top four plots are the error bands for the CC sample. The bottom plot is the corresponding covariance matrix.

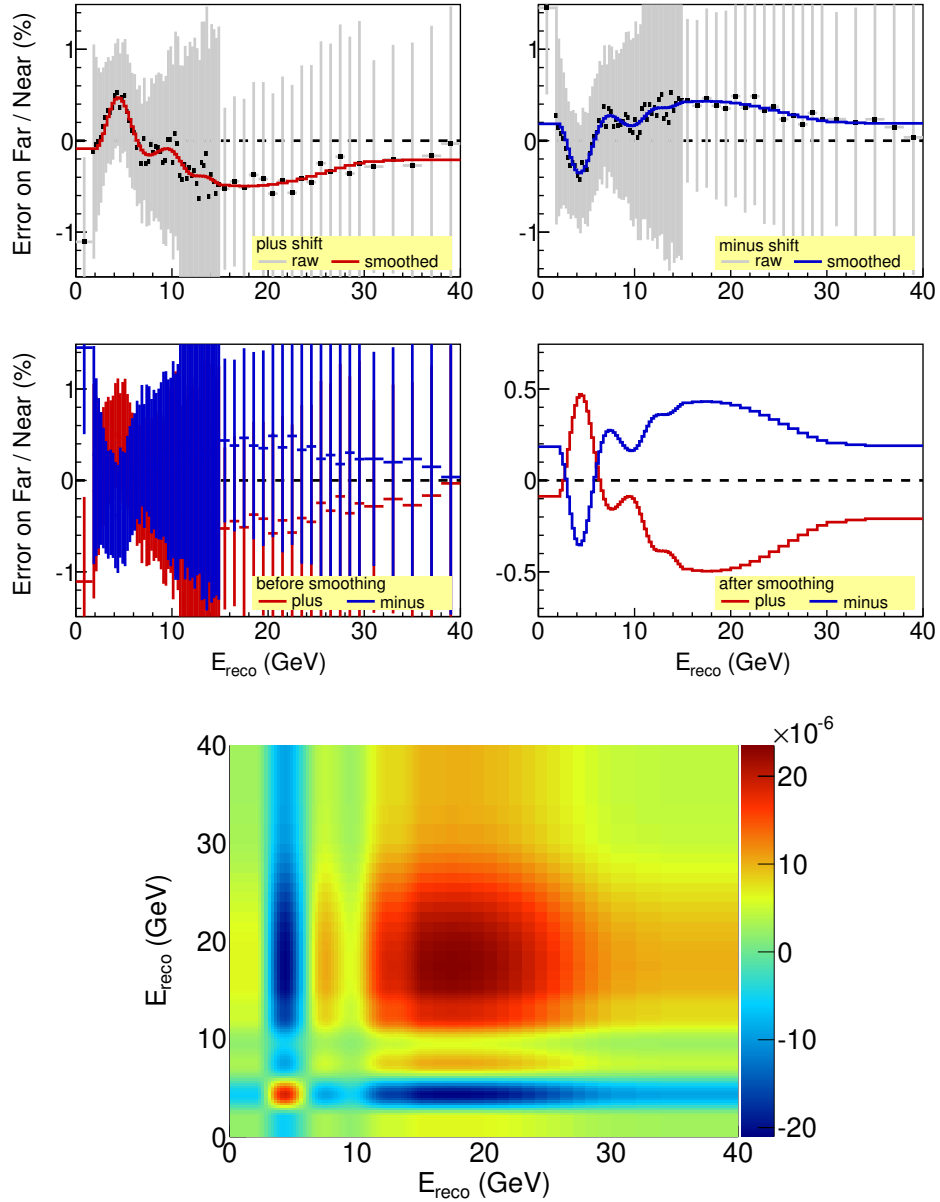


Figure 7.15:  $\nu_\mu$  resonance cross section systematic error.  $M_A^{Res}$  is scaled by  $\pm 15\%$ . The top four plots are the error bands for the CC sample. The bottom plot is the corresponding covariance matrix.



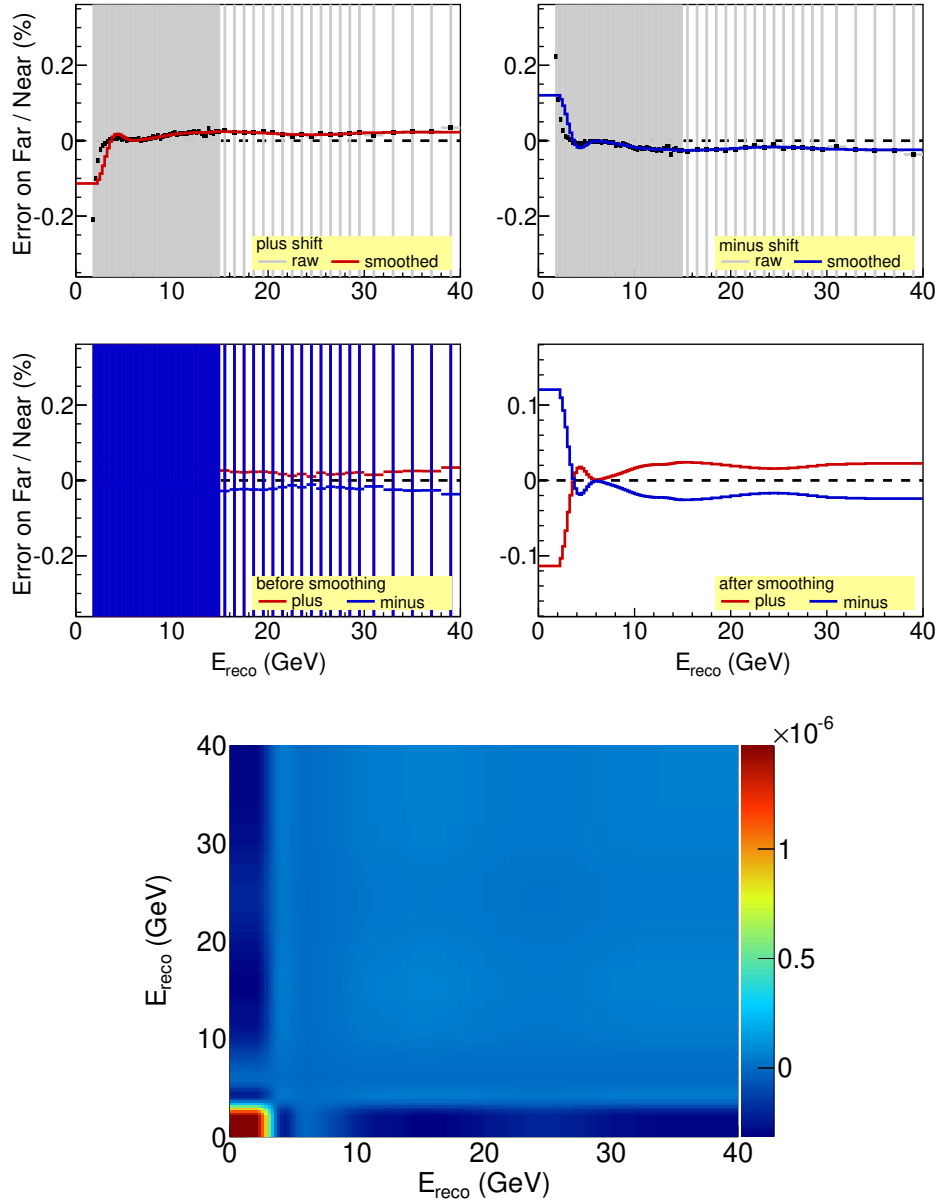


Figure 7.16: Total  $\nu_\mu$  CC cross section systematic error. The total  $\nu_\mu$  CC cross section is scaled by  $\pm 3.5\%$ . The top four plots are the error bands for the CC sample. The bottom plot is the corresponding covariance matrix.

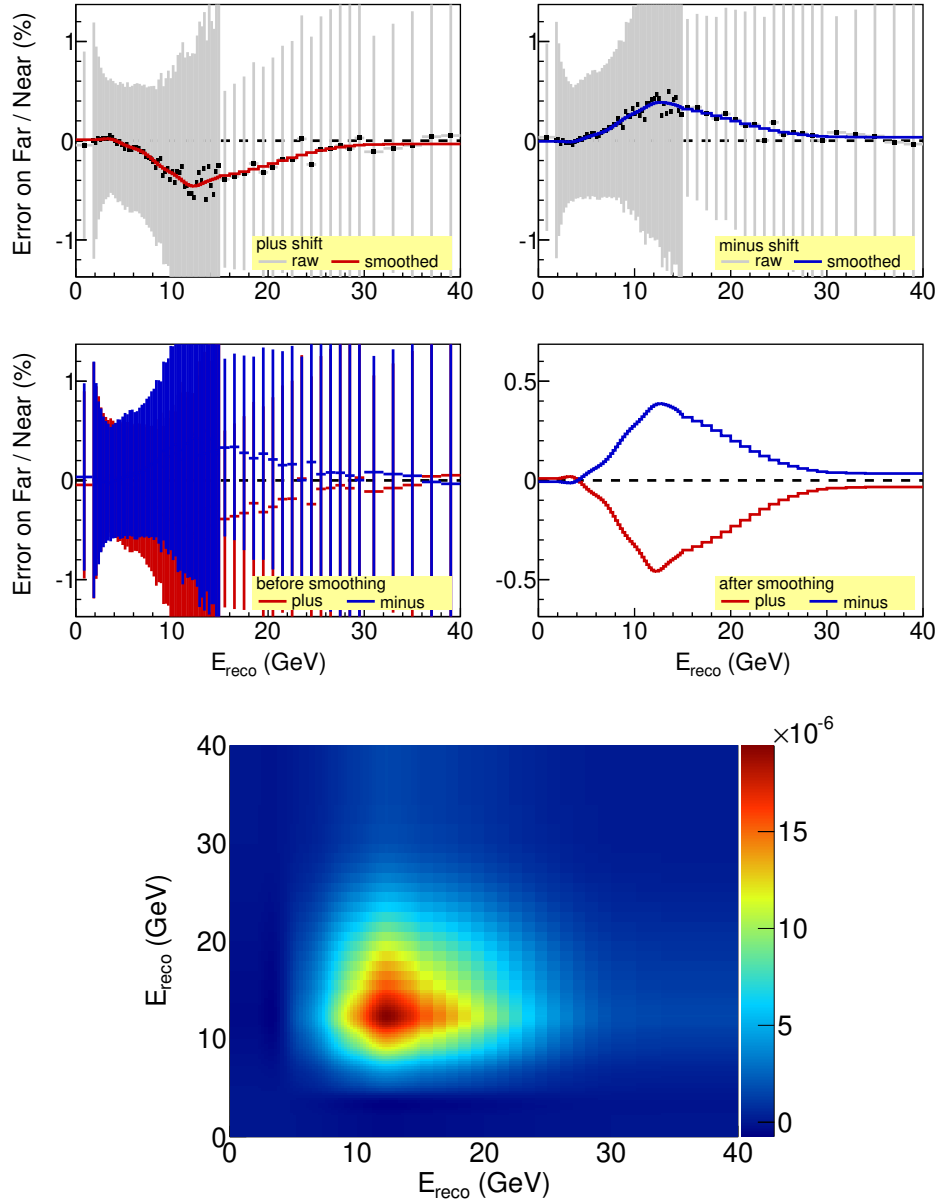


Figure 7.17:  $\bar{\nu}_\mu$  KNO multiplicity systematic error.  $r_{i(3,4)2}$  NEUGEN parameters is shifted by  $\pm 0.2$ . The top four plots are the error bands for the CC sample. The bottom plot is the corresponding covariance matrix.

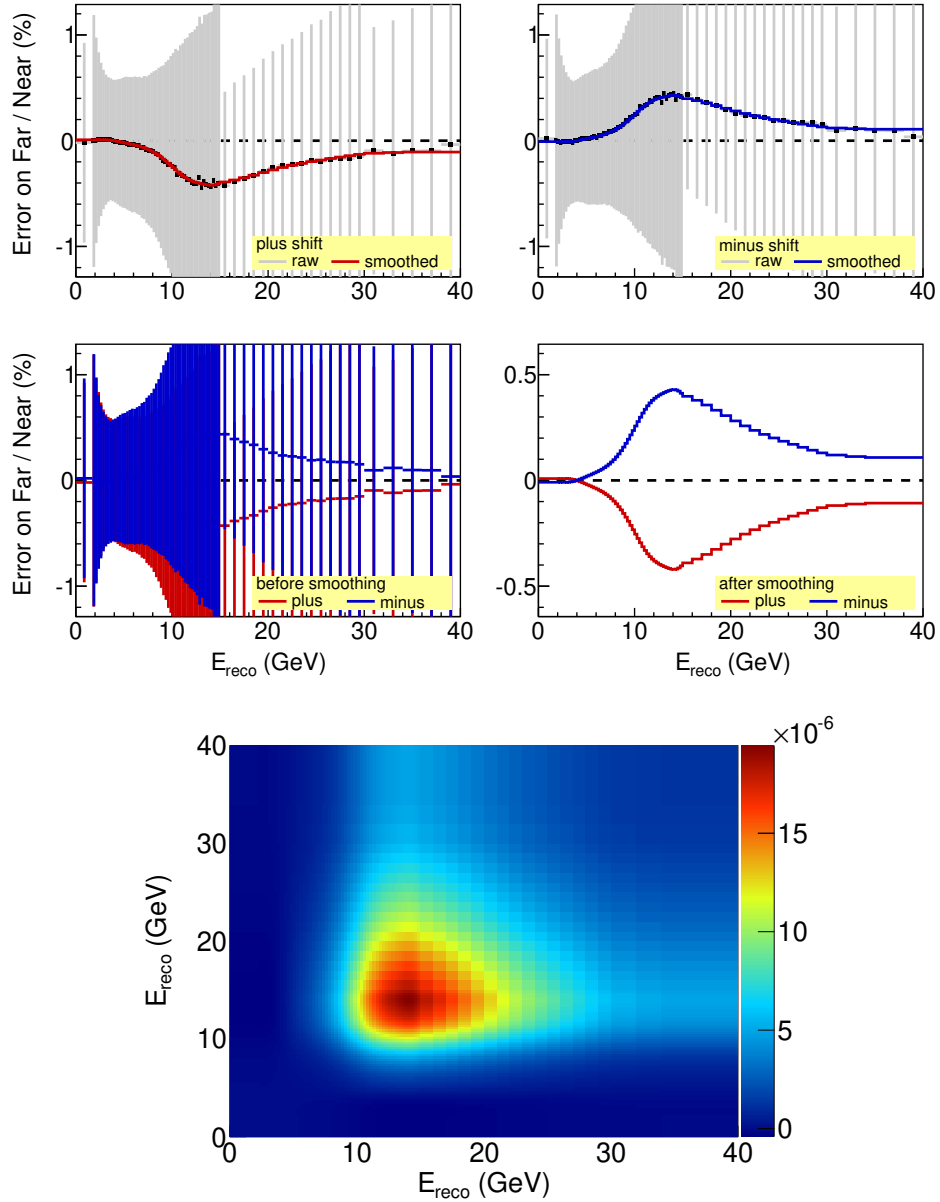


Figure 7.18: Total  $\bar{\nu}_\mu$  CC cross section systematic error. The total  $\bar{\nu}_\mu$  CC cross section is scaled by  $\pm 4\%$ . The top four plots are the error bands for the CC sample. The bottom plot is the corresponding covariance matrix.

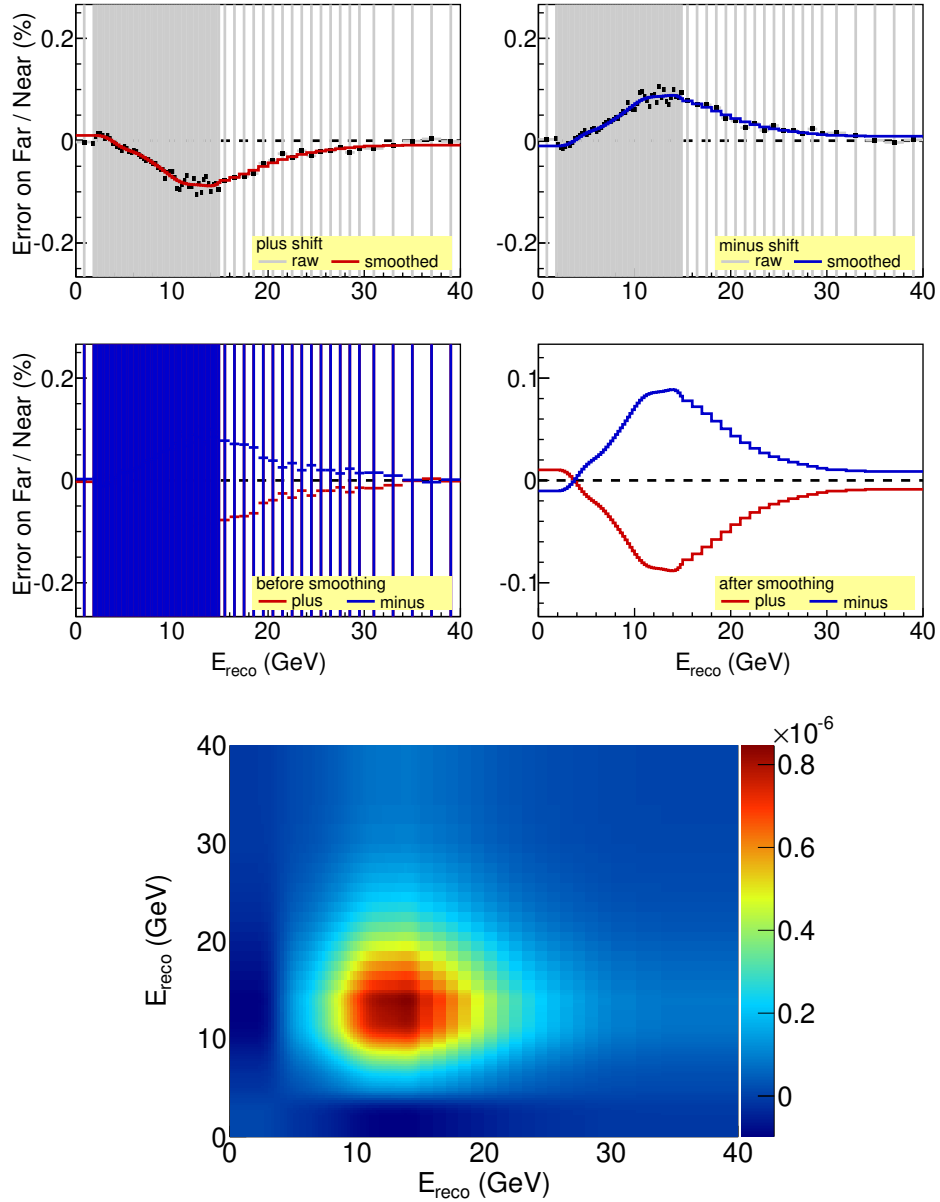


Figure 7.19:  $\bar{\nu}_\mu$  quasi-elastic cross section systematic error.  $\bar{\nu}_\mu$  quasi-elastic cross section is scaled by  $\pm 8\%$ . The top four plots are the error bands for the CC sample. The bottom plot is the corresponding covariance matrix.

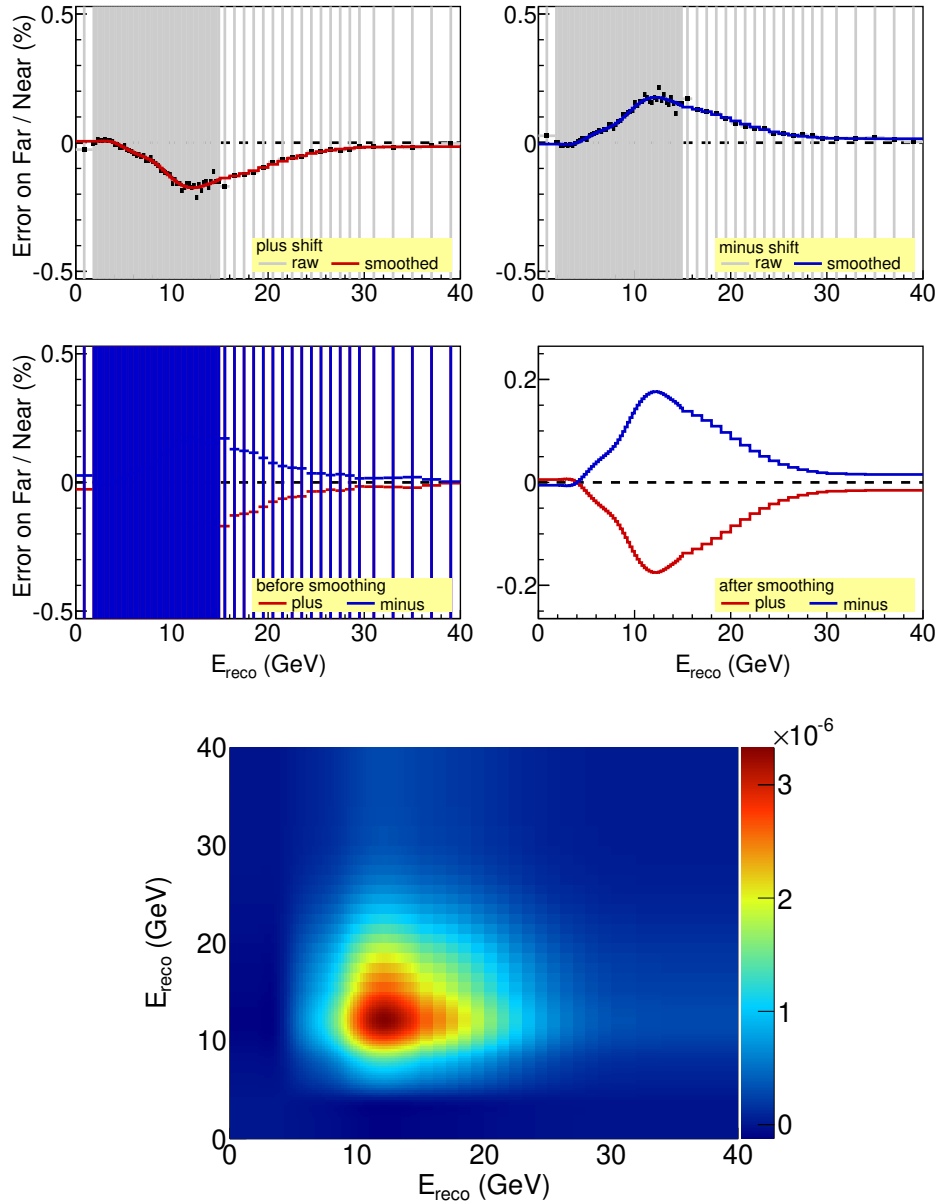


Figure 7.20:  $\bar{\nu}_\mu$  resonance cross section systematic error.  $\bar{\nu}_\mu$  resonance cross section is scaled by  $\pm 8\%$ . The top four plots are the error bands for the CC sample. The bottom plot is the corresponding covariance matrix.

### 7.3 Systematics for NC Sample

NC systematics are listed in Table 7.4. Details are described below.

1. A list of acceptance systematic errors is discussed in Chapter 5. The error bands are shown in Figures 7.21 and 7.22.
2. The ND cleaning systematic error is studied in Chapter 5 and the error band is shown in Figure 7.27.
3. The systematic errors associated with the FD cleaning and cosmic removal are described in [108]. The former removes noise at low energies with a systematic error up to 4.9%. The later cuts off cosmic events with a systematic error up to 2.7% depending on the energy range. The error bands are shown in Figure 7.25 for the FD cleaning and Figure 7.26 for the FD cosmic removal.
4. The absolute hadronic calibration scale uncertainty is evaluated in a procedure similar to that of the CC  $k$ NN shower energy as described in Chapter 4. It reaches 10% at lower shower energies and becomes approximately asymptotical to 6.6% at higher shower energies [100]. The error band is shown in Figure 7.23.
5. The relative hadronic calibration scale uncertainty comes from the conversion of the detector response to hadronic energy in the calibration chain. It has been evaluated to be 2.1% [112]. The error band is shown in Figure 7.29.

6. The uncertainty of CC background selected in NC spectra is evaluated by using different beam configurations to reduce the impact of the wrong modelling of the MC neutral current and charged current cross sections [107]. It is 15% at all energies. The error band is shown in Figure 7.24.
7. The normalization systematic error due to the difference between ND and FD is found to be 2.2% constant over the whole energy spectrum in Reference [113]. The error band is shown in Figure 7.28.

Category	#	Systematic error source	Details
acceptance	1	Left/Right Fiducial Volume	The up and down shifts correspond to the events originating on the left and right half of the fiducial volume.
	2	Tightened Fiducial Z	The shifted distribution is constructed by tightening the fiducial z cut from 4.7368 m to 2.5 m.
others	3	ND Cleaning	The event energy is scaled by up to $\pm 8.2\%$ for MINOS [114] and up to $\pm 50\%$ for MINOS+ at low energies.
	4	FD Cleaning	The event energy is scaled by up to $\pm 4.9\%$ at low energies [108].
	5	FD Cosmics	The event energy is scaled by $\pm 0 - 2.7\%$ depending on the energy [108].
	6	Abs. Hadronic Calibration Scale	The event energy is scaled by $\pm 6.6 - 10\%$ depending on the energy [100].
	7	Rel. Hadronic Calibration Scale	The FD event energy is scaled by $\pm 2.1\%$ [100].
	8	CC Background	The CC background is scaled by $\pm 15\%$ [107].
	9	Normalization	The FD energy spectrum is scaled by $\pm 2.2\%$ [100].

Table 7.4: NC systematics list.



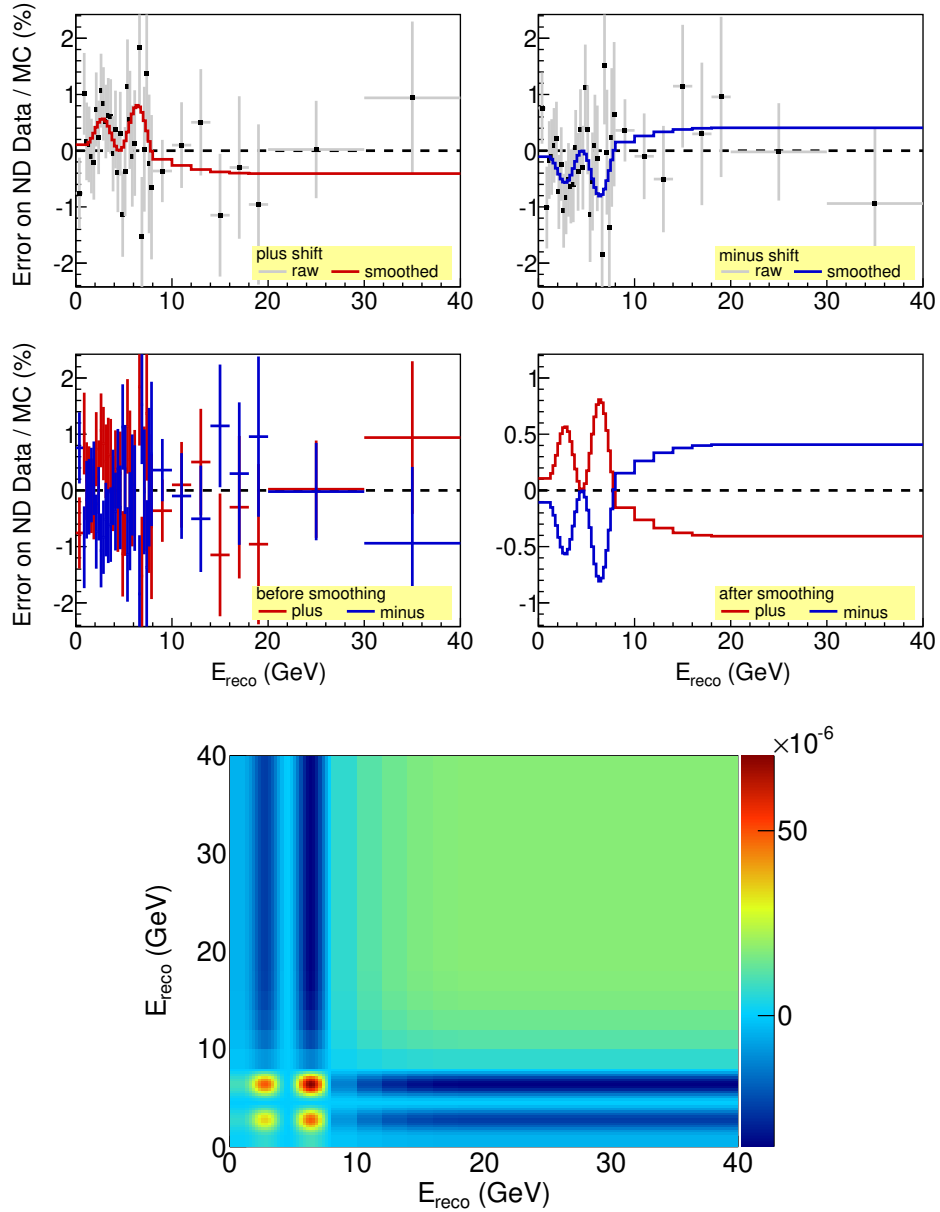


Figure 7.21: An examination of the mis-modeling of the NC fiducial volume. The shifted distribution is constructed by tightening the fiducial Z cut from 4.7368 m to 2.5 m. The top four plots are the error bands for the NC sample. The bottom plot is the corresponding covariance matrix.

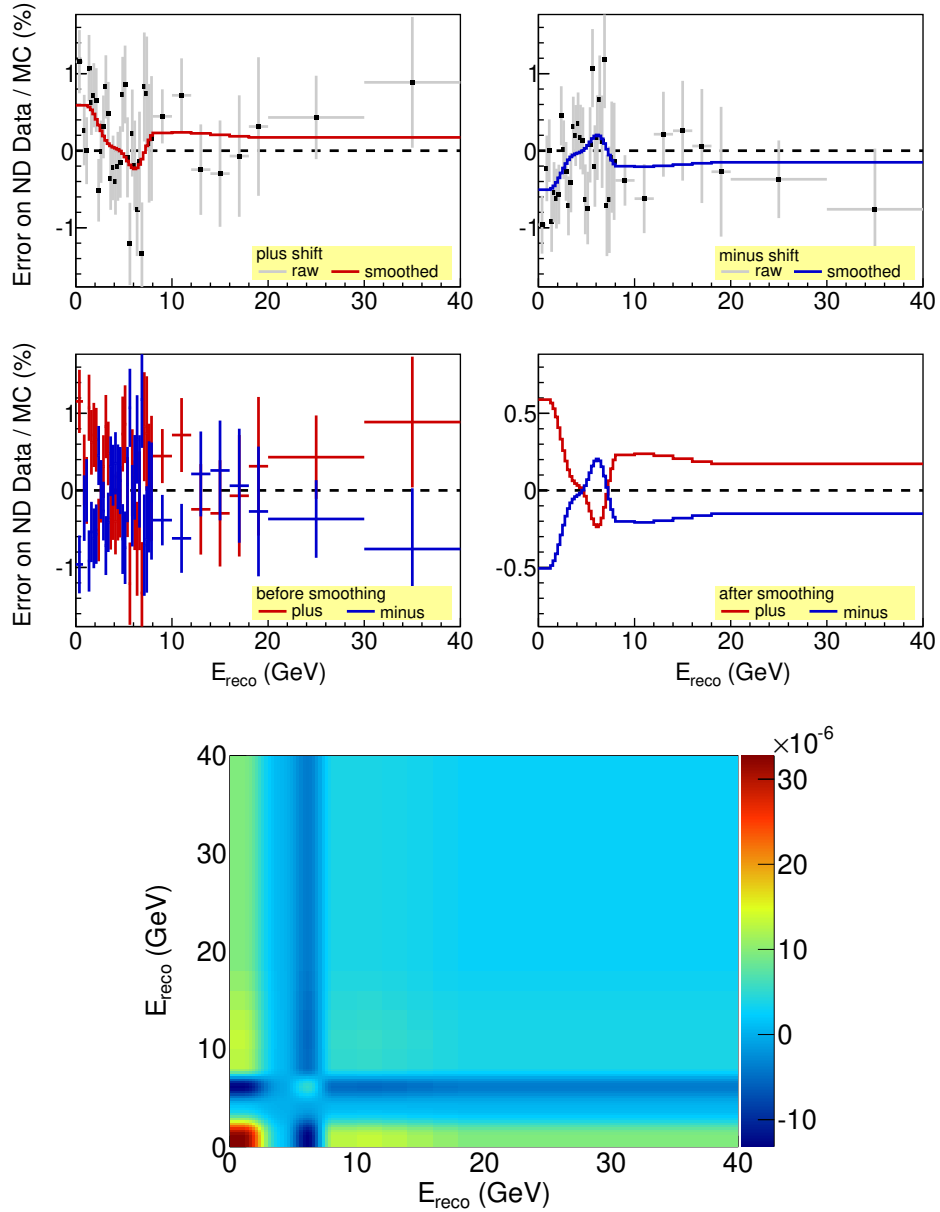


Figure 7.22: An examination of the mis-modeling the across the NC fiducial volume. The plus and minus shifts correspond to the events originating on the left and right half of the fiducial volume. The top four plots are the error bands for the NC sample. The bottom plot is the corresponding covariance matrix.

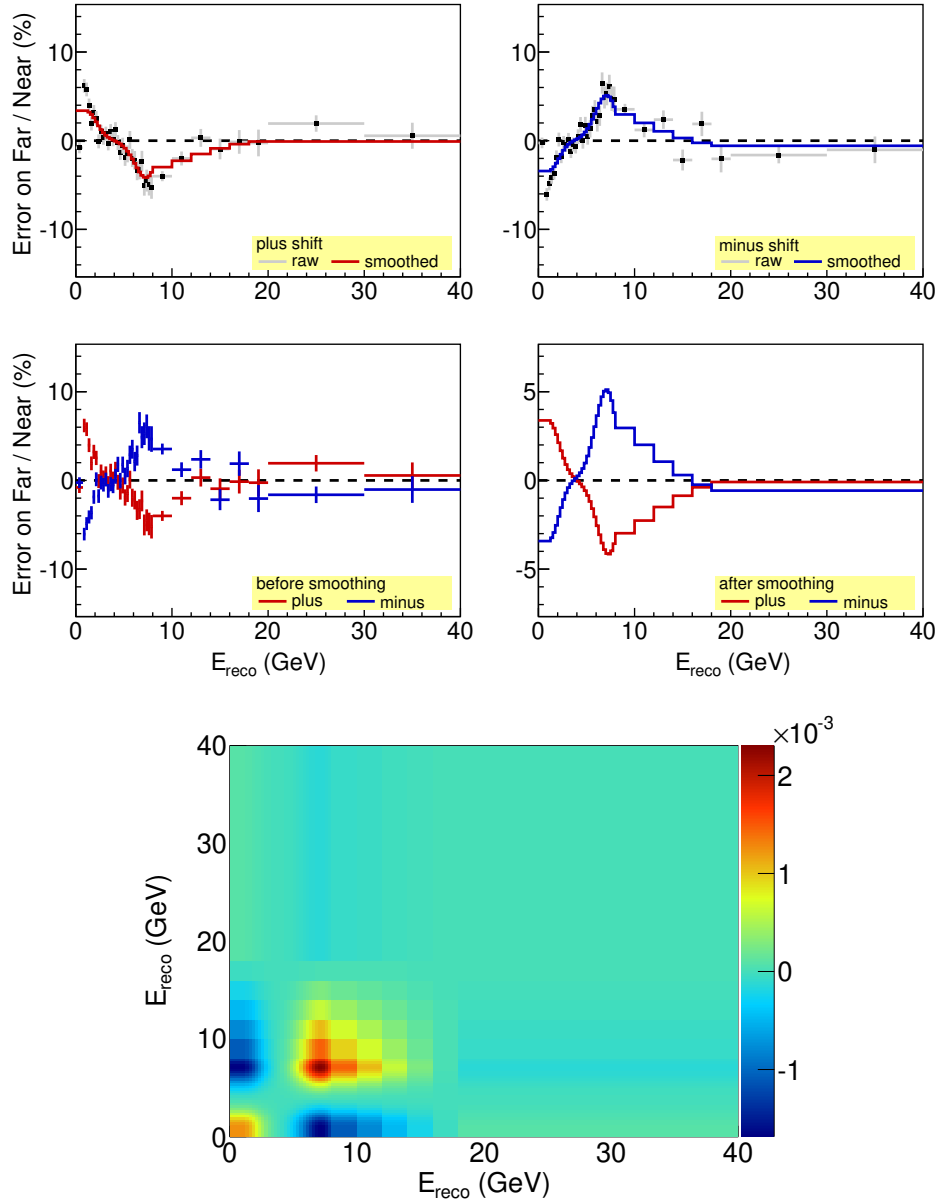


Figure 7.23: Absolute hadronic calibration scale systematic error. The event energy is scaled by  $\pm 6.6 - 10\%$  depending on the energy [100]. The top four plots are the error bands for the NC sample. The bottom plot is the corresponding covariance matrix.

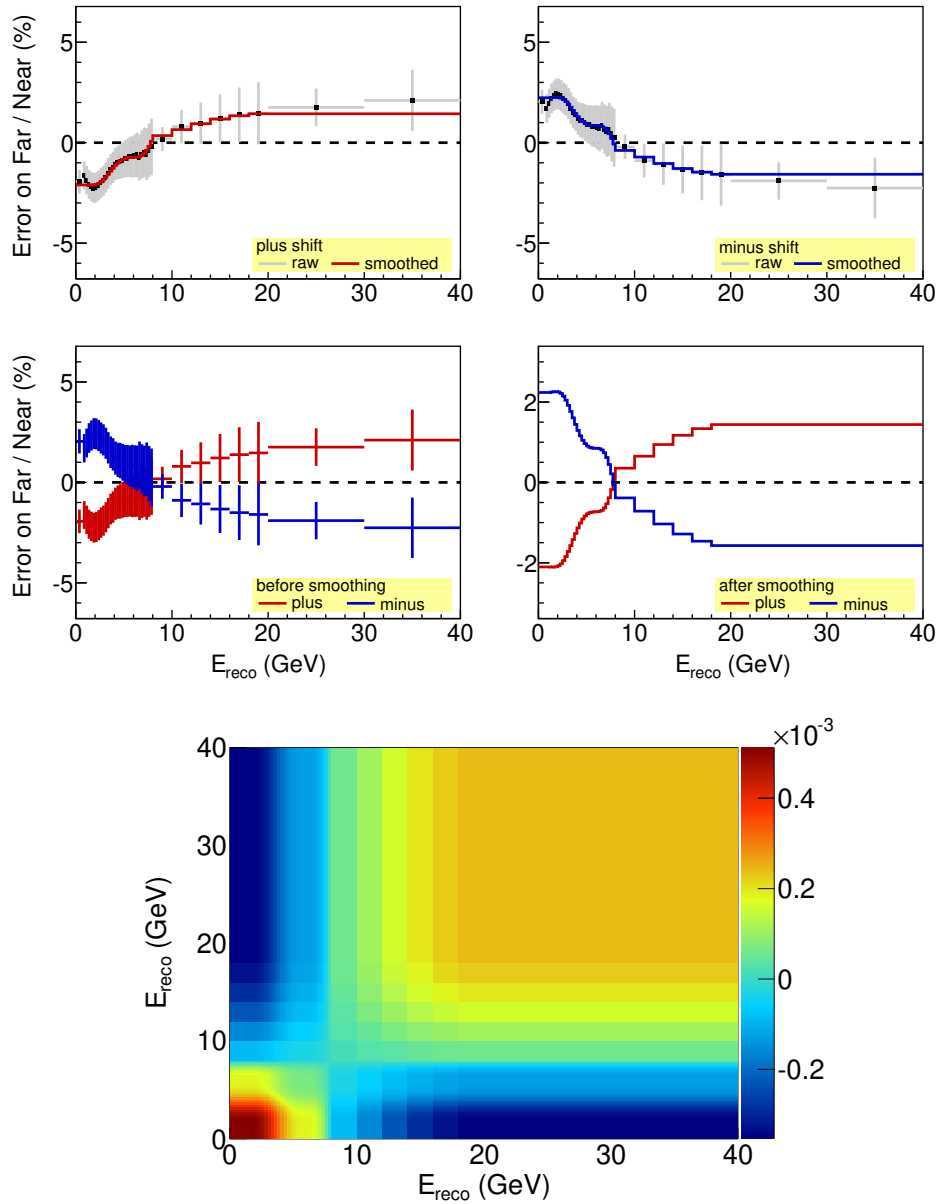


Figure 7.24: CC background systematic error. CC background is scaled by  $\pm 15\%$ . The top four plots are the error bands for the NC sample. The bottom plot is the corresponding covariance matrix.

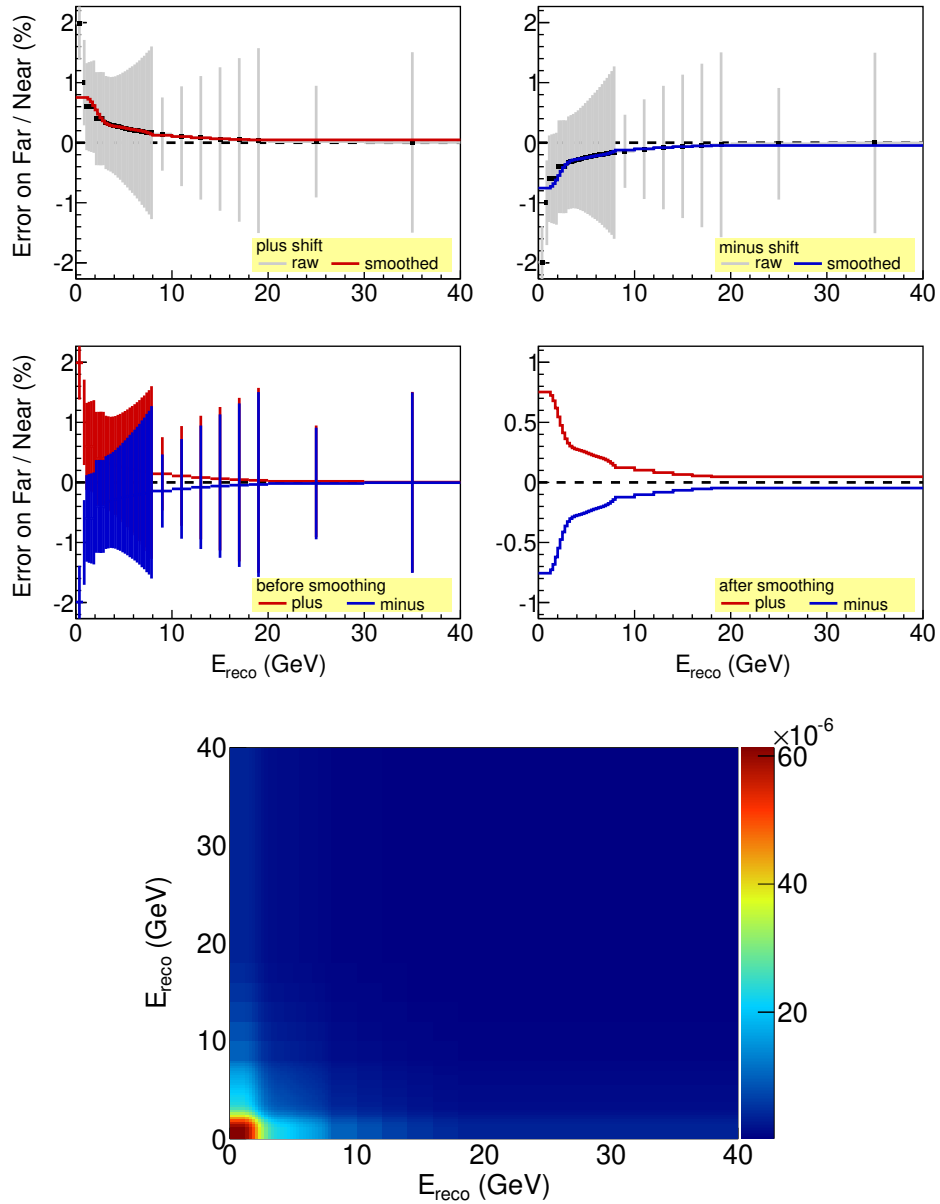


Figure 7.25: FD cleaning systematic error. The event energy is scaled by upto  $\pm 4.9\%$  at low energies [108]. The top four plots are the error bands for the NC sample. The bottom plot is the corresponding covariance matrix.

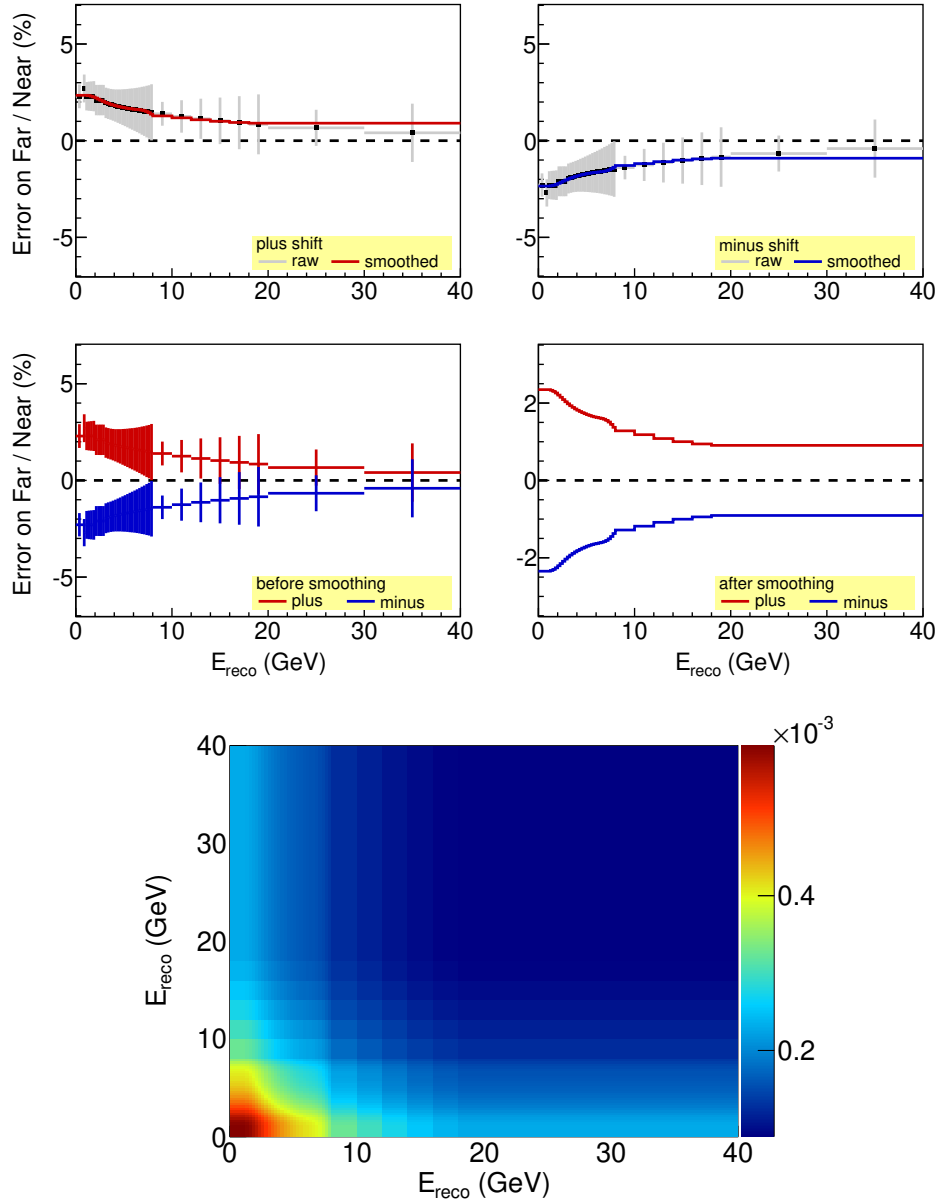


Figure 7.26: FD cosmic removal systematic error. The event energy is scaled by  $\pm 0 - 2.7\%$  depending on the energy [108]. The top four plots are the error bands for the NC sample. The bottom plot is the corresponding covariance matrix.

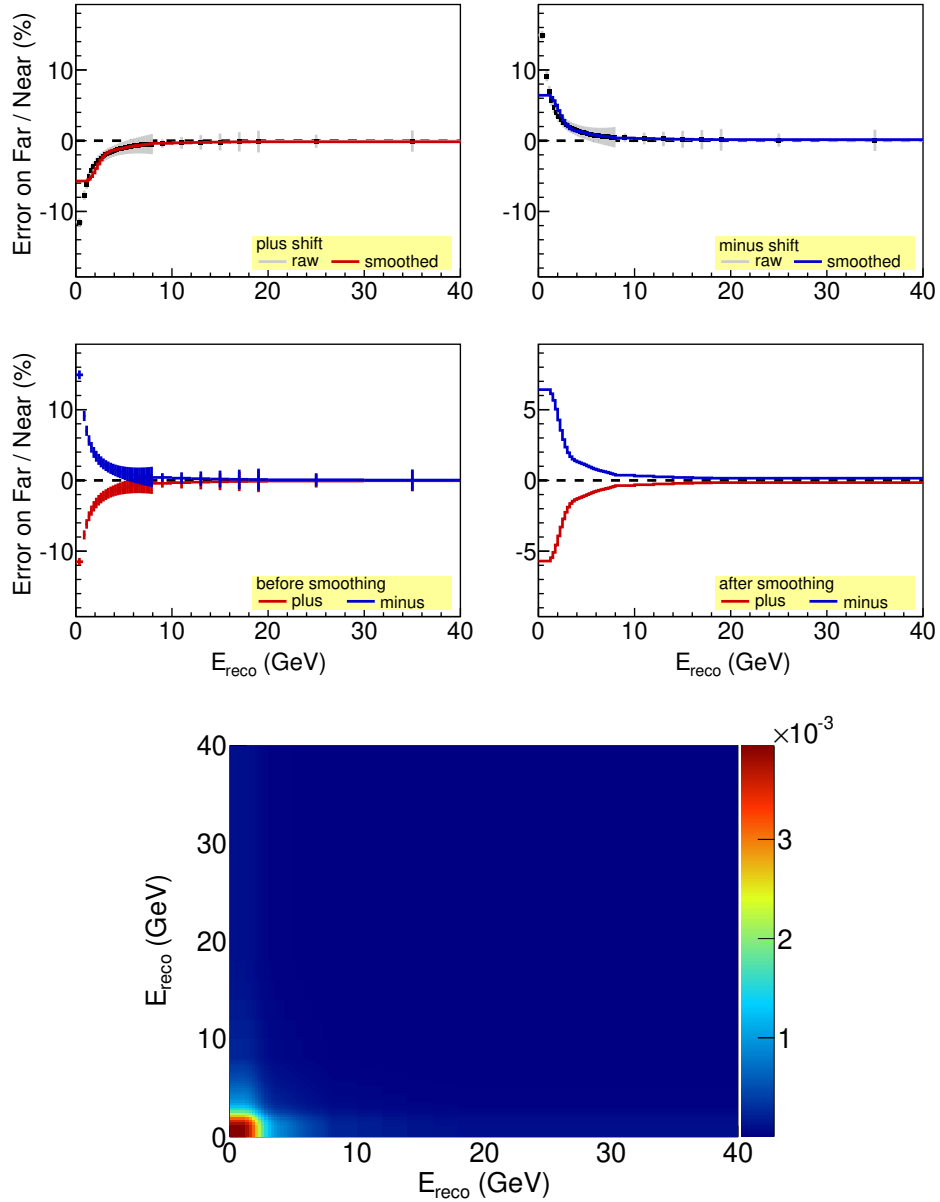


Figure 7.27: ND cleaning systematic error. The event energy is scaled by upto  $\pm 8.2\%$  for MINOS [114] and upto  $\pm 50\%$  for MINOS+ at low energies. The top four plots are the error bands for the NC sample. The bottom plot is the corresponding covariance matrix.

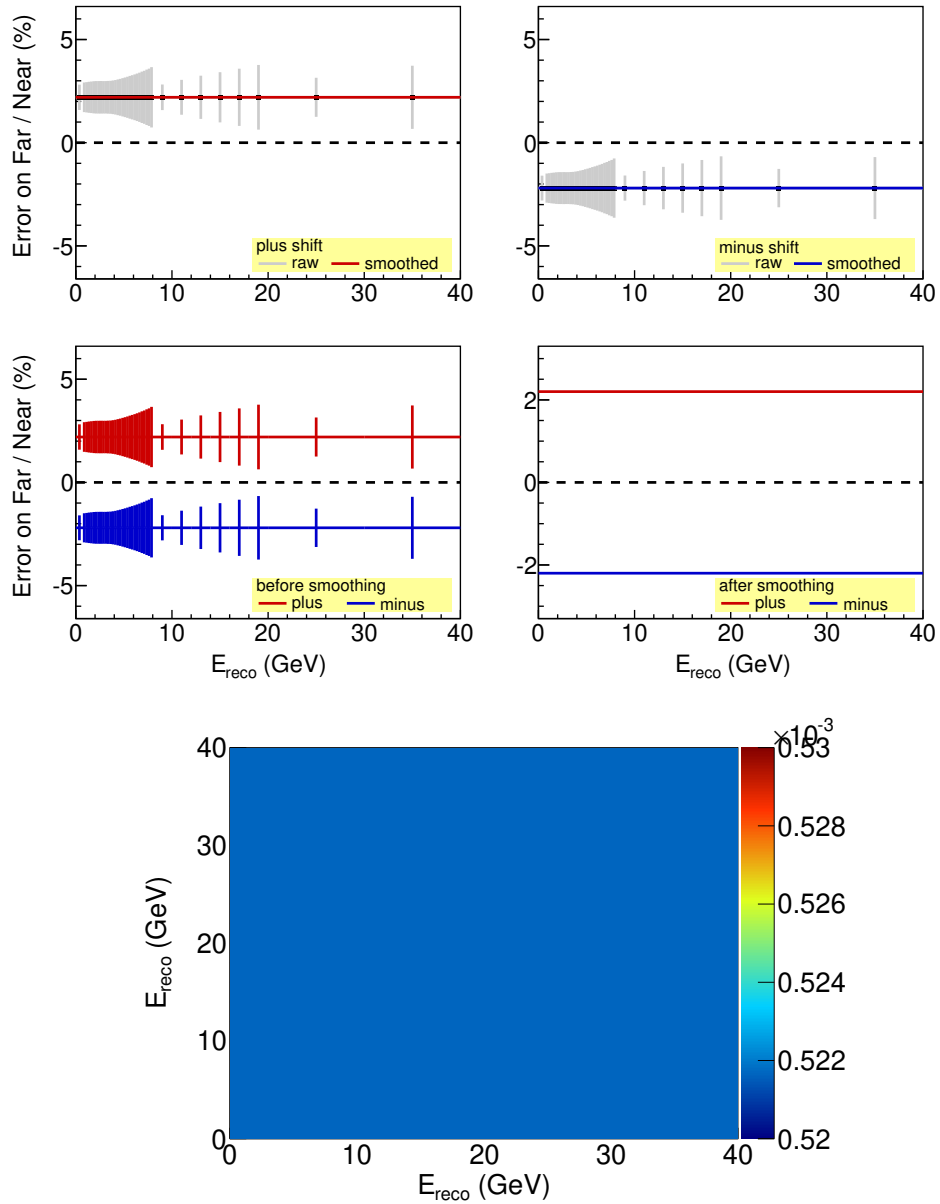


Figure 7.28: Normalization systematic error. The FD energy spectrum is scaled by  $\pm 2.2\%$ . The top four plots are the error bands for the NC sample. The bottom plot is the corresponding covariance matrix.



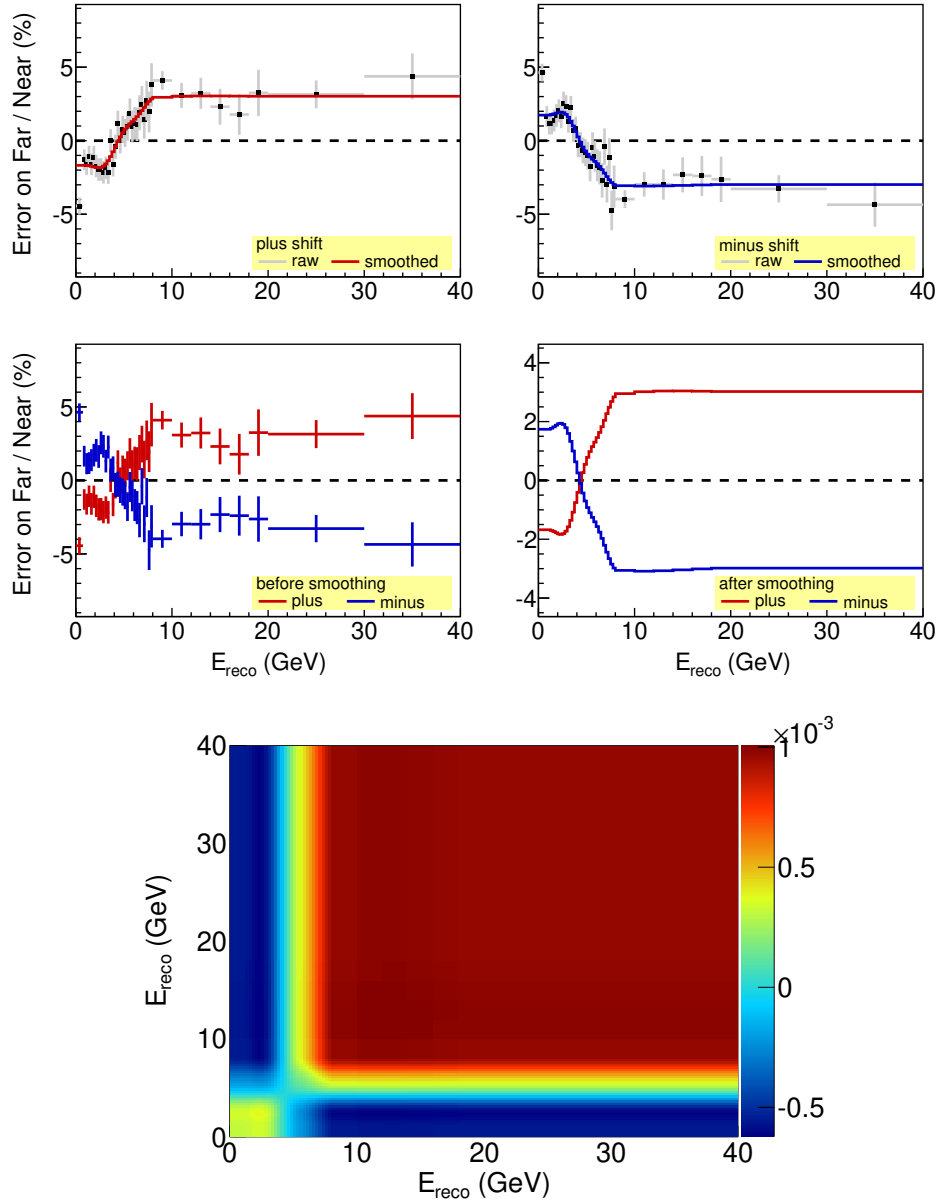


Figure 7.29: Relative hadronic calibration scale systematic error. The FD NC event energy is scaled by  $\pm 2.1\%$ . The top four plots are the error bands for the NC sample. The bottom plot is the corresponding covariance matrix.

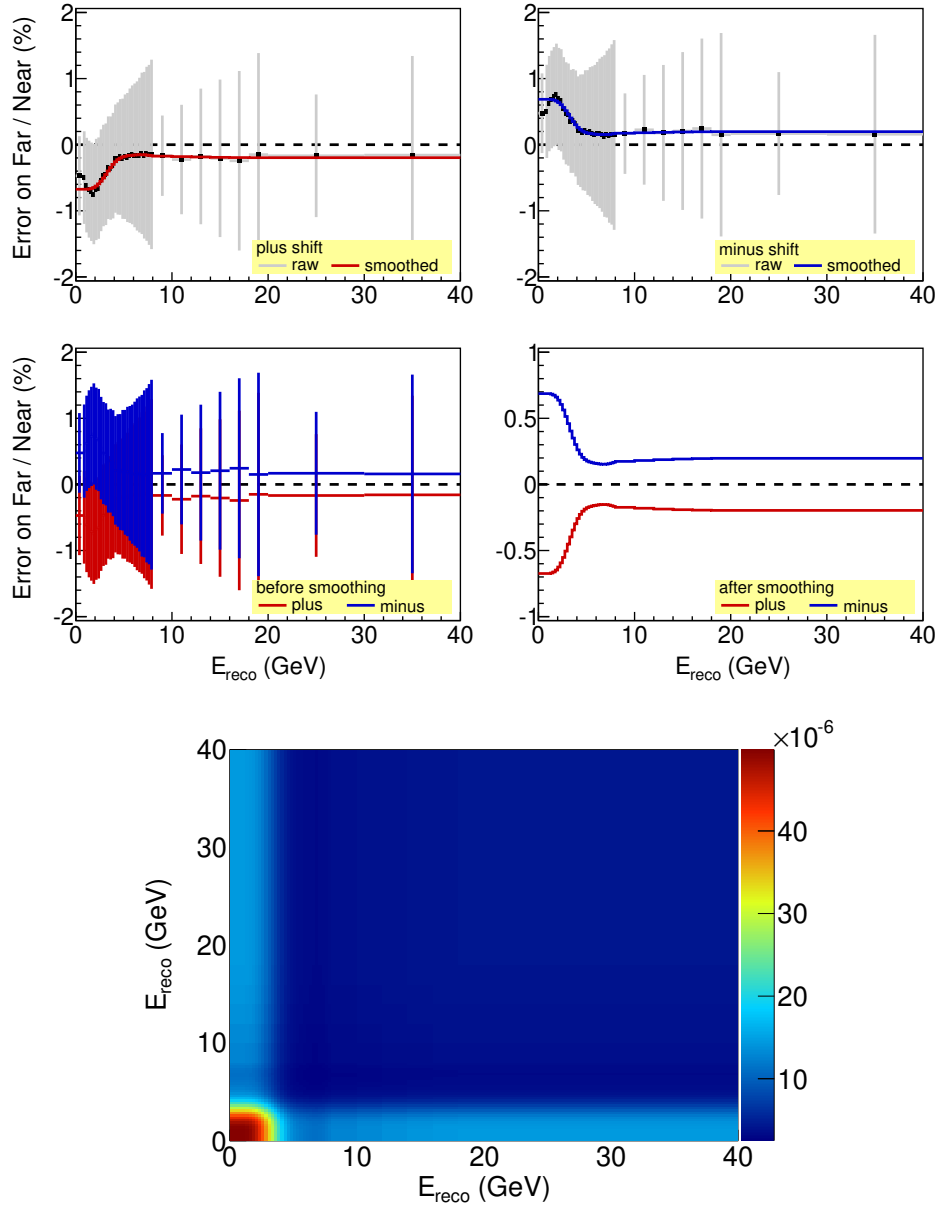


Figure 7.30:  $\nu_\mu$  KNO multiplicity systematic error.  $r_{ij2}$  NEUGEN parameters is shifted by  $\pm 0.1$ . The top four plots are the error bands for the NC sample. The bottom plot is the corresponding covariance matrix.

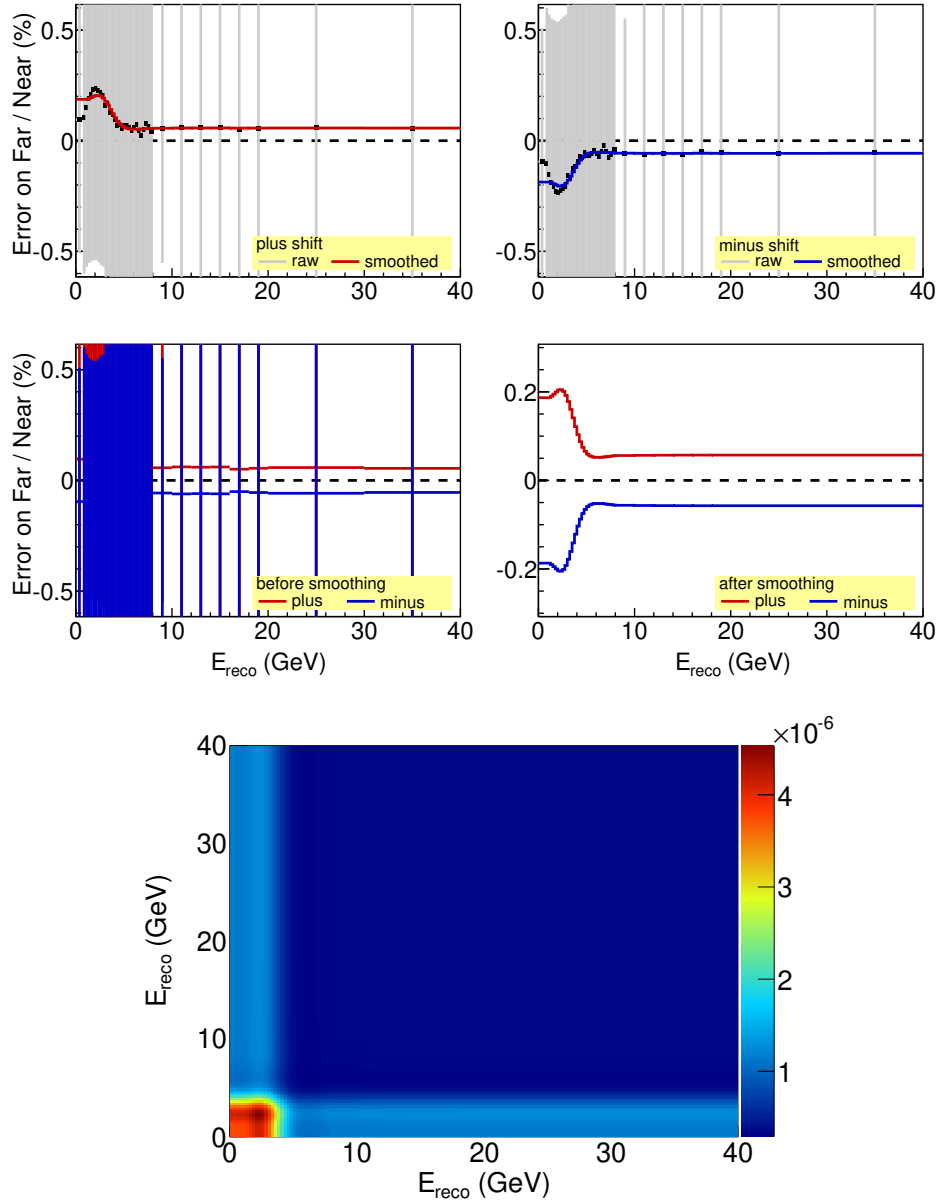


Figure 7.31:  $\nu_\mu$  KNO multiplicity systematic error.  $r_{ij3}$  NEUGEN parameters is shifted by  $\pm 0.2$ . The top four plots are the error bands for the NC sample. The bottom plot is the corresponding covariance matrix.

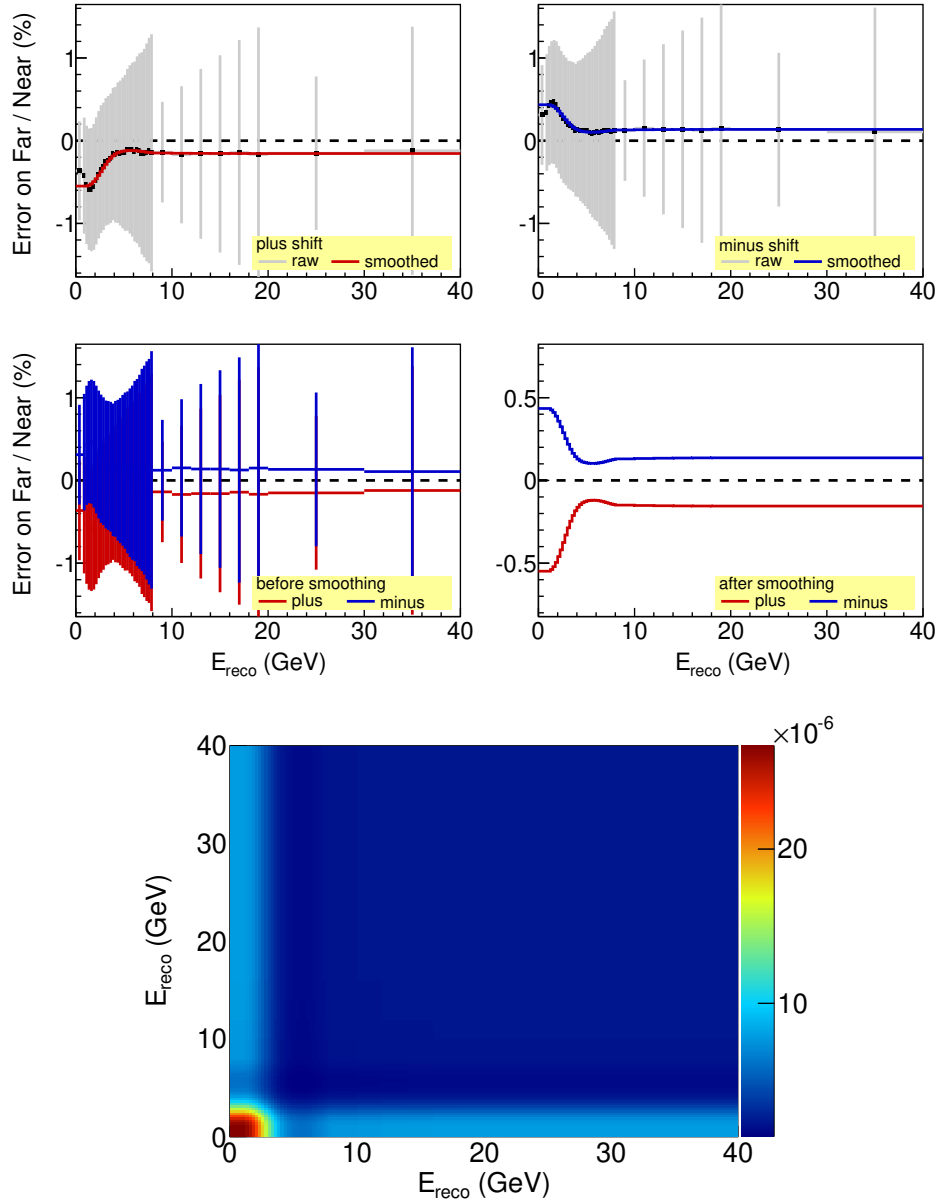


Figure 7.32:  $\nu_\mu$  quasi-elastic cross section systematic error.  $M_A^{QE}$  is scaled by  $\pm 15\%$ . The top four plots are the error bands for the NC sample. The bottom plot is the corresponding covariance matrix.

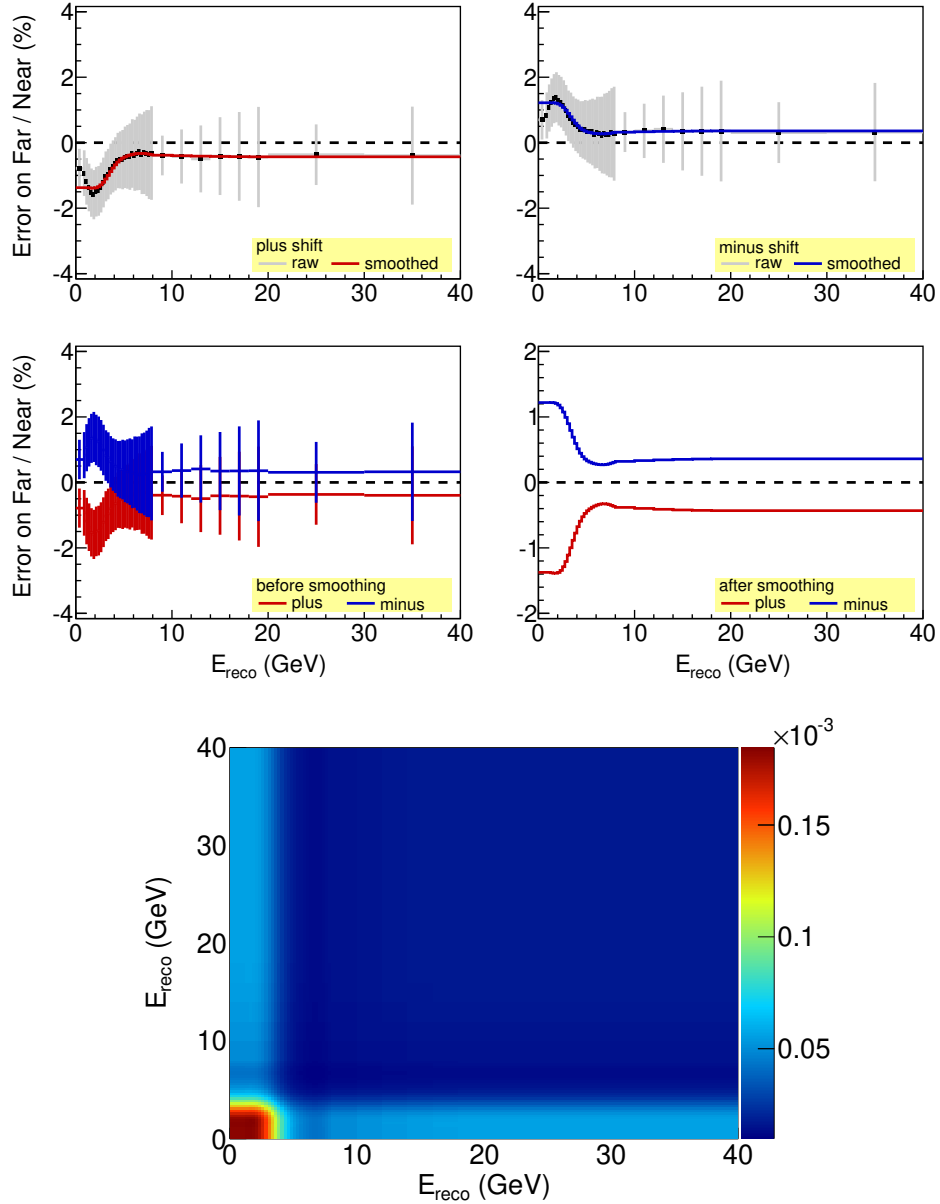


Figure 7.33:  $\nu_\mu$  resonance cross section systematic error.  $M_A^{\text{Res}}$  is scaled by  $\pm 15\%$ . The top four plots are the error bands for the NC sample. The bottom plot is the corresponding covariance matrix.

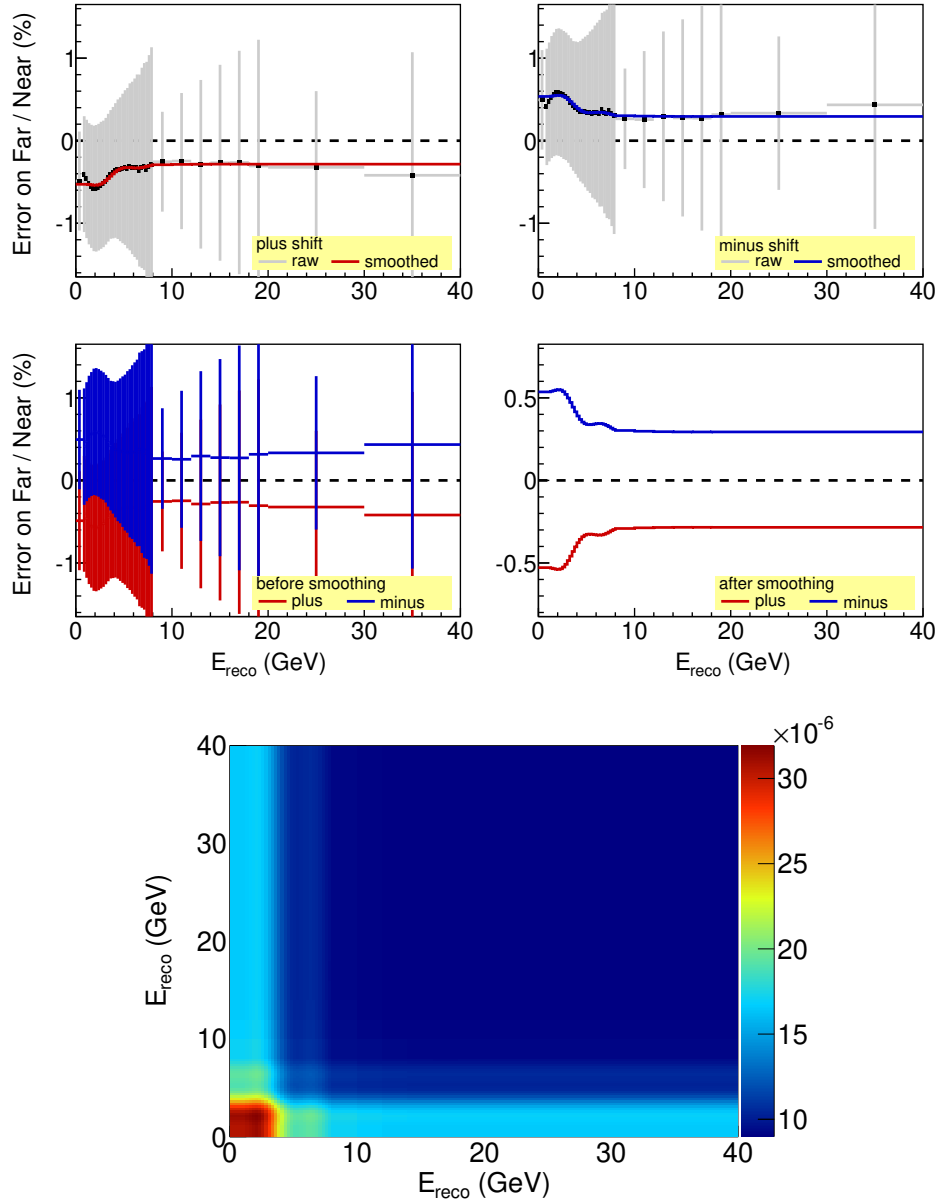


Figure 7.34: Total  $\nu_\mu$  CC cross section systematic error. The total  $\nu_\mu$  CC cross section is scaled by  $\pm 3.5\%$ . The top four plots are the error bands for the NC sample. The bottom plot is the corresponding covariance matrix.

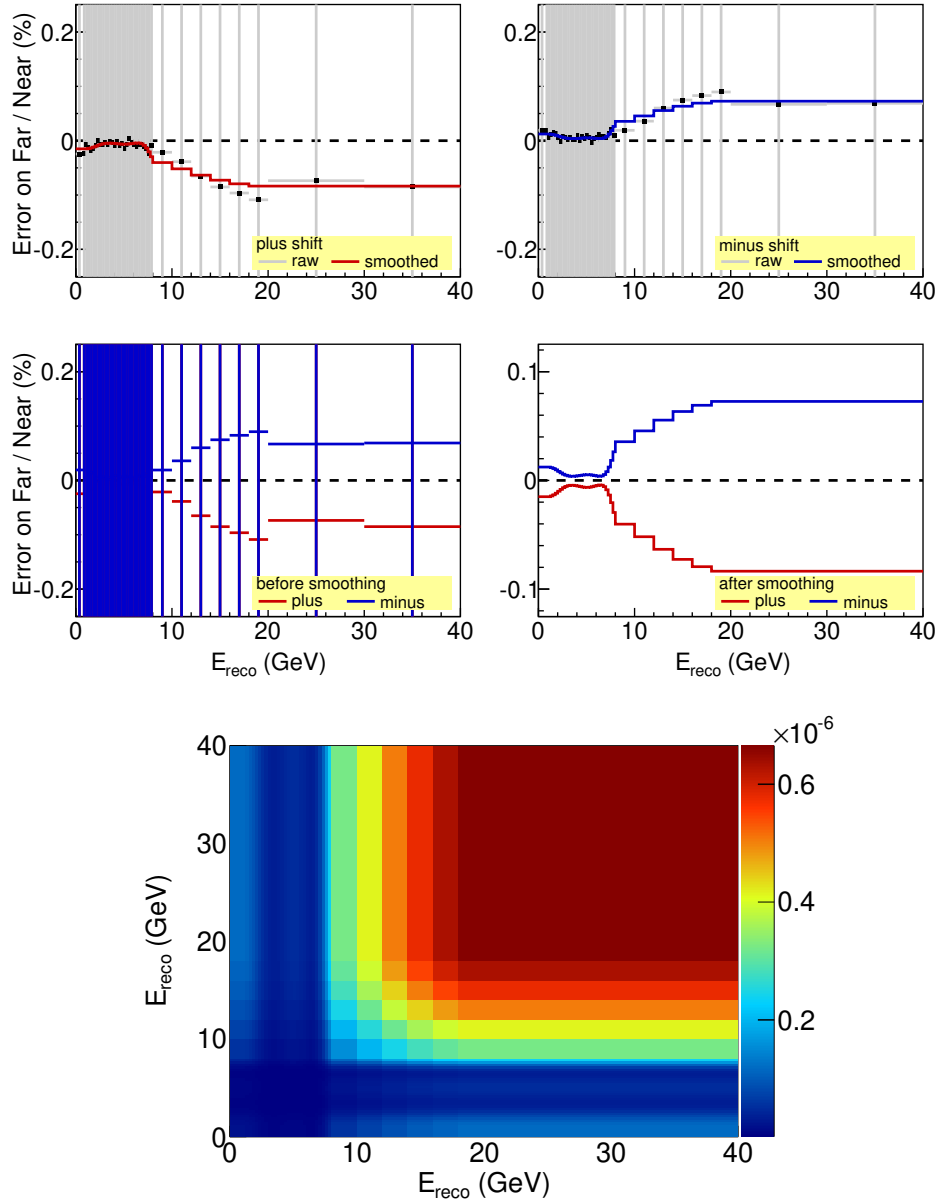


Figure 7.35:  $\bar{\nu}_\mu$  KNO multiplicity systematic error.  $r_{i(3,4)2}$  NEUGEN parameters is shifted by  $\pm 0.2$ . The top four plots are the error bands for the NC sample. The bottom plot is the corresponding covariance matrix.

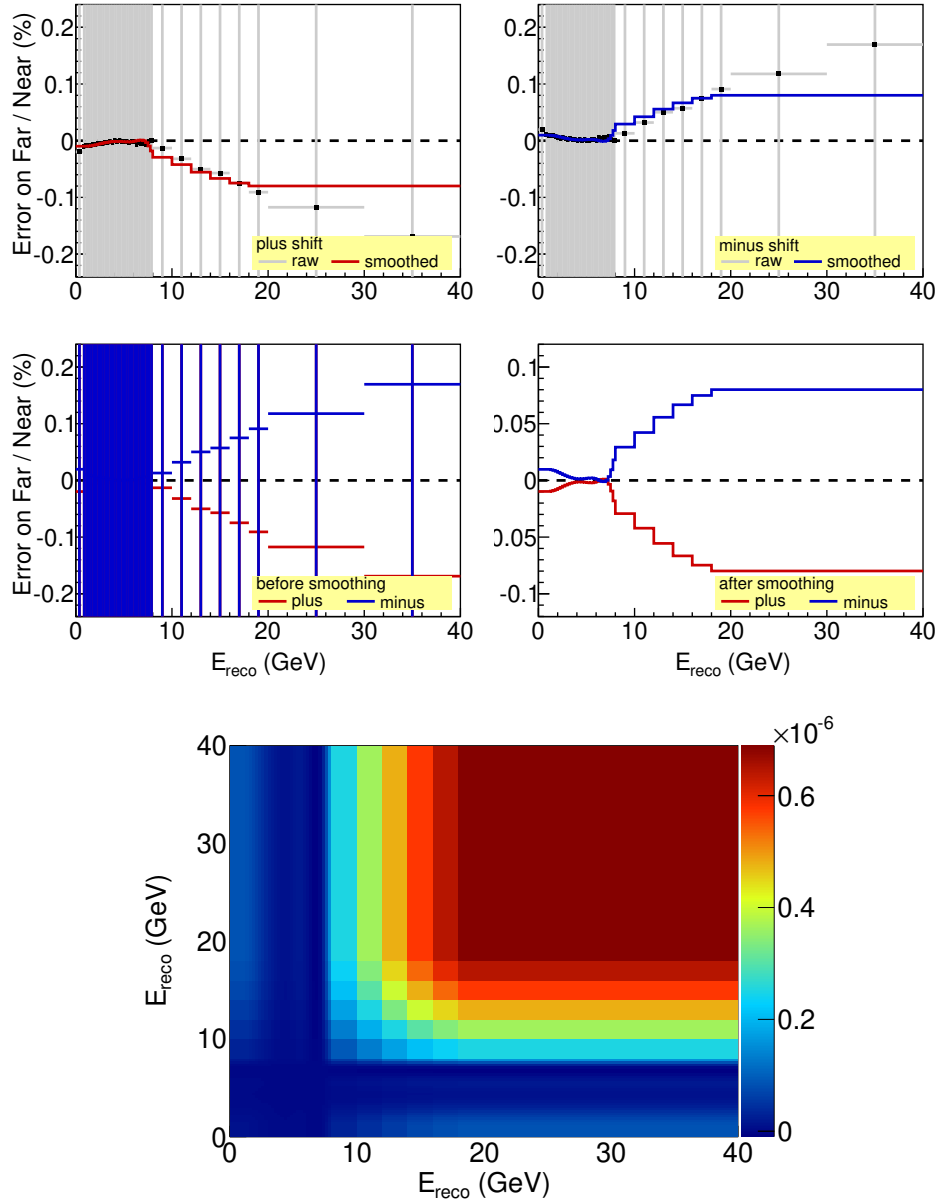


Figure 7.36: Total  $\bar{\nu}_\mu$  CC cross section systematic error. The total  $\bar{\nu}_\mu$  CC cross section is scaled by  $\pm 4\%$ . The top four plots are the error bands for the NC sample. The bottom plot is the corresponding covariance matrix.



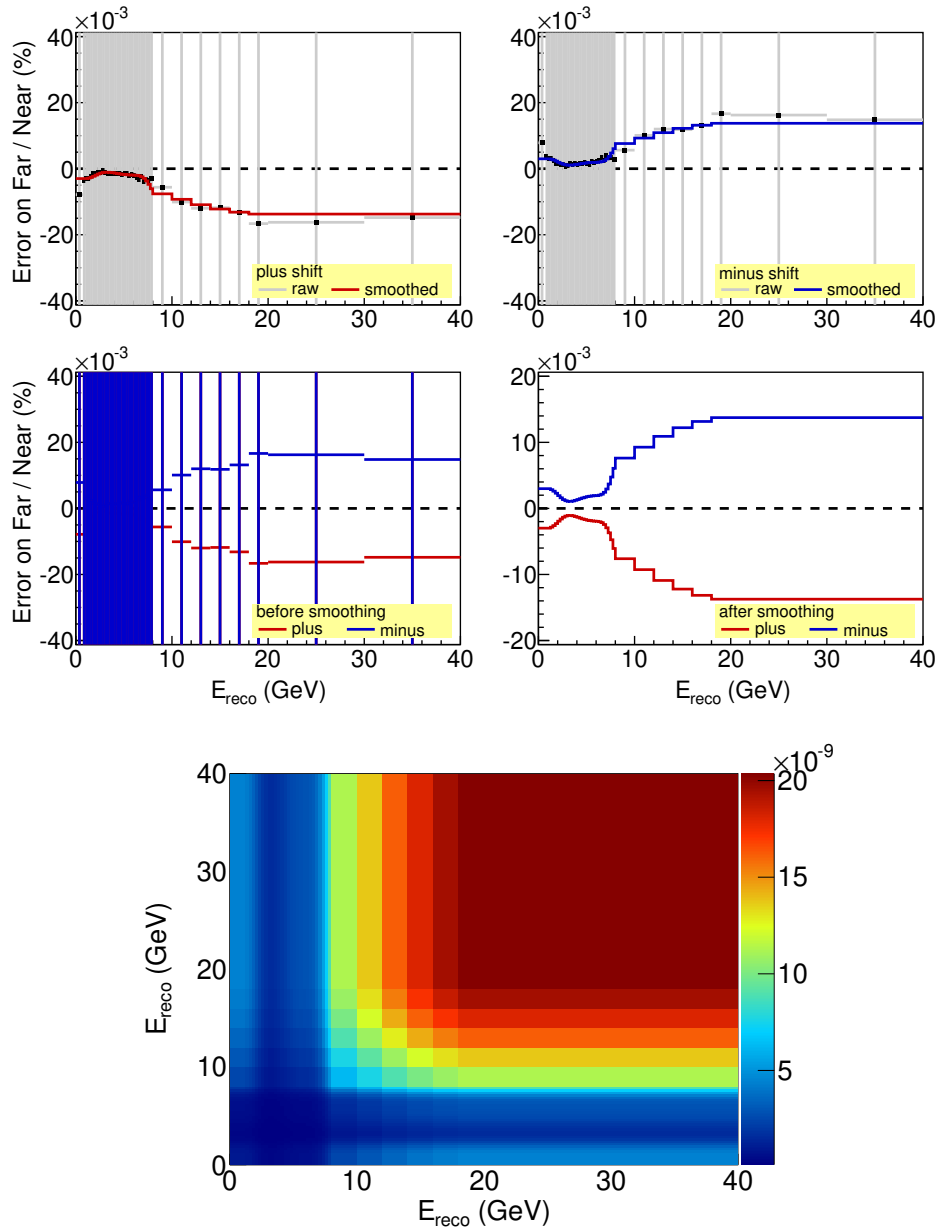


Figure 7.37:  $\bar{\nu}_\mu$  quasi-elastic cross section systematic error.  $\bar{\nu}_\mu$  quasi-elastic cross section is scaled by  $\pm 8\%$ . The top four plots are the error bands for the NC sample. The bottom plot is the corresponding covariance matrix.

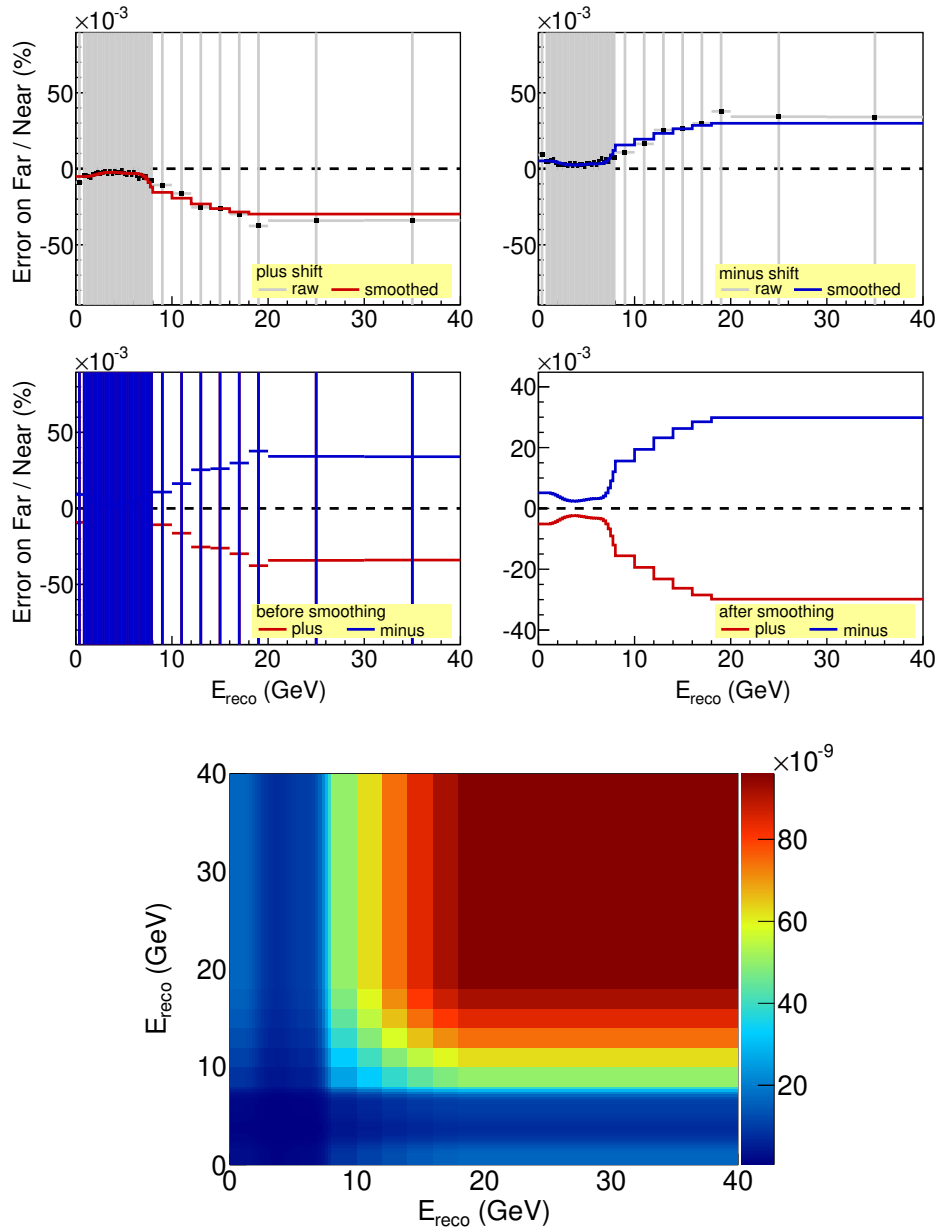


Figure 7.38:  $\bar{\nu}_\mu$  resonance cross section systematic error.  $\bar{\nu}_\mu$  resonance cross section is scaled by  $\pm 8\%$ . The top four plots are the error bands for the NC sample. The bottom plot is the corresponding covariance matrix.

## 7.4 Combined Systematic Errors

In addition to the systematic errors discussed in the previous two sections, the systematic errors coming from the beam should also be considered, including those from hadron production and those from beam optics. The total hadron production uncertainty for MINOS is evaluated in Reference [115] and that for MINOS+ is done by the same authors. The aim is to vary hadron production parameters within reasonable limits, and use the shifted hadron production to create a population of shifted flux histograms from which a covariance matrix is constructed. The covariance matrices for the CC and NC samples are shown in Figure 7.39.

The beam optics systematic errors in MINOS come from the uncertainty in horn current distribution, horn current miscalibration, and the uncertainty in magnetic horn position [80, 116]. For MINOS+, additional factors are included, namely the uncertainties from beam position, beam width, target Z position and material density. The errors in MINOS and MINOS+ are summed together assuming they are not correlated [117]. The covariance matrices for the CC and NC samples are shown in Figure 7.40.

The combined fractional errors on the far-over-near ratios are shown in Figure 7.41 where the error in each bin is the square root of the diagonal elements of the combined covariance matrices.

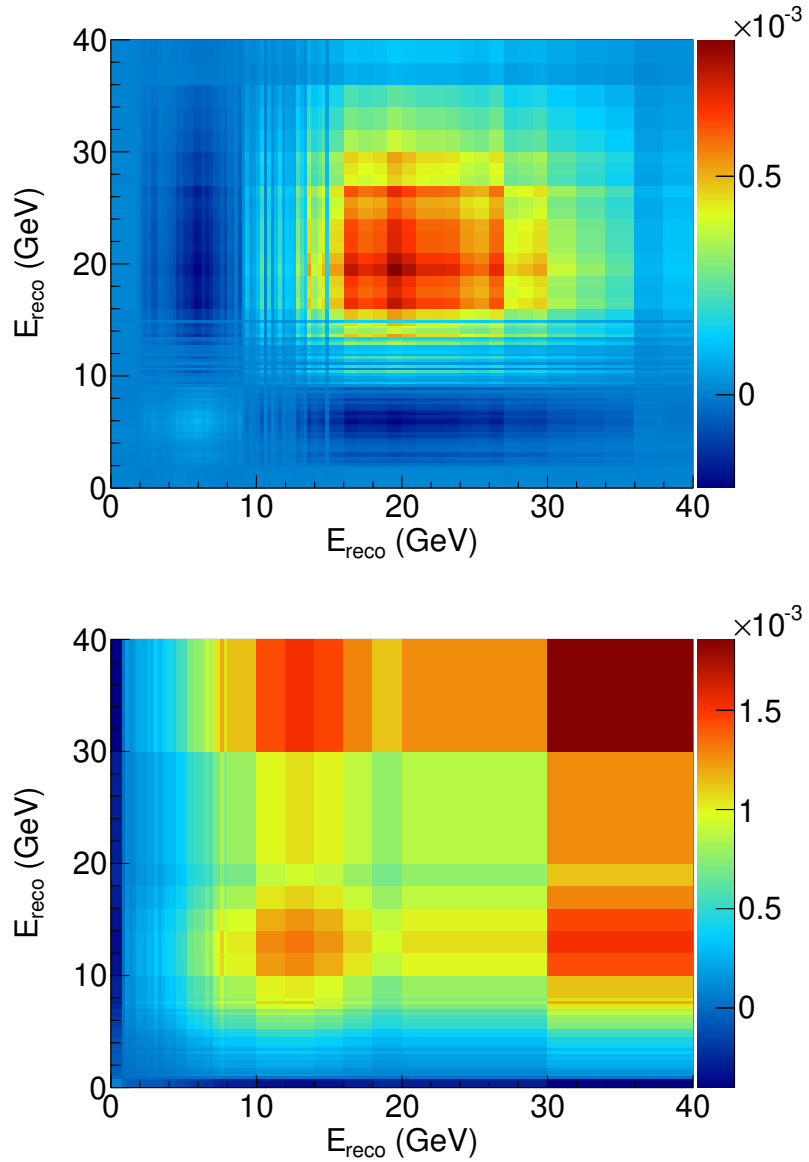


Figure 7.39: Covariance matrix from hadron production uncertainty for the CC sample (top) and the NC sample (bottom). This is calculated by the authors of [115].

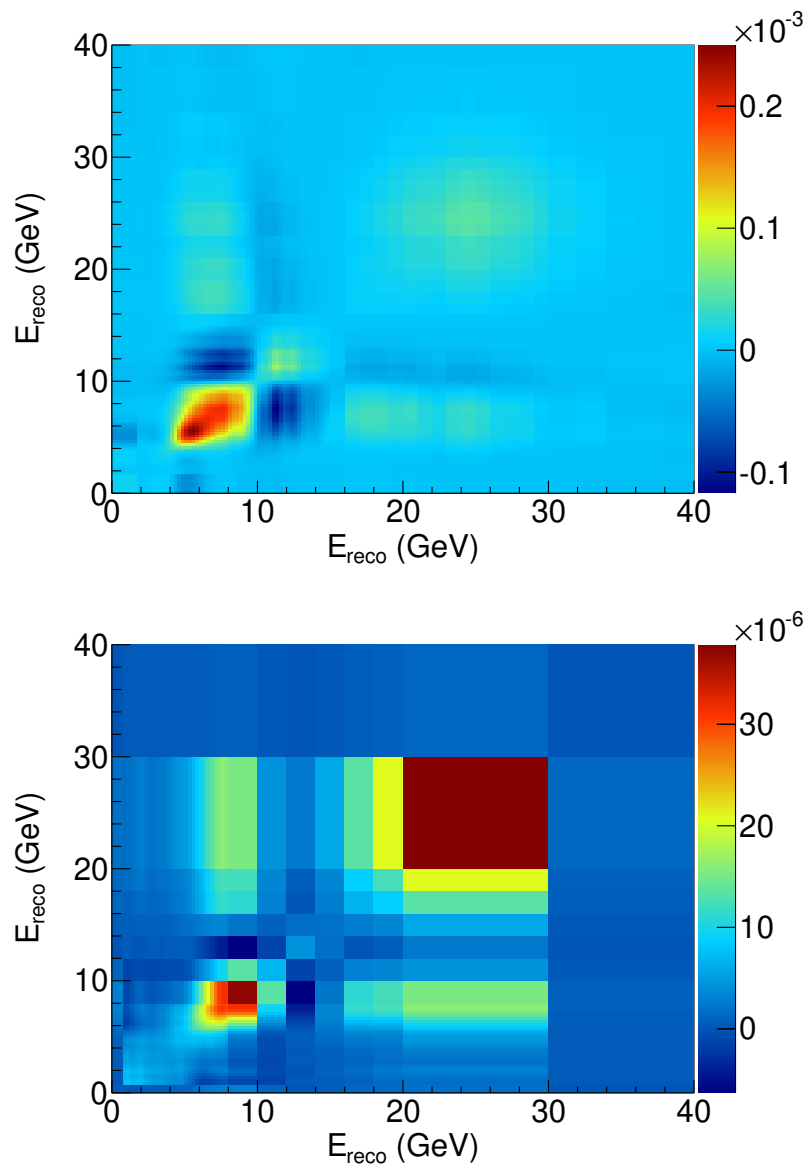


Figure 7.40: Covariance matrix from beam optics uncertainty for the CC sample (top) and NC sample (bottom).

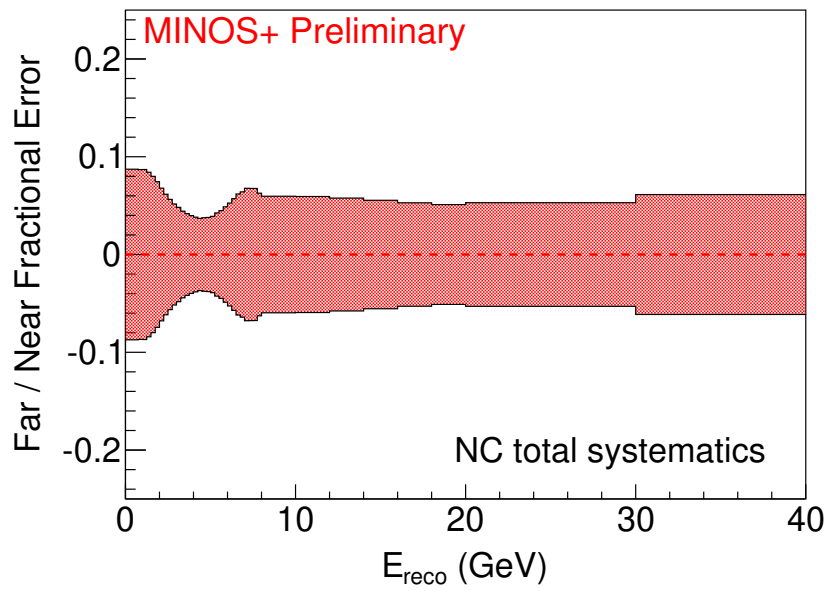
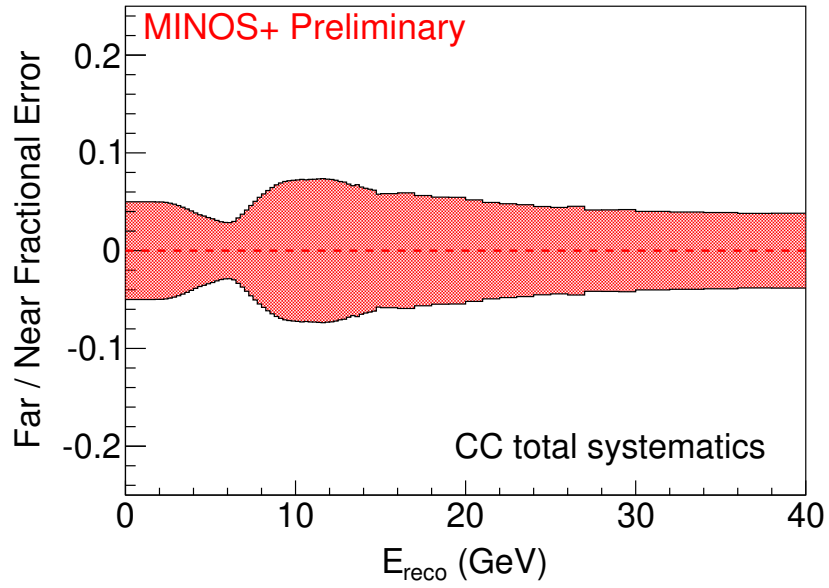


Figure 7.41: Total fractional errors on the far-over-near ratio for the CC (top) and the NC (bottom) samples.

## Chapter 8

### The 3+1 Sterile Neutrino Analysis

This chapter presents the analysis of the 3+1 sterile neutrino model based on the full  $10.56 \times 10^{20}$  POT  $\nu_\mu$  running data of MINOS and  $2.99 \times 10^{20}$  POT  $\nu_\mu$  running data of MINOS+. Given the far-over-near ratio, the expression of  $\chi^2$  and the binning scheme in the first section, the  $\chi^2$  surfaces of sensitivity and data are shown along with the effect of individual systematic uncertainty described in Chapter 7. The Feldman-Cousins procedure is introduced and the corrected 90% C.L. contour is given as the final result of this analysis. Discussions are made on the best fit point in the final section.

#### 8.1 Strategy

The basic idea is to fit to the ratio of the FD spectrum over the ND spectrum, i.e. far-over-near ratio, with a covariance-matrix-based  $\chi^2$ . In order to make model predictions, oscillations are applied to the reconstructed true energy conversion matrices. To combine MINOS and MINOS+ data, the spectra are simply added together. The NC and CC samples are fitted simultaneously, i.e. the total  $\chi^2$  is the sum of the  $\chi^2$ s of the two samples.

### 8.1.1 Far-over-near Ratio

The fit is performed on the far-over-near ratio as shown in Figure 8.1 where the energy window is set to 0-40 GeV. The method was first adopted in the 2014 sterile analysis [118]. In previous MINOS sterile analyses, the fitting was performed on the FD spectrum only and the model prediction was then made based on the ND data [107] assuming that there is no oscillations happening at ND. The beam simulation is tuned so that the MC and data spectra match at ND. In the new far-over-near fit approach, the most important improvement is that the parameter space with ND oscillations is also covered. This especially concerns the space with large  $\Delta m_{41}^2$  and large  $\theta_{24}$  (e.g. see Figure 5.19). Since the tuning of the beam simulation is no longer valid in the presence of the ND oscillations, the untuned beam simulation is taken as the nominal in this analysis. When taking the far-over-near ratio, the beam systematics are largely canceled out.

### 8.1.2 Expression of $\chi^2$

The  $\chi^2$  to be minimized in the fit takes the form

$$\chi^2 = \Delta C^{-1} \Delta + \left( \frac{N_{data} - N_{MC}}{\sigma_N} \right)^2 + \frac{(|\Delta m_{32}^2| - \Delta m^2)^2}{\sigma_{\Delta m^2}^2}. \quad (8.1)$$

The first term makes use of the shape information in the ND and FD energy spectra.  $\Delta \equiv (far/near)_{MC} - (far/near)_{data}$  is a vector with each element corresponding to a reconstructed energy bin.  $C$  is the sum of covariance ma-



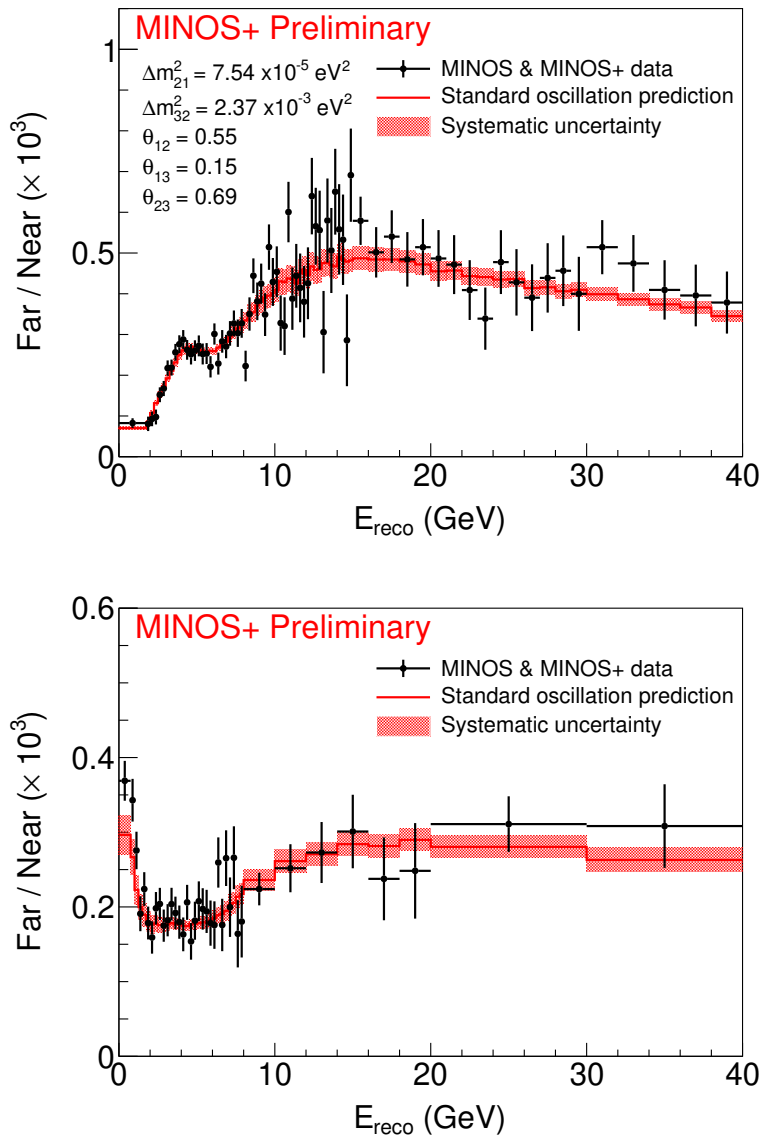


Figure 8.1: Far-over-near ratios for the CC sample (top) and the NC sample (bottom) using the combined data of MINOS and MINOS+. The error bars represent the statistical uncertainty. The standard oscillation predictions are shown as the red histograms along with the systematic uncertainty.

trices

$$C = C^{stat} + \sum_i C_i^{syst}, \quad (8.2)$$

where  $C^{stat}$  is the statistical covariance matrix and  $C_i^{syst}$  is the covariance matrix for systematics  $i$  discussed in Chapter 7. Given that there is no correlation in statistical fluctuation among different energy bins, the  $C^{stat}$  takes the form of a diagonal matrix

$$C^{stat} = \begin{pmatrix} \sigma_1^2 & & & \\ & \sigma_2^2 & & \\ & & \ddots & \\ & & & \sigma_N^2 \end{pmatrix} \quad (8.3)$$

where  $\sigma_i$  is the square root of the number of events in bin  $i$  following the Poisson distribution, and  $N$  is the total number of energy bins.

The second term in Equation 8.1 provides a constraint based on the absolute neutrino beam flux.  $N_{MC}$  and  $N_{data}$  represent the number of MC and data events at ND, respectively. The flux uncertainty  $\sigma_N$  is not precisely known, and  $\sigma_N = 50\%N_{MC}$  is adopted as the typical agreement between hadron production measurements and MC calculations [119].

The last term in Equation 8.1 provides a weak constraint on  $\Delta m_{32}^2$  to keep its value centered around the standard oscillation result in the fit. This is based on the idea of treating the four-flavor oscillation as the perturbation of the standard three-flavor oscillation which can already describe the MINOS data well. The center value  $\Delta m^2 = 2.5 \times 10^{-3} \text{ eV}^2$  is adopted from Daya Bay

three-flavor analysis [120], and  $\sigma_{\Delta m^2} = 0.5 \text{ eV}^2$  is roughly  $2\times$  the uncertainty in the Daya Bay result.

It is worth mentioning that there are two main techniques commonly used in performing the fit with correlated systematics. One is the covariance matrix method as described above. The other is the nuisance parameters method, where each systematic error is assigned with a free floating nuisance parameter playing the same role as the physics model parameters. Assuming Gaussian fluctuations, the two methods are equivalent as demonstrated in Appendix E.

### 8.1.3 Binning Scheme

Covariance matrix approach essentially uses the multivariate Gaussian, which assumes that the statistical and systematics fluctuation follows Gaussian distributions. The binning schemes are chosen such that the minimum number of events in a bin is about 20 for a good Gaussian approximation. The binning scheme for NC and CC are shown in Figure 8.2.

## 8.2 Performing the Fit

The Minuit package [121] is used to minimize the  $\chi^2$  defined in Equation 8.1. To map out the  $\chi^2$  surface in the  $\Delta m_{41}^2 - \theta_{24}$  plane, for each grid point with a fixed pair of  $\Delta m_{41}^2$  and  $\theta_{24}$ ,  $\theta_{23} \in [0, \pi/2]$ ,  $\theta_{34} \in [0, \pi/2]$ , and  $\Delta m_{32}^2$  are set free in the fit. Two initial values of  $\theta_{23}$  for the two octants, and two initial values of  $\Delta m^2$  for the two possible mass hierarchies, are attempted in

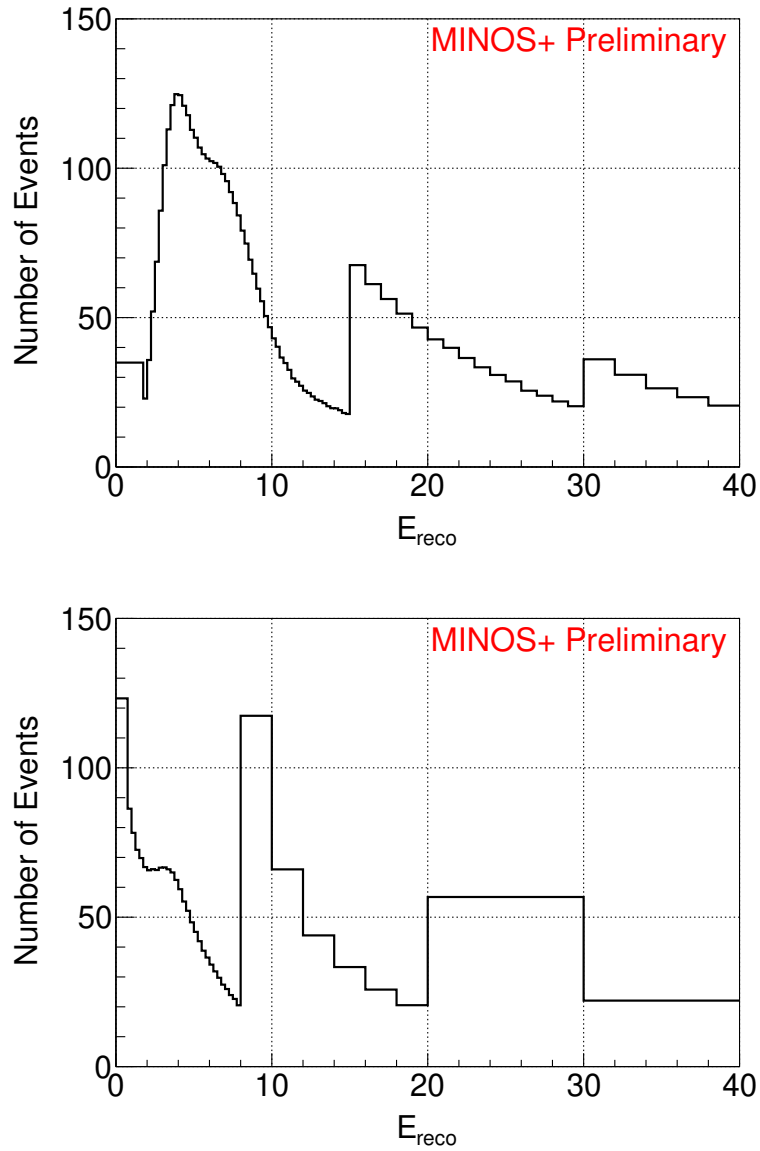


Figure 8.2: Simulated FD spectra with the binning scheme defined for the fitting. There are 74 bins for the CC sample (top), and 38 bins for the NC sample (bottom).

Parameter	Fixed value
$\Delta m_{21}^2$	$7.54 \times 10^{-5} \text{ eV}^2$
$\theta_{12}$	0.554
$\theta_{13}$	0.149
$\theta_{14}$	0
$\delta_{13}$	0
$\delta_{14}$	0
$\delta_{24}$	0

Table 8.1: Fixed parameters used in the 3+1 model fit.

the fit.

The fixed parameters in the fit are listed in Table 8.1. Of those,  $\Delta m_{21}^2$ ,  $\theta_{12}$ ,  $\theta_{13}$  and  $\theta_{14}$  are precisely constrained by other experiments.  $\delta_{13}$  and  $\delta_{14}$  do not affect the oscillation probabilities.  $\delta_{24}$  does have effect on  $P(\nu_\mu \rightarrow \nu_s)$  as shown in Figure 2.9. However, to reduce the complexity of the fit, this analysis is limited to the case of  $\delta_{24} = 0$ .

### 8.2.1 $\chi^2$ Surface

The  $\chi^2$  surface in  $\Delta m_{41}^2 - \theta_{24}$  plane based on data is shown in Figure 8.3. The corresponding sensitivity surface is shown in Figure 8.4 for which the fake data is generated assuming three-flavor oscillations. Assuming a Gaussian probability density function, 90% C.L. contour is drawn at  $\Delta\chi^2 = \chi^2 - \chi_{best}^2 = 4.61$ , where  $\chi_{best}^2$  is the  $\chi^2$  at the best fit point. A comparison between the sensitivity and the data contours is shown in Figure 8.5. The data contour will be further corrected through the Feldman-Cousins procedure in the next section.

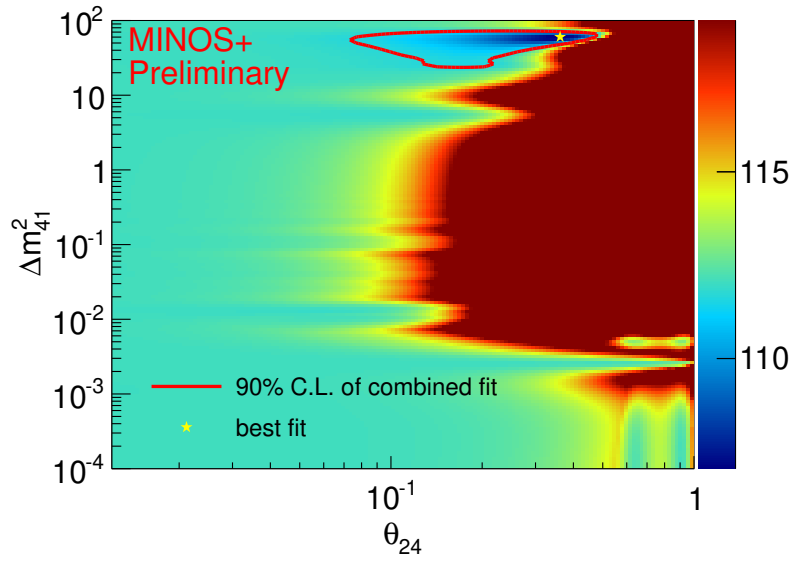


Figure 8.3:  $\chi^2$  surface based on data.

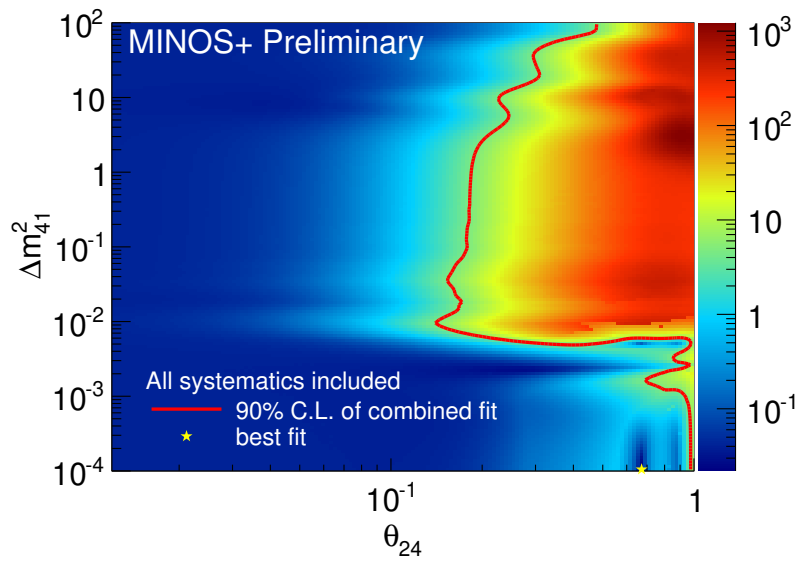


Figure 8.4:  $\chi^2$  surface based on the fake data assuming three-flavor oscillations.

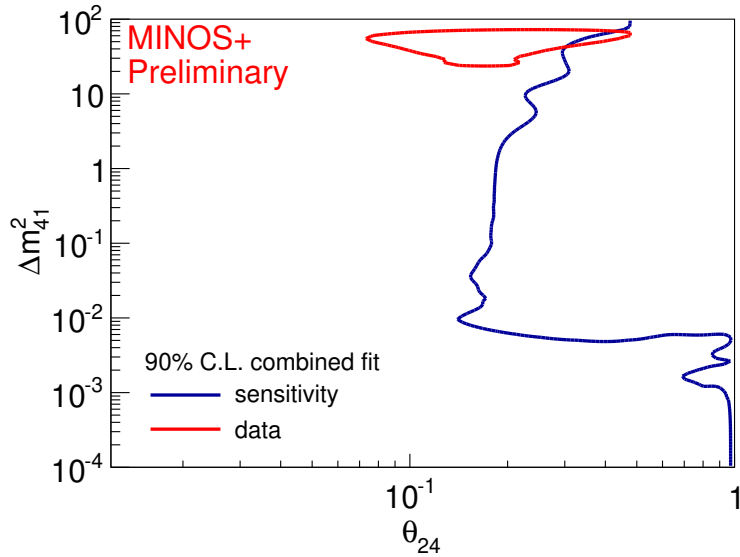


Figure 8.5: A comparison between the data contour and the sensitivity contour.

Common to both Figure 8.3 and Figure 8.4, there are three regions with low  $\chi^2$  in the bottom right of the plots. They roughly correspond three different values of  $\Delta m_{41}^2$ . The explanation goes back to Equation 2.1 as discussed in Reference [122]:

1.  $\Delta m_{41}^2 = \Delta m_{31}^2$ . In this case,  $\Delta_{41} = \Delta_{31}$  and  $\Delta_{43} = 0$ . Equation 2.1 simplifies to  $P(\nu_\mu \rightarrow \nu_\mu) = 1 - (A_{31} + A_{41}) \sin^2(\Delta_{31}/2)$ . For a given  $\theta_{24}$ , the fitter will find values of  $\theta_{23}$  such that  $(A_{31} + A_{41})$  is the same with that of the three-flavor oscillation case leading to a small  $\chi^2$ .
2.  $\Delta m_{41}^2 = 2\Delta m_{31}^2$ . In this case,  $\Delta_{43} = \Delta_{31}$ . Equation 2.1 becomes  $P(\nu_\mu \rightarrow \nu_\mu) = 1 - (A_{31} + A_{43}) \sin^2(\Delta_{31}/2) - A_{41} \sin^2(\Delta_{31})$ . For a given  $\theta_{24}$ , the

fitter will find values of  $\theta_{23}$  such that the probability is the same with that of the three oscillation case.

3.  $\Delta m_{41}^2 \ll \Delta m_{31}^2$ . In this case,  $\Delta_{43} = \Delta_{31}$  and  $\Delta_{41} = 0$ , Equation 2.1 reduces to  $P(\nu_\mu \rightarrow \nu_\mu) = 1 - (A_{31} + A_{43}) \sin^2(\Delta_{31}/2)$ . For a given  $\theta_{24}$ , the fitter will find values of  $\theta_{23}$  such that  $A_{31} + A_{43}$  has the same value with that of the three oscillation case.

### 8.2.2 Effect of the Systematics

To show the effect of the systematics, a comparison of the sensitivity contours made with and without the systematics covariance matrices is shown in the top plot of Figure 8.6. The individual effect of the systematics is presented in two ways. In one way, the systematic covariance matrices are added one by one showing the cumulative effects on the sensitivity as shown in the bottom plot of Figure 8.6. Alternatively, only one systematic covariance matrix is used at a time and the result is shown in Figure 9.10.

### 8.3 Feldman-Cousins Correction

The 90% C.L. contour shown in Figure 8.3 is drawn at  $\Delta\chi^2 = 4.61$  based on the assumption that measurements follow a Gaussian distribution around the true value. However, if one takes a brute force approach, as suggested by Gary Feldman and Robert Cousins in Reference [123],  $\Delta\chi^2 = 4.61$  may not be the correct value to use. As an example, Figure 8.8 shows the  $\Delta\chi^2$  distribution from 1000 fake experiments generated at  $\theta_{24} = 0.2$  and  $\Delta m_{41}^2 =$



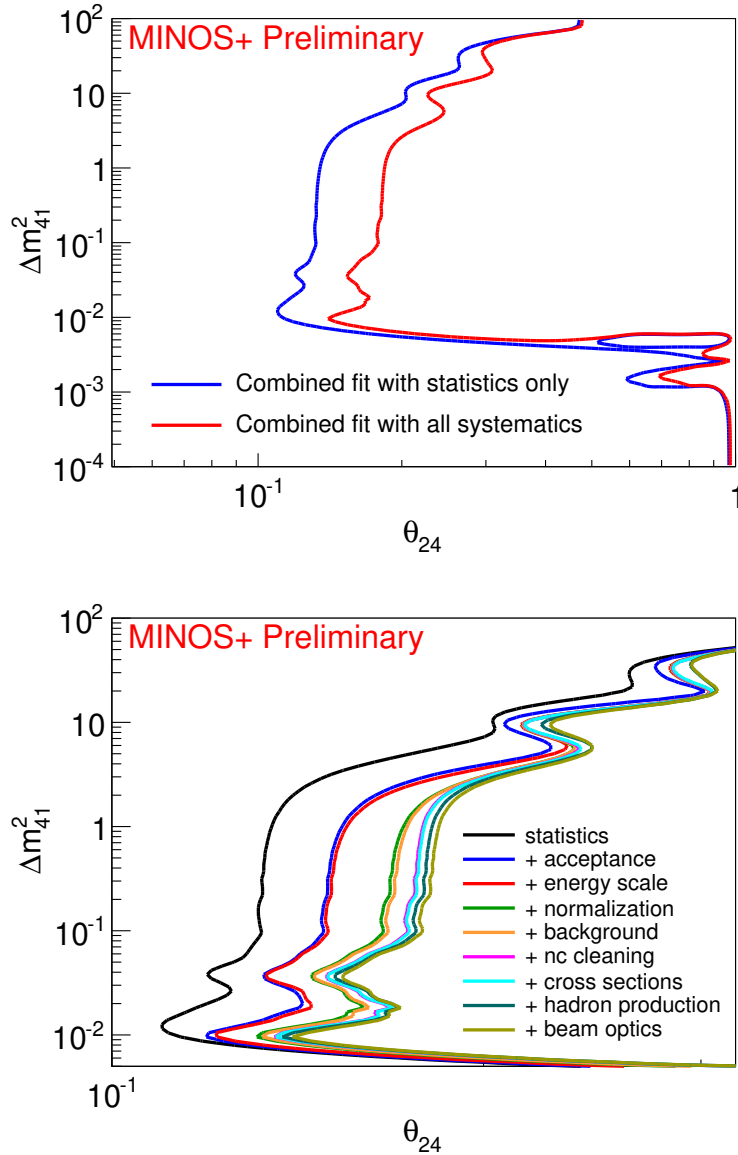


Figure 8.6: Top: 90% C.L. sensitivity contours with and without systematics included. Bottom: Cumulative effect of the systematics on the 90% C.L. sensitivity contour. The systematics covariance matrices are added individually for each contour.

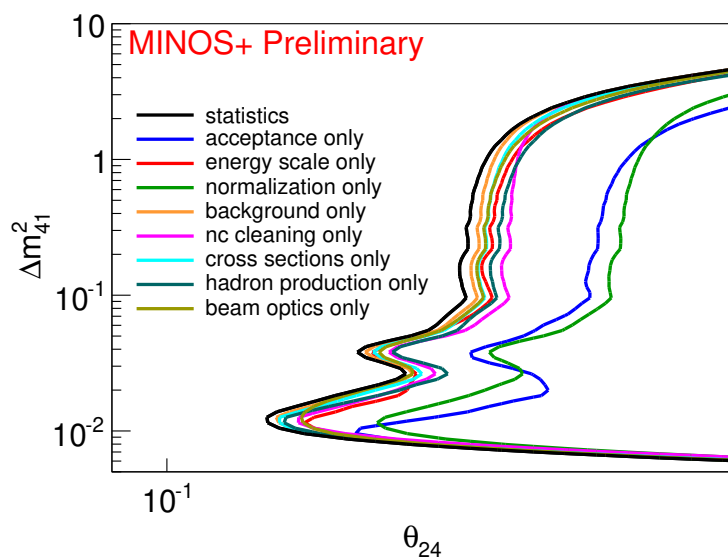
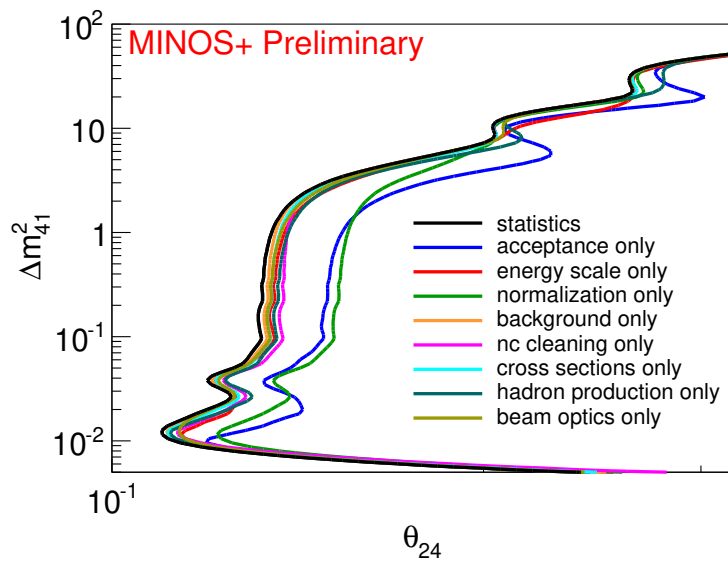


Figure 8.7: Individual effect of systematics on the 90% C.L. sensitivity contour. The bottom plot is a scaled version of the top plot.

20 eV<sup>2</sup> using Gaussian statistical and systematic fluctuations (see Figure 8.9 for an illustration of the fluctuated fake data). 90% of the fake experiments give  $\Delta\chi^2 < 5.78$ , indicating that  $\Delta\chi^2 = 4.61$  should be replaced by  $\Delta\chi^2 = 5.78$  for 90% C.L. at that grid point. There are many factors responsible for this difference, as discussed in Reference [123]. For example, given the sinusoidal nature of the oscillation probabilities, for a set of fluctuated fake data, it is very easy for the fitter to find a global minimum away from the true oscillation parameters, resulting in a lower  $\chi_{best}^2$  and a higher  $\Delta\chi^2$ .

Performing the same procedure at other grid points, one can build a  $\Delta\chi^2$  surface, as shown in Figure 8.10. Note that not the whole surface is covered due the large computing power required. It is nonuniform, in comparison to a homogeneous surface with a global  $\Delta\chi^2 = 4.61$ . The 90% C.L. contour is drawn where the  $\Delta\chi^2$  from data in Figure 8.3 is equal to the  $\Delta\chi^2$  on this surface.

The final 90% C.L. is shown in Figure 8.11 where the limit from the MINOS only and other  $\nu_\mu$  disappearance experiments are shown.

## 8.4 Combining with Bugey

As discussed in Chapter 2, the anomaly seen in LSND or MiniBooNE is based on a two-flavor fit, involving only one mass splitting  $\Delta m^2$  and one angle  $\theta$ . In the 3+1 model, the  $\theta$  there is equivalent to  $\theta_{\mu e}$ , which can be expressed

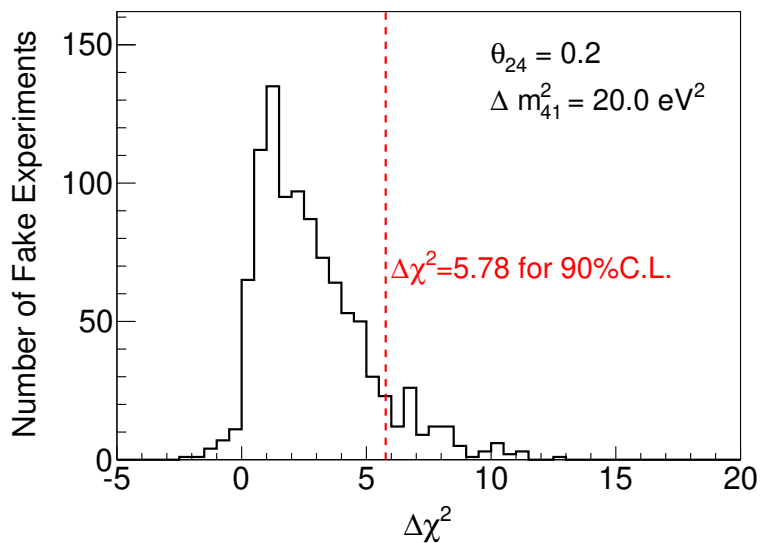


Figure 8.8:  $\Delta\chi^2$  distribution for 1000 fake experiments at point ( $\theta_{24} = 0.2, \Delta m_{41}^2 = 20 \text{ eV}^2$ ) which is represented by a solid green triangle in Figure 8.10. The dashed line is drawn at  $\Delta\chi^2 = 5.78$  such that 90% of the fake experiments give a smaller  $\Delta\chi^2$ . This indicates a deviation from 4.61 for 90% C.L., which is based on an assumption of Gaussian probability density function. A small fraction of the fake experiments has  $\Delta\chi^2 < 0$  due to fitting failure, but they do not affect the result much.

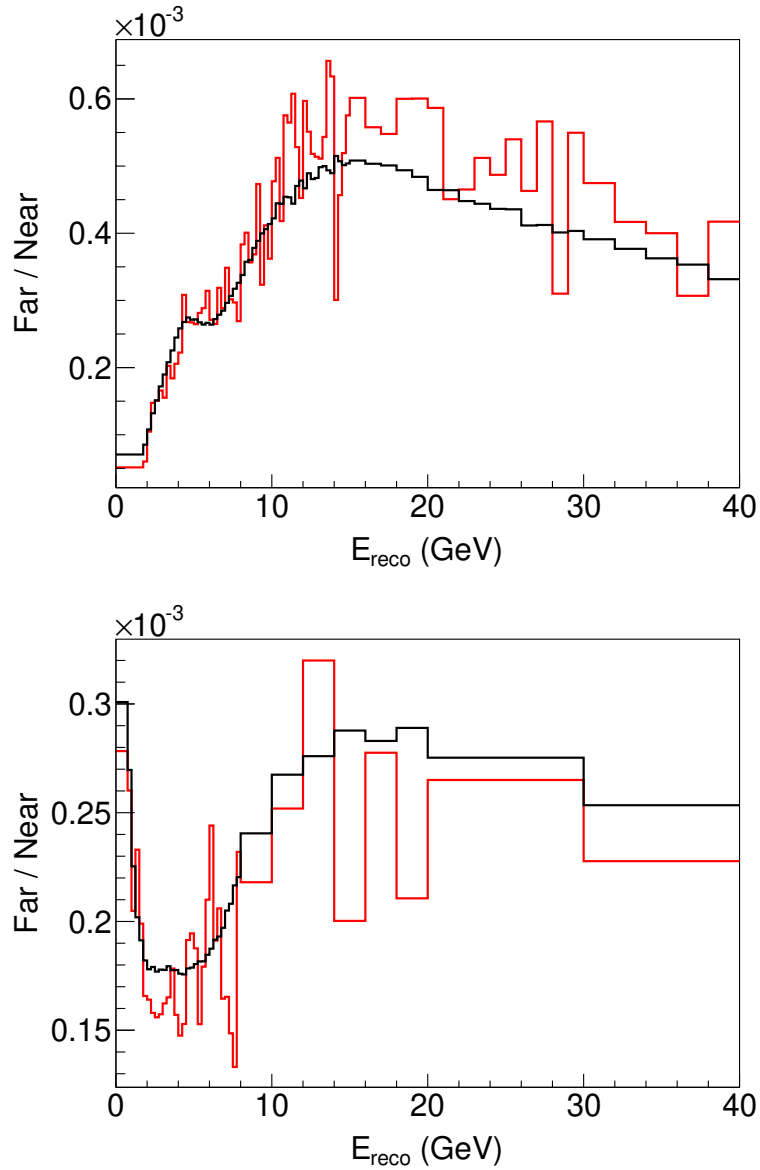


Figure 8.9: Fluctuated fake data, shown as the red, for the CC sample (top) and the NC sample (bottom). They correspond to the grid point represented by the green triangle in the top plot of Figure 8.10. The predictions without fluctuations are shown as black.

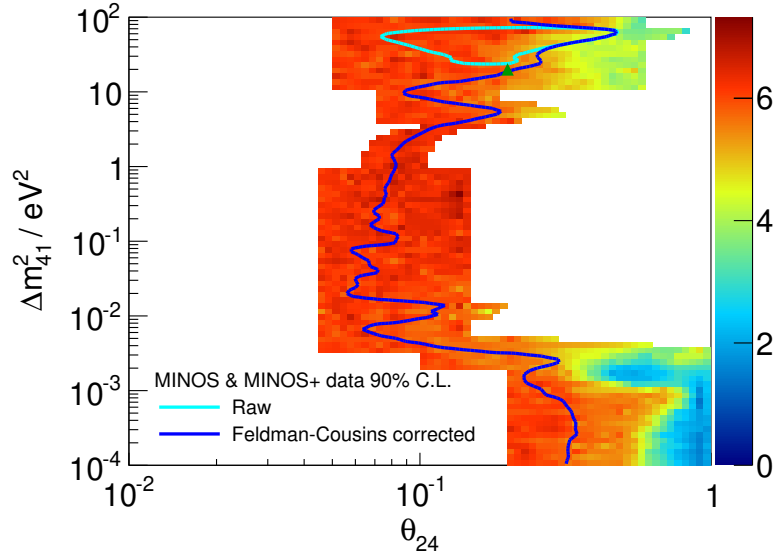


Figure 8.10: 90% C.L.  $\Delta\chi^2$  surface. The 90% C.L. contour before and after the correction are shown as the cyan and the blue, respectively.

in terms of  $\theta_{14}$  and  $\theta_{24}$  satisfying

$$\sin^2 2\theta_{\mu e} = \sin^2 2\theta_{14} \sin^2 \theta_{24}, \quad (8.4)$$

as shown in Appendix B.

In order to address the LSND and MiniBooNE anomaly, the limit on  $\theta_{24}$  from MINOS and MINOS+ can be combined with the constraint on  $\theta_{14}$  from Bugey experiment [57]. Bugey experiment performed high statistics measurements of neutrino energy spectra carried out at 15, 40 and 95 meters from a 2800 Megawatt reactor, using detection modules filled with  ${}^6\text{Li}$ -loaded liquid scintillator. For each  $\Delta m_{41}^2$  and  $\theta_{\mu e}$ , the combined  $\chi^2$  is the smallest possible sum of the  $\chi^2$  from each experiment by iterating through all combinations of

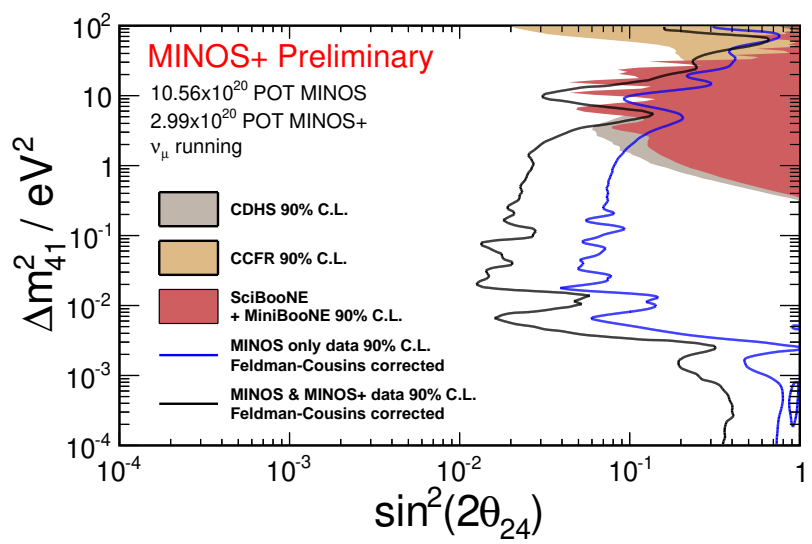


Figure 8.11: 90% C.L. Feldman-Cousins corrected contour. The excluded region is to the right. The limit from MINOS data is shown as the blue curve. The results from other  $\nu_\mu$  disappearance experiments, CDHS [124], CCFR [125], and MiniBooNE/SciBooNE [126] are shown as the shaded region.

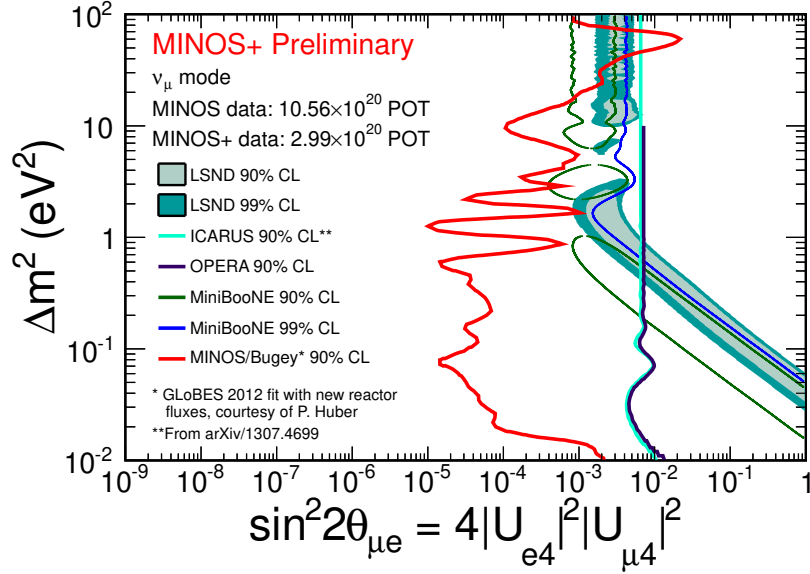


Figure 8.12: Combined limit of MINOS and MINOS+ with Bugey. The excluded region is on the right of the red curve. Results from  $\nu_e/\bar{\nu}_e$  appearance experiments, including LSND [49], MiniBooNE [50, 51], ICARUS [127], and OPERA [128], are also shown.

$\theta_{14}$  and  $\theta_{24}$ . Based on the Bugey limit evaluated by Patrick Huber using the new reactor flux mentioned in the reactor anomaly in Chapter 2, the combined contour is shown in Figure 8.12. One intriguing observation is that the combined limit only agrees with LSND and MiniBooNE results at  $\Delta m_{41}^2 \sim 60 \text{ eV}^2$  which is around the best fit of MINOS and MINOS+.

## 8.5 Discussions

The position of the minimum around  $\Delta m_{41}^2 = 60 \text{ eV}^2$  and  $\theta_{24} = 0.36$  as shown in Figure 8.3 has not yet been fully understood at the time of writing



this dissertation. It may be caused by some unknown systematics, or by the model. Preliminary investigations have been performed, where the full data set is divided in two ways. In the first, MINOS and MINOS+ data are separated, and in the second, NC and CC samples are separated.

The best fit points by fitting to the MINOS and MINOS+ data separately are shown in Table 8.2, along with the result from the combined fit. Note that when fitting to the MINOS+ data, only the statistical covariance matrix is used since the systematic covariance matrices were not available, but this should not have a significant effect on the best fit point. The far-over-near ratio for the data and that for the best fit prediction are shown in Figure 8.13, 8.14, and 8.15 for MINOS only, MINOS+ only, and the combined, respectively. The two ratios are both divided by the standard oscillation prediction which is shown as the blue dashed line at 1 on the Y-axis. The error bars are for the statistical uncertainty only.

The best fit points by fitting to the CC and NC samples separately are shown in Table 8.3, along with the result from the combined fit. The  $\chi^2$  surface are shown in Figure 8.16.

From Table 8.2 and Table 8.3, one can see that the best fit point does not have a strong dependence on how the data are divided. This is very intriguing. Between MINOS and MINOS+, a major difference is the neutrino spectrum: the former uses a low energy beam, and the latter uses a medium energy beam, as shown in Figure 3.4. Between the NC and the CC samples, the energy reconstruction is different: for the former, the event energy is the sum

parameter	best fit values		
	MINOS	MINOS+	combined
$\Delta m_{32}^2$ ( $10^{-3}\text{eV}^2$ )	2.39608	2.82671	2.48836
$\Delta m_{41}^2$ ( $\text{eV}^2$ )	64.5825	55.0124	60.3199
$\theta_{23}$	0.744	0.584549	0.685746
$\theta_{24}$	0.380744	0.43161	0.361625
$\theta_{34}$	0.0356045	0.130066	0.054325

Table 8.2: Best fit values by fitting to MINOS only, MINOS+ only and the combined fit.

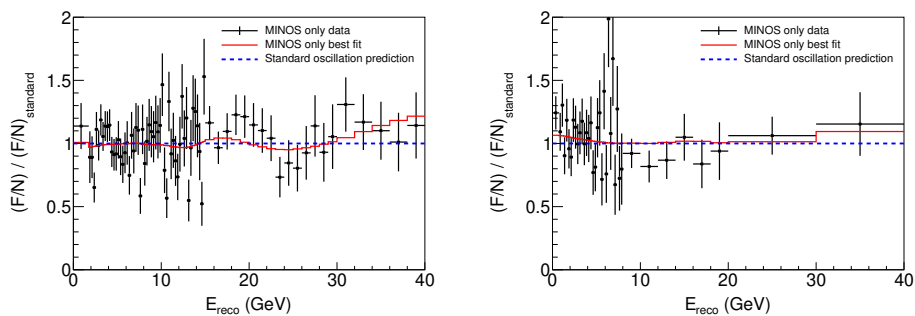


Figure 8.13: Far-over-near double ratio for MINOS only. The CC sample is shown on the left and the NC sample is shown on the right.

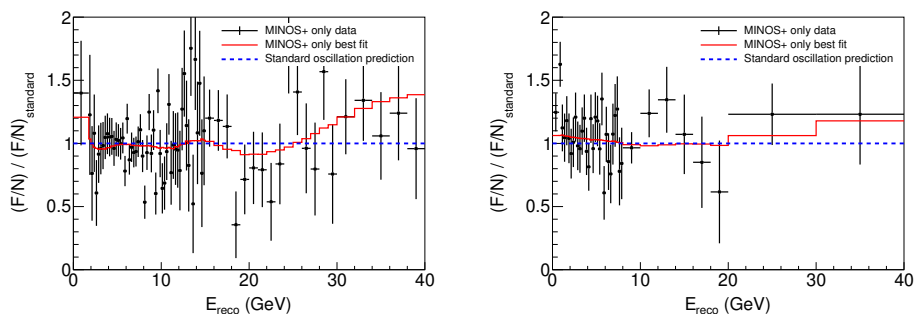


Figure 8.14: Far-over-near double ratio for MINOS+ only. The CC sample is shown on the left and the NC sample is shown on the right.

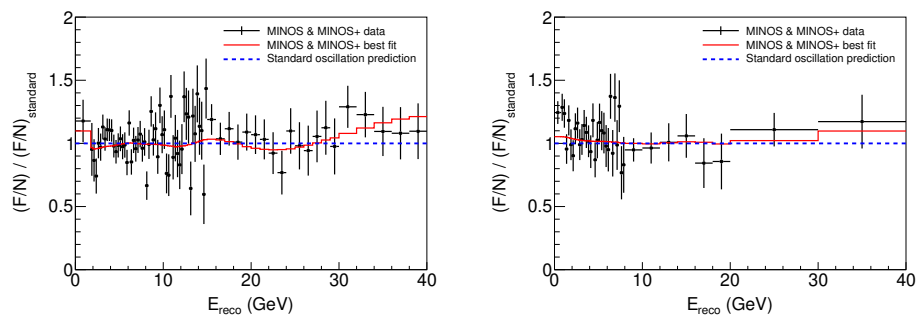


Figure 8.15: Far-over-near double ratio for the combined fit of MINOS and MINOS+. The CC sample is shown on the left and the NC sample is shown on the right.

parameter	best fit values		
	CC only	NC only	CC + NC
$\Delta m_{32}^2$ ( $10^{-3}\text{eV}^2$ )	-2.52908	2.7324	2.48836
$\Delta m_{41}^2$ ( $\text{eV}^2$ )	60.3199	55.0124	60.3199
$\theta_{23}$	0.912045	0.736413	0.685746
$\theta_{24}$	0.331011	0.500171	0.361625
$\theta_{34}$	0.000187863	0.0593616	0.054325

Table 8.3: Best fit values by fitting to CC only, NC only, and CC+NC. Note that  $\theta_{34}$  should not affect CC so the best fit value is close to its initial value 0.

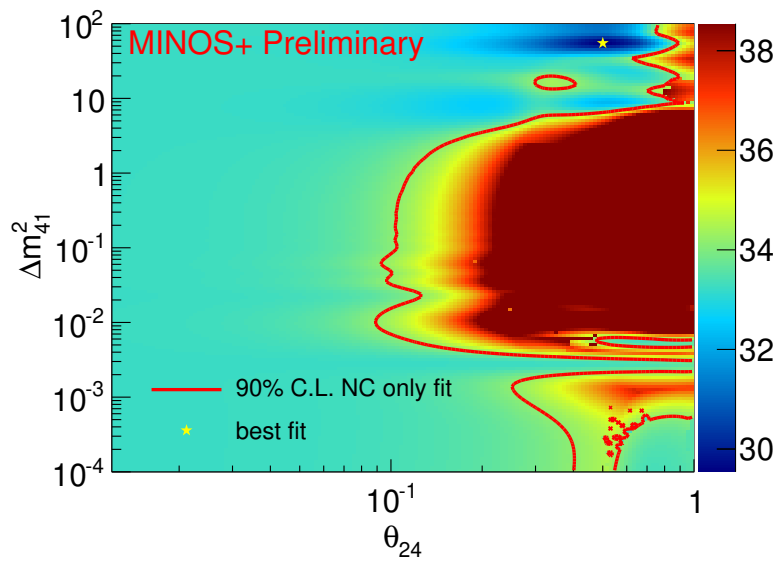
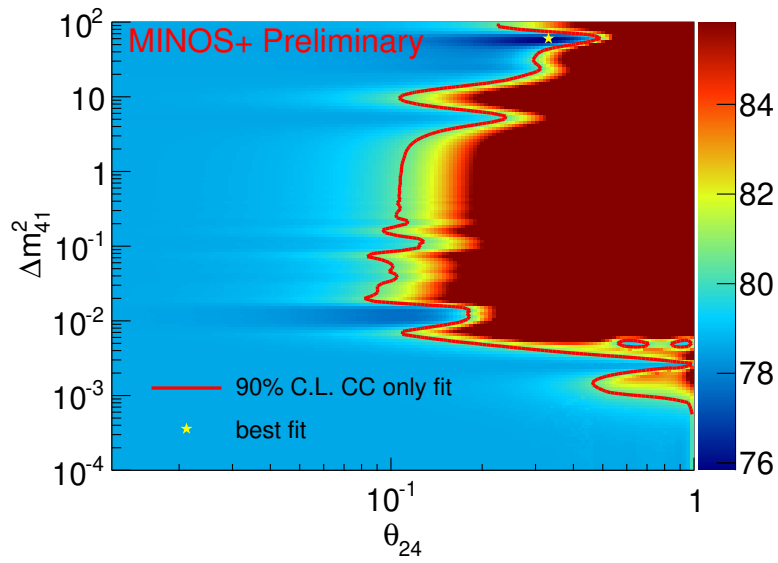


Figure 8.16:  $\chi^2$  surface by fitting to the CC sample only (top) and the NC sample only (bottom).

of the track energy and  $k$ NN shower energy; for the latter, the event energy is directly from the calorimetric shower energy. Additionally, many systematics are different between the CC and the NC samples as shown in Table 7.1, including those from the NC cleaning, which are unique to the NC sample, the acceptance, and the background contamination. The understanding of this result is still being pursued by the MINOS+ collaboration.

## Chapter 9

### Large Extra Dimension Analysis

This chapter presents the analysis of the large extra dimension model based on the full data set of  $10.56 \times 10^{20}$  POT  $\nu_\mu$  running in MINOS. The approach is very similar to that used in the 3+1 model analysis, i.e. a far-over-near fit in combination with a covariance-matrix-based  $\chi^2$ . One major challenge in this analysis is that the oscillation probability calculation is complicated and therefore slow. To solve this problem, the Ghost Fitter method, a term adopted in the MINOS collaboration, is used to perform the fit. The final 90% C.L. contour is obtained after a Feldman-Cousins correction in the last section.

#### 9.1 Strategy

In the early development of this analysis, the beam matrix method used in the MINOS standard oscillation analysis was adopted. In this method, the fit was performed on the FD CC spectrum. A beam matrix which allows a ND neutrino flux to be converted into a FD neutrino flux is constructed using the decay kinematics of the neutrino parent particles (see Appendix D). The model prediction of the energy spectrum at the FD is based on the ND spectrum and

the beam matrix. While perfectly suited for the standard oscillation analysis, it was later realized that for the LED model, this method suffers from two deficiencies:

1. The NC sample which can be used to measure  $\nu_\mu \rightarrow \nu_s$  channel is not used. The standard oscillation analysis solely considers the CC sample.
2. ND data is used to constrain the FD prediction based on the assumption that there are no oscillations at the ND. However, this is only true for small  $m_0$  ( $< 30$  meV) in the LED model.

By adopting the framework used in the 3+1 model analysis described in Chapter 8, both of these problems are solved.

### 9.1.1 Far-over-near Ratio

The fit is performed on the far-over-near ratio which is shown in Figure 9.1. By taking the far-over-near ratio, the assumption of no ND oscillations is no longer required. The analysis can be extended to a broader region, especially for high  $m_0$ . The difference between the beam matrix method and the far-over-near fit method is shown in Figure 9.2, where one can clearly see the two contours diverge at high  $m_0$ , with the far-over-near fit result being more correct.

Both CC and NC samples are used in the far-over-near fit. The total  $\chi^2$  is the sum of the  $\chi^2$  from each sample. The sensitivities of fitting to the individual sample are shown in Figure 9.3. One can see that including NC

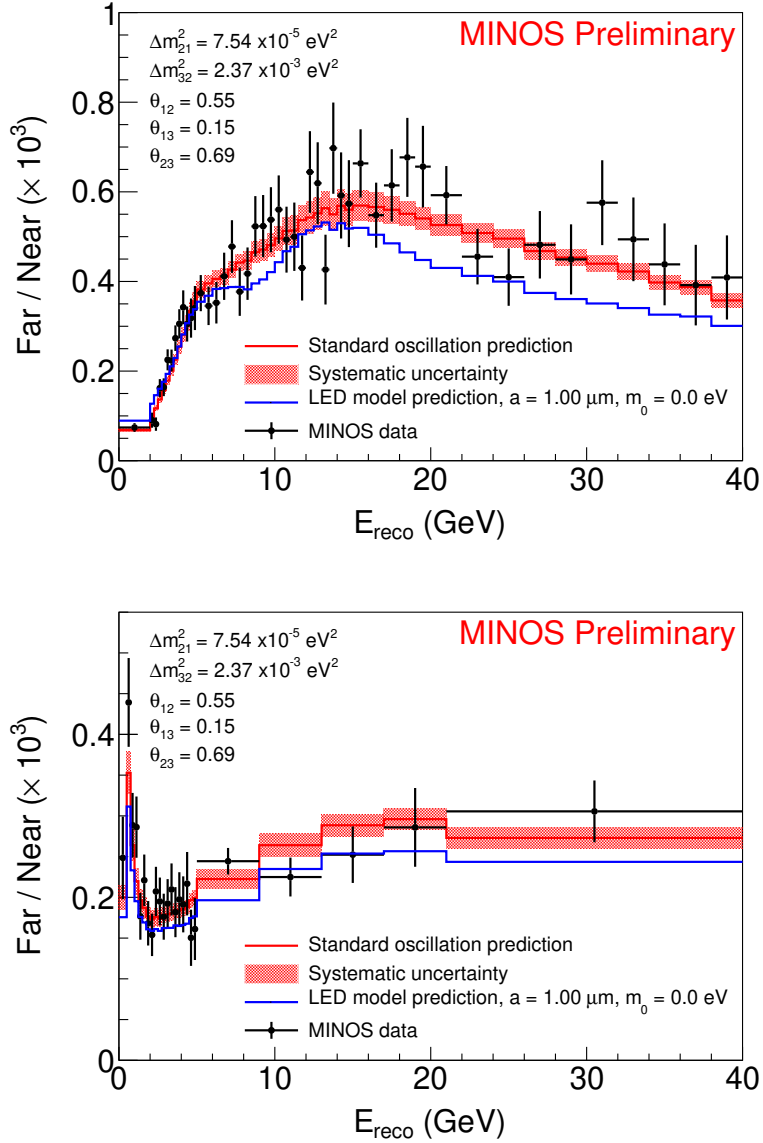


Figure 9.1: Far-over-near ratio of the MINOS CC (top) and NC (bottom) data. The standard oscillation prediction is shown as the red. The LED model prediction with  $a = 1 \mu\text{m}$  and  $m_0 = 0 \text{ eV}$ , as an example, is shown as the blue.



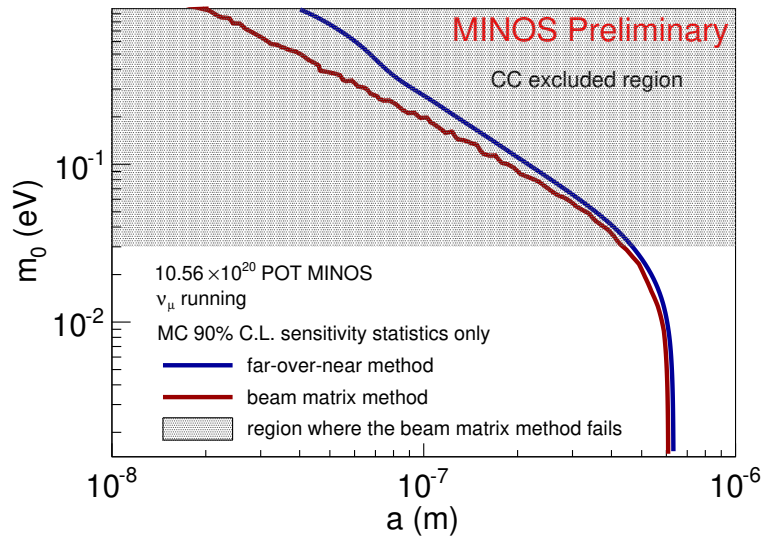


Figure 9.2: Sensitivities for using the beam matrix method and the far-over-near fit method. Only the CC sample is used. The beam matrix method does not apply for  $m_0 > 30$  meV (shaded region) due to ND oscillations.

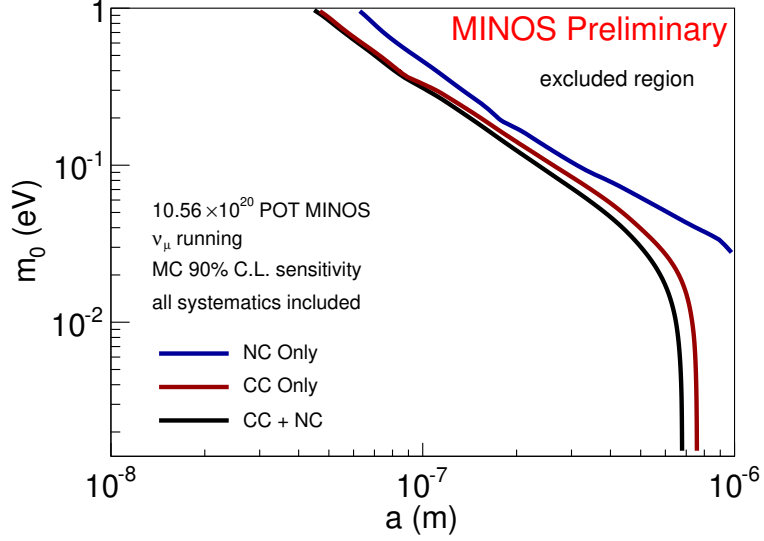


Figure 9.3: Sensitivity for NC sample only, CC sample only, and the combined CC and NC sample.

sample clearly provides a better sensitivity while the dominant contribution is still from the CC sample.

### 9.1.2 Expression of $\chi^2$

Similar to Equation 8.1, the  $\chi^2$  to be minimized in the fit is written as

$$\chi^2 = \Delta C^{-1} \Delta + \left( \frac{N_{data} - N_{MC}}{\sigma_N} \right)^2, \quad (9.1)$$

where  $\Delta$ ,  $C$ ,  $N_{data}$ , and  $N_{MC}$  have the same definition as before. Unlike in Equation 8.1, there is no penalty term for  $\Delta m_{32}^2$ . Instead, a range of  $0 < \Delta m_{32}^2 < 5 \times 10^{-3} \text{ eV}^2$  is used to reduce the difficulty of the fitting, as discussed

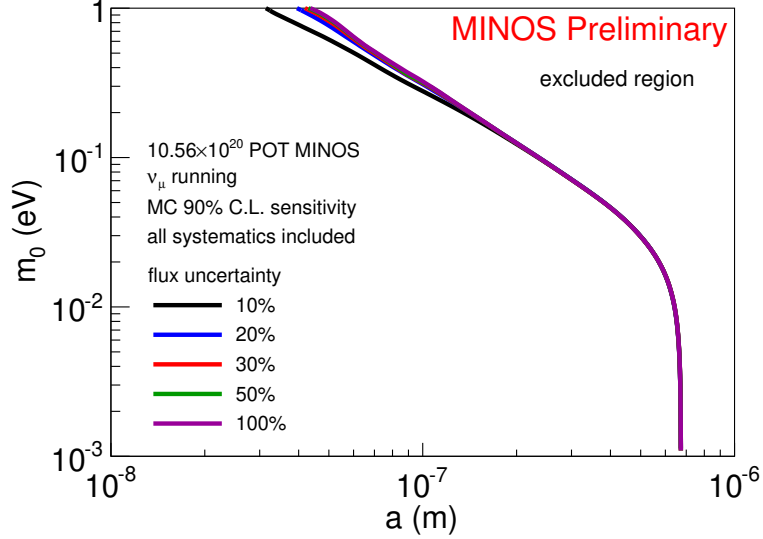


Figure 9.4: Sensitivity for different flux uncertainties.  $50\%N_{MC}$  is used in the current analysis, where  $N_{MC}$  is the number of MC events.

in Section 9.2. The flux uncertainty  $\sigma_N$  is taken as  $50\%N_{MC}$  for the same reason described in Chapter 8. The effect of using different  $\sigma_N$  is shown in Figure 9.4. No significant change is observed once the flux is above 20%, meaning that the flux constraint has very little effect on the result.

## 9.2 Performing the Fit

In performing the fit, the energy window is limited from 0 to 40 GeV. In minimizing the  $\chi^2$  in the plane of  $m_0 - a$ ,  $\Delta m_{32}^2$  and  $\theta_{23}$  are set free in the fit. The parameters that are fixed are listed in Table 9.1 along with their values. Two initial values for  $\theta_{23}$  are attempted: one in the lower octant,  $0 < \theta_{23} < \pi/4$ , and the other in the upper octant,  $\pi/4 < \theta_{23} < \pi/2$ . Only

Fixed parameters	$\Delta m_{21}^2$	$\theta_{12}$	$\theta_{13}$	$\delta_{CP}$
value	$7.59 \times 10^{-5} \text{ eV}^2$	0.6	0.155806	0

Table 9.1: Fixed oscillation parameters used in the fit.

normal hierarchy  $\Delta m_{32}^2$  is considered as mentioned in Chapter 2.

### 9.2.1 Ghost Fitter

The oscillation probability is calculated by solving for the eigenvalues and eigenstates of the Hamiltonian matrix, as shown in Appendix C. Since there is an infinite number of KK states, the matrix has an infinite dimension. However, using only the lowest 5 KK states, which results in a  $18 \times 18$  matrix, provides a good approximation, as mentioned in Reference [71]. In this analysis, the matrix is solved by the GNU Scientific Library. Compared to the case of the 3+1 analysis, the fitting requires a tremendous amount of time simply because the Hamiltonian matrix is significantly larger.

To reduce the computation time, the Ghost Fitter method, which had its successful application in the three flavor analysis in MINOS, is adopted. The idea is to save all possible oscillated predictions in a library before performing the fit. During the fit, instead of calculating the the model predictions, the fitter simply looks it up in the library.

Since all the variables are continuous, the predictions can only be saved at discrete grid points. In the later text, these predictions are referred to as templates (for an example, see Figure 9.6). In the LED model, the parameter

parameter	number of grid points	range
$a$	51	$10^{-8} - 10^{-6}$ m
$m_0$	51	$10^{-3} - 2.5$ eV
$\theta_{23}$	26	$0 - \pi/2$
$\Delta m_{32}^2$	51	$0 - 5 \times 10^{-3}$ eV <sup>2</sup>
total	3,448,926	

Table 9.2: Discrete grid points used in the Ghost Fitter.

space is spanned by four variables:  $m_0$ ,  $a$ ,  $\theta_{23}$ , and  $\Delta m_{32}^2$ . The four-dimensional grid used for the current analysis is shown in Table 9.2. The total size of the templates is 3.9 gigabytes. To get a reasonable template size,  $\Delta m_{32}^2$  is limited to  $0 - 5 \times 10^{-3}$  eV<sup>2</sup>, in the spirit of treating the LED model as a perturbation of the standard oscillation model.

For the parameter set that does not fall onto those grid points, a linear interpolation is performed. An example of two-dimensional linear interpolation is shown in Figure 9.5. In this case, the interpolated value of  $Z_E$  for point  $E$  is a weighted average of the  $Z$  values of its four neighboring points

$$Z_E = \sum_{\alpha=A,B,C,D} W_\alpha Z_\alpha, \quad (9.2)$$

where the weight  $W_\alpha$  is equal to the normalized area of the diagonally opposite sub-rectangle. For instance, the weight for point  $A$  is

$$W_A = \frac{S_D}{S_A + S_B + S_C + S_D} = \frac{(X_2 - X_1)(Y_2 - Y_0)}{(X_1 - X_0)(Y_1 - Y_0)}. \quad (9.3)$$

The two-dimensional linear interpolation is generalized to higher dimensions by replacing the rectangle areas with volume of hyperrectangles. The fitting time is decreased by a factor of about 100 by using the Ghost Fitter.

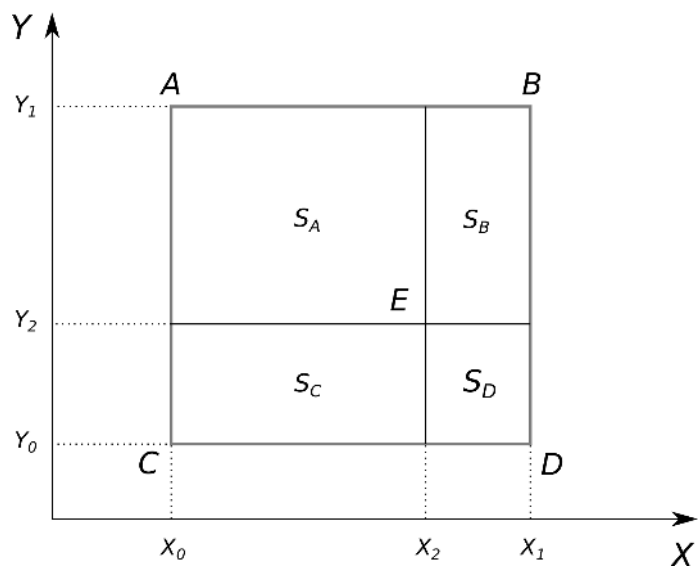


Figure 9.5: An illustration of 2D linear interpolation. The value at point  $E$  is weighted average of the values at the neighboring four points  $A, B, C,$  and  $D$ . The weight for each point is equal to the area of the sub-rectangle on the opposite end. For example the weight for point  $A$  is  $S_D / (S_A + S_B + S_C + S_D)$  as in Equation 9.3.

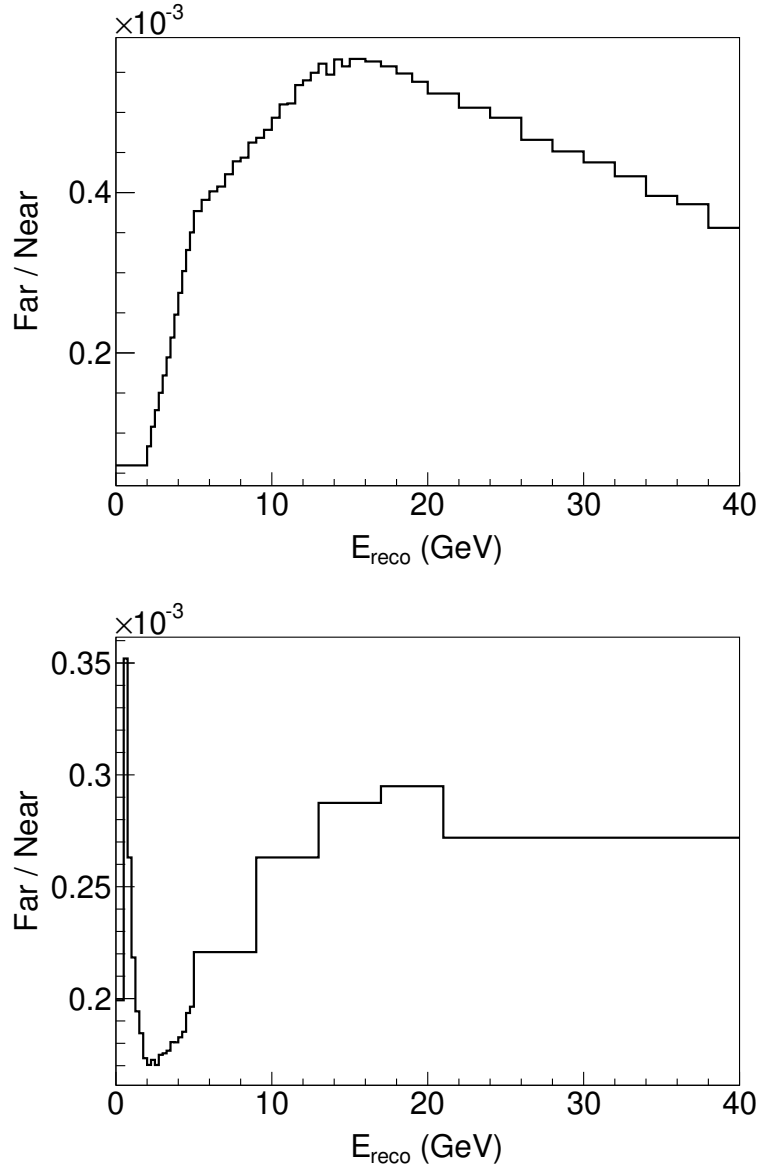


Figure 9.6: An example of a template used in the Ghost Fitter. It consists of the far-over-near ratio for the CC sample (top) and the NC sample (bottom). The two histograms are computed based on the parameters of a grid point in the four dimensional space spanned by  $m_0$ ,  $a$ ,  $\theta_{23}$ , and  $\Delta m_{32}^2$ .

### 9.2.2 $\chi^2$ Surface

The  $\chi^2$  surface for MINOS data is shown in Figure 9.7. The sensitivity surface is shown in Figure 9.8, where the fake data is calculated based on the standard oscillation. A comparison between the data and the sensitivity is shown in Figure 9.9. The data contours will be further corrected by the Feldman-Cousins procedure in the next section.

### 9.2.3 Effect of Systematics

The effect of the systematics is shown in the same way as in Chapter 8. In Figure 9.10, the individual systematics is used for each contour, while in Figure 9.11 the systematics are added one by one for each contour. The X-axis is shown in linear scale so that the separation becomes clearly visible.

## 9.3 Feldman-Cousins Correction

For the same reasons mentioned in Chapter 8, a Feldman-Cousins procedure is also performed for this analysis. Figure 9.12 shows an example of the fluctuated fake data considering the statistical and systematic fluctuations. In Figure 9.13, the top plot is an example of the distribution of  $\Delta\chi^2$ , and the bottom plot is the  $\Delta\chi^2$  surface based on which the corrected contour is made. The final result of this analysis is shown in Figure 9.14.



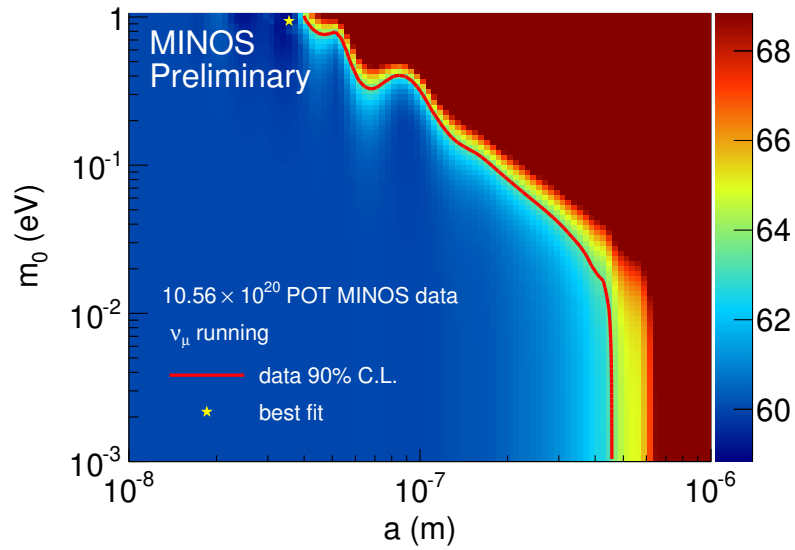
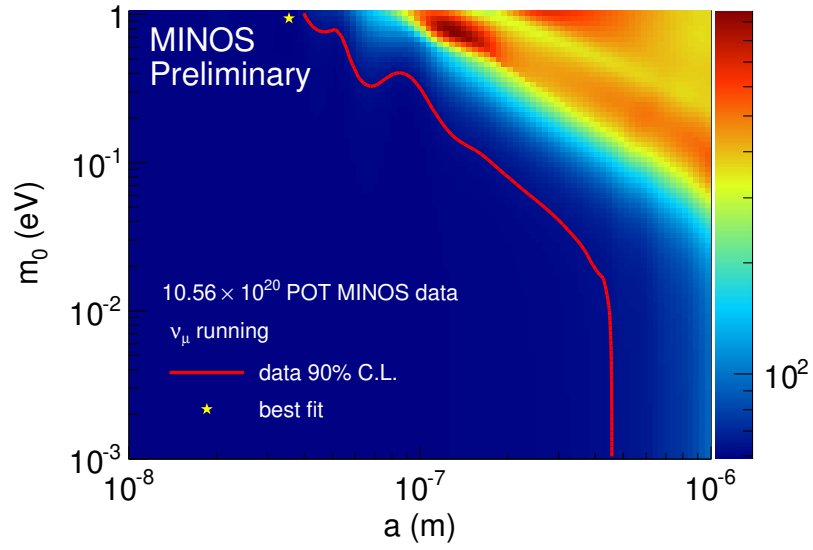


Figure 9.7: Top:  $\chi^2$  surface based on MINOS data.  $m_0$  is the smallest neutrino mass and  $a$  is the large extra dimension size. Z-axis is the  $\chi^2$  value. Bottom: The same as the top plot but with a linear scale for the Z-axis.

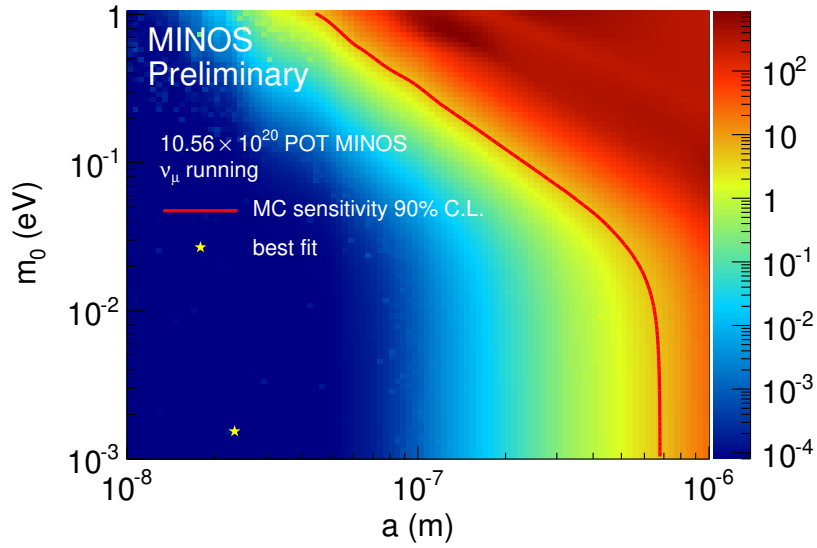


Figure 9.8:  $\chi^2$  surface of the sensitivity. The fake data is made with the standard oscillation assumption.

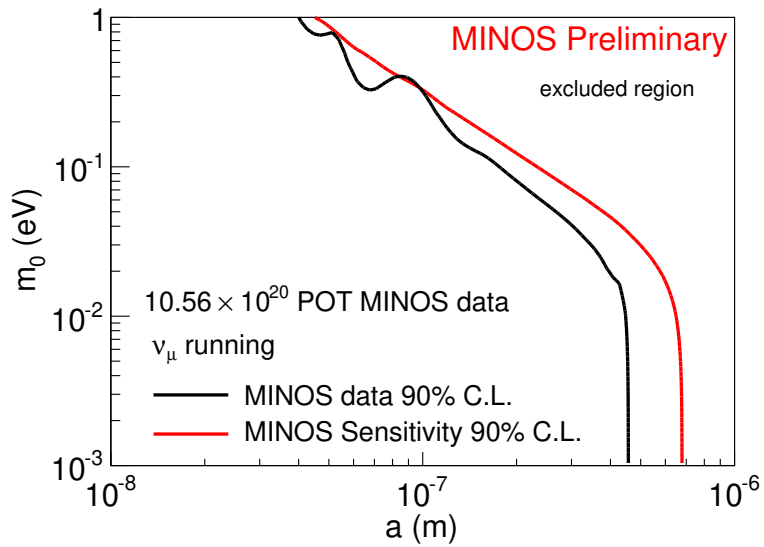


Figure 9.9: A comparison of the 90 C.L. contours between data and sensitivity.

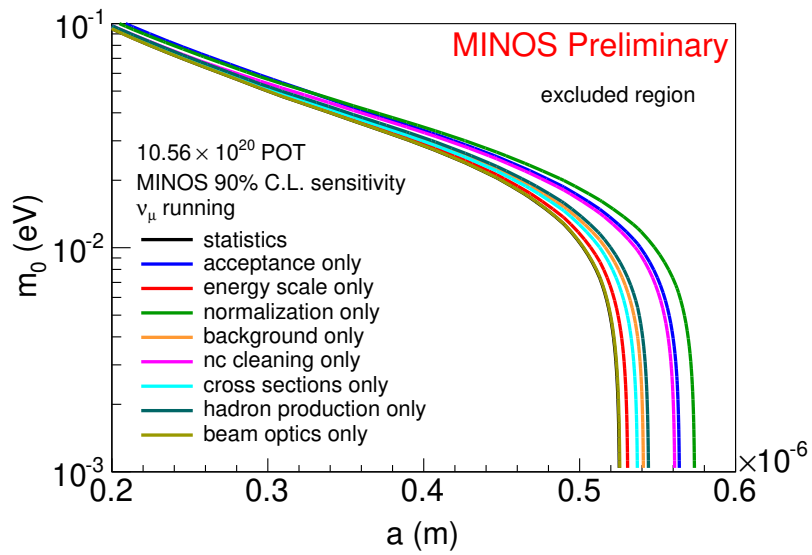


Figure 9.10: Individual effect of the systematics on the 90% C.L. sensitivity contour. The statistics only contour is on the very left, buried under the contour for the beam optics.

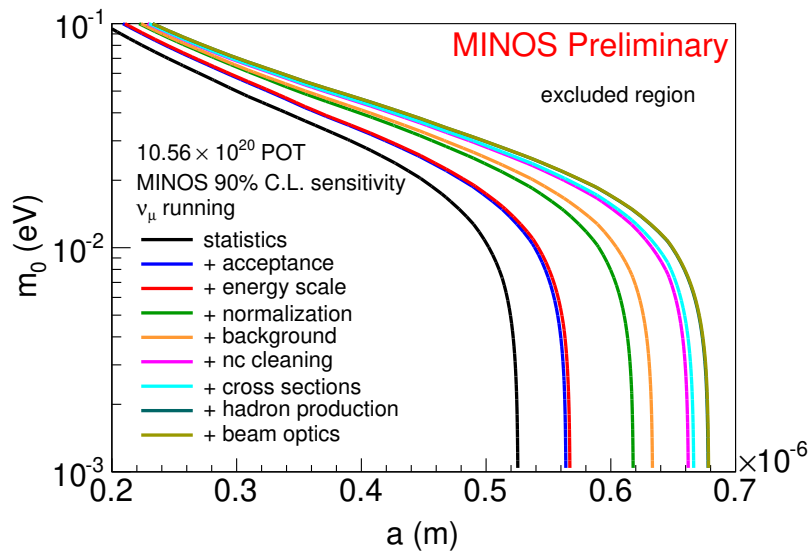


Figure 9.11: Cumulative effect of the systematics on the 90% C.L. sensitivity contour. The systematics covariance matrices are added one by one for each contour.

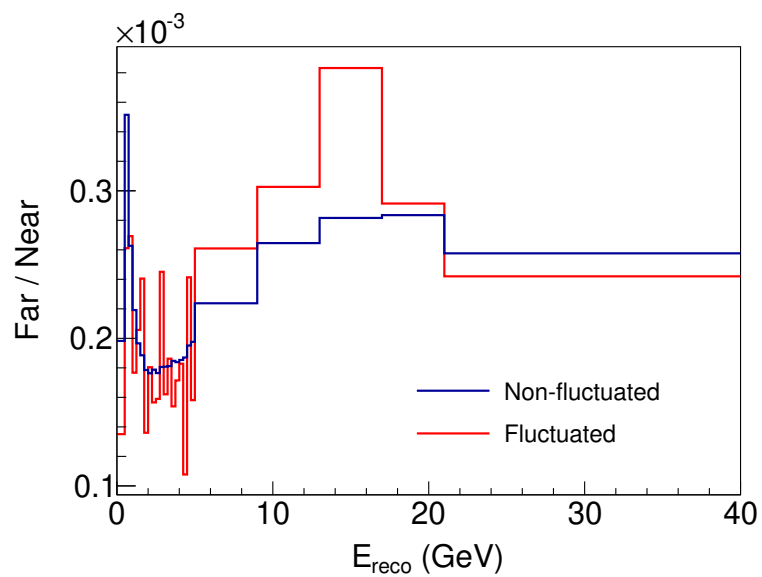
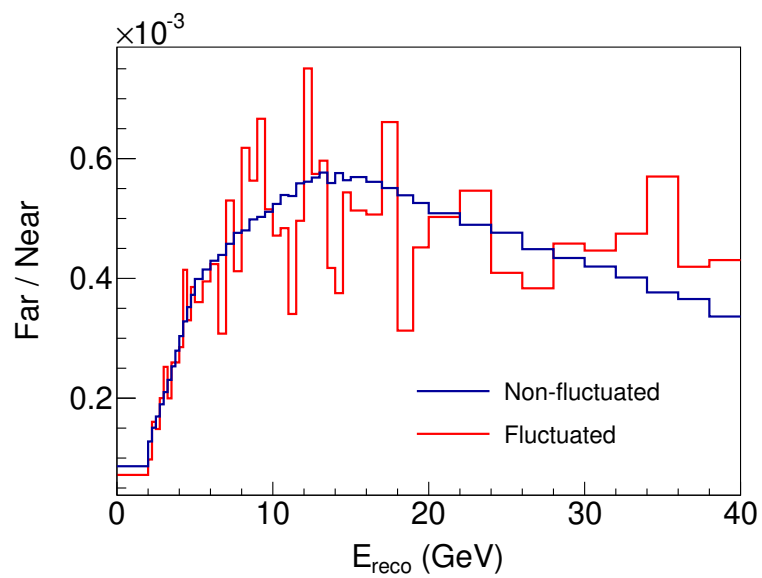


Figure 9.12: Fluctuated far-over-near ratio for the CC sample (top) and the NC sample (bottom).

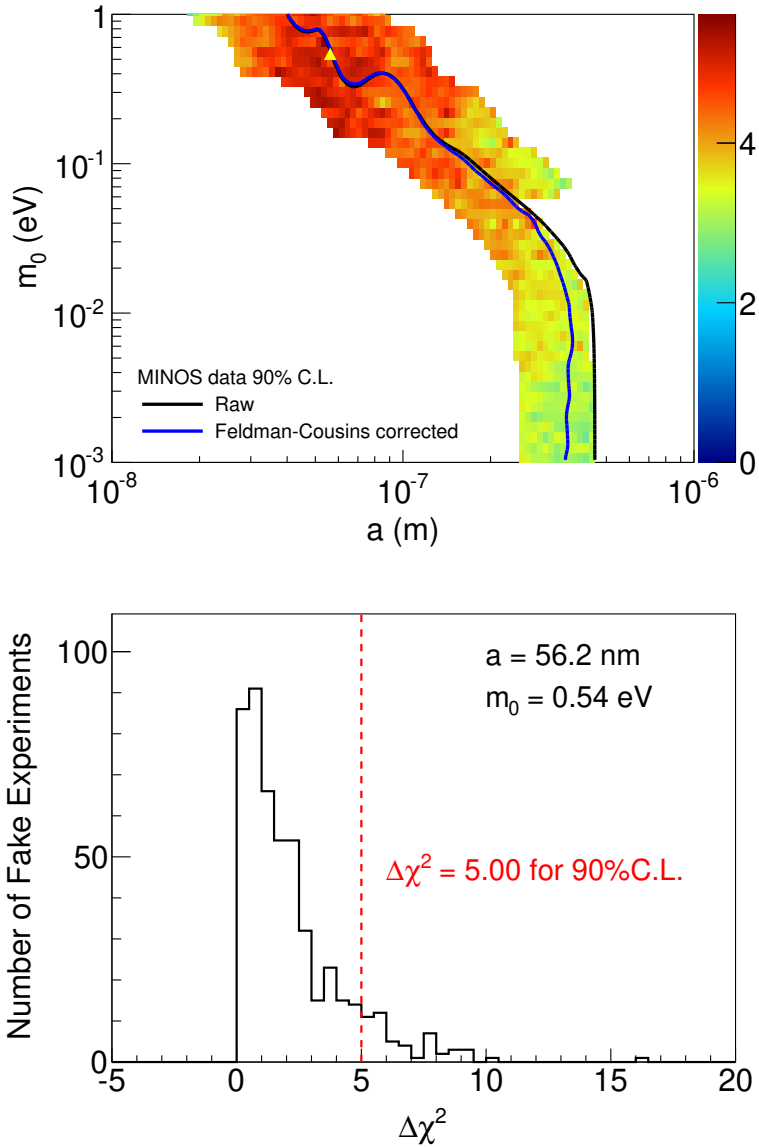


Figure 9.13: Top: 90% C.L. Feldman-Cousins corrected contour. The  $Z$ -axis represents the computed Feldman-Cousins values. The corrected contour is drawn where the  $\chi^2$  is larger than the corresponding Feldman-Cousins value. Bottom:  $\Delta\chi^2$  distribution for the point represented by the solid yellow triangle in the  $m_0 - a$  plane.

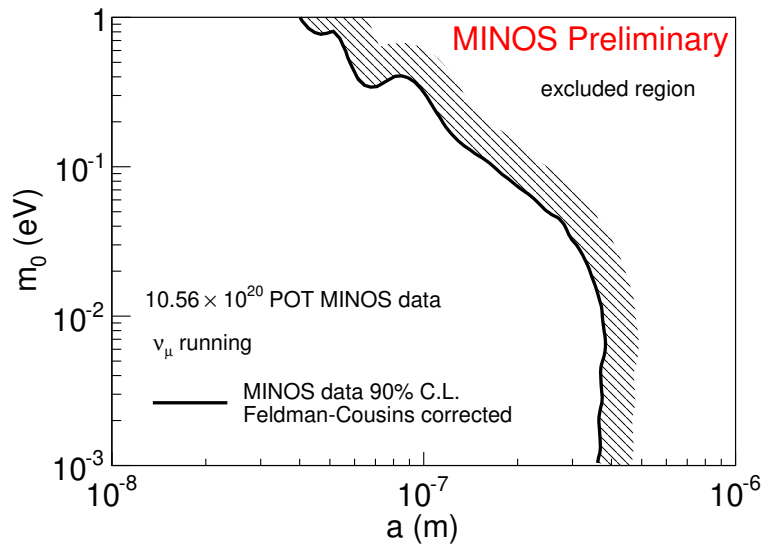
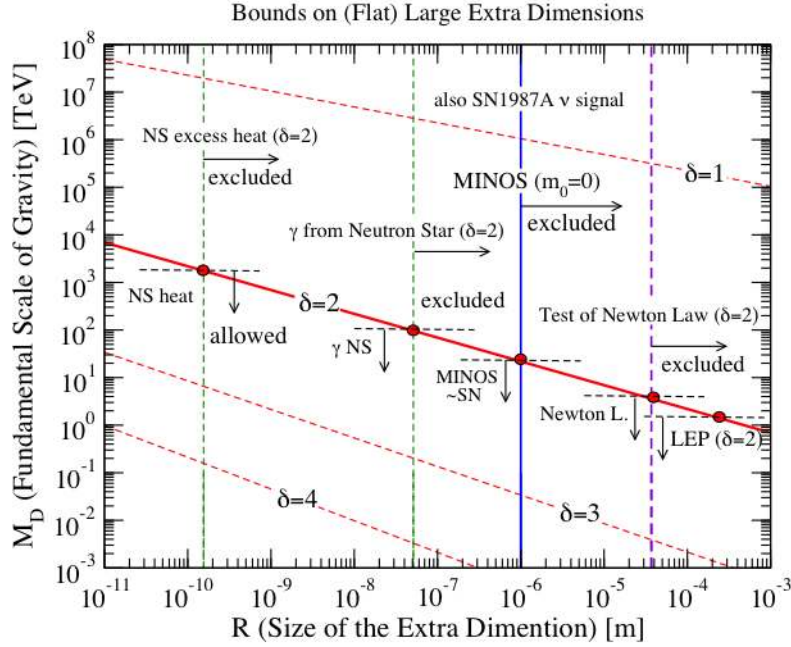


Figure 9.14: 90% C.L. Feldman-Cousins corrected contour for the LED model based on  $10.56 \times 10^{20}$  POT  $\nu_\mu$  running MINOS data.  $m_0$  is the smallest neutrino mass and  $a$  is the large extra dimension size. The shaded area means that the excluded region is to the right of the plot.

## 9.4 Limits from Other Experiments

Constraints on the possible large extra dimensions primarily come from torsion balance experiments, collider experiments, astrophysics, and cosmology. An extensive review on the global search results can be found in Reference [16]. A global picture provided by Machado, Nunokawa and Zukanovich Funchal is shown in Figure 9.15, which includes the limit of MINOS based on the authors' simulation. Various constraints are described in the caption of Figure 9.15.





Refs. Giudice and Wells, PDG2010, JPG37, 075021 (2010), p1354  
Hannestad and Raffelt, PRD67, 125008 (2003) [Erratum, PRD69, 029901 (2004)]

$$\bar{M}_{\text{Pl}}^2 = \bar{M}_D^{2+\delta} (2\pi R)^\delta, \quad M_D = (2\pi)^{\delta/(2+\delta)} \bar{M}_D, \quad \bar{M}_{\text{Pl}} = M_{\text{Pl}}/(2\pi)^{1/2}$$

Figure 9.15: World’s search for extra dimensions. The plot is provided by Machado, Nunokawa and Zukanovich Funchal.  $M_D$ ,  $R$  and  $\delta$  have the same definitions as those of  $m_D$ ,  $a$  and  $n$  in Equation 2.9, representing the fundamental scale, extra dimension size and number of extra dimensions respectively. The left green dashed line ( $M_D > 1700$  TeV for  $\delta = 2$ ) is the limit from requiring that neutron stars are not excessively heated by KK graviton decays into photons [129]. The right green dashed line ( $M_D > 100$  TeV for  $\delta = 2$ ) is the cosmological constraint based on the restriction on the amount of relic gravitons in the universe [130]. The solid blue line ( $M_D > 27$  TeV for  $\delta = 2$ ) is the limit from supernova SN1987A requiring that the graviton luminosity agrees with certain stellar models [131]. It is also the limit of MINOS based on the simulations done by the authors of this plot. The purple dashed line ( $a < 37 \mu\text{m}$  at 95% CL for  $n = 2$ ) is the limit from torsion balance experiments [132]. The right-most red circle ( $M_D > 1.60$  TeV for  $\delta = 2$ ) is the limit from a combination of the LEP results on graviton emission [133, 134].

## Chapter 10

### Summary and outlook

In an effort to search for sterile neutrinos using MINOS and MINOS+  $\nu_\mu$  running data, two relevant models have been tested, 3+1 and LED. No evidence for the sterile neutrinos has been found, nor that of the large extra dimensions. With the 3+1 model, in the range of  $10^{-3} \text{ eV}^2 < \Delta m_{41}^2 < 1 \text{ eV}^2$ , the limit on  $\theta_{24}$  placed by this dissertation is significantly stronger than the previous  $\nu_\mu$  disappearance experiments. With the LED model, to the limit of the lightest neutrino mass equal to zero ( $m_0 = 0$ ), the extra dimension size is constrained to be smaller than  $0.35 \mu\text{m}$  at 90% C.L. While it is a model-dependent result, the limit is very competitive compared to that from other search, such as the torsion balance experiment and collider experiments.

In the future, MINOS+ will continue to take data through year 2016. With more statistics of high energy neutrinos, the constraint on those two models will be further improved. The sensitivity of  $10 \times 10^{20}$  POT MINOS+ to the 3+1 model is shown in Figure 10.1. Additionally, NO $\nu$ A, as the successor of MINOS, began taking data with a 14 kiloton far detector. The methods developed in this dissertation can be easily applied to the sterile neutrino searches in NO $\nu$ A.

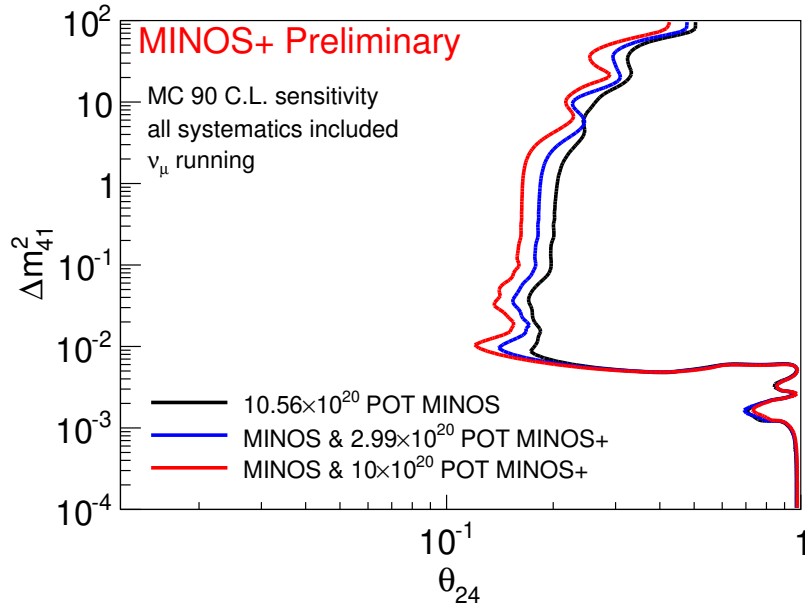


Figure 10.1: Sensitivity of  $10 \times 10^{20}$  POT MINOS+ to the 3+1 model.

On the front of  $\nu_e$  appearance measurement in short baseline neutrino experiments, MicroBooNE with the state-of-the-art Liquid Argon Time Projection Chamber will start to take data in 2015. It will probe the anomaly seen in the MiniBooNE and LSND experiments.

The potential of the NuMI and the booster neutrino beam will continue to be exploited by current and future experiments. Discovering sterile neutrinos, if they exist, would be revolutionary and open the door to many questions. Along with the search for  $\delta_{CP}$  and mass hierarchy, the sterile neutrinos search will continue to be one of the main focuses in the field for years to come.

## Appendices

# Appendix A

## Strip-to-strip Calibration

### A.1 Calibration Chain

The calibration chain of MINOS detectors is illustrated in Figure A.1.

It consists of the following steps:

1. **ADC**: This is the raw signal before any calibration procedure is applied.
2. **sigLin**: This is the result after the calibrations on
  - PMT non-linearity
  - drift, such as the PMT gain caused by the temperature change.
3. **sigCor**: This is the result after the strip-to-strip calibration, which normalizes the variations among scintillator strips caused by the defects in wavelength shifting fibers, and differences on the scintillator light yield, optical connectors and readout cables. The calibration is based on cosmic ray muons because they are abundant and similar amount of energy is deposited in each plane. The results and the systematics of strip-to-strip calibration are shown in the next section.
4. **sigMap**: This is the result after the calibration on fiber attenuation.

- MEU (Muon Energy Unit). This is the median of `sigMap` distribution for the selected hits. 1 MEU is equal to the detector response to a perpendicular 1 GeV muon traversing 1 plane of scintillator.

The results of the full calibration procedure are shown in Figures A.2 to A.5.

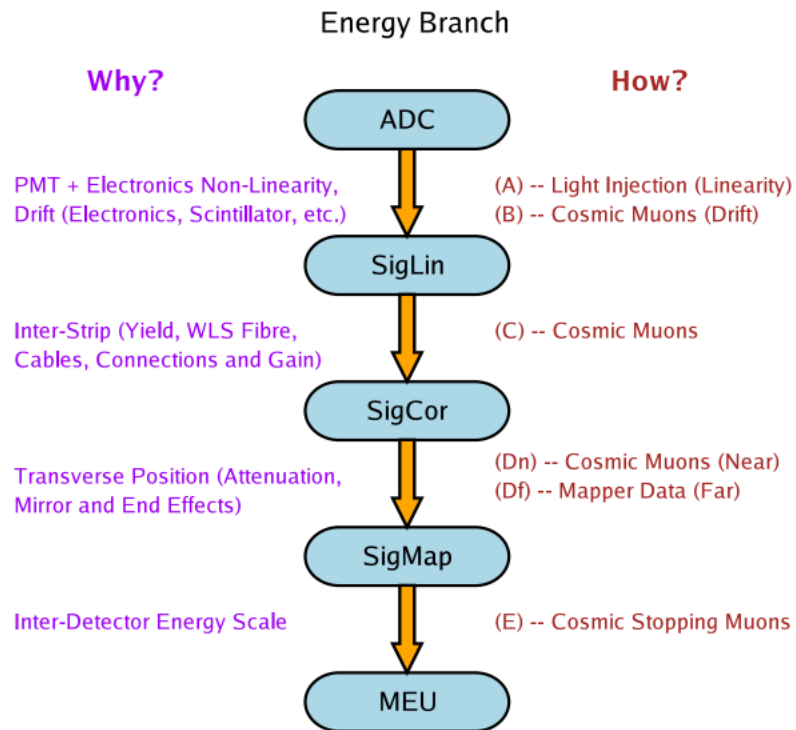


Figure A.1: Calibration chain of the MINOS detectors. The plot is taken from Reference [95].

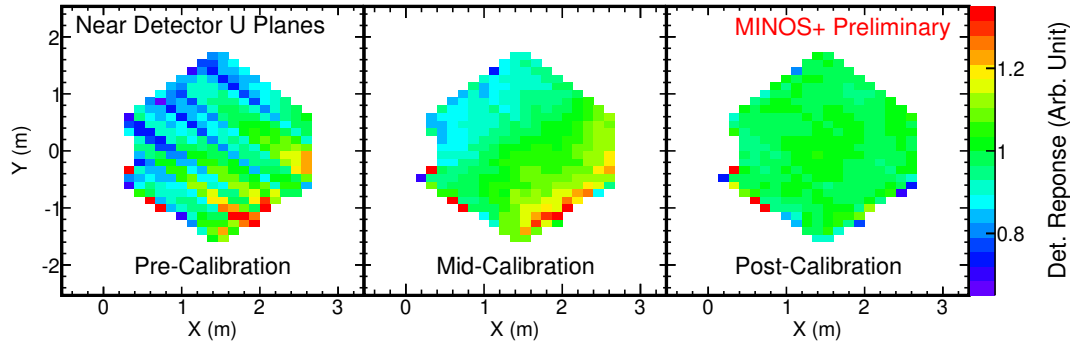


Figure A.2: Response of Near Detector as a function of detector position for U planes using MINOS+ cosmic data. Pre-Calibration plot shows raw ADC distribution. Mid-Calibration plot shows the effect of linearity, drift and strip-to-strip calibrations (`sigCor`). Post-Calibration plot shows the effect of fiber attenuation (`sigMap`) calibration.

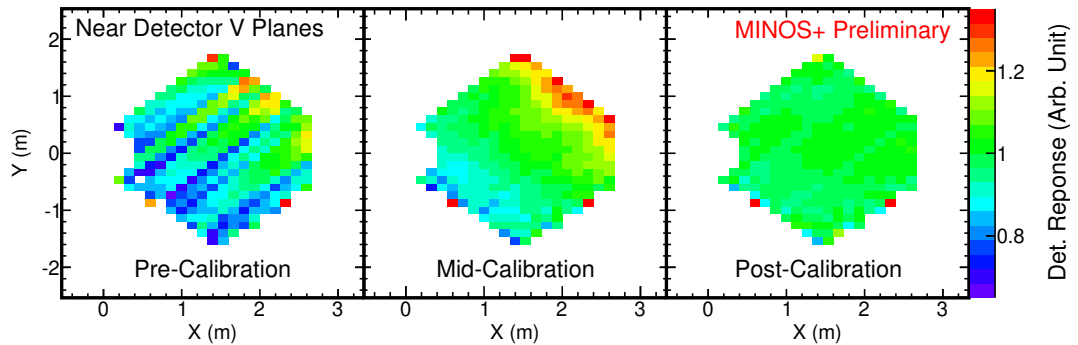


Figure A.3: Response of Near Detector as a function of detector position for V planes using MINOS+ cosmic data. Pre-Calibration plot shows raw ADC distribution. Mid-Calibration plot shows the effect of linearity, drift and strip-to-strip calibrations (`sigCor`). Post-Calibration plot shows the effect of fiber attenuation (`sigMap`) calibration.

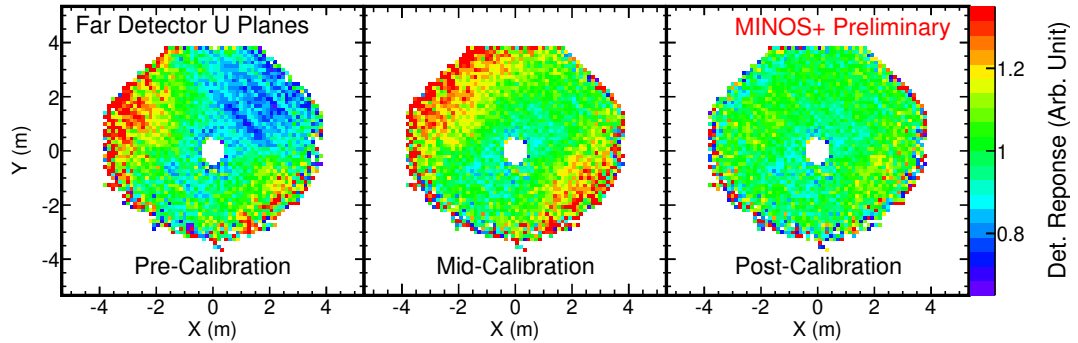


Figure A.4: Response of Far Detector as a function of detector position for U planes using MINOS+ cosmic data. Pre-Calibration plot shows raw ADC distribution. Mid-Calibration plot shows the effect of linearity, drift and strip-to-strip calibrations (`sigCor`). Post-Calibration plot shows the effect of fiber attenuation (`sigMap`) calibration.

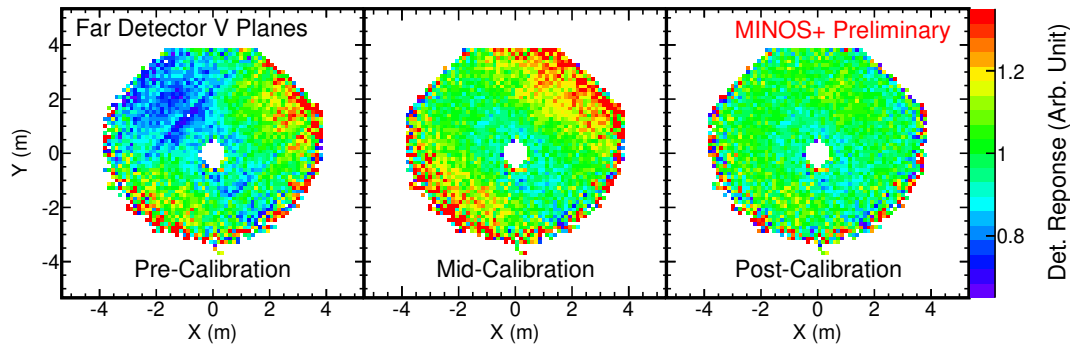


Figure A.5: Response of Far Detector as a function of detector position for V planes using MINOS+ cosmic data. Pre-Calibration plot shows raw ADC distribution. Mid-Calibration plot shows the effect of linearity, drift and strip-to-strip calibrations (`sigCor`). Post-Calibration plot shows the effect of fiber attenuation (`sigMap`) calibration.



## A.2 Results of Strip-to-strip Calibration

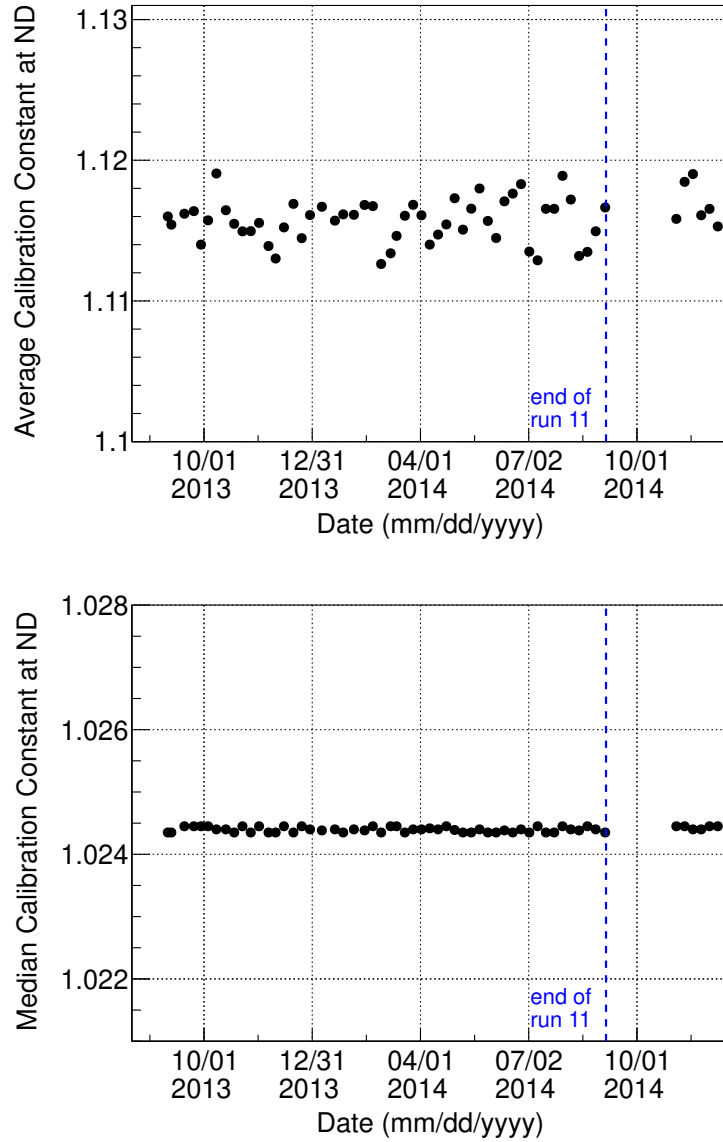


Figure A.6: Mean (top) and median (bottom) of the strip-to-strip calibration constant distribution at ND as a function of time.

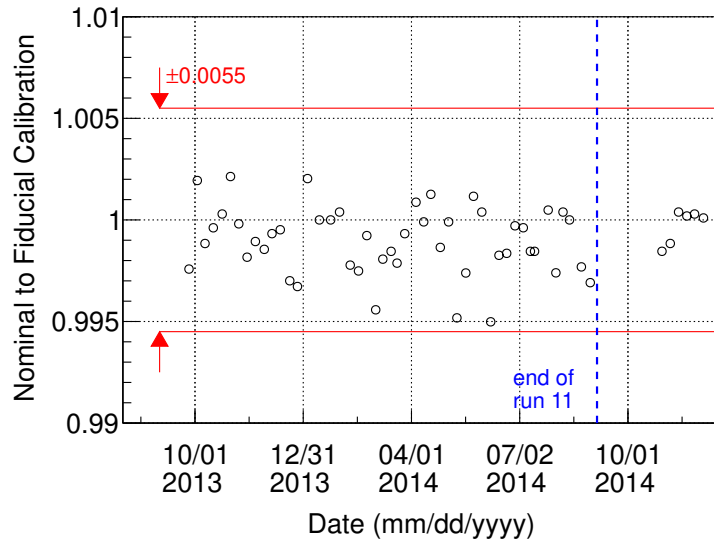
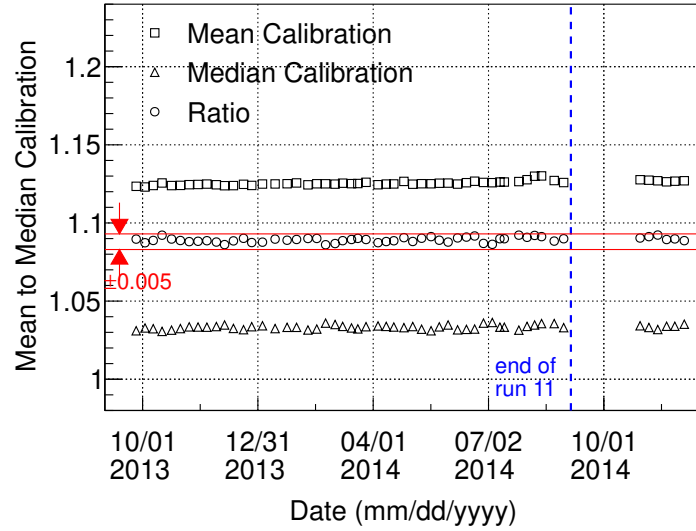


Figure A.7: Systematics of the strip-to-strip calibration at ND. Top: Ratio of the mean and the median (as shown in Figure A.6). Bottom: Ratio of the median for the full detector (nominal) to the median for the fiducial volume.

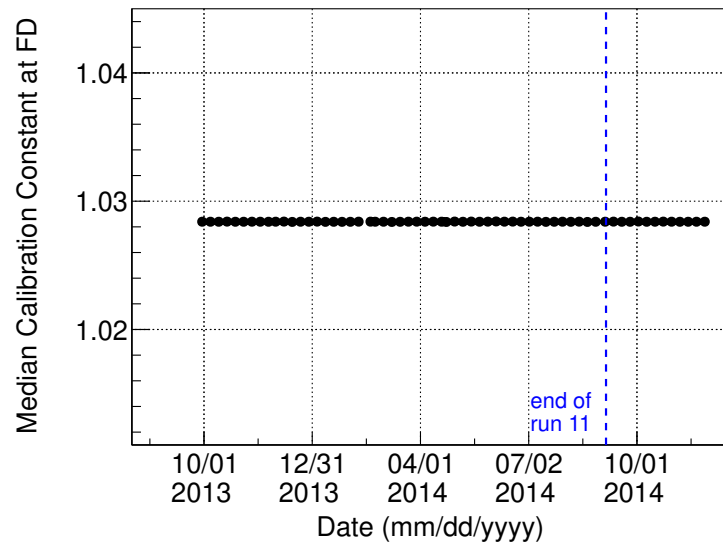
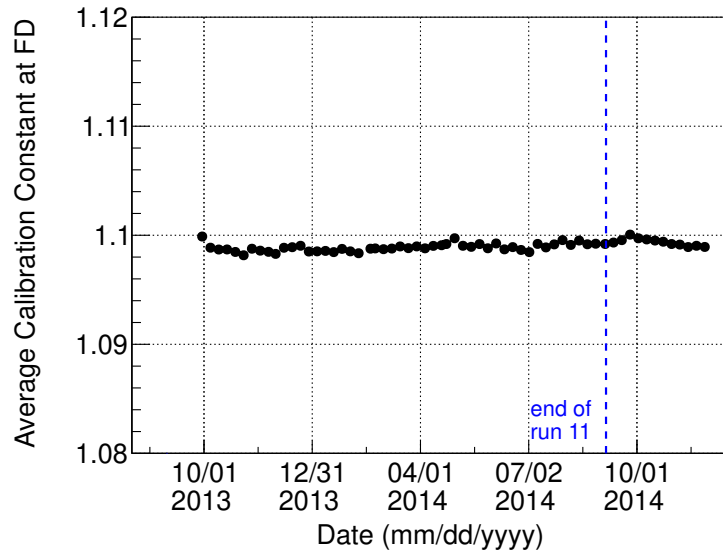


Figure A.8: Mean (top) and median (bottom) of the strip-to-strip calibration constant distribution at FD as a function of time.

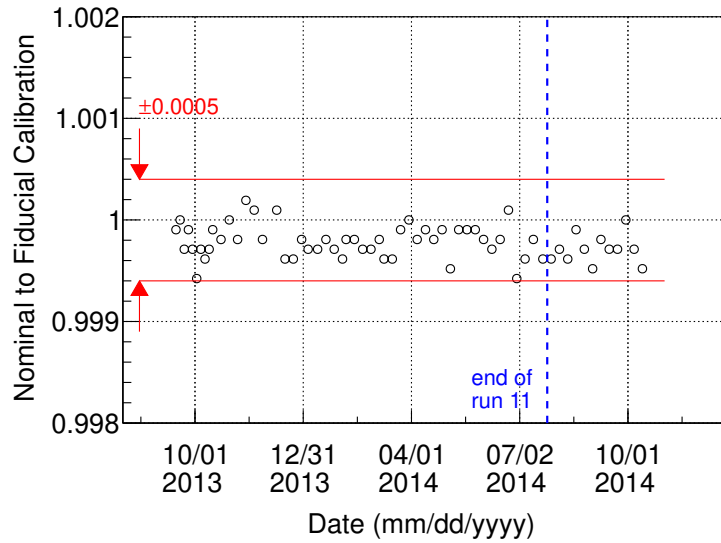
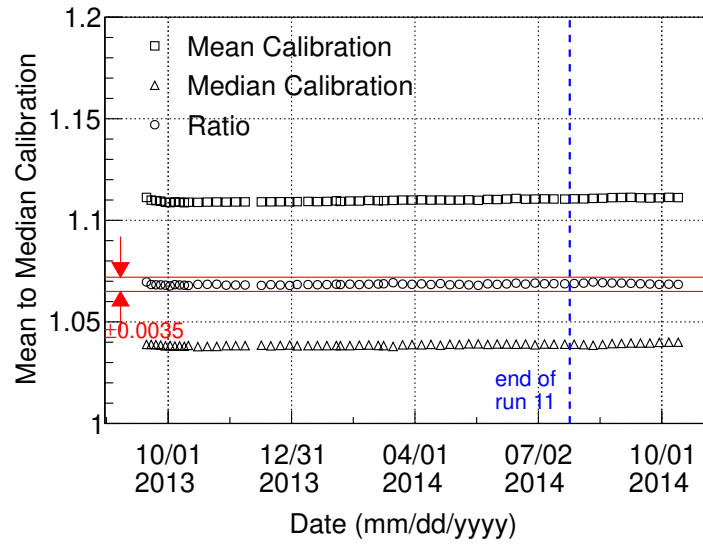


Figure A.9: Systematics of the strip-to-strip calibration at FD. Top: Ratio of the mean and the median (as shown in Figure A.8). Bottom: Ratio of the median for the full detector (nominal) to the median for the fiducial volume.

# Appendix B

## Formulas of 3+1 Model

### B.1 Generic Formulas

One can define a unitary matrix  $U$  as

$$|\nu_\alpha\rangle = \sum_i U_{\alpha i}^* |\nu_i\rangle, \quad (\text{B.1})$$

where  $|\nu_\alpha\rangle$  and  $|\nu_i\rangle$  are the flavor and mass eigen states, respectively. In 3+1 scenario (3 active neutrinos and 1 sterile neutrino),  $U$  is a  $4 \times 4$  matrix. Its complex conjugate can be written as

$$\begin{aligned} \langle \nu_\alpha | &= \left( \sum_i U_{\alpha i}^* |\nu_i\rangle \right)^\dagger \\ &= \sum_i U_{\alpha i} \langle \nu_i | \end{aligned} \quad (\text{B.2})$$

Given  $|\nu_i(t)\rangle = e^{-i(E_i t - p_i L)} |\nu_i\rangle$ , the time evolution of a flavor state can be written as

$$|\nu_\alpha(t)\rangle = \sum_i U_{\alpha i}^* e^{-i(E_i t - p_i L)} |\nu_i\rangle \quad (\text{B.3})$$

The oscillation probability can be written as

$$\begin{aligned}
P(\nu_\alpha \rightarrow \nu_\beta) &= |\langle \nu_\alpha | \nu_\beta(t) \rangle|^2 \\
&= \left| \left( \sum_i U_{\alpha i} \langle \nu_i | \right) \left( \sum_j U_{\beta j}^* e^{-i(E_j t - p_j L)} | \nu_j \rangle \right) \right|^2 \\
&= \left| \sum_{ij} \delta_{ij} U_{\alpha i} U_{\beta j}^* e^{-i(E_j t - p_j L)} \right|^2 \\
&= \left| \sum_i U_{\alpha i} U_{\beta i}^* e^{-i(E_i t - p_i L)} \right|^2 \\
&= \left( \sum_i U_{\alpha i} U_{\beta i}^* e^{-i(E_i t - p_i L)} \right) \left( \sum_j U_{\alpha j} U_{\beta j}^* e^{-i(E_j t - p_j L)} \right)^* \\
&= \sum_{ij} U_{\alpha i} U_{\alpha j}^* U_{\beta i}^* U_{\beta j} e^{-i[(E_i - E_j)t - (p_i - p_j)L]} \\
&= \sum_{ij} U_{\alpha i} U_{\alpha j}^* U_{\beta i}^* U_{\beta j} e^{-i\Delta_{ij}}, \tag{B.4}
\end{aligned}$$

where in the last step  $\Delta_{ij} \equiv (E_i - E_j)t - (p_i - p_j)L$ . Since

$$\begin{aligned}
&\sum_{ij} U_{\alpha i} U_{\alpha j}^* U_{\beta i}^* U_{\beta j} \\
&= \sum_i U_{\alpha i} U_{\alpha j}^* \sum_j U_{\beta i}^* U_{\beta j} \\
&= \delta_{\alpha\beta} \delta_{\alpha\beta} \\
&= \delta_{\alpha\beta}. \tag{B.5}
\end{aligned}$$

Adding and subtracting this term in  $P(\nu_\alpha \rightarrow \nu_\beta)$  we have

$$\begin{aligned}
P(\nu_\alpha \rightarrow \nu_\beta) &= \sum_{ij} U_{\alpha i} U_{\alpha j}^* U_{\beta i}^* U_{\beta j} e^{-i\Delta_{ij}} + \sum_{ij} U_{\alpha i} U_{\alpha j}^* U_{\beta i}^* U_{\beta j} - \sum_{ij} U_{\alpha i} U_{\alpha j}^* U_{\beta i}^* U_{\beta j} \\
&= \delta_{\alpha\beta} + \sum_{ij} U_{\alpha i} U_{\alpha j}^* U_{\beta i}^* U_{\beta j} (e^{-i\Delta_{ij}} - 1). \tag{B.6}
\end{aligned}$$

The second term can be evaluated in terms of  $i > j$ ,  $i = j$  and  $i < j$ .

When  $i = j$  it gives 0. When  $i < j$ ,

$$\begin{aligned}
&\sum_{i < j} U_{\alpha i} U_{\alpha j}^* U_{\beta i}^* U_{\beta j} (e^{-i\Delta_{ij}} - 1) \\
&= \sum_{j < i} U_{\alpha j} U_{\alpha i}^* U_{\beta j}^* U_{\beta i} (e^{-i\Delta_{ji}} - 1) \\
&= \sum_{i > j} [U_{\alpha i} U_{\alpha j}^* U_{\beta i}^* U_{\beta j} (e^{-i\Delta_{ij}} - 1)]^*. \tag{B.7}
\end{aligned}$$

Plugging this into Equation B.6 gives

$$\begin{aligned}
P(\nu_\alpha \rightarrow \nu_\beta) &= \delta_{\alpha\beta} + \sum_{i > j} \{ U_{\alpha i} U_{\alpha j}^* U_{\beta i}^* U_{\beta j} (e^{-i\Delta_{ij}} - 1) + [U_{\alpha i} U_{\alpha j}^* U_{\beta i}^* U_{\beta j} (e^{-i\Delta_{ij}} - 1)]^* \} \\
&= \delta_{\alpha\beta} + \sum_{i > j} 2\Re [U_{\alpha i} U_{\alpha j}^* U_{\beta i}^* U_{\beta j} (e^{-i\Delta_{ij}} - 1)] \\
&= \delta_{\alpha\beta} + 2 \sum_{i > j} \Re [U_{\alpha i} U_{\alpha j}^* U_{\beta i}^* U_{\beta j}] (\cos \Delta_{ij} - 1) \\
&\quad + 2 \sum_{i > j} \Im [U_{\alpha i} U_{\alpha j}^* U_{\beta i}^* U_{\beta j}] \sin \Delta_{ij}. \tag{B.8}
\end{aligned}$$

Considering  $\cos \Delta_{ij} = 1 - 2 \sin^2 (\Delta_{ij}/2)$ , the result can be rewritten as

$$\begin{aligned}
P(\nu_\alpha \rightarrow \nu_\beta) &= \delta_{\alpha\beta} - 4 \sum_{i > j} \Re [U_{\alpha i} U_{\alpha j}^* U_{\beta i}^* U_{\beta j}] \sin^2 (\Delta_{ij}/2) \\
&\quad + 2 \sum_{i > j} \Im [U_{\alpha i} U_{\alpha j}^* U_{\beta i}^* U_{\beta j}] \sin \Delta_{ij}. \tag{B.9}
\end{aligned}$$

$\Delta_{ij}$  can be expressed as a function of the neutrino mass splitting. Since average neutrino speed  $v$  can be approximated as  $(p_i + p_j)/(E_i + E_j)$  given  $\beta = v = p/E$ , the time of flight becomes  $t = L/v \approx L(E_i + E_j)/(p_i + p_j)$ , and

$$\begin{aligned}\Delta_{ij} &= (E_i - E_j)t - (p_i - p_j)L \\ &= \frac{E_i^2 - E_j^2}{p_i + p_j}L - \frac{p_i^2 - p_j^2}{p_i + p_j}L \\ &= \frac{m_i^2 - m_j^2}{2E}L,\end{aligned}\tag{B.10}$$

where  $p_i \approx p_j \approx E$  was used.  $E$  is the initial neutrino energy.

## B.2 $\nu_\mu \rightarrow \nu_e$ Channel

The oscillation probability of  $\nu_\mu \rightarrow \nu_e$  can be written as

$$\begin{aligned}P(\nu_\mu \rightarrow \nu_e) &= \delta_{\mu e} - 4 \sum_{i>j} \Re [U_{\mu i} U_{\mu j}^* U_{e i}^* U_{e j}] \sin^2 (\Delta_{ij}/2) \\ &\quad + 2 \sum_{i>j} \Im [U_{\mu i} U_{\mu j}^* U_{e i}^* U_{e j}] \sin \Delta_{ij}.\end{aligned}\tag{B.11}$$

The Kronecker delta  $\delta_{\mu e}$  gives 0. The sum in the second term can be



broken down

$$\begin{aligned}
& \sum_{i>j} \Re [U_{\mu i} U_{\mu j}^* U_{e i}^* U_{e j}] \sin^2 (\Delta_{ij}/2) \\
&= \Re (U_{\mu 2} U_{\mu 1}^* U_{e 2}^* U_{e 1}) \sin^2 (\Delta_{21}/2) \\
&\quad + \Re (U_{\mu 3} U_{\mu 1}^* U_{e 3}^* U_{e 1}) \sin^2 (\Delta_{31}/2) \\
&\quad + \Re (U_{\mu 4} U_{\mu 1}^* U_{e 4}^* U_{e 1}) \sin^2 (\Delta_{41}/2) \\
&\quad + \Re (U_{\mu 3} U_{\mu 2}^* U_{e 3}^* U_{e 2}) \sin^2 (\Delta_{32}/2) \\
&\quad + \Re (U_{\mu 4} U_{\mu 2}^* U_{e 4}^* U_{e 2}) \sin^2 (\Delta_{42}/2) \\
&\quad + \Re (U_{\mu 4} U_{\mu 3}^* U_{e 4}^* U_{e 3}) \sin^2 (\Delta_{43}/2). \tag{B.12}
\end{aligned}$$

Assuming a large mass splitting between the sterile neutrino and active neutrinos, we have  $\Delta_{41} \approx \Delta_{42} \approx \Delta_{43}$  and  $\sin^2 \Delta_{21} \approx \sin^2 \Delta_{31} \approx \sin^2 \Delta_{32}$ , therefore

$$\begin{aligned}
& -4 \sum_{i>j} \Re (U_{\mu i} U_{\mu j}^* U_{e i}^* U_{e j}) \sin^2 (\Delta_{ij}/2) \\
&= -4 \sin^2 (\Delta_{41}/2) \Re (U_{\mu 4} U_{\mu 1}^* U_{e 4}^* U_{e 1} + U_{\mu 4} U_{\mu 2}^* U_{e 4}^* U_{e 2} + U_{\mu 4} U_{\mu 3}^* U_{e 4}^* U_{e 3}) \\
&= -4 \sin^2 (\Delta_{41}/2) \Re [U_{\mu 4} U_{e 4}^* (U_{\mu 1}^* U_{e 1} + U_{\mu 2}^* U_{e 2} + U_{\mu 3}^* U_{e 3})] \\
&= 4 \sin^2 (\Delta_{41}/2) \Re (U_{\mu 4} U_{e 4}^* U_{\mu 4}^* U_{e 4}) \\
&= 4 \sin^2 (\Delta_{41}/2) |U_{\mu 4}|^2 |U_{e 4}|^2, \tag{B.13}
\end{aligned}$$

where the unitary condition of  $U$  was used

$$U_{\mu 1} U_{e 1}^* + U_{\mu 2} U_{e 2}^* + U_{\mu 3} U_{e 3}^* + U_{\mu 4} U_{e 4}^* = 0. \tag{B.14}$$

Similarly The third term in Equation B.11 is evaluated as

$$\begin{aligned}
& 2 \sum_{i>j} \Im (U_{\mu i} U_{\mu j}^* U_{e i}^* U_{e j}) \sin \Delta_{ij} \\
&= -4 \sin(\Delta_{41}) \Im (|U_{\mu 4}|^2 |U_{e 4}|^2) \\
&= 0.
\end{aligned} \tag{B.15}$$

$\nu_\mu$  to  $\nu_e$  oscillation probability is now simplified to

$$\begin{aligned}
P(\nu_\mu \rightarrow \nu_e) &= 4 \sin^2 (\Delta_{41}/2) |U_{\mu 4}|^2 |U_{e 4}|^2 \\
&\equiv 4 \sin^2 (\Delta_{41}/2) \sin^2 \theta_{\mu e},
\end{aligned} \tag{B.16}$$

where  $\sin^2 \theta_{\mu e} \equiv |U_{\mu 4}|^2 |U_{e 4}|^2$ .

### B.3 $\nu_\mu \rightarrow \nu_\mu$ Channel

In the case of  $\nu_\mu \rightarrow \nu_\mu$ , Equation B.9 takes the form

$$\begin{aligned}
P(\nu_\mu \rightarrow \nu_\mu) &= \delta_{\mu\mu} - 4 \sum_{i>j} \Re (U_{\mu i} U_{\mu j}^* U_{\mu i}^* U_{\mu j}) \sin^2 (\Delta_{ij}/2) \\
&\quad + 2 \sum_{i>j} \Im (U_{\mu i} U_{\mu j}^* U_{\mu i}^* U_{\mu j}) \sin \Delta_{ij} \\
&= 1 - 4 \sum_{i>j} \Re (|U_{\mu i}|^2 |U_{\mu j}|^2) \sin^2 (\Delta_{ij}/2) \\
&\quad + 2 \sum_{i>j} \Im (|U_{\mu i}|^2 |U_{\mu j}|^2) \sin \Delta_{ij} \\
&= 1 - 4 \sum_{i>j} |U_{\mu i}|^2 |U_{\mu j}|^2 \sin^2 (\Delta_{ij}/2)
\end{aligned} \tag{B.17}$$

Using the approximation  $m_1 \approx m_2$ , we have  $\Delta_{21} = 0$ ,  $\Delta_{41} = \Delta_{42}$ ,

$\Delta_{32} = \Delta_{31}$ . The probability becomes

$$\begin{aligned}
P(\nu_\mu \rightarrow \nu_\mu) &= 1 - 4 |U_{\mu 3}|^2 (|U_{\mu 1}|^2 + |U_{\mu 2}|^2) \sin^2 (\Delta_{31}/2) \\
&\quad + 4 |U_{\mu 4}|^2 (|U_{\mu 1}|^2 + |U_{\mu 2}|^2) \sin^2 (\Delta_{41}/2) \\
&\quad + 4 |U_{\mu 4}|^2 |U_{\mu 3}|^2 \sin^2 (\Delta_{43}/2) \\
&= 1 - 4 |U_{\mu 3}|^2 (1 - |U_{\mu 3}|^2 + |U_{\mu 4}|^2) \sin^2 (\Delta_{31}/2) \\
&\quad + 4 |U_{\mu 4}|^2 (1 - |U_{\mu 3}|^2 + |U_{\mu 4}|^2) \sin^2 (\Delta_{41}/2) \\
&\quad + 4 |U_{\mu 4}|^2 |U_{\mu 3}|^2 \sin^2 (\Delta_{43}/2), \tag{B.18}
\end{aligned}$$

where in the last step the unitary condition  $|U_{\mu 1}|^2 + |U_{\mu 2}|^2 + |U_{\mu 3}|^2 + |U_{\mu 4}|^2 = 1$  was used. In the case of  $m_4 \gg m_1$ ,  $\sin^2 (\Delta_{41}/2)$  and  $\sin^2 (\Delta_{43}/2)$  can be taken as 0.5 (e.g. MINOS sterile paper in 2010 [107]). However including them may explain the wiggles that appears in the FD data. Note that  $\Delta_{41} = \Delta_{43} + \Delta_{31}$ .

#### B.4 $\nu_\mu \rightarrow \nu_s$ Channel

In the case of  $\nu_\mu \rightarrow \nu_s$ , Equation B.9 gives

$$\begin{aligned}
P(\nu_\mu \rightarrow \nu_s) &= -4 \sum_{i>j} \Re (U_{\mu i} U_{\mu j}^* U_{s i}^* U_{s j}) \sin^2 (\Delta_{ij}/2) \\
&\quad + 2 \sum_{i>j} \Im (U_{\mu i} U_{\mu j}^* U_{s i}^* U_{s j}) \sin \Delta_{ij} \tag{B.19}
\end{aligned}$$

Using the approximation that  $m_1 \approx m_2$ , we have  $\Delta_{21} = 0$ ,  $\Delta_{41} = \Delta_{42}$ ,

$\Delta_{32} = \Delta_{31}$ , the sum in the first term can be computed as

$$\begin{aligned}
& \sum_{i>j} \Re (U_{\mu i} U_{\mu j}^* U_{s i}^* U_{s j}) \sin^2 (\Delta_{ij}/2) \\
&= \Re (U_{\mu 2} U_{\mu 1}^* U_{s 2}^* U_{s 1}) \sin^2 (\Delta_{21}/2) \\
&\quad + \Re (U_{\mu 3} U_{\mu 1}^* U_{s 3}^* U_{s 1}) \sin^2 (\Delta_{31}/2) \\
&\quad + \Re (U_{\mu 4} U_{\mu 1}^* U_{s 4}^* U_{s 1}) \sin^2 (\Delta_{41}/2) \\
&\quad + \Re (U_{\mu 3} U_{\mu 2}^* U_{s 3}^* U_{s 2}) \sin^2 (\Delta_{32}/2) \\
&\quad + \Re (U_{\mu 4} U_{\mu 2}^* U_{s 4}^* U_{s 2}) \sin^2 (\Delta_{42}/2) \\
&\quad + \Re (U_{\mu 4} U_{\mu 3}^* U_{s 4}^* U_{s 3}) \sin^2 (\Delta_{43}/2) \\
&= \Re [U_{\mu 3} U_{s 3}^* (U_{\mu 1}^* U_{s 1} + U_{\mu 2}^* U_{s 2})] \sin^2 (\Delta_{31}/2) \\
&\quad + \Re [U_{\mu 4} U_{s 4}^* (U_{\mu 1}^* U_{s 1} + U_{\mu 2}^* U_{s 2})] \sin^2 (\Delta_{41}/2) \\
&\quad + \Re (U_{\mu 4} U_{\mu 3}^* U_{s 4}^* U_{s 3}) \sin^2 (\Delta_{43}/2) \\
&= -\Re [U_{\mu 3} U_{s 3}^* (U_{\mu 3}^* U_{s 3} + U_{\mu 4}^* U_{s 4})] \sin^2 (\Delta_{31}/2) \\
&\quad - \Re [U_{\mu 4} U_{s 4}^* (U_{\mu 3}^* U_{s 3} + U_{\mu 4}^* U_{s 4})] \sin^2 (\Delta_{41}/2) \\
&\quad + \Re (U_{\mu 4} U_{\mu 3}^* U_{s 4}^* U_{s 3}) \sin^2 (\Delta_{43}/2) \\
&= -|U_{\mu 3}|^2 |U_{s 3}|^2 \sin^2 (\Delta_{31}/2) - |U_{\mu 4}|^2 |U_{s 4}|^2 \sin^2 (\Delta_{41}/2) \\
&\quad + \Re (U_{\mu 4} U_{\mu 3}^* U_{s 4}^* U_{s 3}) [\sin^2 (\Delta_{43}/2) - \sin^2 (\Delta_{41}/2) - \sin^2 (\Delta_{31}/2)] \quad (\text{B.20})
\end{aligned}$$

Similarly,

$$\begin{aligned}
& \sum_{i>j} \Im (U_{\mu i} U_{\mu j}^* U_{s i}^* U_{s j}) \sin (\Delta_{ij}) \\
&= \Im (U_{\mu 4} U_{\mu 3}^* U_{s 4}^* U_{s 3}) [\sin^2 (\Delta_{43}/2) - \sin^2 (\Delta_{41}/2) + \sin^2 (\Delta_{31}/2)]. \quad (\text{B.21})
\end{aligned}$$

Adding the two terms above gives  $\nu_\mu \rightarrow \nu_s$  oscillation probability

$$\begin{aligned}
P(\nu_\mu \rightarrow \nu_s) &= 4 |U_{\mu 3}|^2 |U_{s 3}|^2 \sin^2 (\Delta_{31}/2) 4 |U_{\mu 4}|^2 |U_{s 4}|^2 \sin^2 (\Delta_{41}/2) \\
&\quad - 4 \Re (U_{\mu 4} U_{\mu 3}^* U_{s 4}^* U_{s 3}) [\sin^2 (\Delta_{43}/2) - \sin^2 (\Delta_{41}/2) - \sin^2 (\Delta_{31}/2)] \\
&\quad + 2 \Im (U_{\mu 4} U_{\mu 3}^* U_{s 4}^* U_{s 3}) [\sin^2 (\Delta_{43}/2) - \sin^2 (\Delta_{41}/2) + \sin^2 (\Delta_{31}/2)].
\end{aligned}
\tag{B.22}$$

## Appendix C

### Formulas of Large Extra Dimension Model

#### C.1 From Action to Lagrangian

In Reference [70], the action of the LED model in  $(4 + 1)$  dimensions is given as

$$S = \int d^4x dy i \bar{\Psi}^\alpha \Gamma^A \partial_A \Psi^\alpha + \int d^4x \left( i \bar{\nu}_L^{\alpha(0)} \gamma^\mu \partial_\mu \nu_L^{\alpha(0)} + \lambda_{\alpha\beta} H \bar{\nu}_L^{\alpha(0)} \psi_R^\beta(x, 0) + \text{h.c.} \right). \quad (\text{C.1})$$

Various notations appearing above will be explained throughout this chapter. Starting from the first term,  $\alpha$  is the flavor index running over  $e, \mu$  and  $\tau$ .  $\Gamma^A$  ( $A = 0, 1, \dots, 4$ ) are 5 dimensional gamma matrices. Using chiral basis [135], we have

$$\Gamma^0 = \begin{pmatrix} & -I_2 \\ -I_2 & \end{pmatrix}, \quad \Gamma^i = \begin{pmatrix} & \sigma^i \\ -\sigma^i & \end{pmatrix} \quad \text{and} \quad \Gamma^5 = \begin{pmatrix} I_2 & \\ & -I_2 \end{pmatrix}, \quad (\text{C.2})$$

where  $I_2$  is the  $2 \times 2$  identity matrix and  $\sigma_i$  ( $i = 1, 2, 3$ ) are Pauli matrices

$$\sigma^1 = \begin{pmatrix} & 1 \\ 1 & \end{pmatrix}, \quad \sigma^2 = \begin{pmatrix} & -i \\ i & \end{pmatrix}, \quad \sigma^3 = \begin{pmatrix} 1 & \\ & -1 \end{pmatrix}. \quad (\text{C.3})$$

According to [136],  $\Gamma^4$  can be constructed as

$$\Gamma^4 = i\Gamma^5 = \begin{pmatrix} iI_2 & \\ & -iI_2 \end{pmatrix}. \quad (\text{C.4})$$

in order to satisfy the Clifford algebra  $\{\Gamma^M, \Gamma^N\} = 2\eta^{MN}$  where  $\eta$  is the metric tensor. Using these definitions, we have the following equivalences

$$\Gamma^0\Gamma^0 = \begin{pmatrix} & -I_2 \\ -I_2 & \end{pmatrix} \begin{pmatrix} & -I_2 \\ -I_2 & \end{pmatrix} = I_4, \quad (\text{C.5})$$

$$\Gamma^0\Gamma^i = \begin{pmatrix} & -I_2 \\ -I_2 & \end{pmatrix} \begin{pmatrix} & \sigma_i \\ -\sigma_i & \end{pmatrix} = \begin{pmatrix} \sigma_i & \\ & -\sigma_i \end{pmatrix}, \quad (\text{C.6})$$

$$\Gamma^0\Gamma^4 = \begin{pmatrix} & -I_2 \\ -I_2 & \end{pmatrix} \begin{pmatrix} iI_2 & \\ & -iI_2 \end{pmatrix} = \begin{pmatrix} & iI_2 \\ -iI_2 & \end{pmatrix}. \quad (\text{C.7})$$

Left-handed and right-handed states are defined as

$$\psi_L = \frac{1}{2} (1 - \Gamma^5) \Psi = \begin{pmatrix} 0 & 0 \\ 0 & I_2 \end{pmatrix} \Psi, \quad (\text{C.8})$$

$$\psi_R = \frac{1}{2} (1 + \Gamma^5) \Psi = \begin{pmatrix} I_2 & 0 \\ 0 & 0 \end{pmatrix} \Psi, \quad (\text{C.9})$$

and one can write

$$\Psi \equiv \begin{pmatrix} \psi_R \\ \psi_L \end{pmatrix}. \quad (\text{C.10})$$

The integrand of the first term in the action decomposes as

$$\bar{\Psi}^\alpha \Gamma^A \partial_A \Psi^\alpha = \bar{\Psi}^\alpha \Gamma^\mu \partial_\mu \Psi^\alpha + \bar{\Psi}^\alpha \Gamma^4 \partial_4 \Psi^\alpha. \quad (\text{C.11})$$

The second term above can be written as

$$\begin{aligned} \bar{\Psi}^\alpha \Gamma^4 \partial_4 \Psi^\alpha &= \bar{\Psi}^{\alpha\dagger} \Gamma^0 \Gamma^4 \partial_4 \Psi^\alpha \\ &= \begin{pmatrix} \psi_R^{\alpha\dagger} & \psi_L^{\alpha\dagger} \end{pmatrix} \begin{pmatrix} & iI_2 \\ -iI_2 & \end{pmatrix} \begin{pmatrix} \partial_4 \psi_R^\alpha \\ \partial_4 \psi_L^\alpha \end{pmatrix} \\ &= -i\psi_L^{\alpha\dagger} \partial_4 \psi_R^\alpha + i\psi_R^{\alpha\dagger} \partial_4 \psi_L^\alpha. \end{aligned} \quad (\text{C.12})$$

Periodicity of the field in the curved dimension  $\Psi(y) = \Psi(y + 2\pi R)$  allows for a Fourier expansion [68, 136]

$$\begin{aligned}\psi_L^\alpha(x, y) &= \sum_{n=-\infty}^{+\infty} \frac{1}{\sqrt{2\pi R}} \psi_L^{\alpha(n)} e^{-i\frac{ny}{R}}, \\ \psi_R^\alpha(x, y) &= \sum_{n=-\infty}^{+\infty} \frac{1}{\sqrt{2\pi R}} \psi_R^{\alpha(n)} e^{-i\frac{ny}{R}}.\end{aligned}\tag{C.13}$$

Inserting Equation C.13 into C.12, we have its first term

$$\begin{aligned}& \int d^4x dy \left( -i\psi_L^{\alpha\dagger} \partial_4 \psi_R^\alpha \right) \\ &= -i \int d^4x dy \left( \sum_{n=-\infty}^{+\infty} \frac{1}{\sqrt{2\pi R}} \psi_L^{\alpha(n)\dagger} e^{i\frac{ny}{R}} \right) \left( \sum_{m=-\infty}^{+\infty} \frac{1}{\sqrt{2\pi R}} \psi_R^{\alpha(m)} \left( -i\frac{m}{R} \right) e^{-i\frac{my}{R}} \right) \\ &= -\frac{1}{2\pi R} \int d^4x \sum_{m,n} \frac{m}{R} \psi_L^{\alpha(n)\dagger} \psi_R^{\alpha(m)} \int dy e^{-i\frac{(m-n)y}{R}} \\ &= -\frac{1}{2\pi R} \int d^4x \sum_{m,n} \frac{m}{R} \psi_L^{\alpha(n)\dagger} \psi_R^{\alpha(m)} (2\pi R \delta_{mn}) \\ &= - \int d^4x \sum_{n=-\infty}^{+\infty} \frac{n}{R} \psi_L^{\alpha(n)\dagger} \psi_R^{\alpha(n)} \\ &= - \int d^4x \sum_{n=1}^{+\infty} \frac{n}{R} \left( \psi_L^{\alpha(n)\dagger} \psi_R^{\alpha(n)} + \psi_L^{\alpha(-n)\dagger} \psi_R^{\alpha(-n)} \right),\end{aligned}\tag{C.14}$$

and the second term is simply the Hermitian conjugate of Equation C.14. By defining a few new states

$$\nu_R^{\alpha(n)} \equiv \frac{1}{\sqrt{2}} \left( \psi_R^{\alpha(n)} + \psi_R^{\alpha(-n)} \right),\tag{C.15}$$

$$\nu_R^{\prime\alpha(n)} \equiv \frac{1}{\sqrt{2}} \left( \psi_R^{\alpha(n)} - \psi_R^{\alpha(-n)} \right),\tag{C.16}$$

$$\nu_L^{\alpha(n)} \equiv \frac{1}{\sqrt{2}} \left( \psi_L^{\alpha(n)} + \psi_L^{\alpha(-n)} \right),\tag{C.17}$$

$$\nu_L^{\prime\alpha(n)} \equiv \frac{1}{\sqrt{2}} \left( \psi_L^{\alpha(n)} - \psi_L^{\alpha(-n)} \right),\tag{C.18}$$



where  $n > 0$ , the integrand of Equation C.14 becomes

$$\sum_{n=1}^{+\infty} \frac{n}{R} \left( \psi_L^{\alpha(n)\dagger} \psi_R^{\alpha(n)} + \psi_L^{\alpha(-n)\dagger} \psi_R^{\alpha(-n)} \right) = \sum_{n=1}^{+\infty} \frac{n}{R} \left( \nu_L^{\alpha(n)\dagger} \nu_R^{\alpha(n)} + \nu_L^{\prime\alpha(-n)\dagger} \nu_R^{\prime\alpha(-n)} \right) \quad (\text{C.19})$$

This is the first mass term that appears in the Lagrangian and the rest comes from the Higgs coupling term  $\lambda_{\alpha\beta} H \bar{\nu}_L^\alpha \psi_R^\beta(x, 0)$  in Equation C.1. Setting the Higgs field to its vacuum expectation value (VEV) and expanding  $\psi_R^\beta(x, 0)$  gives

$$\begin{aligned} & m_{\alpha\beta} \bar{\nu}_L^{\alpha(0)} \psi_R^\beta(x, 0) \\ &= m_{\alpha\beta} \bar{\nu}_L^{\alpha(0)} \left[ \psi_R^{\beta(0)} + \sum_{n=1}^{+\infty} \left( \psi_R^{\beta(n)} + \psi_R^{\beta(-n)} \right) \right] \\ &= m_{\alpha\beta} \bar{\nu}_L^{\alpha(0)} \left[ \nu_R^{\beta(0)} + \sqrt{2} \sum_{n=1}^{+\infty} \nu_R^{\beta(n)} \right], \end{aligned} \quad (\text{C.20})$$

where the following definitions were used

$$\nu_R^{\beta(0)} \equiv \psi_R^{\beta(0)}, \quad (\text{C.21})$$

$$\nu_L^{\beta(0)} \equiv \psi_L^{\beta(0)}. \quad (\text{C.22})$$

Combining Equation C.19 and Equation C.20, we have

$$\begin{aligned} \mathcal{L} &= \sum_{n=1}^{+\infty} \frac{n}{R} \left( \nu_L^{\alpha(n)\dagger} \nu_R^{\alpha(n)} + \nu_L^{\prime\alpha(-n)\dagger} \nu_R^{\prime\alpha(-n)} \right) \\ &\quad + m_{\alpha\beta} \bar{\nu}_L^{\alpha(0)} \left[ \nu_R^{\beta(0)} + \sqrt{2} \sum_{n=1}^{+\infty} \nu_R^{\beta(n)} \right] + \text{h.c.} \end{aligned} \quad (\text{C.23})$$

Since  $\nu_L^{\prime\alpha(-n)\dagger} \nu_R^{\prime\alpha(-n)}$  are decoupled from the rest of the terms and we are only interested in the active neutrino states, the Lagrangian can be simplified to

$$\mathcal{L} = \sum_{n=1}^{+\infty} \frac{n}{R} \left( \nu_L^{\alpha(n)\dagger} \nu_R^{\alpha(n)} \right) + m_{\alpha\beta} \bar{\nu}_L^{\alpha(0)} \left[ \nu_R^{\beta(0)} + \sqrt{2} \sum_{n=1}^{+\infty} \nu_R^{\beta(n)} \right] + \text{h.c.} \quad (\text{C.24})$$

## C.2 From Lagrangian to Oscillation Probabilities

Following Reference [70], the mass terms in the Lagrangian of the LED model take the form

$$m_{\alpha\beta} \left( \bar{\nu}_R^{\alpha(0)} \nu_L^{\beta(0)} + \sqrt{2} \sum_{n=1}^{\infty} \bar{\nu}_R^{\alpha(n)} \nu_L^{\beta(0)} \right) + \sum_{n=1}^{\infty} \frac{n}{R} \bar{\nu}_R^{\alpha(n)} \nu_L^{\alpha(n)} + \text{h.c.}, \quad (\text{C.25})$$

where  $\alpha, \beta = 1, 2, 3$ .  $\nu_L^{\beta(0)}$  are the active neutrino states, i.e.  $\nu_e, \nu_\mu$  and  $\nu_\tau$ .  $\nu_L^{\beta(n)}$  are the excited KK states which do not have standard model charges and therefore are considered as sterile neutrinos.  $m$  is the Dirac mass matrix

$$m = \begin{pmatrix} m_{11} & m_{12} & m_{13} \\ m_{21} & m_{22} & m_{23} \\ m_{31} & m_{32} & m_{33} \end{pmatrix}, \quad (\text{C.26})$$

which can be diagonalized as  $U m_d U^{-1}$  where  $U$  is the PMNS matrix and

$$m_d = \begin{pmatrix} m_1 & & \\ & m_2 & \\ & & m_3 \end{pmatrix}. \quad (\text{C.27})$$

Defining

$$\bar{\nu}_R^{(n)} \equiv \begin{pmatrix} \bar{\nu}_R^{1(n)} \\ \bar{\nu}_R^{2(n)} \\ \bar{\nu}_R^{3(n)} \end{pmatrix} \text{ and } \nu_L^{(n)} \equiv \begin{pmatrix} \nu_L^{1(n)} \\ \nu_L^{2(n)} \\ \nu_L^{3(n)} \end{pmatrix} \text{ where } n = 0, 1, 2, \dots, \quad (\text{C.28})$$

Equation C.25 can be written in the matrix form

$$\begin{pmatrix} \bar{\nu}_R^{(0)} & \bar{\nu}_R^{(1)} & \bar{\nu}_R^{(2)} & \cdots & \bar{\nu}_R^{(N)} \end{pmatrix} \begin{pmatrix} m & & & & \\ \sqrt{2}m & \frac{1}{R}I_3 & & & \\ \sqrt{2}m & & \frac{2}{R}I_3 & & \\ \sqrt{2}m & & & \frac{3}{R}I_3 & \\ \vdots & & & & \ddots \\ \sqrt{2}m & & & & & \frac{N}{R}I_3 \end{pmatrix} \begin{pmatrix} \nu_L^{(0)} \\ \nu_L^{(1)} \\ \nu_L^{(2)} \\ \vdots \\ \nu_L^{(N)} \end{pmatrix}, \quad (\text{C.29})$$

where  $N$  takes the limit of  $+\infty$  (the same for the rest of this note) and  $I_3$  is the  $3 \times 3$  unit matrix

$$I_3 = \begin{pmatrix} 1 & & \\ & 1 & \\ & & 1 \end{pmatrix}. \quad (\text{C.30})$$

This can be simply expressed as  $\bar{\nu}_R M \nu_L$  by defining

$$\bar{\nu}_R \equiv \left( \bar{\nu}_R^{(0)} \quad \bar{\nu}_R^{(1)} \quad \bar{\nu}_R^{(2)} \quad \cdots \quad \bar{\nu}_R^{(N)} \right), \nu_L \equiv \begin{pmatrix} \nu_L^{(0)} \\ \nu_L^{(1)} \\ \nu_L^{(2)} \\ \vdots \\ \nu_L^{(N)} \end{pmatrix} \quad (\text{C.31})$$

and

$$M \equiv \begin{pmatrix} m & & & & & & \\ \sqrt{2}m & \frac{1}{R}I_3 & & & & & \\ \sqrt{2}m & & \frac{2}{R}I_3 & & & & \\ \sqrt{2}m & & & \frac{3}{R}I_3 & & & \\ \vdots & & & & \ddots & & \\ \sqrt{2}m & & & & & & \frac{N}{R}I_3 \end{pmatrix}. \quad (\text{C.32})$$

The strategy is to diagonalize  $M$  and find the matrix that connects mass eigenstates and flavor eigenstates. Firstly, diagonalizing  $m$  within  $M$  gives  $M = PM_dP^{-1}$  where

$$P = \begin{pmatrix} U & & & & & & \\ & U & & & & & \\ & & U & & & & \\ & & & \ddots & & & \\ & & & & U & & \end{pmatrix} \text{ and } M_d \equiv \begin{pmatrix} m_d & & & & & & \\ \sqrt{2}m_d & \frac{1}{R}I_3 & & & & & \\ \sqrt{2}m_d & & \frac{2}{R}I_3 & & & & \\ \sqrt{2}m_d & & & \frac{3}{R}I_3 & & & \\ \vdots & & & & \ddots & & \\ \sqrt{2}m_d & & & & & & \frac{N}{R}I_3 \end{pmatrix}. \quad (\text{C.33})$$

The second step is to diagonalize  $M_d$ . To do this, it is convenient to diagonalize  $R^2 M_d^\dagger M_d$  which is a Hermitian matrix that takes the form

$$R^2 M_d^\dagger M_d = \begin{pmatrix} \xi^2(N + 1/2) & \xi & 2\xi & 3\xi & \dots & N\xi \\ \xi & I_3 & & & & \\ 2\xi & & 2^2 I_3 & & & \\ 3\xi & & & 3^2 I_3 & & \\ \vdots & & & & \ddots & \\ N\xi & & & & & N^2 I_3 \end{pmatrix}, \quad (\text{C.34})$$

where

$$\xi \equiv \sqrt{2} R m_d = \begin{pmatrix} \sqrt{2} R m_1 & & \\ & \sqrt{2} R m_2 & \\ & & \sqrt{2} R m_3 \end{pmatrix} \equiv \begin{pmatrix} \xi_1 & & \\ & \xi_2 & \\ & & \xi_3 \end{pmatrix}. \quad (\text{C.35})$$

Note that  $\xi_i \equiv \sqrt{2} R m_i$  and  $\xi^2 \equiv \xi \xi$ . As a Hermitian matrix,  $R^2 M_d^\dagger M_d$  can be diagonalized by a unitary matrix  $L$ , i.e.

$$R^2 M_d^\dagger M_d = L M_D^2 L^{-1}, \quad (\text{C.36})$$

where  $M_D^2 \equiv M_D M_D$  is a real diagonal matrix with its non-zero diagonal elements being the eigen values of  $R^2 M_d^\dagger M_d$  and the columns of  $L$  are the corresponding eigen states. Introducing a unitary matrix  $V$  allows us to rewrite Equation C.36

$$\begin{aligned} R^2 M_d^\dagger M_d &= L M_D^2 L^{-1} \\ &= L M_D V^\dagger V M_D L^{-1} \\ &= (V M_D L^{-1})^\dagger (V M_D L^{-1}). \end{aligned} \quad (\text{C.37})$$

$V$  can always be defined such that

$$R M_d = V M_D L^{-1} \quad (\text{C.38})$$

or

$$M_d = V (M_D/R) L^{-1}. \quad (\text{C.39})$$

Therefore

$$\begin{aligned} \bar{\nu}_R M \nu_L &= \bar{\nu}_R P M_d P^{-1} \nu_L \\ &= (\bar{\nu}_R P V) (M_D/R) (L^{-1} P^{-1} \nu_L) \\ &= (\bar{\nu}_R P V) (M_D/R) \chi_L, \end{aligned} \quad (\text{C.40})$$

where  $\chi_L \equiv L^{-1} P^{-1} \nu_L$  is the mass eigen state.  $M_D$  and  $L^{-1}$  can be found by solving  $R^2 M^\dagger M$  for its eigen values and eigen states. Eigen value  $\lambda^2$  should satisfy the characteristic equation

$$\begin{vmatrix} \xi^2(N+1/2) - \lambda^2 & \xi & 2\xi & 3\xi & \dots & N\xi \\ \xi & (1^2 - \lambda^2) I_3 & & & & \\ 2\xi & & (2^2 - \lambda^2) I_3 & & & \\ 3\xi & & & (3^2 - \lambda^2) I_3 & & \\ \vdots & & & & \ddots & \\ N\xi & & & & & (N^2 - \lambda^2) I_3 \end{vmatrix} = 0. \quad (\text{C.41})$$

Shifting the rows and columns that contains the same  $\xi_i$  together, we have

$$\begin{vmatrix} \Xi_1 & & \\ & \Xi_2 & \\ & & \Xi_3 \end{vmatrix} = 0, \quad (\text{C.42})$$

where

$$\Xi_i = \begin{pmatrix} \xi_i^2(N + 1/2) - \lambda^2 & \xi_i & 2\xi_i & 3\xi_i & \dots & N\xi_i \\ \xi_i & 1^2 - \lambda^2 & & & & \\ 2\xi_i & & 2^2 - \lambda^2 & & & \\ 3\xi_i & & & 3^2 - \lambda^2 & & \\ \vdots & & & & \ddots & \\ N\xi_i & & & & & N^2 - \lambda^2 \end{pmatrix}. \quad (\text{C.43})$$

Equation C.42 is equivalent to

$$|\Xi_1| |\Xi_2| |\Xi_3| = 0 \quad (\text{C.44})$$

and  $|\Xi_i| = 0$ , i.e.

$$\begin{vmatrix} \xi_i^2(N + 1/2) - \lambda^2 & \xi_i & 2\xi_i & 3\xi_i & \dots & N\xi_i \\ \xi_i & 1^2 - \lambda^2 & & & & \\ 2\xi_i & & 2^2 - \lambda^2 & & & \\ 3\xi_i & & & 3^2 - \lambda^2 & & \\ \vdots & & & & \ddots & \\ N\xi_i & & & & & N^2 - \lambda^2 \end{vmatrix} = 0 \quad (\text{C.45})$$

gives us all the eigen values. Expanding  $|\Xi_i|$  by the first column, the first term is

$$\begin{aligned} & [\xi_i^2(N + 1/2) - \lambda^2] \begin{vmatrix} 1^2 - \lambda^2 & & & & \\ & 2^2 - \lambda^2 & & & \\ & & 3^2 - \lambda^2 & & \\ & & & \ddots & \\ & & & & N^2 - \lambda^2 \end{vmatrix} \\ &= [\xi_i^2(N + 1/2) - \lambda^2] (1^2 - \lambda^2) (2^2 - \lambda^2) (3^2 - \lambda^2) \dots (N^2 - \lambda^2). \quad (\text{C.46}) \end{aligned}$$

The second term is

$$\begin{aligned}
& (-1)^{\xi_i} \begin{vmatrix} \xi_i & 2\xi_i & 3\xi_i & \dots & N\xi_i \\ & 2^2 - \lambda^2 & & & \\ & & 3^2 - \lambda^2 & & \\ & & & \ddots & \\ & & & & N^2 - \lambda^2 \end{vmatrix} \\
&= -\xi_i^2 (2^2 - \lambda^2) (3^2 - \lambda^2) \dots (N^2 - \lambda^2). \tag{C.47}
\end{aligned}$$

The third term is

$$\begin{aligned}
& 2\xi_i \begin{vmatrix} \xi_i & 2\xi_i & 3\xi_i & \dots & N\xi_i \\ 1^2 - \lambda^2 & & & & \\ & 3^2 - \lambda^2 & & & \\ & & \ddots & & \\ & & & & N^2 - \lambda^2 \end{vmatrix} \\
&= 2\xi_i^2 \begin{vmatrix} 0 & 0 & \dots & 0 \\ & 3^2 - \lambda^2 & & \\ & & \ddots & \\ & & & N^2 - \lambda^2 \end{vmatrix} - 2\xi_i (1^2 - \lambda^2) \begin{vmatrix} 2\xi_i & 3\xi_i & \dots & N\xi_i \\ & 3^2 - \lambda^2 & & \\ & & \ddots & \\ & & & N^2 - \lambda^2 \end{vmatrix} \\
&= -(2\xi_i)^2 (1^2 - \lambda^2) (3^2 - \lambda^2) \dots (N^2 - \lambda^2). \tag{C.48}
\end{aligned}$$

The fourth term is

$$\begin{aligned}
& (-3)\xi_i \begin{vmatrix} \xi_i & 2\xi_i & 3\xi_i & 4\xi & \dots & N\xi_i \\ 1^2 - \lambda^2 & & & & & \\ & 2^2 - \lambda^2 & & & & \\ & & 4^2 - \lambda^2 & & & \\ & & & \ddots & & \\ & & & & N^2 - \lambda^2 & \end{vmatrix} \\
&= 3\xi_i(1^2 - \lambda^2) \begin{vmatrix} 2\xi_i & 3\xi_i & 4\xi & \dots & N\xi_i \\ 2^2 - \lambda^2 & & & & \\ & 4^2 - \lambda^2 & & & \\ & & \ddots & & \\ & & & N^2 - \lambda^2 & \end{vmatrix} \\
&= -3\xi_i(1^2 - \lambda^2)(2^2 - \lambda^2) \begin{vmatrix} 3\xi_i & 4\xi & \dots & N\xi_i \\ 4^2 - \lambda^2 & & & \\ & \ddots & & \\ & & N^2 - \lambda^2 & \end{vmatrix} \\
&= -(3\xi_i)^2 (1^2 - \lambda^2) (2^3 - \lambda^2) (4^3 - \lambda^2) \dots (N^2 - \lambda^2). \tag{C.49}
\end{aligned}$$

The  $(n + 1)$  term is

$$-(n\xi_i)^2 (1^2 - \lambda^2) (2^3 - \lambda^2) [(n - 1)^3 - \lambda^2] [(n + 1)^3 - \lambda^2] \dots (N^2 - \lambda^2). \tag{C.50}$$



Therefore

$$\begin{aligned}
|\Xi_i| &= [\xi_i^2(N + 1/2) - \lambda^2] (1^2 - \lambda^2) (2^2 - \lambda^2) (3^3 - \lambda^2) \cdots (N^2 - \lambda^2) \\
&\quad - \xi_i^2 (2^2 - \lambda^2) (3^3 - \lambda^2) \cdots (N^2 - \lambda^2) \\
&\quad - (2\xi_i)^2 (1^2 - \lambda^2) (3^3 - \lambda^2) \cdots (N^2 - \lambda^2) \\
&\quad - (3\xi_i)^2 (1^2 - \lambda^2) (2^3 - \lambda^2) (4^3 - \lambda^2) \cdots (N^2 - \lambda^2). \\
&\quad \dots \\
&\quad - (N\xi_i)^2 (1^2 - \lambda^2) (2^3 - \lambda^2) \cdots [(N-2)^2 - \lambda^2] [(N-1)^2 - \lambda^2] \\
&= 0.
\end{aligned} \tag{C.51}$$

Dividing  $(1^2 - \lambda^2) (2^2 - \lambda^2) (3^3 - \lambda^2) \cdots (N^2 - \lambda^2)$  on both sides gives

$$\xi_i^2 \left( N + \frac{1}{2} + \frac{1}{\lambda^2 - 1^2} + \frac{2}{\lambda^2 - 2^2} + \frac{3}{\lambda^2 - 3^2} + \cdots + \frac{N^2}{\lambda^2 - N^2} \right) = \lambda^2. \tag{C.52}$$

Since

$$\begin{aligned}
&N + \frac{1}{\lambda^2 - 1^2} + \frac{2}{\lambda^2 - 2^2} + \frac{3}{\lambda^2 - 3^2} + \cdots + \frac{N^2}{\lambda^2 - N^2} \\
&= \frac{N(\lambda^2 - 1^2)(\lambda^2 - 2^2) \cdots (\lambda^2 - N^2) + (\lambda^2 - 2^2)(\lambda^2 - 3^2) \cdots (\lambda^2 - N^2) + \cdots}{(\lambda^2 - 1^2)(\lambda^2 - 2^2) \cdots (\lambda^2 - N^2)} \\
&= \frac{\lambda^2}{\lambda^2 - 1^2} + \frac{\lambda^2}{\lambda^2 - 2^2} + \frac{\lambda^2}{\lambda^2 - 3^2} + \cdots + \frac{\lambda^2}{\lambda^2 - N^2} \\
&= \lambda^2 \lim_{N \rightarrow \infty} \sum_{n=1}^N \frac{1}{\lambda^2 - n^2} \\
&= \lambda^2 \left[ \pi \cot(\pi \lambda) - \frac{1}{\lambda} \right] \frac{1}{2\lambda} \\
&= \frac{\lambda \pi}{2} \cot(\pi \lambda) - \frac{1}{2}.
\end{aligned} \tag{C.53}$$

we have

$$\frac{\pi\xi_i^2}{2} \cot(\pi\lambda) = \lambda. \quad (\text{C.54})$$

It has solutions  $\lambda_i^{(0)}, \lambda_i^{(1)}, \lambda_i^{(2)}, \dots, \lambda_i^{(N)}$  where  $i = 1, 2, 3$  and  $N \rightarrow \infty$ .

Therefore,

$$M_D^2 = \begin{pmatrix} (\lambda^{(0)})^2 & & & & \\ & (\lambda^{(1)})^2 & & & \\ & & (\lambda^{(2)})^2 & & \\ & & & \ddots & \\ & & & & (\lambda^{(N)})^2 \end{pmatrix} \quad (\text{C.55})$$

and

$$M_D = \begin{pmatrix} \lambda^{(0)} & & & & \\ & \lambda^{(1)} & & & \\ & & \lambda^{(2)} & & \\ & & & \ddots & \\ & & & & \lambda^{(N)} \end{pmatrix}, \quad (\text{C.56})$$

where

$$\lambda^{(n)} = \begin{pmatrix} \lambda_1^{(n)} & & \\ & \lambda_2^{(n)} & \\ & & \lambda_3^{(n)} \end{pmatrix}. \quad (\text{C.57})$$

Given a eigen value  $\lambda_i^{(n)}$ , one can calculate the corresponding eigenstate

by solving

$$\begin{pmatrix} \xi^2(N + 1/2) - \lambda^2 & \xi & 2\xi & 3\xi & \dots & N\xi \\ \xi & (1^2 - \lambda^2) I_3 & & & & \\ 2\xi & & (2^2 - \lambda^2) I_3 & & & \\ 3\xi & & & (3^2 - \lambda^2) I_3 & & \\ \vdots & & & & \ddots & \\ N\xi & & & & & (N^2 - \lambda^2) I_3 \end{pmatrix} \begin{pmatrix} \zeta^{(0)} \\ \zeta^{(1)} \\ \zeta^{(2)} \\ \zeta^{(3)} \\ \vdots \\ \zeta^{(N)} \end{pmatrix} = 0. \quad (\text{C.58})$$

where

$$\zeta^{(n)} = \begin{pmatrix} \zeta^{1(n)} \\ \zeta^{2(n)} \\ \zeta^{3(n)} \end{pmatrix}. \quad (\text{C.59})$$

Define

$$\zeta^i \equiv \begin{pmatrix} \zeta^{i(0)} \\ \zeta^{i(1)} \\ \zeta^{i(2)} \\ \vdots \\ \zeta^{i(N)} \end{pmatrix}, \quad (\text{C.60})$$

Solving Equation C.58 is equivalent to solve

$$\begin{pmatrix} \Xi_1 & & \\ & \Xi_2 & \\ & & \Xi_3 \end{pmatrix} \begin{pmatrix} \zeta^1 \\ \zeta^2 \\ \zeta^3 \end{pmatrix} = 0. \quad (\text{C.61})$$

For  $\lambda_i^{(n)}$ , we have

$$\Xi_i \left( \lambda_i^{(n)} \right) \zeta^i = 0, \quad (\text{C.62})$$

and  $\Xi_j \left( \lambda_i^{(n)} \right) \zeta^j = 0$  gives  $\zeta^j = 0$  for  $j \neq i$ . Writing Equation C.62 apart,

$$\begin{pmatrix} \xi_i^2(N + 1/2) - \left( \lambda_i^{(n)} \right)^2 & \xi_i & \dots & N\xi_i \\ \xi_i & 1^2 - \left( \lambda_i^{(n)} \right)^2 & & \\ \vdots & & \ddots & \\ N\xi_i & & & N^2 - \left( \lambda_i^{(n)} \right)^2 \end{pmatrix} \begin{pmatrix} \zeta^{i(0)} \\ \zeta^{i(1)} \\ \vdots \\ \zeta^{i(N)} \end{pmatrix} = 0. \quad (\text{C.63})$$

we get a set of linear equations

$$\begin{aligned}
N\xi_i\zeta^{i(0)} + \left[ N^2 - \left( \lambda_i^{(n)} \right)^2 \right] \zeta^{i(N)} &= 0, \\
&\vdots \\
2\xi_i\zeta^{i(0)} + \left[ 2^2 - \left( \lambda_i^{(n)} \right)^2 \right] \zeta^{i(2)} &= 0, \\
\xi_i\zeta^{i(0)} + \left[ 1^2 - \left( \lambda_i^{(n)} \right)^2 \right] \zeta^{i(1)} &= 0, \\
\left[ \xi_i^2(N + 1/2) - \left( \lambda_i^{(n)} \right)^2 \right] \zeta^{i(0)} + \xi_i\zeta^{i(1)} + \dots + N\xi_i\xi_i\zeta^{i(N)} &= 0. \tag{C.64}
\end{aligned}$$

This gives us

$$\begin{aligned}
\zeta^{i(N)} &= \frac{-N\xi_0}{N^2 - \left( \lambda_i^{(n)} \right)^2} \zeta^{i(0)}, \\
&\vdots \\
\zeta^{i(2)} &= \frac{-2\xi_0}{2^2 - \left( \lambda_i^{(n)} \right)^2} \zeta^{i(0)}, \\
\zeta^{i(1)} &= \frac{-\xi_0}{1^2 - \left( \lambda_i^{(n)} \right)^2} \zeta^{i(0)}, \\
0 &= \left[ \xi_i^2(N + 1/2) - \left( \lambda_i^{(n)} \right)^2 + \sum_{i=1}^N \frac{(n\xi_i)^2}{\left( \lambda_i^{(n)} \right)^2 - n^2} \right] \zeta^{i(0)}. \tag{C.65}
\end{aligned}$$

The last equation does not constrain  $\zeta^{i(0)}$  since

$$\xi_i^2(N + 1/2) - \left( \lambda_i^{(n)} \right)^2 + \sum_{i=1}^N \frac{(n\xi_i)^2}{\left( \lambda_i^{(n)} \right)^2 - n^2} = 0 \tag{C.66}$$

according to Equation C.52, but it can be computed from the normalization

condition  $(\zeta^i)^2 = 1$ , in other words,

$$(\zeta^{i(0)})^2 \left[ 1 + \xi_i^2 \sum_{i=1}^N \frac{n^2}{(\lambda_i^{(n)})^2 - n^2} \right] = 1, \quad (\text{C.67})$$

$$\begin{aligned} (\zeta^{i(0)})^2 &= \frac{1}{1 + \xi_i^2 \sum_{i=1}^N \frac{n^2}{(\lambda_i^{(n)})^2 - n^2}} \\ &= \frac{1}{1 + \frac{\pi \xi_i^2}{4\lambda_i^{(n)} R} \left[ -\cot\left(\pi \lambda_i^{(n)} R\right) + \pi \lambda_i^{(n)} R \csc^2\left(\pi \lambda_i^{(n)} R\right) \right]}, \end{aligned} \quad (\text{C.68})$$

where the last step is proved in the Appendix. The non-zero component of the mass eigen state  $\chi_L^{i(n)}$  corresponding to the eigen value  $\lambda_i^{(n)}$  is  $\zeta^{i(0)}\left(\lambda_i^{(n)}\right)$ ,  $\zeta^{i(1)}\left(\lambda_i^{(n)}\right)$ ,  $\zeta^{i(2)}\left(\lambda_i^{(n)}\right)$ ,  $\dots$ ,  $\zeta^{i(N)}\left(\lambda_i^{(n)}\right)$ .  $L^{-1}$  corresponding to Equation C.55 can be written as

$$L^{-1} = \begin{pmatrix} (L^{-1})^{(11)} & (L^{-1})^{(12)} & \dots & (L^{-1})^{(1N)} \\ (L^{-1})^{(21)} & (L^{-1})^{(22)} & \dots & (L^{-1})^{(2N)} \\ (L^{-1})^{(31)} & (L^{-1})^{(32)} & \dots & (L^{-1})^{(3N)} \\ \vdots & \vdots & \vdots & \vdots \\ (L^{-1})^{(N1)} & (L^{-1})^{(N2)} & \dots & (L^{-1})^{(NN)} \end{pmatrix} \quad (\text{C.69})$$

where

$$(L^{-1})^{(ij)} = \begin{pmatrix} \zeta^{1(i)}\left(\lambda_1^{(j)}\right) & & & \\ & \zeta^{2(i)}\left(\lambda_2^{(j)}\right) & & \\ & & \dots & \\ & & & \zeta^{3(i)}\left(\lambda_3^{(j)}\right) \end{pmatrix}. \quad (\text{C.70})$$

After getting  $L$ , the flavor eigenstate can now be expressed in terms of the mass eigenstate as shown in Equation C.40

$$\nu_L = PL\chi_L. \quad (\text{C.71})$$

If we write  $\chi_L$  as

$$\chi_L = \begin{pmatrix} \chi_L^{(0)} \\ \chi_L^{(1)} \\ \chi_L^{(2)} \\ \vdots \\ \chi_L^{(N)} \end{pmatrix}, \text{ where } \chi_L^n = \begin{pmatrix} \chi_L^{1(n)} \\ \chi_L^{2(n)} \\ \chi_L^{3(n)} \end{pmatrix}, \quad (\text{C.72})$$

the mass of  $\chi_L^{i(n)}$  is  $\lambda_i^{(n)}/R$  according to Equation C.40 and C.56. In component form

$$\begin{aligned} \nu_L^{(m)} &= P_{mj} L^{(jn)} \chi_L^{(n)} \\ &= P_{mm} L^{(mn)} \chi_L^{(n)} \\ &= U L^{(mn)} \chi_L^{(n)}. \end{aligned} \quad (\text{C.73})$$

The two sides are  $3 \times 3$  matrices, which means

$$\begin{aligned} \nu_L^{\alpha(m)} &= U L^{(mn)} \chi_L^{(n)} \\ &= U_{\alpha i} L_{ij}^{(mn)} \chi_L^{j(n)} \end{aligned} \quad (\text{C.74})$$

where  $\alpha, i, j = 1, 2, 3$  and  $m, n = 0, 1, 2, \dots, \infty$ . Using the bra-ket notation, the oscillation amplitude from  $\nu_L^{\alpha(m)}$  to  $\nu_L^{\beta(n)}$  can be calculated as

$$\begin{aligned} A\left(\nu_L^{\alpha(m)} \rightarrow \nu_L^{\beta(n)}(t)\right) &= \langle \nu_L^{\alpha(m)} | \nu_L^{\beta(n)}(t) \rangle \\ &= \sum_{i,j,k,l} \sum_{r,s} \langle \chi_L^{j(r)} | \chi_L^{l(s)}(t) \rangle U_{\alpha i}^* L_{ij}^{(mr)*} U_{\beta k} L_{kl}^{(ns)} e^{-i(E_\beta^{(s)} t - p_\beta^{(s)} L)} \\ &= \sum_{i,j,k,l} \sum_{r,s} \delta_{jl} \delta_{rs} U_{\alpha i}^* L_{ij}^{(mr)*} U_{\beta k} L_{kl}^{(ns)} e^{-i(E_\beta^{(s)} t - p_\beta^{(s)} L)} \\ &= \sum_{i,j,k} \sum_r U_{\alpha i}^* L_{ij}^{(mr)*} U_{\beta k} L_{kj}^{(nr)} e^{-i(E_j^{(r)} t - p_j^{(r)} L)}, \end{aligned} \quad (\text{C.75})$$

where

$$\begin{aligned}
E_j^{(r)} &= \left[ \left( p_j^{(r)} \right)^2 + \left( \lambda_j^{(r)} / R \right)^2 \right]^{\frac{1}{2}} \\
&= p_j^{(r)} \left[ 1 + \left( \frac{\lambda_j^{(r)} / R}{p_j^{(r)}} \right)^2 \right]^{\frac{1}{2}} \\
&\approx p_j^{(r)} \left[ 1 + \frac{1}{2} \left( \frac{\lambda_j^{(r)} / R}{p_j^{(r)}} \right)^2 \right] \\
&= p_j^{(r)} + \frac{\left( \lambda_j^{(r)} / R \right)^2}{2p_j^{(r)}}
\end{aligned} \tag{C.76}$$

Let  $E$  be the neutrino energy and  $L$  be the baseline length. Using  $t \approx L$  and  $p_j^{(r)} \approx E$ , the exponent becomes

$$e^{-i(E_j^{(r)}t - p_j^{(r)}L)} = e^{-i \left[ \frac{(\lambda_j^{(r)}/R)^2}{2p_j^{(r)}} t + p_j^{(r)}(t-L) \right]} = e^{-i \frac{(\lambda_j^{(r)})^2 L}{2ER^2}} \tag{C.77}$$

The oscillation amplitude is now

$$A \left( \nu_L^{\alpha(m)} \rightarrow \nu_L^{\beta(n)}(t) \right) = \sum_{i,j,k} \sum_r U_{\alpha i}^* L_{ij}^{(mr)*} U_{\beta k} L_{kj}^{(nr)} e^{-i \frac{(\lambda_j^{(r)})^2 L}{2ER^2}}. \tag{C.78}$$

Active neutrino states  $\nu_e, \nu_\mu, \nu_\tau$  correspond to  $\nu_L^{1(0)}, \nu_L^{2(0)}, \nu_L^{3(0)}$  and  $\nu_L^{i(n)}$  ( $n \neq 0$ ) are considered as sterile neutrinos. Oscillations among active neutrino states can be written as

$$A \left( \nu_\alpha \rightarrow \nu_\beta(t) \right) = A \left( \nu_L^{\alpha(0)} \rightarrow \nu_L^{\beta(0)}(t) \right) = \sum_{i,j,k} \sum_n U_{\alpha i}^* U_{\beta k} L_{ij}^{(0n)*} L_{kj}^{(0n)} e^{-i \frac{(\lambda_\beta^{(0)})^2 L}{2ER^2}}. \tag{C.79}$$

Oscillation amplitude  $A(\nu_\mu \rightarrow \nu_\mu)$  as measured by MINOS charged current deficit can be written as

$$\begin{aligned}
A(\nu_\mu \rightarrow \nu_\mu(t)) &= A\left(\nu_L^{1(0)} \rightarrow \nu_L^{1(0)}(t)\right) \\
&= \sum_{i,j,k} \sum_n U_{1i}^* U_{1k} L_{ij}^{(0n)*} L_{kj}^{(0n)} e^{-i \frac{(\lambda_1^{(0)})^2 L}{2ER^2}}. \quad (\text{C.80})
\end{aligned}$$

Oscillation amplitude from  $\nu_\mu$  to sterile neutrinos  $A(\nu_\mu \rightarrow \nu_s)$  as measured by MINOS neutral current deficit takes the form

$$\begin{aligned}
A(\nu_\mu \rightarrow \nu_s(t)) &= \sum_{n=1}^{+\infty} \sum_{\beta=1}^3 A\left(\nu_L^{1(0)} \rightarrow \nu_L^{\beta(n)}(t)\right) \\
&= \sum_{n=1}^{+\infty} \sum_{\beta=1}^3 \sum_{i,j,k} \sum_r U_{1i}^* L_{ij}^{(0r)*} U_{\beta k} L_{kj}^{(nr)} e^{-i \frac{(\lambda_j^{(r)})^2 L}{2ER^2}}. \quad (\text{C.81})
\end{aligned}$$



## Appendix D

### Neutrino Production

Neutrinos flying through the MINOS near detector (ND) and far detector (FD) are the decay products of pions, kaons and muons:

$$\pi^\pm \rightarrow \nu_\mu/\bar{\nu}_\mu + \mu^\pm, \quad (\text{D.1})$$

$$K^\pm \rightarrow \nu_\mu/\bar{\nu}_\mu + \mu^\pm, \quad (\text{D.2})$$

$$\mu^\pm \rightarrow e^\pm + \nu_e/\bar{\nu}_e + \bar{\nu}_\mu/\nu_\mu. \quad (\text{D.3})$$

To make predictions of the FD flux based the near detector flux, it is crucial to know the decay cross section. Pions and kaons have 0 spin and in the frame of themselves, there is no preference in any particular direction, i.e. the decay process is isotropic. Energies of the progenies can be computed from kinematics. Muon is different, however, for it is a spin 1/2 particle. Its spin can be either parallel or anti-parallel to the direction of travel. This requires more consideration from electroweak theory.

#### D.1 Decays of $\pi^\pm$ and $K^\pm$

In the rest frame of decaying pions or kaons, the isotropy requires

$$\frac{dN}{d\Omega} = C, \quad (\text{D.4})$$

where  $C$  is a constant and can be calculated by integrating the equation above on both sides

$$\begin{aligned} dN &= Cd\Omega \\ N &= 4\pi C \\ C &= N/(4\pi) \end{aligned} \tag{D.5}$$

Considering  $d\Omega = d \cos \theta d\phi$ , Equation D.4 can be rewritten as

$$\begin{aligned} \frac{d^2 N}{d \cos \theta^* d\phi^*} &= \frac{N}{4\pi}, \\ \int \frac{d^2 N}{d \cos \theta^* d\phi^*} d\phi^* &= \int \frac{N}{4\pi} d\phi^*, \\ \frac{dN}{d \cos \theta^*} &= \frac{N}{2}, \end{aligned} \tag{D.6}$$

where the asterisks represent the rest frame. Making a normalization of  $N = 1$ , one has the decaying probability in a particular direction

$$\frac{dN}{d \cos \theta^*} = \frac{1}{2} \tag{D.7}$$

This can be boosted to the lab frame

$$\frac{dN}{d \cos \theta} = \frac{dN}{d \cos \theta^*} \frac{d \cos \theta^*}{d \cos \theta}, \tag{D.8}$$

where  $\theta$  is the angle between the momentum of the parent particle and the neutrino as shown in Figure D.1. Let the Lorentz boost of the parent particle (one dimensional) be  $\beta = |\mathbf{p}_p|/E_p$  and  $\gamma = E_p/m_p$ , we have

$$\begin{pmatrix} E_\nu^* \\ p_\parallel^* \end{pmatrix} = \begin{pmatrix} \gamma & -\gamma\beta \\ -\gamma\beta & \gamma \end{pmatrix} \begin{pmatrix} E_\nu \\ p_\parallel \end{pmatrix} = \begin{pmatrix} \gamma E_\nu - \gamma\beta p_\parallel \\ -\gamma\beta E_\nu + \gamma p_\parallel \end{pmatrix}. \tag{D.9}$$

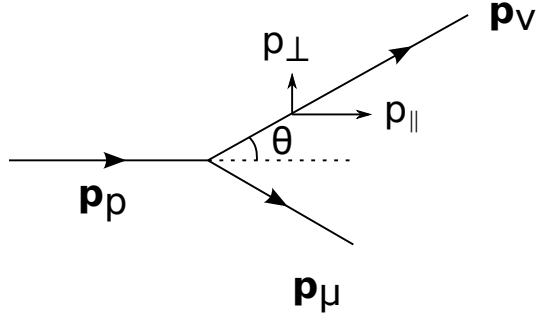


Figure D.1: Schematic of pion/kaon decay in the lab frame.

therefore

$$\begin{aligned}
 \cos \theta^* &= \frac{p_{\parallel}^*}{E_{\nu}^*} = \frac{-\gamma\beta E_{\nu} + \gamma p_{\parallel}}{\gamma E_{\nu} - \gamma\beta p_{\parallel}} \\
 &= \frac{-\beta + p_{\parallel}/E_{\nu}}{1 - \beta p_{\parallel}/E_{\nu}} \\
 &= \frac{-\beta + \cos \theta}{1 - \beta \cos \theta}.
 \end{aligned} \tag{D.10}$$

where  $\cos \theta = p_{\parallel}/|\mathbf{p}_{\nu}| = p_{\parallel}/E_{\nu}$  was used. This gives

$$\begin{aligned}
 \frac{d \cos \theta^*}{d \cos \theta} &= \frac{1}{1 - \beta \cos \theta} - \frac{-\beta + \cos \theta}{(1 - \beta \cos \theta)^2} (-\beta) \\
 &= \frac{1 - \beta \cos \theta - \beta^2 + \beta \cos \theta}{(1 - \beta \cos \theta)^2} \\
 &= \frac{1}{\gamma^2 (1 - \beta \cos \theta)^2}
 \end{aligned} \tag{D.11}$$

Combining Equation D.11 and D.7 gives the angular distribution of the neutrino

$$\frac{dN}{d \cos \theta} = \frac{1}{2\gamma^2 (1 - \beta \cos \theta)^2}. \tag{D.12}$$

It should be noted that  $\theta$  has an one-to-one correspondence with the neutrino energy. In the rest frame of the parent particle, let  $q_p$ ,  $q_{\nu}$  and  $q_{\mu}$  be the four

momentum of the parent particle (pion or kaon), the neutrino and the muon,  
i.e.

$$\begin{aligned}
q_p &= (E_p^*, \mathbf{0}), \\
q_\nu &= (E_\nu^*, \mathbf{p}_\nu^*), \\
q_\mu &= (E_\mu^*, \mathbf{p}_\mu^*),
\end{aligned}
\tag{D.13}$$

They obey

$$q_p = q_\nu + q_\mu, \tag{D.14}$$

The neutrino energy is uniquely determined, i.e.

$$\begin{aligned}
q_\mu &= q_p - q_\nu \\
q_\mu \cdot q_\mu &= (q_p - q_\nu) \cdot (q_p - q_\nu) \\
E_\mu^2 - p_\mu^2 &= q_p \cdot q_p + q_\nu \cdot q_\nu - 2q_\nu \cdot q_p \\
m_\mu^2 &= m_p^2 + m_\nu^2 - 2E_\nu^* E_p^* \\
E_\nu^* &= \frac{m_p^2 - m_\mu^2}{2m_p}.
\end{aligned}
\tag{D.15}$$

To boost it to the lab frame, consider the Lorentz scalar

$$\begin{aligned}
q_p^* \cdot q_\nu^* &= q_p \cdot q_\nu \\
E_p^* E_\nu^* &= E_p E_\nu - |\mathbf{p}_p| |\mathbf{p}_\nu| \cos \theta \\
E_\nu &= \frac{m_p E_\nu^*}{E_p - |\mathbf{p}_p| \cos \theta} \\
E_\nu &= \frac{E_\nu^*}{\gamma - \beta \cos \theta}
\end{aligned}
\tag{D.16}$$

Combining Equation D.15 and D.16, we have

$$E_\nu = \frac{1}{\gamma - \beta \cos \theta} \frac{m_p^2 - m_\mu^2}{2m_p} \quad (\text{D.17})$$

## D.2 Decays of $\mu^\pm$

Due to its spin, the decaying of a muon is not isotropic and therefore more complicated. The treatment involves computations with electroweak theory. Instead of only considering

$$\mu^- \rightarrow e^- + \bar{\nu}_e + \nu_\mu, \quad (\text{D.18})$$

following Reference [137], this note presents a more general case of three-body purely leptonic decay of a spin 1/2 lepton  $l_a$

$$l_a^-(p_1, s_a) \rightarrow \bar{\nu}_b(p_2) + \nu_a(p_3) + l_b^-(p_4, s_b), \quad (\text{D.19})$$

The correspondence is shown in Table D.1.

	$\mu^-$	$e^-$	$\bar{\nu}_e$	$\nu_\mu$
symbol	$l_a^-$	$l_b^-$	$\bar{\nu}_b$	$\nu_a$
state	$u_1$	$u_4$	$v_2$	$u_3$
mass	$m_a$	$m_b$	0	0
momentum	$p_1$	$p_4$	$p_2$	$p_3$

Table D.1: Correspondence between the general notations for leptons used in Equation D.18 and the notations of a special case used in Equation D.19.

According to the Feynman diagram shown in Figure D.2, two vertices

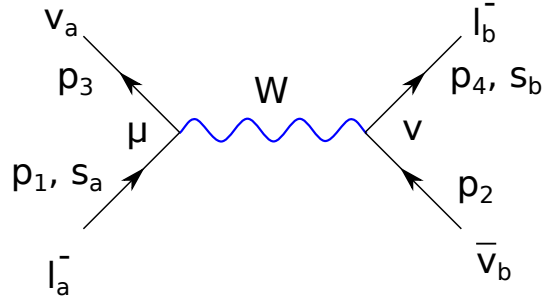


Figure D.2: Feynman diagram of a lepton decaying into another lepton plus two neutrinos.

give

$$-\frac{ig}{2^{1/2}}\gamma_\mu\frac{1-\gamma^5}{2}, \quad -\frac{ig}{2^{1/2}}\gamma_\nu\frac{1-\gamma^5}{2}. \quad (\text{D.20})$$

The propagator represents

$$\frac{i(g^{\mu\nu} + q^\mu q^\nu / M_W^2)}{q^2 - M_W^2}, \quad (\text{D.21})$$

where  $q = p_1 - p_3 = p_2 + p_4$ . Multiplying all the elements together, we have

$$\begin{aligned} M_{fi} &= \frac{-ig^2}{8} [\bar{u}_3\gamma_\mu(1-\gamma^5)u_1] \left[ \frac{-g^{\mu\nu} + q^\mu q^\nu / M_W^2}{q^2 - M_W^2} \right] [\bar{u}_4\gamma_\nu(1-\gamma^5)v_2] \\ &= \frac{-ig^2}{8(q^2 - M_W^2)} [-\bar{u}_3\gamma_\mu(1-\gamma^5)u_1\bar{u}_4\gamma^\mu(1-\gamma^5)v_2 \\ &\quad + \bar{u}_3\gamma_\mu(1-\gamma^5)u_1(q^\mu q^\nu / M_W^2)\bar{u}_4\gamma_\nu(1-\gamma^5)v_2] \quad (\text{D.22}) \end{aligned}$$

Using Dirac equations

$$\begin{aligned} (\not{q} - m_a)u_1 &= 0, \\ \bar{u}_4(\not{q} - m_a) &= 0, \end{aligned} \quad (\text{D.23})$$

the second term in the bracket can be rewritten as

$$\begin{aligned}
& \bar{u}_3 \gamma_\mu (1 - \gamma^5) u_1 (q^\mu q^\nu / M_W^2) \bar{u}_4 \gamma_\nu (1 - \gamma^5) v_2 \\
&= 1/M_W^2 \bar{u}_3 (1 + \gamma^5) (\gamma_\mu q^\mu u_1) (\bar{u}_4 q^\nu \gamma_\nu) (1 - \gamma^5) v_2 \\
&= (m_a m_b / M_W^2) \bar{u}_3 (1 + \gamma^5) u_1 \bar{u}_4 (1 - \gamma^5) v_2
\end{aligned} \tag{D.24}$$

where  $\{\gamma_\mu, \gamma^5\} = 0$  was used. This leads to

$$\begin{aligned}
M_{fi} = \frac{-ig^2}{8(q^2 - M_W^2)} & [-\bar{u}_3 \gamma_\mu (1 - \gamma^5) u_1 \bar{u}_4 \gamma^\mu (1 - \gamma^5) v_2 + \\
& + (m_a m_b / M_W^2) \bar{u}_3 (1 + \gamma^5) u_1 \bar{u}_4 (1 - \gamma^5) v_2]
\end{aligned} \tag{D.25}$$

Considering the mass of the W boson  $M_W = 80.385$  GeV, we can take  $q^2 \ll M_W$  and  $m_a m_b \ll M_W^2$ . The equation above becomes

$$M_{fi} = \frac{-ig^2}{8(q^2 - M_W^2)} [-\bar{u}_3 \gamma_\mu (1 - \gamma^5) u_1] [\bar{u}_4 \gamma^\mu (1 - \gamma^5) v_2] \tag{D.26}$$

Its complex conjugate is

$$M_{fi}^* = \frac{ig^2}{8(q^2 - M_W^2)} [-\bar{u}_3 \gamma_\mu (1 - \gamma^5) u_1]^* [\bar{u}_4 \gamma^\mu (1 - \gamma^5) v_2]^*. \tag{D.27}$$

The first bracket is evaluated as

$$\begin{aligned}
[-\bar{u}_3 \gamma_\mu (1 - \gamma^5) u_1]^* &= [-\bar{u}_3 \gamma_\mu (1 - \gamma^5) u_1]^\dagger \\
&= -u_1^\dagger (1 - \gamma^5)^\dagger \gamma_\mu^\dagger \bar{u}_3^\dagger \\
&= (\bar{u}_1 \gamma_0) (1 - \gamma^5) (\gamma_0 \gamma_\mu \gamma_0) (\gamma_0 u_3) \\
&= \bar{u}_1 \gamma_\nu (1 - \gamma^5) u_3,
\end{aligned} \tag{D.28}$$

where the following relations were used

$$\begin{aligned}
\bar{u} &= u^\dagger \gamma_0, \\
u^\dagger &= \bar{u} \gamma_0, \\
\gamma_0^\dagger &= \gamma_0.
\end{aligned} \tag{D.29}$$

Thus

$$M_{fi}^* = \frac{ig^2}{8(q^2 - M_W^2)} [\bar{u}_1 \gamma_\nu (1 - \gamma^5) u_3] [\bar{v}_2 \gamma^\nu (1 - \gamma^5) u_4]. \tag{D.30}$$

The differential rate is given by

$$d\omega = (2\pi)^4 \frac{\delta^4(p_i - p_f) |M_{fi}|^2 d^3 p_2 d^3 p_3 d^3 p_4}{2E_1 (2\pi)^9 8E_2 E_3 E_4}. \tag{D.31}$$

Multiplying  $M_{fi}$  and  $M_{fi}^*$  gives

$$\begin{aligned}
|M_{fi}|^2 &= \frac{g^4}{64M_W^4} [-\bar{u}_3 \gamma_\mu (1 - \gamma^5) u_1] [\bar{u}_1 \gamma_\nu (1 - \gamma^5) u_3] \\
&\quad \times [\bar{u}_4 \gamma^\mu (1 - \gamma^5) v_2] [\bar{v}_2 \gamma^\nu (1 - \gamma^5) u_4] \\
&\equiv \frac{g^4}{64M_W^4} L_{\mu\nu} M^{\mu\nu}.
\end{aligned} \tag{D.32}$$

Using the trace technology,

$$\begin{aligned}
L_{\mu\nu} &= [\bar{u}_3 \gamma_\mu (1 - \gamma^5) u_1] [\bar{u}_1 \gamma_\nu (1 - \gamma^5) u_3] \\
&= \text{tr}[(u_3 \bar{u}_3) \gamma_\mu (1 - \gamma^5) (u_1 \bar{u}_1) \gamma_\nu (1 - \gamma^5)]
\end{aligned} \tag{D.33}$$

Consider the dependence on the spin of the parent particle and there only exists right-handed neutrino

$$u_1 \bar{u}_1 = (\not{p}_1 + m_a)(1 + \gamma^5 \not{\epsilon}_a) \tag{D.34}$$

$$u_3 \bar{u}_3 = \not{p}_1 \frac{1}{2} \tag{D.35}$$



$L_{\mu\nu}$  becomes

$$L_{\mu\nu} = \frac{1}{2} \text{tr}[\not{p}_3 \gamma_\mu (1 - \gamma^5) (\not{p}_1 + m_a) (1 + \gamma^5 \not{s}_a) \gamma_\nu (1 - \gamma^5)]. \quad (\text{D.36})$$

Using the property that the trace of odd number of  $\gamma_\mu$  is zero,  $L_{\mu\nu}$  can be simplified to

$$\begin{aligned} L_{\mu\nu} &= \frac{1}{2} \text{tr}[\not{p}_3 \gamma_\mu (1 - \gamma^5) (\not{p}_1 + m_a \gamma^5 \not{s}_a) \gamma_\nu (1 - \gamma^5)] \\ &= \text{tr}[\not{p}_3 \gamma_\mu (\not{p}_1 + m_a \gamma^5 \not{s}_a) \gamma_\nu (1 - \gamma^5)] \\ &= \text{tr}[\not{p}_3 \gamma_\mu (\not{p}_1 - m_a \not{s}_a) \gamma_\nu (1 - \gamma^5)] \\ &= p_3^\alpha (p_1 - m_a s_a)^\beta \text{tr}[\gamma_\alpha \gamma_\mu \gamma_\beta \gamma_\nu (1 - \gamma^5)] \end{aligned} \quad (\text{D.37})$$

where  $\gamma^5 \gamma^5 = 1$  was used. Similar we obtain

$$M^{\mu\nu} = (p_4 - m_b s_b)_\theta (p_2)_\phi \text{tr}[\gamma^\theta \gamma^\mu \gamma^\phi \gamma^\nu (1 - \gamma^5)]. \quad (\text{D.38})$$

Using the following property

$$\begin{aligned} T &= \text{tr}[\gamma^\alpha \gamma^\mu \gamma^\beta \gamma^\nu (C_1 - C_2 \gamma^5)] \text{tr}[\gamma_\theta \gamma_\mu \gamma_\phi \gamma_\nu (C_3 - C_4 \gamma^5)] \\ &= 32 [C_1 C_3 (\delta_\theta^\alpha \delta_\phi^\beta + \delta_\phi^\alpha \delta_\theta^\beta) + C_2 C_4 (\delta_\theta^\alpha \delta_\phi^\beta - \delta_\phi^\alpha \delta_\theta^\beta)] \end{aligned} \quad (\text{D.39})$$

In the case of  $C_1 = C_2 = C_3 = C_4 = 1$ ,

$$T = 64 \delta_\theta^\alpha \delta_\phi^\beta. \quad (\text{D.40})$$

Therefore we have

$$\begin{aligned} |M_{fi}|^2 &= \frac{g^4}{64 M_W^4} 64 p_3^\alpha (p_1 - m_a s_a)^\beta (p_4 - m_a s_a)_\alpha p_{2\beta} \\ &= \frac{g^4}{M_W^4} [p_3 \cdot (p_4 - m_a s_a)] [p_2 \cdot (p_1 - m_a s_a)]. \end{aligned} \quad (\text{D.41})$$

Following Reference [137], first we get the rate for the electrons and then discuss that of the neutrinos. For electrons, we should integrate out the part involving the neutrinos

$$\begin{aligned}
d\omega &= (2\pi)^4 \frac{\delta^4(p_i - p_f) |M_{fi}|^2 d^3 p_2 d^3 p_3 d^3 p_4}{2E_1 (2\pi)^9 8E_2 E_3 E_4} \\
&= \frac{g^4}{16(2\pi)^5 M_W^4} \frac{(p_4 - m_b s_b)^\alpha (p_1 - m_b s_a)^\beta d^3 p_4}{E_1 E_4} \\
&\quad \times \int \frac{p_{2\beta} p_{3\alpha} \delta^4(p_1 - p_2 - p_3 - p_4)}{E_2 E_3} d^3 p_2 d^3 p_3 \\
&\equiv \frac{g^4}{16(2\pi)^5 M_W^4} \frac{(p_4 - m_b s_b)^\alpha (p_1 - m_b s_a)^\beta d^3 p_4}{E_1 E_4} I_{\alpha\beta} \tag{D.42}
\end{aligned}$$

where

$$I_{\alpha\beta} \equiv \int \frac{p_{2\beta} p_{3\alpha} \delta^4(p_1 - p_2 - p_3 - p_4)}{E_2 E_3} d^3 p_2 d^3 p_3. \tag{D.43}$$

$p_{2\beta}$  and  $p_{3\alpha}$  can indeed be pulled out of the integral. For example, for  $p_{20}$  it is obvious since it is not involved in the integral. For  $p_{2i}$  where  $i = 1, 2, 3$  we have

$$\begin{aligned}
\int p_{2i} \delta(p_i - p_{2i} - p_{3i}) dp_{2i} &= \int p_{2i} \delta(p_i - p_{2i} - p_{3i}) dp_{2i} \\
&= p_i - p_{3i} \\
&= p_{2i} \\
&= p_{2i} \int \delta(p_i - p_{2i} - p_{3i}) dp_{2i} \tag{D.44}
\end{aligned}$$

In the rest frame of two neutrinos where  $|\mathbf{p}_2| = |\mathbf{p}_3| = E_3 = E_3$ , we can

evaluate the quantity

$$\begin{aligned}
I &= \int \frac{\delta^4(p - p_3 - p_4)}{E_2 E_3} d^3 p_2 d^3 p_3 \\
&= \int \frac{\delta^3(\mathbf{p} - \mathbf{p}_3 - \mathbf{p}_4) \delta(E - E_3 - E_4)}{E_2 E_3} d^3 p_2 d^3 p_3 \\
&= \int \frac{d^3 p_2 \delta(E - 2E_2)}{E_2^2} \\
&= \int \frac{p_2^2 d\Omega dp_2 \delta(E - 2E_2)}{E_2^2} \\
&= 4\pi \int dp_2 \delta(E - 2E_2) \\
&= 2\pi.
\end{aligned} \tag{D.45}$$

Since  $d\omega$  is a scalar, the only way to construct  $I_{\alpha\beta}$  is the following

$$I_{\alpha\beta} = g_{\alpha\beta} A(p^2) + p_\alpha p_\beta B(p^2). \tag{D.46}$$

we have

$$\begin{aligned}
g^{\alpha\beta} I_{\alpha\beta} &= 4A + p^2 B = (p^2/2)I, = \pi p^2, \\
p^\alpha p^\beta I_{\alpha\beta} &= p^2 A + p^4 B = (p^4/4)I = p^4 \pi/2,
\end{aligned} \tag{D.47}$$

where  $p^2 = 2p_2 \cdot p_3$  was used. By solving  $A$  and  $B$  we have

$$A = \frac{\pi}{6} p^2, \tag{D.48}$$

$$B = \frac{\pi}{3} p^4. \tag{D.49}$$

Thus

$$I_{\alpha\beta} = \frac{\pi}{6} (g_{\alpha\beta} p^2 + 2p_\alpha p_\beta) \tag{D.50}$$

The rate can now be written as

$$d\omega = \frac{g^4[(p_4 - m_b s_b) \cdot (p_1 - m_a s_a) p^2 + p \cdot (p_4 - m_b s_b) p \cdot (p_1 - m_a s_a)]}{192(2\pi)^4 M_W^4 E_1 E_4}. \quad (\text{D.51})$$

To evaluate this, it is convenient to use the rest frame of the decaying lepton, in which we have

$$p_1 = (m_a, \mathbf{0}) \quad (\text{D.52})$$

$$s_a = (0, \hat{\mathbf{s}}_a) \quad (\text{D.53})$$

$$p_4 = (E_4, \mathbf{p}_4) \quad (\text{D.54})$$

$$s_b = \left( \frac{\mathbf{p}_4 \cdot \hat{\mathbf{s}}_b}{m_b}, \hat{\mathbf{s}}_b + \frac{(\mathbf{p}_4 \cdot \hat{\mathbf{s}}_b) \mathbf{p}_4}{m_b(E_4 + m_b)} \right), \quad (\text{D.55})$$

where  $s_b$  was obtained from a boost in arbitrary direction. In a general case consider a particle of mass  $M$  at rest,  $\mathbf{P}=(M,0)$ . Under a Lorentz boost  $\beta$  it acquires four-momentum

$$\mathbf{P}' = (E', \mathbf{P}') = (\gamma M, \gamma \beta M). \quad (\text{D.56})$$

For a general four momentum  $p = (\varepsilon, \mathbf{p})$ , the boost gives

$$\varepsilon' = (\varepsilon E' + \mathbf{p} \cdot \mathbf{P}')/M, \quad (\text{D.57})$$

$$\mathbf{p}' = \mathbf{p} + \mathbf{P}'(\varepsilon + \varepsilon')/(E' + M). \quad (\text{D.58})$$

In the  $s_b$  case, we boost from the rest frame of electron  $(0, \hat{\mathbf{s}}_b)$  to the rest frame of the parent particle where the electron travels with  $p_4 = (E_4, \mathbf{p}_4)$ , i.e.

$$s_b = \left( \frac{\mathbf{p}_4 \cdot \hat{\mathbf{s}}_b}{m_b}, \hat{\mathbf{s}}_b + \frac{(\mathbf{p}_4 \cdot \hat{\mathbf{s}}_b) \mathbf{p}_4}{m_b(E_4 + m_b)} \right). \quad (\text{D.59})$$

Together with  $p = p_1 - p_4 = (m_a - E_4, -\mathbf{p}_4)$  and  $p^2 = m_a^2 + m_b^2 - 2m_a E_4$ , we have

$$\begin{aligned}
& (p_4 - m_b s_b) \cdot (p_1 - m_a s_a) p^2 \\
&= (m_a^2 + m_b^2 - 2M - aE_4) \\
& \quad \times \left[ m_a(E_4 - \mathbf{p}_4 \cdot \hat{\mathbf{s}}_b) + m_a \left( \mathbf{p}_4 - m_b \hat{\mathbf{s}}_b - \frac{(\mathbf{p}_4 \cdot \hat{\mathbf{s}}_b) \mathbf{p}_4}{m_b(E_4 + m_b)} \right) \cdot \hat{\mathbf{s}}_a \right] \quad (\text{D.60})
\end{aligned}$$

Define  $\hat{\mathbf{n}}$  to be the unit vector along  $\mathbf{p}_4$  and  $\cos \theta = \hat{\mathbf{s}}_a \cdot \hat{\mathbf{n}}$ . Neglecting the electron mass  $m_b$  gives

$$\begin{aligned}
& (p_4 - m_b s_b) \cdot (p_1 - m_a s_a) p^2 \\
&= \frac{m_a^4 x(1-x)}{2} (1 - \hat{\mathbf{s}}_b \cdot \hat{\mathbf{n}}) (1 + \cos \theta), \quad (\text{D.61})
\end{aligned}$$

where  $x = E_4/E_4^{\max}$  and  $E_4^{\max} = m_a/2$  is the maximum allowed value of  $E_4$ . Similarly,

$$\begin{aligned}
& p \cdot (p_4 - m_b s_b) p \cdot (p_1 - m_a s_a) \\
&= m_a^4 x \left[ 1 - \frac{x}{2} (1 + \cos \theta) \right] (1 - \hat{\mathbf{s}}_b \cdot \hat{\mathbf{n}}) \quad (\text{D.62})
\end{aligned}$$

Writing  $d^3 p_4 = p_4^2 d\Omega dp_4$ , the rate becomes

$$\begin{aligned}
d\omega &= \frac{g^4 p_4 dE_4 d\Omega}{192(2\pi)^4 M_W^4 E_1 E_4} \\
& \quad \times \left\{ \frac{m_a^4 x(1-x)}{2} (1 - \hat{\mathbf{s}}_b \cdot \hat{\mathbf{n}}) (1 + \cos \theta) + m_a^4 x \left[ 1 - \frac{x}{2} (1 + \cos \theta) \right] (1 - \hat{\mathbf{s}}_b \cdot \hat{\mathbf{n}}) \right\} \\
&= \frac{g^4 p_4 dE_4 d\Omega}{192(2\pi)^4 M_W^4 E_1 E_4} \left[ m_a^4 \frac{x(3-2x)}{2} (1 - \hat{\mathbf{s}}_b \cdot \hat{\mathbf{n}}) \left( 1 + \frac{1-2x}{3-2x} \cos \theta \right) \right]. \quad (\text{D.63})
\end{aligned}$$

$$n(x) = 2x^2(3 - 2x), \quad (\text{D.64})$$

$$\alpha(x) = (1 - 2x)/(3 - 2x), \quad (\text{D.65})$$

we have

$$d\omega = \left( \frac{g^4}{32M_W^4} \right) \frac{m_a^5}{192\pi^3} n(x) [1 - \alpha(x) \cos \theta] \left[ \frac{1 - \hat{\mathbf{s}}_b \cdot \hat{\mathbf{n}}}{2} \right] \frac{dx d \cos \theta d\phi}{4\pi}. \quad (\text{D.66})$$

Note that

$$\sum_{\hat{\mathbf{s}}_b} \frac{1 - \hat{\mathbf{s}}_b \cdot \hat{\mathbf{n}}}{2} = \frac{1 - 1/2}{2} + \frac{1 + 1/2}{2} = 1 \quad (\text{D.67})$$

$$\int (1 + \alpha(x) \cos \theta) \frac{d \cos \theta d\phi}{4\pi} = 1. \quad (\text{D.68})$$

Summing over the spin states and integrate over the solid angle, we get

$$\frac{d\omega}{dx} = \left( \frac{g^4}{32M_W^4} \right) \frac{m_a^5}{192\pi^3} n(x). \quad (\text{D.69})$$

Summing over the spin states and integrate over  $d\phi$  only, we get

$$\frac{d^2\omega}{dx d \cos \theta} = \frac{1}{2} \left( \frac{g^4}{32M_W^4} \right) \frac{m_a^5}{192\pi^3} n(x) [1 - \alpha(x) \cos \theta] \frac{dx d \cos \theta d\phi}{4\pi}. \quad (\text{D.70})$$

If we make a normalization such that Equation D.69 is equal to one (number of events in a particular energy bin), we have

$$\begin{aligned} \frac{d^2\omega}{dx d \cos \theta} &= \frac{1}{2} [1 - \alpha(x) \cos \theta], \\ &= \frac{1}{2} \left[ 1 - \frac{1 - 2x}{3 - 2x} \cos \theta \right] \end{aligned} \quad (\text{D.71})$$

Since the muons are the decay products of pions, for  $l_a^+$  we simply make a change of

$\theta \rightarrow 180 - \theta$ . To change from the rest frame of  $l_a^-$  to the lab from, a factor  $1/\gamma^2(1 - \beta \cos \theta)^2$  from Equation D.11 should be applied, i.e.

$$\frac{d^2\omega}{dx d \cos \theta} = \frac{1}{2\gamma^2(1 - \beta \cos \theta)^2} \left( 1 - \frac{1 - 2x}{3 - 2x} \cos \theta \right) \quad (\text{D.72})$$

This is sketched in Figure D.3. Considering the Equation D.51 and the approximation we made that  $m_b = 0$ , this rate is exactly the same for the  $\nu_a$  ( $\nu_\mu$ ).

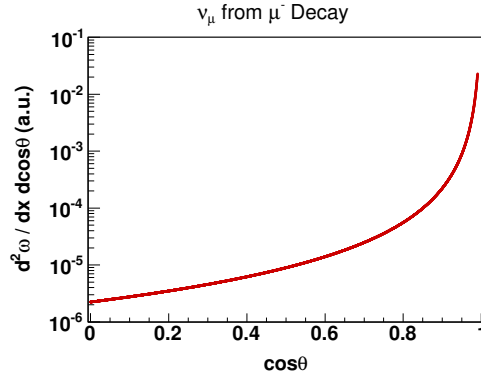


Figure D.3: Sketch of  $d^2\omega/dx d \cos \theta$  as a function of  $\cos \theta$  for a 50 GeV  $\mu^-$  and  $x = 0.5$ .  $\theta$  is the angle between the momentum of  $\nu_\mu$  and that of  $\mu^-$  in the lab frame.

# Appendix E

## Fitting with Correlated Systematics

### E.1 Two Methods

There are two ways to include correlated systematic uncertainties in  $\chi^2$ . One is the best-fit method where for each systematic uncertainty source there is a free parameter associated with it in the fit. Its  $\chi^2$  can be written as

$$\chi^2 = \sum_{i=1}^N \frac{\left(d_i - t_i - \sum_{j=1}^K \alpha_j s_{ji}\right)^2}{\sigma_i^2} + \sum_{j=1}^K \alpha_j^2, \quad (\text{E.1})$$

where  $N$  is the number of bins,  $K$  is the number of systematic sources,  $\sigma_i$  is the statistical uncertainty for bin  $i$ ,  $\alpha_j$  is the free parameter (nuisance parameter) for systematic source  $j$ ,  $s_{ji}$  is the uncertainty in bin  $i$  caused by systematic source  $j$ .

The other way is the covariance matrix method for which

$$\chi^2 = \Delta^T C^{-1} \Delta, \quad (\text{E.2})$$

where  $\Delta_i \equiv d_i - t_i$  and  $C$  is the covariance matrix. Reference [138] shows that the approaches are equivalent. This will be detailed in the next section.



## E.2 Equivalence

Starting from the best-fit approach, with the following definition

$$R_{ji} \equiv \frac{s_{ji}}{\sigma_i}, \quad (\text{E.3})$$

$$u_i \equiv \frac{d_i - t_i}{\sigma_i}, \quad (\text{E.4})$$

where  $R$  is a  $K \times N$  matrix and  $u$  is a  $N$  vector,  $\chi^2$  can be rewritten as

$$\begin{aligned} \chi^2 &= (u_i - \alpha_j R_{ji})(u_i - \alpha_j R_{ji}) + \alpha_j \alpha_j \\ &= (u - R^T \alpha)^T (u - R^T \alpha) + \alpha^T \alpha \\ &= (u^T - \alpha^T R)(u - R^T \alpha) + \alpha^T \alpha \\ &= u^T u - u^T R^T \alpha - \alpha^T R u + \alpha^T R R^T \alpha + \alpha^T \alpha. \end{aligned} \quad (\text{E.5})$$

To minimize  $\chi^2$ ,  $\alpha_{min}$  should satisfy  $\partial\chi^2/\partial\alpha = 0$ , i.e.

$$\begin{aligned} \frac{\partial\chi^2}{\partial\alpha_k} &= \frac{\partial}{\partial\alpha_k} (-\alpha_i^T R_{ij} u_j - u_i^T R_{ij}^T \alpha_j + \alpha_i^T R_{ij} R_{jl}^T \alpha_l + \alpha_i^T \alpha_i) \\ &= -\delta_{ik} R_{ij} u_j - u_i^T R_{ij}^T \delta_{jk} + \delta_{ik} R_{ij} R_{jl}^T \alpha_l + \alpha_i^T R_{ij} R_{jl}^T \delta_{kl} + 2\delta_{ki} \alpha_i \\ &= -R_{kj} u_j - u_i^T R_{ik}^T + R_{kj} R_{jl}^T \alpha_l + \alpha_i^T R_{ij} R_{jk}^T + 2\alpha_k \\ &= -R_{kj} u_j - u_j^T R_{kj} + R_{kj} R_{lj} \alpha_l + \alpha_l R_{lj} R_{kj} + 2\alpha_k \\ &= 2(-R_{kj} u_j + R_{kj} R_{lj} \alpha_l + \alpha_k) \\ &= 0. \end{aligned} \quad (\text{E.6})$$

Written in matrix form, this is

$$-R u + R R^T \alpha_{min} + \alpha_{min} = 0. \quad (\text{E.7})$$

Solving for  $\alpha_{min}$  gives

$$\begin{aligned}
\alpha_{min} &= (1 + RR^T)^{-1}Ru \\
&= (1 + RR^T)^{-1}R(1 + R^T R)(1 + R^T R)^{-1}u \\
&= (1 + RR^T)^{-1}(1 + RR^T)R(1 + R^T R)^{-1}u \\
&= R(1 + R^T R)^{-1}u,
\end{aligned} \tag{E.8}$$

where  $1 + RR^T$  is invertible according to Woodbury Formula

$$(A + UCV)^{-1} = A^{-1} - A^{-1}U(C^{-1} + VA^{-1}U)^{-1}VA^{-1} \tag{E.9}$$

( $A$ ,  $U$ ,  $C$  and  $V$  all denote matrices of the correct size). Inserting  $\alpha_{min}$  in Equation E.5 gives us  $\chi_{min}^2$ , the minimized  $\chi^2$ . As a shortcut, multiplying Equation E.7 with  $\alpha_{min}^T$  on the left gives

$$-\alpha_{min}^T Ru + \alpha_{min}^T RR^T \alpha_{min} + \alpha_{min}^T \alpha_{min} = 0. \tag{E.10}$$

This indicates the sum of the last three terms in Equation E.5 are equal to 0.

This leaves us

$$\begin{aligned}
\chi^2 &= u^T u - u^T R^T \alpha_{min} \\
&= u^T u - u^T R^T R(1 + R^T R)^{-1}u \\
&= u^T (1 + R^T R)^{-1}u.
\end{aligned} \tag{E.11}$$

Recall that

$$u_i \equiv \frac{d_i - t_i}{\sigma_i}, \tag{E.12}$$

$$\Delta_i \equiv d_i - t_i, \tag{E.13}$$

we have  $\Delta_i = u_i \sigma_i$ . Defining the matrix

$$S \equiv \begin{pmatrix} \sigma_1 & & & \\ & \sigma_2 & & \\ & & \ddots & \\ & & & \sigma_N \end{pmatrix}, \quad (\text{E.14})$$

or  $S_{ij} = \sigma_i \delta_{ij}$  (no sum on  $i$ ), we can write  $\Delta = Su$  or  $u = S^{-1}\Delta$ . Therefore

$$\begin{aligned} \chi_{min}^2 &= \Delta^T (S^{-1})^T (1 + R^T R)^{-1} S^{-1} \Delta \\ &= \Delta^T [S (1 + R^T R) S^T]^{-1} \Delta \\ &= \Delta^T C^{-1} \Delta, \end{aligned} \quad (\text{E.15})$$

where  $C \equiv S (1 + R^T R) S^T$ . Writing  $C$  in component form, we have

$$\begin{aligned} C_{ij} &= S_{il} (\delta_{lk} + R_{lm}^T R_{mk}) S_{kj}^T \\ &= \sigma_i \delta_{il} (\delta_{lk} + R_{lm}^T R_{mk}) \delta_{jk} \sigma_j \\ &= \sigma_i (\delta_{ij} + R_{lm}^T R_{mk}) \sigma_j \\ &= \sigma_i \sigma_j \delta_{ij} + R_{lm}^T R_{mk} \sigma_i \sigma_j \\ &= \sigma_i \sigma_j \delta_{ij} + \frac{s_{mi}}{\sigma_i} \frac{s_{mj}}{\sigma_j} \sigma_i \sigma_j \\ &= \sigma_i \sigma_j \delta_{ij} + s_{mi} s_{mj}. \end{aligned} \quad (\text{E.16})$$

Given  $s_{ij}$ , covariance matrix  $C$  can be computed according to Equation E.16.

## Bibliography

- [1] J. Chadwick, “The intensity distribution in the magnetic spectrum of beta particles from radium (B + C),” *Verh.Phys.Gesell.*, vol. 16, pp. 383–391, 1914.
- [2] W. Pauli, “Dear radioactive ladies and gentlemen,” *Phys.Today*, vol. 31N9, p. 27, 1978.
- [3] C. Cowan, F. Reines, F. Harrison, H. Kruse, and A. McGuire, “Detection of the free neutrino: A Confirmation,” *Science*, vol. 124, pp. 103–104, 1956.
- [4] B. Pontecorvo, “Electron and Muon Neutrinos,” *Sov.Phys.JETP*, vol. 10, pp. 1236–1240, 1960.
- [5] G. Danby, J. Gaillard, K. A. Goulianos, L. Lederman, N. B. Mistry, *et al.*, “Observation of High-Energy Neutrino Reactions and the Existence of Two Kinds of Neutrinos,” *Phys.Rev.Lett.*, vol. 9, pp. 36–44, 1962.
- [6] M. L. Perl, G. Abrams, A. Boyarski, M. Breidenbach, D. Briggs, *et al.*, “Evidence for Anomalous Lepton Production in  $e^+ - e^-$  Annihilation,” *Phys.Rev.Lett.*, vol. 35, pp. 1489–1492, 1975.
- [7] K. Kodama *et al.*, “Observation of tau neutrino interactions,” *Phys.Lett.*, vol. B504, pp. 218–224, 2001.

- [8] S. Schael *et al.*, “Precision electroweak measurements on the  $Z$  resonance,” *Phys.Rept.*, vol. 427, pp. 257–454, 2006.
- [9] P. Ade *et al.*, “Planck 2015 results. XIII. Cosmological parameters,” 2015.
- [10] G. Hinshaw *et al.*, “Nine-Year Wilkinson Microwave Anisotropy Probe (WMAP) Observations: Cosmological Parameter Results,” *Astrophys.J.Suppl.*, vol. 208, p. 19, 2013.
- [11] C. Wu, E. Ambler, R. Hayward, D. Hoppes, and R. Hudson, “Experimental Test of Parity Conservation in Beta Decay,” *Phys.Rev.*, vol. 105, pp. 1413–1414, 1957.
- [12] M. Goldhaber, L. Grodzins, and A. Sunyar, “Helicity of Neutrinos,” *Phys.Rev.*, vol. 109, pp. 1015–1017, 1958.
- [13] B. Pontecorvo, “Mesonium and anti-mesonium,” *Sov.Phys.JETP*, vol. 6, p. 429, 1957.
- [14] B. Pontecorvo, “Inverse beta processes and nonconservation of lepton charge,” *Sov.Phys.JETP*, vol. 7, pp. 172–173, 1958.
- [15] Z. Maki, M. Nakagawa, and S. Sakata, “Remarks on the unified model of elementary particles,” *Prog.Theor.Phys.*, vol. 28, pp. 870–880, 1962.
- [16] K. Olive *et al.*, “Review of Particle Physics,” *Chin.Phys.*, vol. C38, p. 090001, 2014.

- [17] J. N. Bahcall, A. M. Serenelli, and S. Basu, “New solar opacities, abundances, helioseismology, and neutrino fluxes,” *Astrophys.J.*, vol. 621, pp. L85–L88, 2005.
- [18] J. N. Bahcall, “Home page <http://www.sns.ias.edu/~jnb/>.”
- [19] J. Davis, Raymond, D. S. Harmer, and K. C. Hoffman, “Search for neutrinos from the sun,” *Phys.Rev.Lett.*, vol. 20, pp. 1205–1209, 1968.
- [20] K. Hirata *et al.*, “Observation of B-8 Solar Neutrinos in the Kamiokande-II Detector,” *Phys.Rev.Lett.*, vol. 63, p. 16, 1989.
- [21] A. Abazov, O. Anosov, E. Faizov, V. Gavrin, A. Kalikhov, *et al.*, “Search for neutrinos from sun using the reaction Ga-71 (electron-neutrino e-) Ge-71,” *Phys.Rev.Lett.*, vol. 67, pp. 3332–3335, 1991.
- [22] P. Anselmann *et al.*, “Solar neutrinos observed by GALLEX at Gran Sasso,” *Phys.Lett.*, vol. B285, pp. 376–389, 1992.
- [23] Q. Ahmad *et al.*, “Measurement of the rate of  $\nu_e + d \rightarrow p + p + e^-$  interactions produced by  $^8B$  solar neutrinos at the Sudbury Neutrino Observatory,” *Phys.Rev.Lett.*, vol. 87, p. 071301, 2001.
- [24] Q. Ahmad *et al.*, “Direct evidence for neutrino flavor transformation from neutral current interactions in the Sudbury Neutrino Observatory,” *Phys.Rev.Lett.*, vol. 89, p. 011301, 2002.

- [25] C. Arpesella *et al.*, “First real time detection of Be-7 solar neutrinos by Borexino,” *Phys.Lett.*, vol. B658, pp. 101–108, 2008.
- [26] A. Renshaw *et al.*, “First Indication of Terrestrial Matter Effects on Solar Neutrino Oscillation,” *Phys.Rev.Lett.*, vol. 112, no. 9, p. 091805, 2014.
- [27] M. Honda, T. Kajita, K. Kasahara, and S. Midorikawa, “A New calculation of the atmospheric neutrino flux in a 3-dimensional scheme,” *Phys.Rev.*, vol. D70, p. 043008, 2004.
- [28] M. Honda, T. Kajita, K. Kasahara, S. Midorikawa, and T. Sanuki, “Calculation of atmospheric neutrino flux using the interaction model calibrated with atmospheric muon data,” *Phys.Rev.*, vol. D75, p. 043006, 2007.
- [29] G. Barr, T. Gaisser, P. Lipari, S. Robbins, and T. Stanev, “A Three - dimensional calculation of atmospheric neutrinos,” *Phys.Rev.*, vol. D70, p. 023006, 2004.
- [30] G. Battistoni, A. Ferrari, T. Montaruli, and P. Sala, “The FLUKA atmospheric neutrino flux calculation,” *Astropart.Phys.*, vol. 19, pp. 269–290, 2003.
- [31] Y. Fukuda *et al.*, “Evidence for oscillation of atmospheric neutrinos,” *Phys.Rev.Lett.*, vol. 81, pp. 1562–1567, 1998.

- [32] T. Mueller, D. Lhuillier, M. Fallot, A. Letourneau, S. Cormon, *et al.*, “Improved Predictions of Reactor Antineutrino Spectra,” *Phys.Rev.*, vol. C83, p. 054615, 2011.
- [33] K. Eguchi *et al.*, “First results from KamLAND: Evidence for reactor anti-neutrino disappearance,” *Phys.Rev.Lett.*, vol. 90, p. 021802, 2003.
- [34] Y. Abe *et al.*, “Indication for the disappearance of reactor electron antineutrinos in the Double Chooz experiment,” *Phys.Rev.Lett.*, vol. 108, p. 131801, 2012.
- [35] F. An *et al.*, “Observation of electron-antineutrino disappearance at Daya Bay,” *Phys.Rev.Lett.*, vol. 108, p. 171803, 2012.
- [36] J. Ahn *et al.*, “Observation of Reactor Electron Antineutrino Disappearance in the RENO Experiment,” *Phys.Rev.Lett.*, vol. 108, p. 191802, 2012.
- [37] S. E. Kopp, “Accelerator-based neutrino beams,” *Phys.Rept.*, vol. 439, pp. 101–159, 2007.
- [38] M. Ahn *et al.*, “Measurement of Neutrino Oscillation by the K2K Experiment,” *Phys.Rev.*, vol. D74, p. 072003, 2006.
- [39] P. Adamson *et al.*, “Combined analysis of  $\nu_\mu$  disappearance and  $\nu_\mu \rightarrow \nu_e$  appearance in MINOS using accelerator and atmospheric neutrinos,” *Phys.Rev.Lett.*, vol. 112, p. 191801, 2014.



- [40] P. Adamson *et al.*, “First direct observation of muon antineutrino disappearance,” *Phys.Rev.Lett.*, vol. 107, p. 021801, 2011.
- [41] P. Adamson *et al.*, “An improved measurement of muon antineutrino disappearance in MINOS,” *Phys.Rev.Lett.*, vol. 108, p. 191801, 2012.
- [42] K. Abe *et al.*, “First Muon-Neutrino Disappearance Study with an Off-Axis Beam,” *Phys.Rev.*, vol. D85, p. 031103, 2012.
- [43] A. Pastore, “Talk at the eps hep 2013 conference, july 18-24, 2013, stockholm.”
- [44] C. Giunti, “The Phase of neutrino oscillations,” *Phys.Scripta*, vol. 67, pp. 29–33, 2003.
- [45] H. Harari and M. Leurer, “Recommending a Standard Choice of Cabibbo Angles and KM Phases for Any Number of Generations,” *Phys.Lett.*, vol. B181, p. 123, 1986.
- [46] J. Hewett, H. Weerts, R. Brock, J. Butler, B. Casey, *et al.*, “Fundamental Physics at the Intensity Frontier,” 2012.
- [47] F. Capozzi, G. Fogli, E. Lisi, A. Marrone, D. Montanino, *et al.*, “Status of three-neutrino oscillation parameters, circa 2013,” *Phys.Rev.*, vol. D89, no. 9, p. 093018, 2014.
- [48] V. Gribov and B. Pontecorvo, “Neutrino astronomy and lepton charge,” *Phys.Lett.*, vol. B28, p. 493, 1969.

- [49] A. Aguilar-Arevalo *et al.*, “Evidence for neutrino oscillations from the observation of anti-neutrino(electron) appearance in a anti-neutrino(muon) beam,” *Phys.Rev.*, vol. D64, p. 112007, 2001.
- [50] A. Aguilar-Arevalo *et al.*, “Event Excess in the MiniBooNE Search for  $\bar{\nu}_\mu \rightarrow \bar{\nu}_e$  Oscillations,” *Phys.Rev.Lett.*, vol. 105, p. 181801, 2010.
- [51] A. Aguilar-Arevalo *et al.*, “Improved Search for  $\bar{\nu}_\mu \rightarrow \bar{\nu}_e$  Oscillations in the MiniBooNE Experiment,” *Phys.Rev.Lett.*, vol. 110, p. 161801, 2013.
- [52] G. Mention, M. Fechner, T. Lasserre, T. Mueller, D. Lhuillier, *et al.*, “The Reactor Antineutrino Anomaly,” *Phys.Rev.*, vol. D83, p. 073006, 2011.
- [53] P. Anselmann *et al.*, “First results from the Cr-51 neutrino source experiment with the GALLEX detector,” *Phys.Lett.*, vol. B342, pp. 440–450, 1995.
- [54] W. Hampel *et al.*, “Final results of the Cr-51 neutrino source experiments in GALLEX,” *Phys.Lett.*, vol. B420, pp. 114–126, 1998.
- [55] D. Abdurashitov, V. Gavrin, S. Girin, V. Gorbachev, T. V. Ibragimova, *et al.*, “The Russian-American gallium experiment (SAGE) Cr neutrino source measurement,” *Phys.Rev.Lett.*, vol. 77, pp. 4708–4711, 1996.
- [56] J. Abdurashitov *et al.*, “Measurement of the response of the Russian-American gallium experiment to neutrinos from a Cr-51 source,” *Phys.Rev.*, vol. C59, pp. 2246–2263, 1999.

- [57] Y. Declais, J. Favier, A. Metref, H. Pessard, B. Achkar, *et al.*, “Search for neutrino oscillations at 15-meters, 40-meters, and 95-meters from a nuclear power reactor at Bugey,” *Nucl.Phys.*, vol. B434, pp. 503–534, 1995.
- [58] A. Romosan *et al.*, “A High statistics search for muon-neutrino (anti-muon-neutrino)  $\rightarrow$  electron-neutrino (anti-electron-neutrino) oscillations in the small mixing angle regime,” *Phys.Rev.Lett.*, vol. 78, pp. 2912–2915, 1997.
- [59] D. Autiero, “Talk presented at the 1998 international conference on high energy physics in vancouver, canada..”
- [60] K. Eitel, “talk presented at the 2000 international neutrino conference in sudbury, canada..”
- [61] C. Athanassopoulos *et al.*, “Candidate events in a search for anti-muon-neutrino  $\rightarrow$  anti-electron-neutrino oscillations,” *Phys.Rev.Lett.*, vol. 75, pp. 2650–2653, 1995.
- [62] C. Athanassopoulos *et al.*, “Evidence for anti-muon-neutrino  $\rightarrow$  anti-electron-neutrino oscillations from the LSND experiment at LAMPF,” *Phys.Rev.Lett.*, vol. 77, pp. 3082–3085, 1996.
- [63] C. Athanassopoulos *et al.*, “Evidence for  $\nu(\mu) \rightarrow \nu(e)$  neutrino oscillations from LSND,” *Phys.Rev.Lett.*, vol. 81, pp. 1774–1777, 1998.

- [64] C. Athanassopoulos *et al.*, “Evidence for muon-neutrino  $\rightarrow$  electron-neutrino oscillations from pion decay in flight neutrinos,” *Phys.Rev.*, vol. C58, pp. 2489–2511, 1998.
- [65] B. Armbruster *et al.*, “Upper limits for neutrino oscillations muon-anti-neutrino  $\rightarrow$  electron-anti-neutrino from muon decay at rest,” *Phys.Rev.*, vol. D65, p. 112001, 2002.
- [66] A. Palazzo, “An estimate of  $\theta_{14}$  independent of the reactor antineutrino flux determinations,” *Phys.Rev.*, vol. D85, p. 077301, 2012.
- [67] N. Arkani-Hamed, S. Dimopoulos, and G. Dvali, “The Hierarchy problem and new dimensions at a millimeter,” *Phys.Lett.*, vol. B429, pp. 263–272, 1998.
- [68] N. Arkani-Hamed, S. Dimopoulos, G. Dvali, and J. March-Russell, “Neutrino masses from large extra dimensions,” *Phys.Rev.*, vol. D65, p. 024032, 2002.
- [69] N. Arkani-Hamed and S. Dimopoulos, “New origin for approximate symmetries from distant breaking in extra dimensions,” *Phys.Rev.*, vol. D65, p. 052003, 2002.
- [70] H. Davoudiasl, P. Langacker, and M. Perelstein, “Constraints on large extra dimensions from neutrino oscillation experiments,” *Phys.Rev.*, vol. D65, p. 105015, 2002.

- [71] P. Machado, H. Nunokawa, and R. Zukanovich Funchal, “Testing for Large Extra Dimensions with Neutrino Oscillations,” *Phys.Rev.*, vol. D84, p. 013003, 2011.
- [72] P. Machado, H. Nunokawa, F. Pereira dos Santos, and R. Zukanovich Funchal, “Large extra dimensions and reactor antineutrino anomaly,” *J.Phys.Conf.Ser.*, vol. 375, p. 042047, 2012.
- [73] J. S. Mitchell, “Measuring  $\nu_\mu$  Disappearance with the MINOS Experiment,” 2011.
- [74] A. Holin and P. Adamson, “Numi beam brag plots, minos document 9258,” May 2012.
- [75] G. Tzanankos *et al.*, “MINOS+: a Proposal to FNAL to run MINOS with the medium energy NuMI beam,” 2011.
- [76] A. Blake, “Pot counting for run period 11, minos document 10799,” September 2014.
- [77] A. Holin, A. Radovic, and A. Schreckenberger, “Blessed plots for the 2014 beam systematics group, minos document 10630,” May 2014.
- [78] P. Adamson, “Beam status, minos document 10748,” September 2014.
- [79] J. Evans, “The MINOS experiment: results and prospects,” *Adv.High Energy Phys.*, vol. 2013, p. 182537, 2013.

- [80] P. Adamson *et al.*, “A Study of Muon Neutrino Disappearance Using the Fermilab Main Injector Neutrino Beam,” *Phys.Rev.*, vol. D77, p. 072002, 2008.
- [81] D. Michael *et al.*, “The Magnetized steel and scintillator calorimeters of the MINOS experiment,” *Nucl.Instrum.Meth.*, vol. A596, pp. 190–228, 2008.
- [82] J. J. Evans, “Measuring Antineutrino Oscillations with the MINOS Experiment,” 2008.
- [83] P. Adamson *et al.*, “Measurement of the neutrino mass splitting and flavor mixing by MINOS,” *Phys.Rev.Lett.*, vol. 106, p. 181801, 2011.
- [84] T. M. Cover and P. E. Hart, “Nearest neighbor pattern classification,” *IEEE Trans. Inf. Theory*, vol. 13, p. 21, 1967.
- [85] C. J. Backhouse, “Measuring neutrino oscillation parameters using  $\nu_\mu$  disappearance in MINOS,” 2011.
- [86] J. S. Marshall, “A study of muon neutrino disappearance with the MINOS detectors and the NuMI neutrino beam,” 2008.
- [87] J. L. Bentley, “Multidimensional binary search trees used for associative searching,” *Commun. ACM*, vol. 18, pp. 509–517, Sept. 1975.
- [88] J. K. Uhlmann, “Satisfying general proximity / similarity queries with metric trees,” *Information Processing Letters*, vol. 40, no. 4, pp. 175 – 179, 1991.

- [89] P. N. Yianilos, "Data structures and algorithms for nearest neighbor search in general metric spaces," in *Proceedings of the Fifth Annual ACM-SIAM Symposium on Discrete Algorithms (SODA)*, 1993.
- [90] P. C. Mahalanobis, "On the generalised distance in statistics," *Proceedings of the National Institute of Sciences of India*, vol. 2, no. 1, p. 49, 1936.
- [91] J. E. Gentle, *Numerical Linear Algebra for Applications in Statistics*. Berlin: Springer-Verlag, 1998.
- [92] P. v. Laarhoven and E. Aarts, *Simulated Annealing: Theory and Applications*. Springer Science & Business Media, 1987.
- [93] A. Hoecker, P. Speckmayer, J. Stelzer, J. Therhaag, E. von Toerne, and H. Voss, "TMVA: Toolkit for Multivariate Data Analysis," *PoS*, vol. ACAT, p. 040, 2007.
- [94] M. A. Kordosky, "Hadronic interactions in the MINOS detectors," 2004.
- [95] J. DeJong, "2009 position paper on calibration of runs i-ii-iii, minos document 6717," January 2010.
- [96] S. Dytman, "New intranuke model for neugen - ha, minos document 3484," August 2007.
- [97] M. Kordosky, "A procedure to re-weight events to account for uncertainties in final state interactions, minos document 3449," August 2007.

- [98] T. Yang, C. Andreopoulos, H. Gallagher, K. Hoffmann, and P. Kehayias, “A Hadronization Model for Few-GeV Neutrino Interactions,” *Eur.Phys.J.*, vol. C63, pp. 1–10, 2009.
- [99] J. Evans, “Absolute (calorimetric) shower energy uncertainty, minos document 7173,” April 2010.
- [100] G. M. Tinti, “Sterile neutrino oscillations in MINOS and hadron production in pC collisions,” 2010.
- [101] T. H. Osiecki, “A search for sterile neutrinos in MINOS,” 2007.
- [102] R. Ospanov, “A measurement of muon neutrino disappearance with the MINOS detectors and NuMI beam,” 2008.
- [103] J. S. Ratchford, “Identifying Muons for Neutrino Oscillation and Cross Section Experiments,”
- [104] J. Evans, K. Lang, and R. Nichol, “Position paper on the 2010 analysis of charged current events from runs i, ii and iii, minos document 7218,” April 2010.
- [105] A. Aurisano, “A position paper on constructing systematic covariance matrices for the 2014 sterile analysis, minos document 10581,” April 2014.
- [106] J. Musser *et al.*, “Range curvature task force position paper, minos document 3134,” June 2007.



- [107] P. Adamson *et al.*, “Search for sterile neutrino mixing in the MINOS long baseline experiment,” *Phys.Rev.*, vol. D81, p. 052004, 2010.
- [108] J. DeJong, “Position paper for the runs i-iii fd nc cleaning, minos document 7165,” April 2010.
- [109] J. Evans, “Systematic uncertainties for the 2010 cc analysis, minos document 7145,” April 2010.
- [110] H. Gallagher, “The NEUGEN neutrino event generator,” *Nucl.Phys.Proc.Suppl.*, vol. 112, pp. 188–194, 2002.
- [111] P. Rodrigues, “Notes on the normalization systematic, minos document 6636,” January 2009.
- [112] J. DeJong *et al.*, “Calibration position paper for pre-shutdown data, minos document 3941,” March 2008.
- [113] P. Rodrigues, “A Sterile-Neutrino Search with the MINOS Experiment,” 2010.
- [114] J. O’Connor, “Position paper for the nd cleaning systematic re-evaluation in the 2013 sterile analysis, minos document 9819,” May 2013.
- [115] A. Radovic and M. Kordosky, “A position paper describing a hadron production uncertainty covariance matrix, minos document 10569,” April 2014.

- [116] A. Timmons, “Position paper: Beam optic systematic matrices for the 2014 sterile analysis, minos document 10580,” April 2014.
- [117] A. Timmons, “Minos and minos+ beam focusing covariance matrices, minos document 10964,” March 2015.
- [118] A. Timmons, “Position paper about the f/n fit for the 2014 sterile neutrino analysis, minos document 10575,” November 2014.
- [119] J. Coelho, J. Evans, and M. Kordosky, “Searching for sterile neutrinos, minos document 10583,” April 2014.
- [120] F. An *et al.*, “Spectral measurement of electron antineutrino oscillation amplitude and frequency at Daya Bay,” *Phys.Rev.Lett.*, vol. 112, p. 061801, 2014.
- [121] F. James and M. Roos, “Minuit - a system for function minimization and analysis of the parameter errors and correlations,” *Computer Physics Communications*, vol. 10, no. 6, pp. 343 – 367, 1975.
- [122] J. Coelho, “Sterile neutrinos group report, minos document 10992-,” February 2015.
- [123] G. J. Feldman and R. D. Cousins, “A Unified approach to the classical statistical analysis of small signals,” *Phys.Rev.*, vol. D57, pp. 3873–3889, 1998.

- [124] F. Dydak, G. Feldman, C. Guyot, J. Merlo, H. Meyer, *et al.*, “A Search for Muon-neutrino Oscillations in the Delta  $m^{**2}$  Range 0.3-eV $^{**2}$  to 90-eV $^{**2}$ ,” *Phys.Lett.*, vol. B134, p. 281, 1984.
- [125] I. Stockdale, A. Bodek, F. Borcharding, N. Giokaris, K. Lang, *et al.*, “Limits on Muon Neutrino Oscillations in the Mass Range 55-eV $^{**2}$  ; Delta  $m^{**2}$  ; 800-eV $^{**2}$ ,” *Phys.Rev.Lett.*, vol. 52, p. 1384, 1984.
- [126] K. Mahn *et al.*, “Dual baseline search for muon neutrino disappearance at  $0.5\text{eV}^2 < \Delta m^2 < 40\text{eV}^2$ ,” *Phys.Rev.*, vol. D85, p. 032007, 2012.
- [127] M. Antonello *et al.*, “Search for anomalies in the  $\nu_e$  appearance from a  $\nu_\mu$  beam,” *Eur.Phys.J.*, vol. C73, p. 2599, 2013.
- [128] N. Agafonova *et al.*, “Search for  $\nu_\mu \rightarrow \nu_e$  oscillations with the OPERA experiment in the CNGS beam,” *JHEP*, vol. 1307, p. 004, 2013.
- [129] S. Hannestad and G. G. Raffelt, “Supernova and neutron star limits on large extra dimensions reexamined,” *Phys.Rev.*, vol. D67, p. 125008, 2003.
- [130] L. J. Hall and D. Tucker-Smith, “Cosmological constraints on theories with large extra dimensions,” *Phys.Rev.*, vol. D60, p. 085008, 1999.
- [131] C. Hanhart, J. A. Pons, D. R. Phillips, and S. Reddy, “The Likelihood of GODs’ existence: Improving the SN1987a constraint on the size of large compact dimensions,” *Phys.Lett.*, vol. B509, pp. 1–9, 2001.

- [132] E. Adelberger, J. Gundlach, B. Heckel, S. Hoedl, and S. Schlamminger, “Torsion balance experiments: A low-energy frontier of particle physics,” *Prog.Part.Nucl.Phys.*, vol. 62, pp. 102–134, 2009.
- [133] “Aleph, delphi, l3, opal collaborations and the lep exotica working group, lep exotica wg 2004-03, aleph 2004-007, delphi 2004-033 conf 708, l3 note 2798, opal technical note tn743..” <http://lepexotica.web.cern.ch/LEPEXOTICA/>, 2004.
- [134] J. Abdallah *et al.*, “Search for one large extra dimension with the DELPHI detector at LEP,” *Eur.Phys.J.*, vol. C60, pp. 17–23, 2009.
- [135] M. Kaku, “Quantum field theory: A Modern introduction,” 1993.
- [136] A. Perez-Lorenzana, “An Introduction to extra dimensions,” *J.Phys.Conf.Ser.*, vol. 18, pp. 224–269, 2005.
- [137] P. Renton, *Electroweak Interactions, An Introduction to the Physics of Quarks and Leptons*. Cambridge University Press, 1990.
- [138] L. Demortier, “Equivalence of the best-fit and covariance-matrix methods for comparing binned data with a model in the presence of correlated systematic uncertainties.” [http://www-cdf.fnal.gov/physics/statistics/notes/cdf8661\\_chi2fit\\_w\\_corr\\_syst.pdf](http://www-cdf.fnal.gov/physics/statistics/notes/cdf8661_chi2fit_w_corr_syst.pdf), April 1999.

## Vita

Junting Huang was born in Yining, Xinjiang Province of China on October 6, 1984, the son of Jinxin Huang and Fen Deng. He graduated from *National Base for the Training of Research and Teaching Personnel in Physics* and received a Bachelor of Science degree in Physics from Lanzhou University (China) in 2007. He then received a Master of Science degree in Physics from Texas A&M University-Commerce in 2009 under the supervision of Dr. Carlos Bertulani. He was accepted and started the Ph.D. program in the University of Texas at Austin in August, 2009.

Permanent address: The University of Texas at Austin  
Department of Physics  
2515 Speedway, C1600  
Austin, TX 78712-1192

This dissertation was typeset with L<sup>A</sup>T<sub>E</sub>X<sup>†</sup> by the author.

---

<sup>†</sup>L<sup>A</sup>T<sub>E</sub>X is a document preparation system developed by Leslie Lamport as a special version of Donald Knuth's T<sub>E</sub>X Program.